

# **Non-Collinear Magnetism at Surfaces and in Ultrathin Films**

Der Fakultät für Mathematik, Informatik und Naturwissenschaften  
der Rheinisch-Westfälischen Technischen Hochschule Aachen  
vorgelegte Dissertation zur Erlangung des akademischen Grades  
eines Doktors der Naturwissenschaften

von

Diplom-Physiker

Philipp Kurz

aus Haan



# Abstract

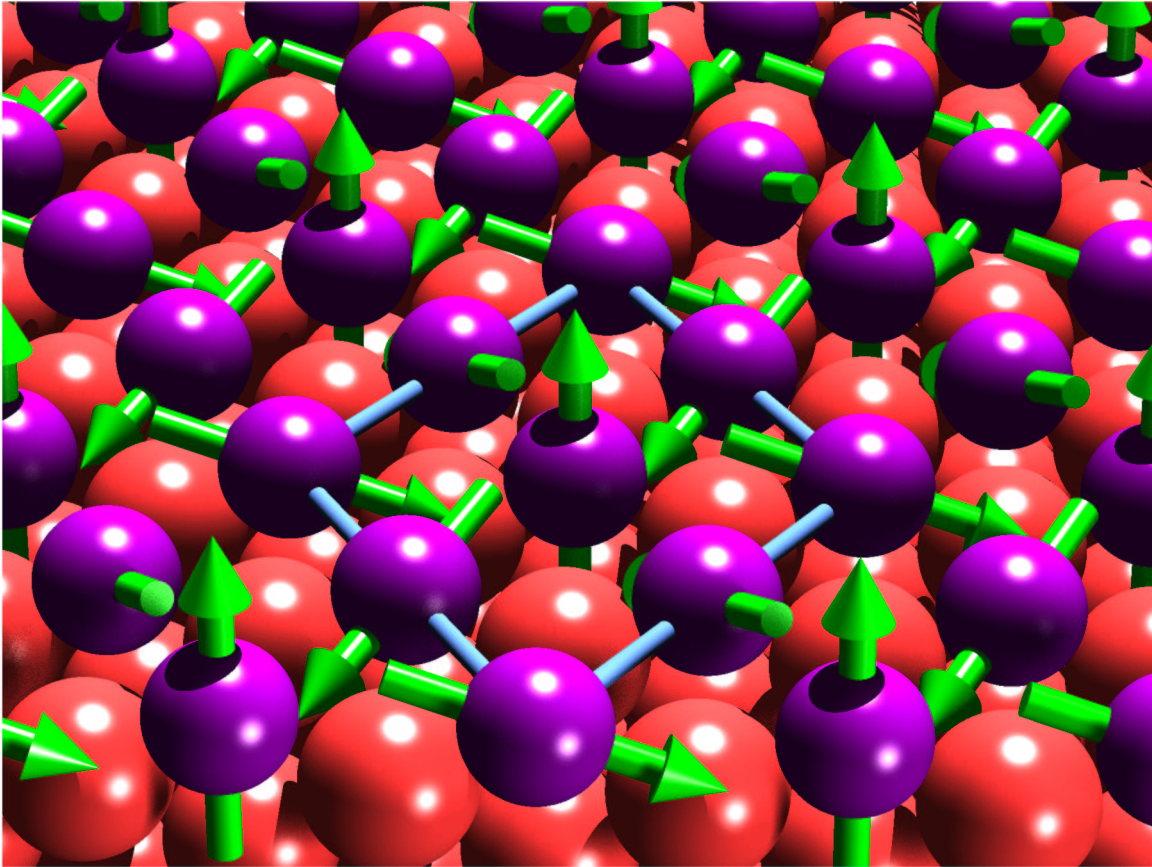
On the basis of the FLAPW method we developed and applied a self-consistent full-potential non-collinear vector spin-density ab-initio program for bulk, surfaces and thin films. In order to be able to deal with arbitrary magnetic configurations, which are not necessarily the magnetic ground state or a stationary state of the system under consideration, we implemented the constrained local moment method. On the basis of a generalization of the Bloch theorem for spiral magnetic states we have extended the vector spin-density FLAPW method to also allow commensurate and incommensurate spin-spiral calculations. We give an account of the implementation and discuss the importance of the approximations that are used.

We have applied this method to the problem of geometric frustration of the two-dimensional antiferromagnet on a triangular lattice. We have performed self-consistent calculations for the  $3d$  transition metal monolayers V, Cr, Mn and Fe on the (111) oriented surfaces of Cu and Ag. We investigated the magnetism, the interlayer relaxation, and the energetics of a nearly complete set of magnetic states and found an amazing variety of different magnetic ground states: ferromagnetic for Fe/Cu(111) and Fe/Ag(111); row-wise antiferromagnetic for Mn/Ag(111); the  $120^\circ$  Néel state for V/Ag(111), Cr/Cu(111) and Cr/Ag(111); and the so-called 3Q state, a complex three-dimensional non-collinear state, shown on the next page, for Mn/Cu(111). By comparing the self-consistent calculations to the Heisenberg model, we show that higher order spin-interactions, like the biquadratic of the 4-spin interaction, play an important role for the itinerant  $3d$  metals. In fact, it is the 4-spin interaction that leads to the stabilization of the 3Q state in the case of Mn/Cu(111). From these results we conclude that any realistic description of two-dimensional itinerant antiferromagnets on a triangular lattice requires exchange interactions not only beyond the nearest neighbors but also exchange interactions beyond the Heisenberg model.

The localized  $4f$  states of Gd represent a challenge for first-principle theory. By comparing different methods to treat the  $4f$ -states, we show that the large unphysical density of states at the Fermi energy due to the minority  $4f$  electrons are the origin of the incorrect prediction of the antiferromagnetic ground state for hcp Gd by many LDA and GGA calculations. Methods that remove these states from the region close to the Fermi energy, lead to the prediction of the correct ferromagnetic ground state and allow the calculation of ground state properties like the magnetic moment and the equilibrium lattice constant in good agreement with experiment. After almost a decade of intense research, the temperature dependence of the spin-splitting of the  $d_{z^2}$  surface state of Gd is very controversial. To model the temperature dependence of the electronic structure of the Gd(0001) surface, we performed non-collinear spin-spiral calculations. We calculated the local density of states, which is probed by scanning tunneling spectroscopy (STS) experiments, as function of the spin-spiral  $q$ -vector. In the ferromagnetic configuration we found two pronounced peaks in the local density of states in the vacuum, which originate from the spin-split  $d_{z^2}$  surface state of Gd. With increasing  $q$ -vector, corresponding to increasing temperature, the splitting of

the two peaks decreases and finally vanishes. However, in all magnetic configurations we found a finite valence magnetic moment, Hence, the vanishing splitting cannot be taken as support for the applicability of a pure Stoner model.





This complex three-dimensional non-collinear magnetic state, the so-called 3Q-state, a particular superposition of three spin-waves, is the magnetic ground state of a two-dimensional manganese monolayer with chemically identical manganese atoms on a (111) oriented copper substrate.



# Contents

<b>1</b>	<b>Introduction</b>	<b>1</b>
<b>2</b>	<b>The Density Functional Theory</b>	<b>9</b>
2.1	The Theorem of Hohenberg and Kohn . . . . .	9
2.2	The Kohn-Sham Equations . . . . .	10
2.3	Spin Density Functional Theory . . . . .	12
2.4	The Local Spin Density Approximation . . . . .	13
2.5	Determination of the Total Energy . . . . .	14
2.6	The Stoner Model of Itinerant Magnetism . . . . .	15
<b>3</b>	<b>The FLAPW Method</b>	<b>19</b>
3.1	The FLAPW Method . . . . .	19
3.1.1	The APW Method and its Problems . . . . .	19
3.1.2	The Concept of LAPW . . . . .	21
3.1.3	The Concept of FLAPW . . . . .	23
3.1.4	The Generalized Eigenvalue Problem . . . . .	24
3.1.5	Film Calculations within FLAPW . . . . .	25
3.2	Relativity in Valence Electron Calculations . . . . .	27
3.2.1	The Kohn-Sham-Dirac Equation . . . . .	28
3.2.2	The Scalar Relativistic Approximation . . . . .	29
3.3	Construction of the Hamiltonian Matrix . . . . .	32
3.3.1	Contribution of the Muffin-Tins . . . . .	33
3.3.2	The Vacuum Contribution . . . . .	35
3.3.3	The Interstitial Contribution . . . . .	36
3.3.4	The Muffin-Tin A- and B-Coefficients . . . . .	38
3.4	Brillouin Zone Integration and Fermi Energy . . . . .	42
3.5	Representation of the Density and the Potential . . . . .	43
3.6	Construction of the Electron Density . . . . .	44
3.6.1	“ <i>l</i> -like” Charge . . . . .	45
3.6.2	Determination of the Optimal Energy Parameter . . . . .	46
3.6.3	Construction of the Electron Density in the Muffin-Tins . . . . .	47
3.6.4	Construction of the Electron Density in the Interstitial Region . . . . .	47
3.6.5	Construction of the Electron Density in the Vacuum Region . . . . .	48
3.7	Construction of the Coulomb Potential . . . . .	50



3.7.1	The Pseudocharge Method . . . . .	50
3.7.2	Determination of the interstitial Coulomb Potential in Bulk Calculations . . . . .	52
3.7.3	Determination of the interstitial and vacuum Coulomb Potential in Film Calculations . . . . .	52
3.8	Computation of the Exchange Correlation Potential . . . . .	54
3.8.1	Calculation of $\epsilon_{xc}^\sigma$ and $V_{xc}^\sigma$ in the Interstitial-Region . . . . .	54
3.8.2	Calculation of $\epsilon_{xc}^\sigma$ and $V_{xc}^\sigma$ in the Vacuum-Region . . . . .	55
3.8.3	Calculation of $\epsilon_{xc}^\sigma$ and $V_{xc}^\sigma$ in the Muffin-Tin Spheres . . . . .	55
3.9	Minimization of the Energy Functional . . . . .	55
3.9.1	“simple mixing” . . . . .	56
3.9.2	The Newton-Raphson Method . . . . .	57
3.9.3	Quasi-Newton Methods . . . . .	57
<b>4</b>	<b>Non-Collinear Magnetism</b> . . . . .	<b>59</b>
4.1	Constrained magnetic moments . . . . .	61
4.2	Spin-Spirals . . . . .	63
4.3	Generalized Bloch Theorem . . . . .	65
<b>5</b>	<b>Implementation of Non-Collinear Magnetism into FLAPW</b> . . . . .	<b>67</b>
5.1	Setup of the Hamiltonian Matrix . . . . .	69
5.2	Construction of the Charge and Magnetization Density . . . . .	73
5.3	Construction of the Potential Matrix . . . . .	74
5.4	Constrained local moments (CLM) in FLAPW . . . . .	77
5.4.1	Hamiltonian setup in constrained local moment calculations . . . . .	78
5.4.2	Test calculations . . . . .	80
5.5	Spin-Spirals in FLAPW . . . . .	87
5.5.1	Setup of the Hamiltonian Matrix . . . . .	89
5.5.2	Construction of the Charge and Magnetization Density . . . . .	90
5.5.3	Construction of the Potential Matrix . . . . .	91
5.5.4	Test Calculations on fcc Iron . . . . .	91
<b>6</b>	<b>Magnetism of 3d-monolayers on Cu and Ag (111)</b> . . . . .	<b>95</b>
6.1	Unsupported monolayers: Rotation in real space . . . . .	99
6.1.1	Computational details . . . . .	100
6.1.2	Results for the real-space rotation . . . . .	101
6.2	Model Hamiltonians: Heisenberg model and beyond . . . . .	107
6.2.1	The Heisenberg model on a Bravais lattice . . . . .	107
6.2.2	The Heisenberg model on the 2D hexagonal lattice . . . . .	109
6.2.3	Energetics of high symmetry states on the triangular lattice within the Heisenberg model . . . . .	113
6.2.4	The four-spin and the biquadratic interaction . . . . .	117
6.3	Unsupported monolayers: Spin-spirals and the 3Q-state . . . . .	122
6.3.1	Computational details . . . . .	122

6.3.2	Results for the spin-spirals . . . . .	123
6.3.3	Tests of the convergence with respect to numerical cutoffs . .	128
6.4	Discussion of the results for the unsupported monolayers . . . . .	130
6.4.1	Estimate of exchange parameters . . . . .	130
6.4.2	Discussion and classification of the results in terms of the ex- change parameters . . . . .	133
6.5	Results for monolayers on substrate . . . . .	137
6.5.1	Structural optimization of 3d-monolayers on Cu(111) and Ag(111) . . . . .	138
6.5.2	Results for the monolayers on the Cu(111) and Ag(111) substrate	140
6.5.3	Tests of the convergence with respect to numerical cutoffs . .	145
6.6	Calculated STM images of non-collinear magnetic states . . . . .	146
6.6.1	Principle of the SP-STM on the atomic scale . . . . .	147
6.6.2	Calculated SP-STM images of Cr/Ag(111) and Mn/Cu(111) .	151
<b>7</b>	<b>Magnetism and electronic structure of hcp Gd and the Gd(0001) surface</b>	<b>157</b>
7.1	hcp bulk Gd . . . . .	161
7.1.1	Computational details . . . . .	162
7.1.2	Results . . . . .	162
7.2	Results for the Gd(0001) surface . . . . .	167
7.2.1	Spin-spirals at the Gd(0001) surface . . . . .	173
7.2.2	The nearest neighbor Heisenberg model for hcp bulk and the hcp (0001) surface . . . . .	176
7.2.3	The electronic structure of the Gd(0001) surface as function of the spin-spiral q-vector . . . . .	179
<b>8</b>	<b>Conclusions and Outlook</b>	<b>185</b>
<b>A</b>	<b>Spin Rotations and Coordinate Transformations</b>	<b>189</b>
A.1	Euler Angles . . . . .	189
A.2	Coordinate frame transformations . . . . .	190
A.3	Spin Rotation Matrices . . . . .	191



# Chapter 1

## Introduction

The recent years have witnessed a renaissance in the field of magnetism. Magnetism, in particular surface and interface magnetism, magnetism of layered structures and ultrathin films, has become one of the most active and rapidly growing areas in solid state physics. The increasing interest in magnetism and new magnetic materials is driven by the discovery of new quantum effects like interlayer exchange coupling, the giant magnetoresistance (GMR) and tunnel magnetoresistance (TMR). These new effects have undergone an extremely rapid transition from discovery to commercialization, a success story comparable that of the transistor effect, which was discovered in 1947 in the Bell Laboratories, and became the starting point for the development of the modern solid state electronics industry. Only six years after the discovery of the GMR [GSP<sup>+</sup>86] effect the first commercial magnetic sensor devices that were based on the effect became available. Another three years later the application in read heads of computer hard drives by IBM represented the commercial breakthrough of GMR technology in a billion dollar market. An even larger industrial impact is expected from the development of magnetic random access memory (MRAM), which is currently being developed with enormous effort. MRAM has several advantages over conventional semiconductor based RAM, the most important being that it is non-volatile, i.e. no permanent supply of power is needed to retain the stored information, which makes it ideal for mobile devices. It is the immense commercial potential of devices based on both the TMR and the GMR effect, that made magnetoelectronics become one of the most rapidly growing fields in solid state physics.

These enormous technological advances have only become possible after the development of new scientific tools that allow the preparation and characterization of new “artificial” magnetic materials, like layered systems and ultrathin films which, under normal conditions do not exist in nature. The preparation of such specimen has become feasible with state of the art epitaxy in combination with sophisticated vacuum technology. With molecular beam epitaxy (MBE), for example, layered structures and thin films can be grown in a precise and controlled way on an atomic scale. Sputter techniques have been exploited to compromise on the speed of the preparation, the cost and the quality of the sample to show the same effects in less well characterized samples. The simultaneous development techniques like photoemission (PE),

low energy electron diffraction (LEED) and Helium scattering allowed us to monitor the growth and to characterize materials chemically, structurally and electronically. With new techniques like photoelectron emission microscopy (PEEM) the magnetic properties can be investigated at the surface and at interfaces. This technique is element specific and allows not only the mapping of ferromagnetic, but also the antiferromagnetic domain structure with resolution of up to 20 nm. With the invention of the scanning tunneling microscope by Binnig and Rohrer [BR82] in 1982, who were awarded the Nobel Prize in 1986, a new tool has become available that, for the first time, allows the imaging of surfaces in real space with atomic resolution. Very recently it has been shown [HBK<sup>+</sup>00] that, with a magnetic STM tip, it is possible to resolve the magnetic structure of an antiferromagnetic surface on the atomic scale. The spin-polarized STM (SP-STM) can distinguish single atoms with a different spin orientation. The magnetic super-cell of a surface with chemically equivalent atoms can be observed directly.

In addition to the experimental progress, theory has made an important contribution to the understanding of the properties of the new materials. State of the art ab-initio methods have become powerful tools that, on one hand, help us to understand and interpret experimental results, and on the other hand, explore new materials and predict their properties prior to performing experiments. Their application to a sequence of different materials or elements of the periodic table can establish chemical trends, thus enabling the development of the ideal material for a particular purpose, without the need for a large number of experiments. The prerequisite condition for the predictive power of ab-initio methods is the fact that they are parameter free. Hence, no additional external information is needed except the charge of the nuclei. The basis of ab-initio calculations is the density functional theory (DFT) by Hohenberg and Kohn [HK64] and Kohn and Sham [KS65], which states, that the ground state properties of a many electron system are completely determined by the electronic (charge) density and that the quantum mechanical many particle problem, which cannot be solved for large systems, can be replaced by a much simpler effective single particle problem. Due to the enormous progress of the numerical methods that are applied when solving the single particle (Kohn-Sham) equations, and due to the availability of powerful supercomputers and modern workstations, it has become possible to apply ab-initio methods to larger complex systems with reduced symmetry like surfaces, large molecules and even clusters deposited on a surface or step edges. The large success of the density functional theory was acknowledged with the Nobel Prize for Walter Kohn in 1998.

Among the different numerical methods used to solve the Kohn-Sham equations, the full-potential linearized augmented planewave method (FLAPW) is one of the most accurate. It is an all-electron method that does not rely on any shape approximations to the potential or the charge density and is therefore well suited to open structures with low symmetry, such as surfaces and thin films. Due to its elaborate expansion of the wave functions, including radial functions in spheres around the atomic nuclei, the FLAPW method can be applied to systems with localized states

---

like the  $3d$  or  $4f$  electrons. The FLEUR code, the FLAPW program that has been used throughout this thesis, is both a bulk and film program. Used as a film code the surfaces are not modeled by a super-cell, but rather by a finite slab. This means that in this case the program is truly two-dimensional. The vacuum is treated semi-infinately. This, together with the specially adopted expansion of the wave functions in the vacuum region, allows a very accurate description of the wave functions in that region, which is a major advantage, in particular for the simulation of STM experiments. With its high accuracy the FLAPW method is ideal for total energy calculations. Thus, it is optimally suited for the determination of the magnetic, and in combination with the calculation of forces exerted on the atoms, the structural ground state of complex systems.

When we hear the word magnetism, most of us will think of ferromagnetic materials which have the local magnetic moments of all atoms aligned in parallel or, at least have domains of thousands or tens of thousands of atoms with their moments aligned parallel. Some might also think of antiferromagnetism like in bcc Cr, where the local moments are aligned anti-parallel. However, magnetic structures can be more complex than just parallel or anti-parallel. In the most general case the local moments of the single atoms in a solid can point in arbitrary directions. Such complex magnetic states are called non-collinear. One possible reason for the formation of non-collinear magnetic states is frustration, i.e. the inability to satisfy the competing magnetic interactions in a magnetic material. A classical example of magnetic frustration are step edges at the interface between ferromagnetic and antiferromagnetic materials. Such interfaces are the origin of the exchange bias effect, which is a technologically important effect in the magnetic recording industry and magnetoelectronics. In fact, non-collinear (perpendicular) coupling has been observed in exchange bias systems. Very recently a first-principle study [TNJ<sup>+</sup>00] investigated the possibility of non-collinear coupling in layered magnetic systems. The authors showed that by a sophisticated choice of materials that leads to perpendicular coupling between the magnetic layers, the sensitivity of GMR sensors can be improved. Other examples of frustration are small antiferromagnetic clusters in the gas phase, deposited on a surface or the tip of an STM. In particular, in situations with little symmetry or for systems in low dimensions magnetic frustration becomes more likely. With decreasing size of the structures of magnetoelectronic devices or in the context of nano-magnetism, magnetic clusters and molecules the effects of non-collinearity will become more important and the need for a quantum-mechanical first-principles description of non-collinear magnetism will grow. But frustration can also occur in a highly symmetric environment. In fcc iron, for example, it is the competition between ferromagnetic and antiferromagnetic interactions of the different nearest neighbor shells that causes the frustration and leads to the famous spiral magnetic ground state. Also domain walls between the domains of a ferromagnetic material represent a magnetic frustration, where the material tries to rotate the moment relatively slowly from the direction of one domain to another at the lowest energetical expense. But systems that possess a non-collinear ground state are not the only motivation

to study non-collinear magnetism. Magnetic excitations, magnons, also represent a non-collinear configuration. Hence, non-collinear ab-initio methods can be used to calculate, for example, magnon dispersion curves, and thus the effect of temperature in magnetic materials.

By far the majority of the ab-initio programs available today are restricted to collinear magnetic structures, although already in their original publication on spin-polarized DFT von Barth and Hedin [vBH72] treated the magnetization as a vector field without any limitation to its direction. However, the restriction to collinear magnetism leads to a Hamiltonian that is diagonal in the two spin directions. This does not only save a large amount of computer time, but it also greatly simplifies the implementation of magnetism into a non-spin-polarized program, because the spin-up and spin-down problem can be treated independently, almost like two non-magnetic calculations. The aim of the present work was to develop and apply a non-collinear ab-initio method on the basis of the FLAPW method.

The first self-consistent non-collinear ab-initio calculations for periodic solids, e.g. [SG86, KHSW88a, MLSG91], applied the so-called atomic sphere approximation for the magnetization direction, i.e. the magnetization direction is held fixed (collinear) within each Wigner-Seitz sphere. Only inter-atomic non-collinearity between the magnetic moments of different atomic sites was allowed in these calculations. The neglect of intra-atomic non-collinearity, i.e. the change of the magnetization direction within one Wigner-Seitz sphere, can lead to problems. This occurs, for example, for systems where relativistic effects are very important the interplay of the local exchange and spin-orbit coupling can result in intra-atomic non-collinearity. Very recently several groups [NS96, OPC98, BK98, IA99, HKH00] developed fully unconstrained non-collinear ab-initio programs, that treat the magnetization as a continuous vector field. We adopted a “hybrid” approach, treating the magnetization density as a continuous vector field everywhere, except within non-overlapping spheres around each atomic site. For transition metals the non-collinearity in these spheres is expected to be small, and we show that this is a very good approximation for these systems.

An arbitrary magnetic configuration is in general not a stationary state of the magnetic system. Requiring that the magnetic moments assemble a prescribed configuration means to constrain the phase space of possible solutions. Within the framework of DFT such a constraint is taken into account by a Lagrange parameter. The Lagrange parameter represents a “constraining force” or magnetic field applied to the magnetic moments of the atoms to keep the system in the desired magnetic configuration, i.e. to make that configuration stationary. We have implemented for the first time the constrained local moment method in a “full-potential” program that works with the vector magnetization density. We will show in chapter 5 and 6 that this implementation allows us to test the functional form of the energy and magnetization with respect to external parameters, i.e. the angles of the local atomic magnetic moments, and compare the results with model Hamiltonians. We demonstrate that this approach is very powerful, as deviations from the anticipated forms lead to important

and far-reaching conclusions.

An important class of non-collinear configurations are spiral magnetic states or spin-spirals. These are configurations, where the local moment is rotated by a constant angle from atom to atom along a certain direction through the crystal. Spin-spiral states occur as ground states in nature, e.g. in fcc Fe and in rare earth metals. Spin-spirals can also be understood as a model for magnons or domain walls. When spin-orbit coupling is neglected, a generalization of the Bloch theorem for spiral magnetic configurations can be derived. On the basis of this generalized Bloch theorem, we have implemented a method that allows us to deal with spin-spiral states using only the chemical unit cell of the crystal without the need for large super-cells. With the implementation of non-collinear magnetism, spin-spirals and the constrained local moment method, into a bulk and film FLAPW program, we have developed a unique tool to investigate non-collinearity in bulk and in particular at magnetic surfaces, in thin films and low dimensional magnets in general.

Compared with non-magnetic or collinear magnetic calculations the computational effort of non-collinear calculations is enormous. Since the spin-up and spin-down problem cannot be solved separately anymore the size of the Hamiltonian matrix that has to be diagonalized doubles. In addition, the matrix becomes complex hermitian, rather than real symmetric. In most cases the non-collinear magnetic structures have a lower symmetry and often have also a larger unit cell than, for example, the ferromagnetic configuration. Therefore, non-collinear ab-initio calculations represent a cutting edge problem in super-computing. Parallel to my project, the FLAPW program was parallelized. Without this parallelized version of the program and the access to massively parallel supercomputers most of the calculations presented in this thesis would not have been possible.

The principles of non-collinear magnetism, the constrained local moment method and spin-spiral calculations, including the generalization of the Bloch theorem, are described in chapter 4. Before we start with the discussion of non-collinear magnetism, we explain the basics of the density functional theory and the local spin-density approximation in chapter 2, and present a detailed review of the FLAPW method in chapter 3, where we emphasize those aspects which are altered by the implementation of non-collinear magnetism. A very detailed description of the actual implementation is then given in chapter 5, which also includes tests of the constrained local moment and the spin-spiral method.

As we have mentioned above spin frustration is one possible origin of non-collinear magnetism. The classical example of a frustrated magnetic system is the topological frustration of an antiferromagnet on the triangular lattice. Such a two-dimensional magnetic system can be realized by a mono-atomic layer of an antiferromagnetic material on a hexagonal surface of a non-magnetic substrate, e.g. the (111) surface of an fcc noble metal. Such thin films, in particular transition metal films, have attracted a lot of interest due to their special properties. Because of the filled  $d$ -bands of the noble metals, the  $d$ -bands of the transition-metal monolayers hybridize very little with the substrate. This leads to an enhancement of the magnetic moments



in the overlayer. However, most work has been done on (100) oriented substrates, where the atoms in the monolayer are arranged on a square lattice. Fe and Mn on the Cu (100) surface belong to the most extensively investigated systems. Previous ab-initio calculations [BWD88] show, that the early 3*d*-transition metals V, Cr and Mn prefer a two-dimensional antiferromagnetic order on the (100) oriented substrates, while monolayer films of Fe, Co and Ni are ferromagnetic. Little work has been done on the (111) oriented substrates. So far, the antiferromagnetism on the triangular lattice has almost exclusively been discussed within the Heisenberg model. However, it is by no means clear how far the Heisenberg model can be applied to itinerant magnets like the 3*d*-transition metals.

In chapter 6 we present an extensive study of the magnetism of V, Cr, Mn and Fe monolayers on the Cu (111) and the Ag (111) surface. We cover a complete set of relevant spin states, including non-collinear spin structures and, in particular, incommensurate spin-spirals. In a detailed discussion of the Heisenberg model on the triangular lattice we show that, in the nearest neighbor approximation, the ground state of a Heisenberg antiferromagnet is the 120° Néel state, a coplanar non-collinear magnetic configuration, where all magnetic moments lie in one plane and span 120° angles. In fact, our ab-initio calculations show that this is the magnetic ground state of Cr monolayers on Cu and Ag(111) substrates. When interactions beyond the nearest neighbors are included other magnetic states, like spin-spiral states, can become the ground state. The results of our calculations show that not only terms that go beyond the nearest neighbor interaction, but also terms that go beyond the Heisenberg model, like the biquadratic and 4-spin interaction, have to be included to model the itinerant 3*d*-metals. In the case of a Mn monolayer on Cu (111) these higher order terms lead to the stabilization of a very complex three-dimensional spin structure, the so-called 3Q-state. A picture of this state is shown at the beginning of this thesis. At the end of the chapter we discuss how these complex non-collinear ground states can be identified with the spin-polarized STM.

The treatment of the localized 4*f* states of Gd represent a challenge for first-principle theory. There has been an ongoing discussion for a long time about how these states are best treated in ab-initio calculations. Including them into the valence region in an LDA calculation leads to the prediction of the wrong antiferromagnetic ground state for hcp Gd. We have performed calculations for hcp Gd that compare different methods of dealing with the 4*f* states. The results show that the minority 4*f* bands, that lie too close to the Fermi energy in an LDA calculation, are the origin of the antiferromagnetic coupling in such calculations.

On the basis of the knowledge gained from the Gd bulk calculations we investigated the electronic structure of the Gd(0001) surface. The temperature dependence of the electronic structure of the Gd(0001) surface has been a matter of extensive debate. In particular, the change of the binding energy of both, the majority and minority part of the  $d_{z^2}$  surface state, with temperature has been discussed controversially in the literature. Some experimental studies found a collapse of the spin-splitting of the surface state at a temperature of 350 K, which is taken as support

---

for the applicability of the Stoner picture for the Gd surface, while others observed a finite splitting of 400 meV at the same temperature. To reveal trends in the temperature variation of the conduction electron states of the Gd(0001) surface we studied non-collinear spin-spiral magnetic configurations. Such spin-spiral configurations can be interpreted as a model for magnetic excitations. Therefore, they are frequently referred to as “frozen magnons”. To allow a comparison with scanning tunneling spectroscopy experiments we calculated the local density of states in the vacuum, which is measured by such experiments, as a function of the strength of the magnetic fluctuations. Our results nicely resemble the trends found in temperature dependent scanning tunneling spectroscopy experiments. However, a direct comparison of the theoretical results with an experiment at a certain temperature is difficult. With the strength of the fluctuations the character of the surface states change drastically due to hybridization with other states, also with states that originally had a different spin-character in the ferromagnetic configuration. Finally only a single peak in the vacuum local density of states is present. In that configuration the valence magnetic moment is still as large as  $0.4 \mu_B$  at the surface. Hence, the decreasing and finally vanishing splitting of the peak of the density of states due to the surface state cannot be taken as support for the applicability of the Stoner model in the sense of a vanishing valence magnetic moment.



# Chapter 2

## The Density Functional Theory

In order to establish a deep understanding of the physical properties of solids, it is of major importance to develop a valid quantum-mechanical description of these systems. However, the atom nuclei and the electrons constitute a complex many-body problem. A simplification of this problem can be achieved employing the Born-Oppenheimer-approximation, within which the atomic nuclei are considered point charges at fixed positions. Thus, all quantum effects of the nuclei are neglected. This approximation, which is made in the vast majority of first-principle calculations, leads to the following Schrödinger equation.

$$\begin{aligned} \mathcal{H}\Psi &= \left\{ -\sum_{i=1}^N \frac{\hbar^2}{2m} \nabla^2 + \sum_{\substack{i,j=1 \\ i \neq j}}^N \frac{e^2}{|\mathbf{r}_i - \mathbf{r}_j|} + \sum_{i=1}^N \sum_{\mu=1}^M \frac{e^2 Z^\mu}{|\mathbf{r}_i - \boldsymbol{\tau}^\mu|} \right\} \Psi(\mathbf{r}_1, \dots, \mathbf{r}_N) \\ &= E\Psi(\mathbf{r}_1, \dots, \mathbf{r}_N) \end{aligned} \tag{2.1}$$

However, due to the large dimension of  $\Psi$  and the requirement of antisymmetry, which means that  $\Psi$  has to be expanded into a sum of Slater determinants, rather than simple product-functions, this equation can be solved only for tiny systems, including few electrons. In order to deal with realistic materials, relevant in solid state physics, further approximations have to be made.

A breakthrough in the parameter-free ab-initio description of complex electronic systems has been achieved with the development of the density functional theory by Hohenberg and Kohn [HK64] and Kohn and Sham [KS65].

### 2.1 The Theorem of Hohenberg and Kohn

The all-electron wavefunction contains all information available about an electronic system. However, not the whole information is needed to determine the ground state properties of a physical system. The measurable quantities are given by expectation values of the quantum-mechanical operators corresponding to the observable under consideration. The central idea of the density functional theory [JG89] is to replace

the complex many particle wavefunction by a far simpler quantity, the electron density, given by

$$n(\mathbf{r}) = \langle \Psi | \sum_{i=1}^N \delta(\mathbf{r} - \mathbf{r}_i) | \Psi \rangle. \quad (2.2)$$

Hohenberg and Kohn were able to show for systems with a non-degenerate ground state, that:

- For a given external Potential  $V_{ext}$ , the ground state energy and all other ground state properties of the system are unique functionals of the electron density  $n(\mathbf{r})$ .
- The energy functional is variational, i.e. the ground state density  $n_0(\mathbf{r})$  minimizes the energy functional  $E[n]$ , under the subsidiary condition that the number of electrons is kept constant.

$$E[n] > E[n_0] = E_0 \quad \text{for all } n(\mathbf{r}) \neq n_0(\mathbf{r}) \quad (2.3)$$

The density functional formalism can be extended to degenerate ground states [Koh85, DG90]. The second part of the theorem implies, that the ground state density can be obtained from the minimization of the energy functional.

$$\delta E[n] = 0 \quad (2.4)$$

Levy [Lev79] provided a simpler and more general derivation of the above theorems, defining the energy functional by

$$E[n] = \min_{\Psi, n[\Psi]=n} \langle \Psi | \mathcal{H} | \Psi \rangle. \quad (2.5)$$

However, no explicit representation of  $E[n]$  has been derived so far.

## 2.2 The Kohn-Sham Equations

An important step on the way to finding an applicable approximation of the energy functional is the idea of Kohn and Sham [KS65]. The central concept of their theory is to split the energy functional into three contributions.

$$E[n] = T_s[n] + U[n] + E_{xc}[n] \quad (2.6)$$

Where  $T_s$  is the kinetic energy of non-interacting electrons. The Coulomb energy  $U$  consists of the interaction of the electrons with the external potential, which is usually due to the atomic nuclei, and the electron-electron interaction in Hartree approximation.

$$\begin{aligned} U[n] &= E_{ext}[n] + E_H[n] \\ E_{ext}[n] &= \int V_{ext}(\mathbf{r})n(\mathbf{r})d^3r \\ E_H[n] &= 4\pi \frac{e^2}{2} \int \frac{n(\mathbf{r})n(\mathbf{r}')}{|\mathbf{r} - \mathbf{r}'|} d^3r d^3r' \end{aligned} \quad (2.7)$$

Equation 2.6 can be regarded as a definition of the exchange correlation functional  $E_{xc}[n]$ , which contains all remaining contributions to  $E[n]$ , i.e. the exchange and correlation energy and correction to the kinetic energy due to the electron-electron interaction. The importance of this representation of  $E[n]$  has two reasons. The kinetic energy of the non-interacting electrons  $T_s$ , which is a significant contribution to the total energy, can be calculated exactly. By that, many deficiencies due to inaccurate treatment of the kinetic energy by the Thomas-Fermi method are removed. In addition approximations to  $E_{xc}[n]$  can be found, that lead to excellent results for the ground state properties calculated for a wide variety of systems.

An explicit formula for  $T_s[n]$  can be obtained using a special ansatz for the electron density. The density can be written as a sum of single particle wavefunctions, as in the case of non-interacting electrons.

$$n(\mathbf{r}) = 2 \sum_{i=1}^N |\psi_i(\mathbf{r})|^2 \quad (2.8)$$

Where, where the sum is over the occupied states and the factor “2” accounts for the spin degeneracy. With this ansatz the kinetic energy can be written as:

$$T_s[n] = -2 \sum_{i=1}^N \int \psi_i^*(\mathbf{r}) \frac{\hbar^2}{2m} \nabla^2 \psi_i(\mathbf{r}) d^3r \quad (2.9)$$

Instead of minimizing the energy functional with respect to the electron density, it can also be minimized with respect to the wavefunctions  $\psi_i$  (or their complex conjugates). In this case the subsidiary condition of particle conservation is replaced by the requirement of normalized wavefunctions.

$$\int |\psi_i(\mathbf{r})|^2 d^3r = 1 \quad (2.10)$$

This requirement is taken into account by Lagrange parameters  $\epsilon_i$ . Applying the variational principle yields the Kohn-Sham equations.

$$\left\{ -\frac{\hbar^2}{2m} \nabla^2 + V_{eff}(\mathbf{r}) \right\} \psi_i(\mathbf{r}) = \epsilon_i \psi_i(\mathbf{r}) \quad (2.11)$$

with

$$V_{eff}(\mathbf{r}) = V_{ext}(\mathbf{r}) + V_H(\mathbf{r}) + V_{xc}(\mathbf{r}) \quad (2.12)$$

These equations have the form of a single particle Schrödinger equations. However, the potential has been replaced by an effective potential consisting of three contributions: The external potential  $V_{ext}$ , the Hartree potential

$$V_H(\mathbf{r}) = 4\pi e^2 \int \frac{n(\mathbf{r}')}{|\mathbf{r} - \mathbf{r}'|} d^3r' \quad (2.13)$$

and the exchange correlation potential

$$V_{xc}(\mathbf{r}) = \frac{\delta E_{xc}[n(\mathbf{r})]}{\delta n(\mathbf{r})} \quad (2.14)$$

Since  $V_H$  and  $V_{xc}$  depend on the electron density, this formalism constitutes a self-consistency problem.

Even though the Kohn-Sham equations have the form of a single-electron Schrödinger equation, the formalism does not provide any justification to interpret the Lagrange parameters  $\epsilon_i$  as excitation energies, nor to regard the wavefunctions as physical electron wavefunctions. Nevertheless, experience shows, that doing so without formal justification can be meaningful, and helps to understand the properties of the system under consideration.

## 2.3 Spin Density Functional Theory

In order to describe magnetic effects the density functional theory has to be extended to the case of spin polarized electrons. This is important for systems that possess non-zero ground state magnetization, which is the case for most atoms, magnetic solids and surfaces and electronic systems exposed to an external magnetic field. The necessary extension to the Hohenberg-Kohn theory can be formulated replacing the electron density by the electron density plus the magnetization density as fundamental variables. In this case, the variational principle becomes

$$E[n(\mathbf{r}), \mathbf{m}(\mathbf{r})] \geq E[n_0(\mathbf{r}), \mathbf{m}_0(\mathbf{r})]. \quad (2.15)$$

An alternative, but completely equivalent, formulation can be obtained using a four component density matrix  $\rho_{\alpha\beta}$  instead of  $n(\mathbf{r})$  and  $\mathbf{m}(\mathbf{r})$  [vBH72, Küb95]. In order to gain a generalized form of the Kohn-Sham equations, it is necessary at least to introduce two component Pauli wavefunctions, that reproduce the electron and magnetization density.

$$\boldsymbol{\psi}_i(\mathbf{r}) = \begin{pmatrix} \psi_{1,i}(\mathbf{r}) \\ \psi_{2,i}(\mathbf{r}) \end{pmatrix} \quad (2.16)$$

$$n(\mathbf{r}) = \sum_{i=1}^N |\boldsymbol{\psi}_i(\mathbf{r})|^2$$

$$\mathbf{m}(\mathbf{r}) = \sum_{i=1}^N \boldsymbol{\psi}_i^*(\mathbf{r}) \boldsymbol{\sigma} \boldsymbol{\psi}_i(\mathbf{r}) \quad (2.17)$$

Applying the variational principle again yields the Kohn-Sham equations, which now have the form of Schrödinger-Pauli equations.

$$\left\{ -\frac{\hbar^2}{2m} \nabla^2 + V_{eff}(\mathbf{r}) + \boldsymbol{\sigma} \cdot \mathbf{B}_{eff}(\mathbf{r}) \right\} \boldsymbol{\psi}_i(\mathbf{r}) = \epsilon_i \boldsymbol{\psi}_i(\mathbf{r}) \quad (2.18)$$

The additional effective magnetic field consists of two terms. One of them is due to the variation of the exchange correlation energy with respect to the magnetization

density. The second term is the external B-field, if present.

$$\begin{aligned}\mathbf{B}_{eff}(\mathbf{r}) &= \mathbf{B}_{xc}(\mathbf{r}) + \mathbf{B}_{ext}(\mathbf{r}) \\ \mathbf{B}_{xc}(\mathbf{r}) &= \frac{\delta E_{xc}[n(\mathbf{r}), \mathbf{m}(\mathbf{r})]}{\delta \mathbf{m}(\mathbf{r})}\end{aligned}\quad (2.19)$$

In many applications, like for example ferromagnetic and antiferromagnetic solids, the magnetization is orientated along one particular direction. For these collinear cases the problem can be simplified further. The z-axis can be chosen along the direction of the magnetic field. Therefore, the Hamiltonian of equation 2.18 becomes diagonal in the two spin components of the wavefunction, i.e. the spin-up and -down problems become completely decoupled and can be solved independently. The energy and all other physical observables become functionals of the electron density and the magnitude of the magnetization density  $m(\mathbf{r}) = |\mathbf{m}(\mathbf{r})|$  rather than  $\mathbf{m}(\mathbf{r})$ , or, equivalently, of the spin-up and spin-down electron densities  $n_{\uparrow}(\mathbf{r})$  and  $n_{\downarrow}(\mathbf{r})$  which are given by

$$n_{\sigma}(\mathbf{r}) = \sum_{i=1}^N |\psi_{i\sigma}(\mathbf{r})| \quad (2.20)$$

The vast majority of the spin-polarized density functional calculations have been performed using this formalism.

## 2.4 The Local Spin Density Approximation

So far, no approximations have been made. The density functional formalism, outlined in the previous sections, could in principle reproduce all ground state properties of any complex many-electron system exactly, if the exchange correlation energy  $E_{xc}$  was known. Unfortunately, no explicit representation of this functional, that contains all many-body effects, has been found yet. Thus, approximations to  $E_{xc}$  have to be used. The most widely used and very successful approximation is the local spin density approximation (LSDA). The underlying idea is very simple. At each point of space  $E_{xc}$  is approximated locally by the exchange correlation energy of a homogeneous electron gas with the same electron and magnetization density. Hence, the approximate functional  $E_{xc}$  is of the form

$$E_{xc}[n(\mathbf{r}), |\mathbf{m}(\mathbf{r})|] = \int n(\mathbf{r}) \epsilon_{xc}(n(\mathbf{r}), |\mathbf{m}(\mathbf{r})|) d^3r \quad (2.21)$$

It is important to note, that  $\epsilon_{xc}$  is not a functional, but a function of  $n(\mathbf{r})$  and  $|\mathbf{m}(\mathbf{r})|$  at a particular point of space. As a consequence of its local definition  $\epsilon_{xc}$  and thus  $E_{xc}$  depend only of the magnitude of the magnetization. This, in terms, leads to the fact that  $\mathbf{B}_{xc}(\mathbf{r})$  and  $\mathbf{m}(\mathbf{r})$  do always have the same direction. Therefore, the exchange correlation potential and magnetic field derived from 2.21 become

$$V_{xc}(\mathbf{r}) = \epsilon_{xc}(n(\mathbf{r}), |\mathbf{m}(\mathbf{r})|) + n(\mathbf{r}) \frac{\delta \epsilon_{xc}(n(\mathbf{r}), |\mathbf{m}(\mathbf{r})|)}{\delta n(\mathbf{r})}$$



$$\mathbf{B}_{xc}(\mathbf{r}) = n(\mathbf{r}) \frac{\delta \epsilon_{xc}(n(\mathbf{r}), |\mathbf{m}(\mathbf{r})|)}{\delta |\mathbf{m}(\mathbf{r})|} \hat{\mathbf{m}}(\mathbf{r}). \quad (2.22)$$

Using the LSDA the Kohn-Sham equations take exactly the same form as the Hartree equations, and they are no more difficult to solve. In particular, they are far easier to deal with than the Hartree-Fock equations because of the local effective potential. Intuitively one should expect, that the LSDA is valid only for slowly varying densities. Nevertheless, it has been applied successfully to inhomogeneous systems.

Explicit parameterizations of  $\epsilon_{xc}$  can be obtained for example from Hartree-Fock calculations for the homogeneous electron gas. Of course, such calculations do only take into account the exchange effects, but neglect correlation. Modern parameterizations of  $\epsilon_{xc}$  are based on quantum-mechanical many-body calculations. Most commonly used are the parameterizations of v. Barth and Hedin [vBH72] and Moruzzi, Janak and Williams [MJW78], which have been obtained applying the random phase approximation (RPA), the parameterization of Vosko, Wilk and Nusair [VWN80], that is based on Quantum-Monte-Carlo simulations by Ceperley and Alder [CA80], and goes beyond the RPA, and the parameterization of Perdew and Zunger [PZ81], which is, in a certain sense, a mixture of the previous two. The results of the present work have been obtained using the parameterization of Moruzzi, Janak and Williams.

## 2.5 Determination of the Total Energy

If the total energy of a system is needed, for example in order to calculate the equilibrium lattice constant of a crystal, the Coulomb interaction of the atomic nuclei has to be taken into account. This extra contribution  $E_{ii}$  (ion-ion) has to be added to the electronic energy, given by 2.6.

$$E[n] = T_s[n] + U[n] + E_{xc}[n] + E_{ii}, \quad E_{ii} = e^2 \sum_{\substack{\mu, \mu'=1 \\ \mu \neq \mu'}}^M \frac{Z^\mu Z^{\mu'}}{|\boldsymbol{\tau}^\mu - \boldsymbol{\tau}^{\mu'}|}, \quad (2.23)$$

where  $\mu$  sums over all atoms of the crystal with the position  $\boldsymbol{\tau}^\mu$ . In principle, this formula could be used to calculate the total energy. However, for numerical reasons it is desirable to avoid the explicit application of the operator  $\nabla^2$ . Therefore, the kinetic energy is calculated from the sum of the single particle eigenvalues  $\epsilon_i$ . Rewriting the Schrödinger-Pauli equation 2.18 yields

$$-\frac{\hbar^2}{2m} \nabla^2 \psi_i(\mathbf{r}) = \epsilon_i \psi_i(\mathbf{r}) - V_{eff}(\mathbf{r}) \psi_i(\mathbf{r}) - \boldsymbol{\sigma} \cdot \mathbf{B}_{eff}(\mathbf{r}) \psi_i(\mathbf{r}) \quad (2.24)$$

Multiplying from the left with  $\int d^3r \psi_i^*(\mathbf{r}, \sigma)$  and summing over the occupied states gives the kinetic energy.

$$T_s[n] = \sum_{i=1}^N \epsilon_i - \int n(\mathbf{r}) V_{eff}(\mathbf{r}) d^3r - \int \mathbf{m}(\mathbf{r}) \cdot \mathbf{B}_{eff}(\mathbf{r}) d^3r \quad (2.25)$$

Using (2.7), (2.21) and assuming that the external potential is given by the atomic nuclei and that no external magnetic field is present,

$$V_{ext}(\mathbf{r}) = -4\pi e^2 \sum_{\mu=1}^M \frac{Z^\mu}{|\mathbf{r} - \boldsymbol{\tau}^\mu|}, \quad \mathbf{B}_{ext}(\mathbf{r}) = 0 \quad (2.26)$$

the total energy becomes

$$\begin{aligned} E[n, \mathbf{m}] &= \sum_{i=1}^N \epsilon_i - \int n(\mathbf{r}) V_{eff}(\mathbf{r}) d^3 r - \int \mathbf{m}(\mathbf{r}) \cdot \mathbf{B}_{xc}(\mathbf{r}) d^3 r \\ &- 4\pi e^2 \sum_{\mu=1}^M \int \frac{n(\mathbf{r}) Z^\mu}{|\mathbf{r} - \boldsymbol{\tau}^\mu|} d^3 r + 4\pi e^2 \frac{1}{2} \int \frac{n(\mathbf{r}) n(\mathbf{r}')}{|\mathbf{r} - \mathbf{r}'|} d^3 r d^3 r' \\ &+ \int n(\mathbf{r}) \epsilon_{xc}(n(\mathbf{r}), |\mathbf{m}(\mathbf{r})|) d^3 r + 4\pi e^2 \sum_{\substack{\mu, \mu'=1 \\ \mu \neq \mu'}}^M \frac{Z^\mu Z^{\mu'}}{|\boldsymbol{\tau}^\mu - \boldsymbol{\tau}^{\mu'}|}. \end{aligned} \quad (2.27)$$

Using 2.7 and 2.22 this can be simplified further.

$$\begin{aligned} E[n, \mathbf{m}] &= \sum_{i=1}^N \epsilon_i - \int n(\mathbf{r}) V_{xc}(\mathbf{r}) d^3 r - \int \mathbf{m}(\mathbf{r}) \cdot \mathbf{B}_{xc}(\mathbf{r}) d^3 r \\ &- 4\pi e^2 \frac{1}{2} \int \frac{n(\mathbf{r}) n(\mathbf{r}')}{|\mathbf{r} - \mathbf{r}'|} d^3 r d^3 r' \\ &+ \int n(\mathbf{r}) \epsilon_{xc}(n(\mathbf{r}), |\mathbf{m}(\mathbf{r})|) d^3 r + 4\pi e^2 \sum_{\substack{\mu, \mu'=1 \\ \mu \neq \mu'}}^M \frac{Z^\mu Z^{\mu'}}{|\boldsymbol{\tau}^\mu - \boldsymbol{\tau}^{\mu'}|} \end{aligned} \quad (2.28)$$

Equation (2.28) holds exactly for the selfconsistent electron and magnetization density. During the iterations on the way to selfconsistency this result represents only an approximation to the total energy. Another difficulty arises, because the Hartree energy and the contribution from the Coulomb interaction of the nuclei are divergent. Weinert, Wimmer and Freeman [WWF82] showed how these singularities can be canceled analytically.

## 2.6 The Stoner Model of Itinerant Magnetism

Although all results of the present work have been obtained from ab-initio calculations, a brief discussion of the Stoner Model will be given in this section. This model provides a framework within which to interpret the results of the calculations. It is very important to keep these simple models in mind, in order to build ones physical intuition. Comparing ones “intuitive” expectations with the outcome of the calculations is certainly the most important step on the way to understanding the physics of a system. The magnetism of solid is determined by the interplay of the gain of exchange energy due to the formation of a local moment and the increase of the kinetic

energy, if not all  $\mathbf{k}$ -states are double occupied within the Fermi sphere. This effect can most easily be illustrated within the Stoner model for ferromagnets.

The magnetization density  $m(\mathbf{r}) = |\mathbf{m}(\mathbf{r})|$  of solids is usually small compared to the electron density  $n(\mathbf{r})$ . Expanding the exchange correlation energy  $\epsilon_{xc}(n(\mathbf{r}), m(\mathbf{r}))$  into a Taylor series in terms of the parameter  $\xi = \frac{m}{n}$  yields

$$\epsilon_{xc}(n, \xi) = \epsilon_{xc}(n, 0) + \frac{1}{2}\epsilon_{xc}''(n, 0)\xi^2 + \dots \quad (2.29)$$

Thus, the magnetic field  $\mathbf{B}_{xc}$  becomes

$$\mathbf{B}_{xc} = \frac{1}{n^2}\epsilon_{xc}''(n, 0)\mathbf{m}. \quad (2.30)$$

In the case of ferromagnetism  $\mathbf{B}_{xc}$  acts as an extra potential term  $\tilde{V}_{xc}$ , that adds to the non-magnetic exchange correlation potential  $V_{xc}^0$ . This term, which is proportional to  $m$ , has the same magnitude for both spin-directions, but it is attractive for the majority-spin (+) and repulsive for the minority-spin(-).

$$V_{xc}^{\pm}(\mathbf{r}) = V_{xc}^0(\mathbf{r}) \mp \tilde{V}_{xc}(\mathbf{r})m(\mathbf{r}) \quad (2.31)$$

Within the Stoner theory this rising and lowering of the potential is expressed by a constant.

$$V_{xc}^{\pm}(\mathbf{r}) = V_{xc}^0(\mathbf{r}) \mp \frac{1}{2}IM \quad (2.32)$$

Where  $M$  is the total magnetic moment per atom, and  $I$  is the exchange integral (Stoner parameter). Because of this constant shift the spatial shape of the potential remains the same as in the non-magnetic case. Consequently, the solutions of the Kohn-Sham equations also remain unchanged, only the single particle energies  $\epsilon_i$  are shifted by the same amount as the potential.

$$\psi_i^{\pm}(\mathbf{r}) = \psi_i^0(\mathbf{r}), \quad \epsilon_i^{\pm} = \epsilon_i^0 \mp \frac{1}{2}IM \quad (2.33)$$

Hence, the whole band structure is spin-split, but the shape of the bands remains unchanged. As a result, the local densities of states projected on an atom for the spin-directions  $\pm, n^{\pm}(\epsilon)$ , are also shifted by  $\pm\frac{1}{2}IM$ .

$$n^{\pm}(\epsilon) = n^0(\epsilon \pm \frac{1}{2}IM) \quad (2.34)$$

From this property of the density of states a criterion for the existence of ferromagnetism can be derived. Integrating the density of states up to the Fermi energy  $E_F$  yields the number of electrons  $N$  and the total magnetic moment per atom  $M$ .

$$\begin{aligned} N &= \int_{\epsilon < E_F} \left[ n^0(\epsilon + \frac{1}{2}IM) + n^0(\epsilon - \frac{1}{2}IM) \right] d\epsilon \\ M &= \int_{\epsilon < E_F} \left[ n^0(\epsilon + \frac{1}{2}IM) - n^0(\epsilon - \frac{1}{2}IM) \right] d\epsilon \end{aligned} \quad (2.35)$$

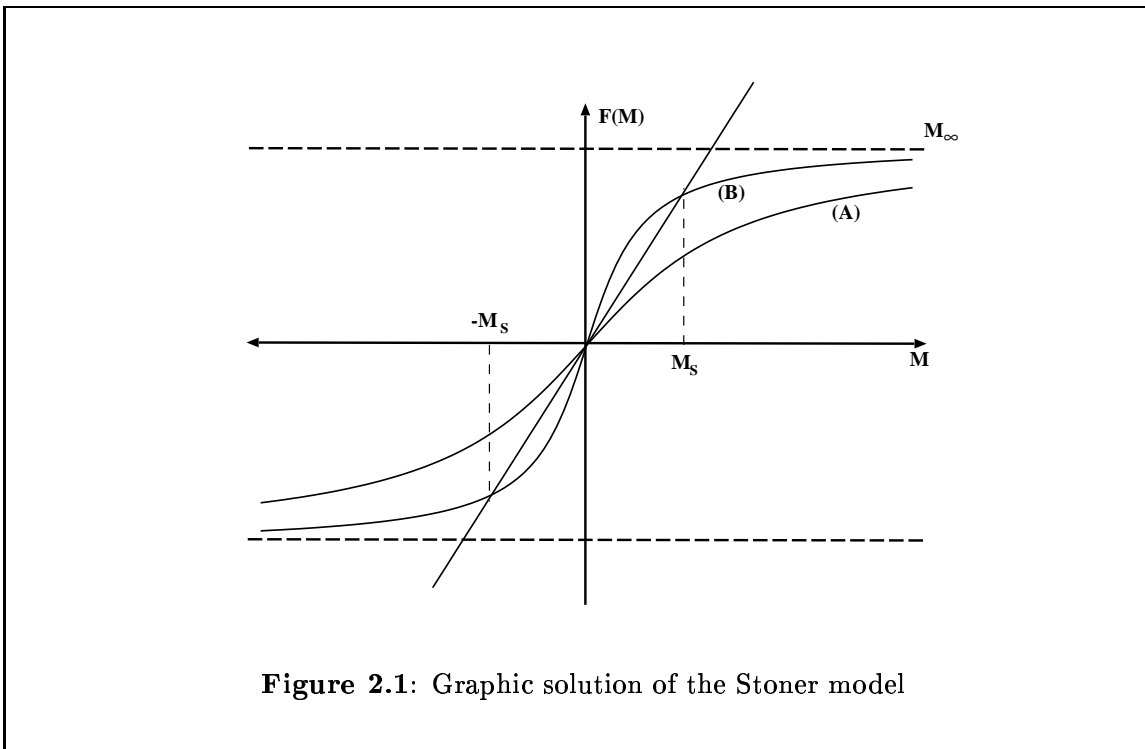
These two equations determine the unknown Fermi energy and magnetic moment. Requiring charge neutrality the first equation can be used to obtain the Fermi energy as a function of the magnetization  $E_F = E_F(M)$ . Substituting this into the second equation leads to a selfconsistency problem for  $M$ .

$$M = F(M), \quad F(M) = \int_{\epsilon < E_F(M)} \left[ n^{\uparrow}(\epsilon + \frac{1}{2}IM) - n^{\downarrow}(\epsilon - \frac{1}{2}IM) \right] d\epsilon \quad (2.36)$$

The function  $F(M)$  has the following properties.

- $F(0) = 0$
- $F(M) = -F(-M)$
- $F(\pm\infty) = \pm M_{\infty}$
- $F'(M) > 0$

Where  $M_{\infty}$  is the largest possible magnetization, reached when only majority-spin states are occupied. The graphic solution of 2.36 is illustrated in Fig. 2.1. Two



functions  $F(M)$ , consistent with the above properties, are plotted. In case A only the trivial non-magnetic solution  $M = 0$  is present, whereas in case B three solutions exist, two of which have non-zero magnetization. From the properties of  $F(M)$  follows, that 2.36 always has solutions with non-zero magnetization, if the slope of

$F(M)$  at  $M = 0$  is larger than 1. From 2.36 follows that the slope of  $F(M)$  is given by

$$F'(0) = In^0(E_F). \quad (2.37)$$

This finally is the Stoner criterion for ferromagnetism:

$$In^0(E_F) > 1. \quad (2.38)$$

A big exchange integral and a large non-magnetic density of states at the Fermi energy favors ferromagnetism. This result is not surprising, because a large  $n^0(E_F)$  means, that only a small increase in kinetic energy has to be accepted to obtain a large magnetization, and thus a large gain of exchange energy. In the most simple approximation the size of the density of states is proportional to the inverse of the bandwidth  $W$ . Thus, the smaller the bandwidth is, the larger the tendency towards magnetism becomes. The limiting case of zero bandwidth are atoms. Here the Stoner criterion is always satisfied, and the magnetic moments are determined by Hund's rule, with the exception of the Lanthanides and the Actinides. The only bulk materials that fulfill the Stoner criterion are Fe, Co and Ni. However, due to the reduced coordination, the bandwidth at surfaces is smaller than in bulk materials. Thus, from the Stoner model one should expect an enhancement of magnetism at surfaces and even new magnetic materials, which are non-magnetic in their bulk crystalline phase, but become magnetic at the surface.

# Chapter 3

## The FLAPW Method

### 3.1 The FLAPW Method

There are many possible ways to solve the Kohn-Sham equations. One very common method is to use some kind of basis set to represent the wavefunctions. A very suitable choice that is already suggested by Bloch's theorem are plane waves. They have a lot of advantages: They are orthogonal, they are diagonal in momentum and any power of momentum and the implementation of planewave based methods is rather straightforward because of their simplicity. However, since the electron wavefunctions are varying very quickly near the core, large wavevectors are needed to represent the wavefunctions accurately. This makes planewaves very inefficient. To overcome this problem one can employ pseudopotential techniques, which allow an accurate description of the wavefunctions between the atoms, but avoid the fast oscillations near the core. Thus, less basis functions are needed. Another way to solve this problem is to use a basis set, which contains radial wavefunctions to describe the oscillations near the core. This has already been suggested by Slater [Sla37]. The corresponding technique is called the augmented planewave method (APW).

#### 3.1.1 The APW Method and its Problems

Within the APW approach, space is divided into spheres centered at each atom site, the so-called muffin-tins, and the remaining interstitial region (cf. fig. 3.1). Inside the muffin-tins the potential is approximated to be spherically symmetric, and in many implementations the interstitial potential is set constant. The restrictions to the potential are commonly called shape-approximations. Noting that planewaves solve the Schrödinger equation in a constant potential, while spherical harmonics times a radial function are the solution in a spherical potential, suggests to expand the single

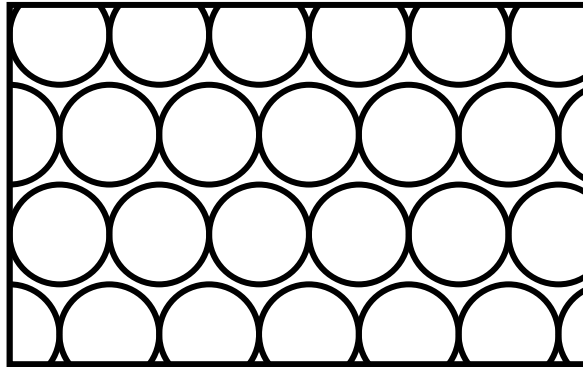


**Figure 3.1:** The division of space in the APW method. The muffin-tin spheres are surrounded by the interstitial region.

particle wavefunctions<sup>1</sup>  $\phi_\nu(\mathbf{k}, \mathbf{r})$  in terms of the following basis functions:

$$\varphi_{\mathbf{G}}(\mathbf{k}, \mathbf{r}) = \begin{cases} e^{i(\mathbf{G}+\mathbf{k})\mathbf{r}} & \text{interstitial region} \\ \sum_{lm} A_L^{\mu\mathbf{G}}(\mathbf{k}) u_l(r) Y_L(\hat{\mathbf{r}}) & \text{muffin-tin } \mu \end{cases} \quad (3.1)$$

Where  $\mathbf{k}$  is the Bloch vector,  $\Omega$  is the cell volume,  $\mathbf{G}$  is a reciprocal lattice vector,  $L$  abbreviates the quantum numbers  $l$  and  $m$  and  $u_l$  is the regular solution of the radial Schrödinger equation

$$\left\{ -\frac{\hbar^2}{2m} \frac{\partial^2}{\partial r^2} + \frac{\hbar^2}{2m} \frac{l(l+1)}{r^2} + V(r) - E_l \right\} r u_l(r) = 0 \quad (3.2)$$

Here  $E_l$  is an energy parameter and  $V(r)$  is the spherical component of the potential. The coefficients  $A_L^{\mu\mathbf{G}}(\mathbf{k})$  are determined from the requirement, that the wavefunctions have to be continuous at the boundary of the muffin-tin spheres.

Hence, the APW's form a set of continuous basis functions that cover all space. Where each function consists of a planewave in the interstitial region plus a sum of functions, which are solutions of the Schrödinger equation to a given set of angular momentum quantum numbers  $lm$  and a given parameter  $E_l$ , inside the muffin-tin spheres.

If the  $E_l$  were kept fixed, used only as a parameter during the construction of the basis, the hamiltonian could be set up in terms of this basis. This would lead to a standard secular equation for the band energies. Unfortunately, it turns out, that the

<sup>1</sup>I will only discuss the application of FLAPW to systems that possess either 2- or 3-dimensional translational symmetry, i.e. bulk crystals or thin crystal films.

APW basis does not offer enough variational freedom if the  $E_l$  are kept fixed. An accurate description can only be achieved if they are set to the corresponding band energies. However, requiring the  $E_l$ 's to equal the band energies, the latter can no longer be determined by a simple diagonalization of the Hamiltonian matrix. Since the  $u_l$ 's depend on the band energies, the solution of the secular equation becomes a nonlinear problem, which is computationally much more demanding than a secular problem.

Another disadvantage of the APW method is, that it is difficult to extend beyond the spherically averaged muffin-tin potential approximation, because in the case of a general potential the optimal choice of  $E_l$  is no longer the band energy. And finally, but less serious, if, for a given choice of  $E_l$ , the radial functions  $u_l$  vanish at the muffin tin radius, the boundary conditions on the spheres cannot be satisfied, i.e. the planewaves and the radial functions become decoupled. This is called the asymptote problem. It can already cause numerical difficulties if  $u_l$  becomes very small at the sphere boundary.

Further information about the APW method can be found in the book by Loucks [Lou67], which also reprints several early papers including Slater's original publication [Sla37].

### 3.1.2 The Concept of LAPW

The basic idea of the linearized augmented planewave method (LAPW) is to add extra variational freedom to the basis inside the muffin-tins, so that it is not necessary to set the  $E_l$  equal to the band energy. This is done by using not only the radial solution of the Schrödinger equation, but also its derivative with respect to the energy. This construction, which was first suggested by Andersen [And75], can be regarded as a linearization of the APW. To realize this recall that in the APW method the  $u_l$ 's depend on the band energies and can thus be understood as functions of  $r$  and  $\epsilon$ . Hence,  $u_l$  can be expanded into a Taylor-series around  $E_l$ .

$$u_l(\epsilon, r) = u_l(E_l, r) + \dot{u}_l(E_l, r)(\epsilon - E_l) + O[(\epsilon - E_l)^2] \quad (3.3)$$

Here  $\dot{u}_l$  denotes the energy derivative of  $u_l$ ,  $\partial u_l(\epsilon, r)/\partial \epsilon$ , and  $O[(\epsilon - E_l)^2]$  denotes errors that are quadratic in the energy difference. Ergo, the LAPW method introduces an error of order  $(\epsilon - E_l)^2$  in the wavefunction. Therefore, according to the variational principle the error in the calculated band energies is of the order  $(\epsilon - E_l)^4$ . Because of this high order, the linearization works very well even over rather broad energy regions. In most cases a single set of energy parameters is sufficient for the whole valence band. However, sometimes the energy region has to be split up in two (very rarely more) windows with separate sets of energy parameters.

But let's turn to some important properties of the LAPW basis first, before dis-



cussing its quality and accuracy. The LAPW basis functions are of the form

$$\varphi_{\mathbf{G}}(\mathbf{k}, \mathbf{r}) = \begin{cases} e^{i(\mathbf{G}+\mathbf{k})\mathbf{r}} & \text{interstitial region} \\ \sum_L A_L^{\mu\mathbf{G}}(\mathbf{k}) u_l(r) Y_L(\hat{\mathbf{r}}) + B_L^{\mu\mathbf{G}}(\mathbf{k}) \dot{u}_l(r) Y_L(\hat{\mathbf{r}}) & \text{muffin-tin } \mu \end{cases} \quad (3.4)$$

with the extra term  $B_L^{\mu\mathbf{G}} \dot{u}_l(r) Y_L(\hat{\mathbf{r}})$  compared to the APW method. The additional coefficient is determined by requiring that not only the basis functions, but also their derivatives with respect to  $r$  are continuous at the sphere boundaries. It is useful to require the following normalization.

$$\langle u|u \rangle = \int_0^{R_{MT}} u_l^2(r) r^2 dr = 1 \quad (3.5)$$

Here  $R_{MT}$  is the muffin-tin radius. Taking the derivative of (3.5) with respect to the energy it can easily be shown, that  $u_l$  and  $\dot{u}_l$  are orthogonal.  $\dot{u}_l$  is calculated from a Schrödinger-like equation, derived by taking the energy derivative of (3.2).

$$\left\{ -\frac{\hbar^2}{2m} \frac{\partial^2}{\partial r^2} + \frac{\hbar^2}{2m} \frac{l(l+1)}{r^2} + V(r) - E_l \right\} r \dot{u}_l(r) = r u_l(r) \quad (3.6)$$

Still the solution of this equation has to be made orthogonal to  $u_l$ , since any linear combination of  $\dot{u}_l$  and  $u_l$  also solves the equation. Once the  $u_l$  and  $\dot{u}_l$  are made orthogonal the basis functions inside the spheres form a completely orthogonal basis set, since the angular functions  $Y_{lm}(\hat{\mathbf{r}})$  are also orthogonal. However, the LAPW functions are in general not orthogonal to the core states, which are treated separately in the LAPW method. This fact can cause problems in the presence of high lying core states. A detailed discussion of these problems and strategies to circumvent them can be found in the book by Singh [Sin94], which includes a very comprehensive review of many aspects of the LAPW method.

With the construction of the LAPW basis the main problems of the APW method are solved:

- Since it is no longer necessary to set the energy parameters equal the band energies, the later can be determined by a single diagonalization of the Hamiltonian matrix.
- The LAPW method can be extended to nonspherical muffin tin potentials with little difficulty, because the basis offers enough variational freedom. This leads then to the full-potential linearized augmented planewave method (FLAPW).
- If  $u_l$  is zero at the sphere boundary, its radial derivative and  $\dot{u}_l$  are in general nonzero. Hence, the boundary conditions can always be satisfied and there is no asymptote problem.

As a final remark it is worth mentioning, that the nonlinearity inherent to the APW method can only be circumvented at the expense of a larger eigenvalue problem. To

see this, recall that within LAPW (and also within APW) the basis functions are represented by plane waves. The functions inside the muffin tins are coupled to the plane waves via the boundary conditions, and can only vary indirectly by a variation of the plane wave coefficients. Clearly, with a finite number of plane waves, at maximum the same number of functions inside the spheres can be varied independently. Hence, to make use of the extra variational freedom, that the LAPW basis set allows compared to the APW basis, i.e. to vary the  $u_l$ 's and the  $\hat{u}_l$ 's independently, more plane waves have to be used.

### 3.1.3 The Concept of FLAPW

In the past the majority of applications of APW and LAPW<sup>2</sup> method employed shape-approximations on the potential used in the Hamiltonian. Typically, the potential in the unit cell  $V(\mathbf{r})$  is approximated by  $V_0(\mathbf{r})$ ,

$$V(\mathbf{r}) = \begin{cases} V_I^0 = \text{const.} & \text{interstitial region} \\ V_{MT}^0(r) & \text{muffin-tin} \end{cases} \quad (3.7)$$

using a constant potential in the interstitial region and a spherically symmetric potential inside each sphere.

While the LAPW method yields accurate results for close-packed metal systems the shape-approximation becomes difficult to justify for crystals with open structures such as silicides, perovskides, surfaces or clusters.

In the full-potential LAPW method (FLAPW) [Ham79, WKWF81] any shape-approximations in the interstitial region and inside the muffin-tins are dropped. This generalization is achieved by relaxing the constant interstitial potential  $V_I^0$  and the spherical muffin-tin approximation  $V_{MT}^0(r)$  due to the inclusion of a warped interstitial  $\sum V_I^{\mathbf{G}} e^{i\mathbf{G}\mathbf{r}}$  and the non-spherical terms inside the muffin-tin spheres:

$$V(\mathbf{r}) = \begin{cases} \sum_{\mathbf{G}} V_I^{\mathbf{G}} e^{i\mathbf{G}\mathbf{r}} & \text{interstitial region} \\ \sum_L V_{MT}^L(r) Y_L(\hat{\mathbf{r}}) & \text{muffin-tin} \end{cases} \quad (3.8)$$

This method became possible with the development of a technique for obtaining the Coulomb potential for a general periodic charge density without shape-approximations and with the inclusion of the Hamiltonian matrix elements due to the warped interstitial and non-spherical terms of the potential. The charge density is represented in the same way as the potential:

$$\rho(\mathbf{r}) = \begin{cases} \sum_{\mathbf{G}} \rho_I^{\mathbf{G}} e^{i\mathbf{G}\mathbf{r}} & \text{interstitial region} \\ \sum_L \rho_{MT}^L(r) Y_L(\hat{\mathbf{r}}) & \text{muffin-tin} \end{cases} \quad (3.9)$$

---

<sup>2</sup>There are APW and LAPW methods available which include the warped interstitial potential [Koe72].

Detail of the solution of the Poisson equation for an arbitrarily shaped periodic potential are described in section 3.7.

### 3.1.4 The Generalized Eigenvalue Problem

After discussing the FLAPW basis it is necessary to say a few words about the eigenvalue problem. The solution of the eigenvalue problem has to be carried out separately for every Bloch vector. And, of course, the basis set and the Hamiltonian matrix have to be set up for each Bloch vector. However, I will not add the index  $\mathbf{k}$  to the basis functions and the Hamiltonian matrix.

There is one important fact that I have not mentioned so far. Even though plane-waves form an orthogonal basis set, the FLAPW functions do not. The plane-waves in the interstitial-region are non-orthogonal, because the muffin-tin are cut out, i.e. the integration, in terms of which orthogonality is defined, does not stretch over the whole unit cell, but only over interstitial region. An additional contribution comes from the muffin-tin. Even though the  $u_l(r)Y_L$  and  $\dot{u}_l(r)Y_L$  are mutually orthogonal, in general each plane-wave couples to all functions in the spheres.

Due to the non-orthogonality of the basis functions the overlap matrix  $\mathbf{S}$ , defined by (3.10), is not a diagonal, but a hermitian matrix.

$$S^{\mathbf{G}'\mathbf{G}} = \int \varphi_{\mathbf{G}'}^*(\mathbf{r})\varphi_{\mathbf{G}}(\mathbf{r})d^3r \quad (3.10)$$

In (the more convenient) Dirac notation the eigenvalue problem has the following form.

$$\mathcal{H}|\phi_i\rangle = \epsilon_i|\phi_i\rangle \quad (3.11)$$

Where  $|\phi_i\rangle$  denotes the eigenfunction corresponding to the  $i^{\text{th}}$  eigenvalue  $\epsilon_i$ . Substituting the expansion of the eigenfunctions

$$|\phi_i\rangle = \sum_{\mathbf{G}} c_{i\mathbf{G}}|\varphi_{\mathbf{G}}\rangle \quad (3.12)$$

we obtain

$$\sum_{\mathbf{G}} c_{i\mathbf{G}}\mathcal{H}|\varphi_{\mathbf{G}}\rangle = \epsilon_i \sum_{\mathbf{G}} c_{i\mathbf{G}}|\varphi_{\mathbf{G}}\rangle \quad (3.13)$$

Multiplying this from the left with  $\langle\varphi_{\mathbf{G}'}|$  we find

$$\sum_{\mathbf{G}} c_{i\mathbf{G}}\langle\varphi_{\mathbf{G}'}|\mathcal{H}|\varphi_{\mathbf{G}}\rangle = \epsilon_i \sum_{\mathbf{G}} c_{i\mathbf{G}}\langle\varphi_{\mathbf{G}'}|\varphi_{\mathbf{G}}\rangle \quad (3.14)$$

which can be written in matrix form

$$\{\mathbf{H} - \epsilon_i\mathbf{S}\}\mathbf{c}_i = 0 \quad (3.15)$$

where the eigenvector  $\mathbf{c}_i$  is the coefficient vector corresponding to the  $i^{\text{th}}$  eigenvalue. (3.15) is called a generalized eigenvalue problem.

However, this problem can be reduced to a standard eigenvalue problem using the Cholesky decomposition. It can be shown (e.g. Stoer [Sto94]), that any hermitian and positive definite matrix can be decomposed into a matrix product of a lower triangular with only positive diagonal elements matrix and its transposed. Clearly, the overlap matrix satisfies these conditions and can be written

$$\mathbf{S} = \mathbf{L}\mathbf{L}^{tr} \quad (3.16)$$

Therefore (3.15) becomes

$$\mathbf{H}\mathbf{c}_i = \epsilon_i \mathbf{L}\mathbf{L}^{tr} \mathbf{c}_i \quad (3.17)$$

multiplying from the left with  $\mathbf{L}^{-1}$  and introducing a unit matrix we get

$$\mathbf{L}^{-1}\mathbf{H}(\mathbf{L}^{-1})^{tr} \mathbf{L}^{tr} \mathbf{c}_i = \epsilon_i \mathbf{L}^{tr} \mathbf{c}_i \quad (3.18)$$

defining

$$\mathbf{P} = \mathbf{L}^{-1}\mathbf{H}(\mathbf{L}^{-1})^{tr}, \quad \mathbf{x}_i = \mathbf{L}^{tr} \mathbf{c}_i \quad (3.19)$$

we finally have

$$\mathbf{P}\mathbf{x}_i = \epsilon_i \mathbf{x}_i \quad (3.20)$$

Thus the generalized eigenvalue problem has been reduced to a simple eigenvalue problem. The eigenvectors  $\mathbf{c}_i$  can be obtained by the back-transformation

$$\mathbf{c}_i = (\mathbf{L}^{tr})^{-1} \mathbf{x}_i \quad (3.21)$$

### 3.1.5 Film Calculations within FLAPW

Nowadays the physics of surfaces is an field of major interest and investigation. However, surfaces are difficult to treat, because they break the translational symmetry, i.e. there is only the 2-dimensional symmetry parallel to the surface left to be used to reduce the problem, and a semi-infinite problem is left perpendicular to the surface. In our approach surfaces are approximated by thin films, typically 10–15 atomic layers thick. Obviously, this approximation, which is called the thin-slab approximation, can only yield good results if the interaction between the two surfaces of the film is weak enough, so that each of them shows the properties of the surfaces of an ideal semi-infinite crystal.

In the case of film calculations space is divided into three distinct regions, the muffin-tins, the interstitial and the vacuum region (cf. fig. 3.2). The interstitial region now stretches from  $-D/2$  to  $D/2$  in  $z$ -direction, which is defined to be the direction perpendicular to the film. The representation of the wavefunctions inside the muffin-tin spheres remains exactly the same as in the bulk case. Since the periodicity along the  $z$ -direction is lost, the unit cell extends principally from  $-\infty$  to  $\infty$  in  $z$ -direction. Still the wavefunctions can be expanded in terms of planewaves. However, the wavevectors perpendicular to the film are not defined in terms of  $D$ , but in terms

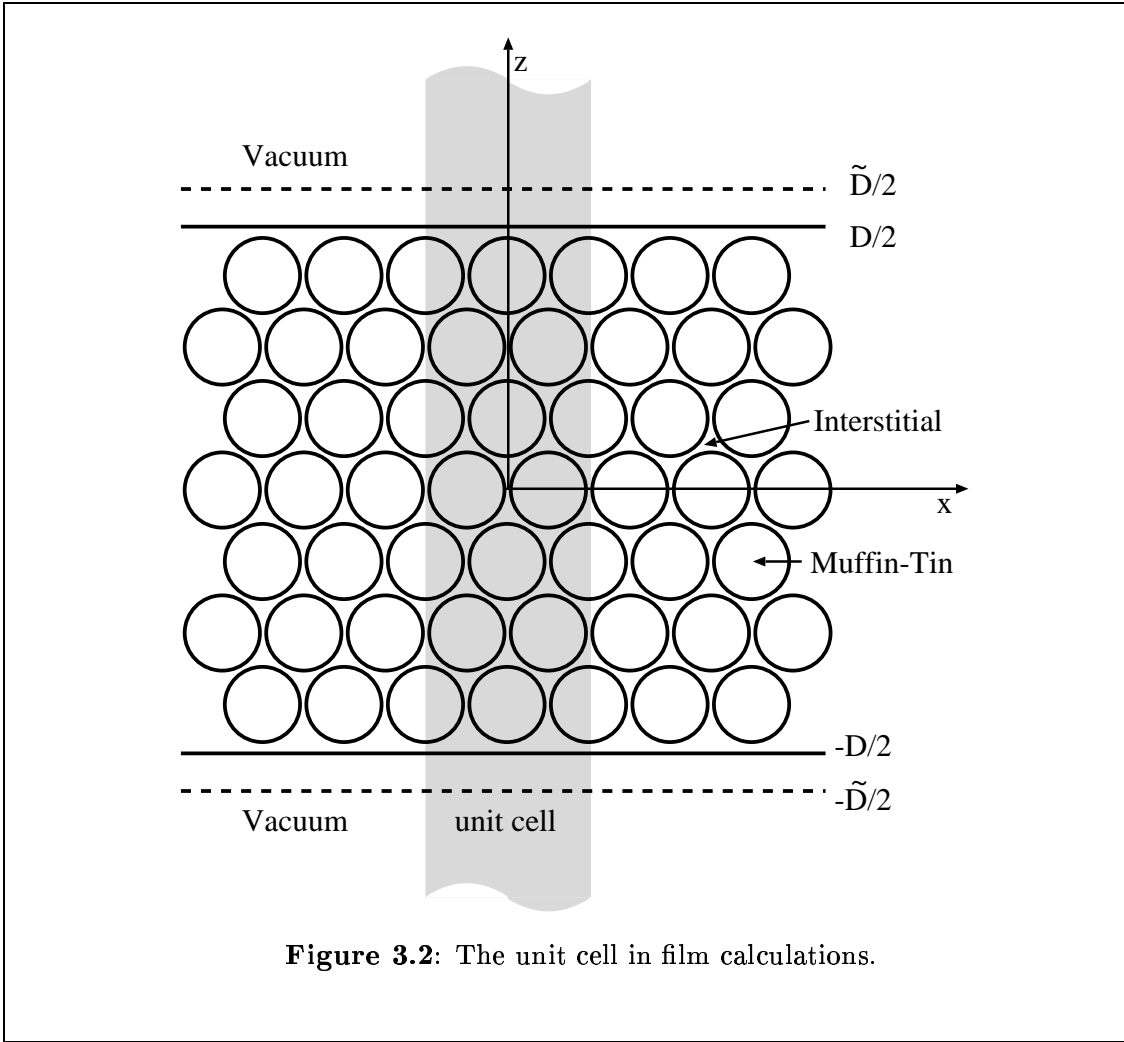


**Figure 3.2:** The unit cell in film calculations.

of  $\tilde{D}$ , which is chosen larger than  $D$  to gain greater variational freedom. Therefore, the planewaves have the form

$$\varphi_{\mathbf{G}_{\parallel}G_{\perp}}(\mathbf{k}_{\parallel}, \mathbf{r}) = e^{i(\mathbf{G}_{\parallel} + \mathbf{k}_{\parallel})\mathbf{r}_{\parallel}} e^{iG_{\perp}z} \quad (3.22)$$

with

$$G_{\perp} = \frac{2\pi n}{\tilde{D}} \quad (3.23)$$

where  $\mathbf{G}_{\parallel}$  and  $\mathbf{k}_{\parallel}$  are the 2-dimensional wave- and Bloch vectors,  $\mathbf{r}_{\parallel}$  is the parallel component of  $\mathbf{r}$  and  $G_{\perp}$  is the wavevector perpendicular to the film. The basis functions in the vacuum region are constructed in the same spirit as the functions in the muffin-tins. They consist of planewaves parallel to the film, and a  $z$ -dependent function  $u_{\mathbf{G}_{\parallel}}(\mathbf{k}_{\parallel}, z)$ , which solves the corresponding 1-dimensional Schrödinger equation (3.24), plus its energy derivative  $\dot{u}_{\mathbf{G}_{\parallel}}(\mathbf{k}_{\parallel}, z)$ .

$$\left\{ -\frac{\hbar^2}{2m} \frac{\partial^2}{\partial z^2} + V_0(z) - E_{vac} + \frac{\hbar^2}{2m} (\mathbf{G}_{\parallel} + \mathbf{k}_{\parallel})^2 \right\} u_{\mathbf{G}_{\parallel}}(\mathbf{k}_{\parallel}, z) = 0 \quad (3.24)$$

$E_{vac}$  is the vacuum energy parameter and  $V_0(z)$  is the planar averaged part of the vacuum potential. As in the case of  $\dot{u}_l$  in the muffin-tins, the function  $\dot{u}_{\mathbf{G}_{\parallel}}(\mathbf{k}_{\parallel}, z)$  is calculated from a Schrödinger-like equation, which can be obtained by deriving (3.24) with respect to the energy.

$$\left\{ -\frac{\hbar^2}{2m} \frac{\partial^2}{\partial z^2} + V_0(z) - E_{vac} + \frac{\hbar^2}{2m} (\mathbf{G}_{\parallel} + \mathbf{k}_{\parallel})^2 \right\} \dot{u}_{\mathbf{G}_{\parallel}}(\mathbf{k}_{\parallel}, z) = u_{\mathbf{G}_{\parallel}}(\mathbf{k}_{\parallel}, z) \quad (3.25)$$

The resulting basis functions have the form

$$\varphi_{\mathbf{G}_{\parallel}G_{\perp}}(\mathbf{k}_{\parallel}, \mathbf{r}) = \left\{ A_{\mathbf{G}_{\parallel}G_{\perp}}(\mathbf{k}_{\parallel}) u_{\mathbf{G}_{\parallel}}(\mathbf{k}_{\parallel}, z) + B_{\mathbf{G}_{\parallel}G_{\perp}}(\mathbf{k}_{\parallel}) \dot{u}_{\mathbf{G}_{\parallel}}(\mathbf{k}_{\parallel}, z) \right\} e^{i(\mathbf{G}_{\parallel} + \mathbf{k}_{\parallel})\mathbf{r}_{\parallel}} \quad (3.26)$$

The coefficients  $A_{\mathbf{G}_{\parallel}G_{\perp}}(\mathbf{k}_{\parallel})$  and  $B_{\mathbf{G}_{\parallel}G_{\perp}}(\mathbf{k}_{\parallel})$  are determined in exactly the same way as it is done for the muffin-tins by requiring that the functions are continuous and differentiable at the vacuum boundary. It should be mentioned, that the vacuum basis functions offer less variational freedom than the basis set in the interstitial region does. This can be seen by noting that there are only two functions,  $u_{\mathbf{G}_{\parallel}}$  and  $\dot{u}_{\mathbf{G}_{\parallel}}$  times the corresponding planar planewave, to be matched to all planewaves of the interstitial region with the same  $\mathbf{G}_{\parallel}$ . But there are generally far more than two different  $G_{\perp}$ 's, i.e the number of basis functions in the vacuum region is significantly smaller than in the interstitial region. However, this can be improved rather easily. In equation 3.24 only one energy parameter  $E_{vac}$  is used. Instead one can use a whole series of parameters  $E_{vac}^i$  to cover an energy region. A possible choice of the energy parameters could be  $E_{vac}^i = E_{vac}^{G_{\perp}} = E_{vac} - \frac{\hbar^2}{2m} G_{\perp}^2$ , which leads correspondingly to  $G_{\perp}$  dependent basis functions  $u_{\mathbf{G}_{\parallel}G_{\perp}}(\mathbf{k}_{\parallel}, z)$ . For more details see [NKD86]. In general, however, the present approximations is accurate, the energy spectrum of the electrons in the vacuum region is small due to the work-function.

Finally we would like to summarize the basis set used for thin film calculation with the FLAPW method.

$$\varphi_{\mathbf{G}_{\parallel}G_{\perp}}(\mathbf{k}_{\parallel}, \mathbf{r}) = \begin{cases} e^{i(\mathbf{G}_{\parallel} + \mathbf{k}_{\parallel})\mathbf{r}_{\parallel}} e^{iG_{\perp}z} & \text{Int.} \\ \left\{ A_{\mathbf{G}_{\parallel}G_{\perp}}(\mathbf{k}_{\parallel}) u_{\mathbf{G}_{\parallel}}(\mathbf{k}_{\parallel}, z) + B_{\mathbf{G}_{\parallel}G_{\perp}}(\mathbf{k}_{\parallel}) \dot{u}_{\mathbf{G}_{\parallel}}(\mathbf{k}_{\parallel}, z) \right\} e^{i(\mathbf{G}_{\parallel} + \mathbf{k}_{\parallel})\mathbf{r}_{\parallel}} & \text{Vac.} \\ \sum_L A_L^{\mu\mathbf{G}}(\mathbf{k}) u_l(r) Y_L(\hat{\mathbf{r}}) + B_L^{\mu\mathbf{G}}(\mathbf{k}) \dot{u}_l(r) Y_L(\hat{\mathbf{r}}) & \text{MT } \mu \end{cases} \quad (3.27)$$

This expansion has been suggested by H. Krakauer, M. Posternak and A.J. Freeman [KPF79].

## 3.2 Relativity in Valence Electron Calculations

Relativistic effects are important for the correct numerical description of core or valence electrons. Both core and valence electrons have finite wavefunctions near the

nucleus, where the kinetic energy is large. This kinetic energy enhancement becomes more significant for heavier elements and compounds. Additionally, only relativistic effects, in particular the spin-orbit-coupling, introduce a link between spatial and spin coordinates. Thus, information about the orientation of spins relative to the lattice can only be gained if relativity is taken into account. For fully relativistic description of the electronic structure all relativistic effects (mass-velocity, Darwin-term, spin-orbit coupling) have to be taken into account [SDKW96]. However, in many applications an approximation is used, where the spin-orbit interaction is neglected. This approximation is called the scalar relativistic approximation.

### 3.2.1 The Kohn-Sham-Dirac Equation

In a relativistic density functional theory the Kohn-Sham equation has the form of a single particle Dirac equation

$$\{c\boldsymbol{\alpha} \cdot \mathbf{p} + (\beta - 1)mc^2 + V^{eff}(\mathbf{r})\} \Psi = E\Psi \quad (3.28)$$

$$\boldsymbol{\alpha} = \left( \left( \begin{pmatrix} 0 & \sigma_x \\ \sigma_x & 0 \end{pmatrix}, \begin{pmatrix} 0 & \sigma_y \\ \sigma_y & 0 \end{pmatrix}, \begin{pmatrix} 0 & \sigma_z \\ \sigma_z & 0 \end{pmatrix} \right)^{tr} = \begin{pmatrix} 0 & \boldsymbol{\sigma} \\ \boldsymbol{\sigma} & 0 \end{pmatrix} \quad (3.29)$$

$$\beta = \begin{pmatrix} \mathbf{I}_2 & 0 \\ 0 & -\mathbf{I}_2 \end{pmatrix} \quad (3.30)$$

Here,  $\sigma_x$   $\sigma_y$   $\sigma_z$  are the Pauli matrices and  $\boldsymbol{\sigma}$  is the vector of Pauli matrices,  $\mathbf{p}$  is the momentum operator, and  $I_n$  denotes an  $(n \times n)$  unit matrix.  $V^{eff}$  is the effective potential, that contains electron-nucleon Coulomb potential, Hartree potential and exchange-correlation potential. In the case of non-zero spin-polarization,  $V^{eff}$  becomes spin-dependent. Finally,  $\Psi$  is the relativistic four component wavefunction.

The straightforward way to solve this problem would be to expand each of the four components of  $\Psi$  in terms of the FLAPW basis. However, if all four components were treated with the same accuracy, this would result in a basis set which contains four times as many functions as in the non-relativistic (non-magnetic) case. Since the numerical effort of the Hamiltonian diagonalization scales with the dimension of the matrix to the power of three, this would increase the computing time needed for the diagonalization by a factor of 64.

The FLAPW implementation we use introduces some approximations to make relativistic calculations more efficient. One of these approximations is the scalar relativistic approximations, which has been suggested by D.D. Koelling and B.N. Harmon [KH77], where the spin-orbit term is neglected, and spin and spatial coordinates become decoupled. Hence, the Hamiltonian matrix reduces to two matrices of half the size, which can be diagonalized separately. This saves a factor of four in computing time. The scalar relativistic approximation will be discussed more detailed in

the next section. It should be noted, that relativistic effects are only significant close to the nucleus, where the kinetic energy is large. It is therefore reasonable to treat the interstitial region and the vacuum non-relativistically. Thus, merely within the muffin-tins the electrons are treated relativistically. And only the large component of  $\Psi$  is matched to the non-relativistic wavefunctions at the boundary between the muffin-tins and the interstitial region, because the small component is already negligible at this distance from the nucleus. The small component is attached to the large component, and cannot be varied independently. However, this is a sensible approximation for two reasons: Firstly even inside the muffin-tin sphere the large component is still much bigger than the small component, and plays the more important role, and secondly the two components are determined by solving the scalar relativistic equations for the spherically averaged potential. Therefore, they are very well suited to describe the wavefunctions.

Hence, the size of the basis set and the Hamiltonian matrix remains the same as in non-relativistic calculations, but the problem has to be solved twice, once for each direction of spin. This amounts to a numerical effort, that is equal to that needed in spin-polarized non-relativistic calculations.

### 3.2.2 The Scalar Relativistic Approximation

As I pointed out in the previous section, the electrons are only treated relativistically inside the muffin-tin spheres. Thus, the first problem that has to be addressed is the construction of the relativistic radial function. This is done by solving the scalar relativistic equation, including only the spherically averaged part of the potential. The starting point is the following Dirac equation.

$$\{c\boldsymbol{\alpha} \cdot \mathbf{p} + (\beta - 1)mc^2 + V(r)\} \Psi = E\Psi \quad (3.31)$$

The solution of (3.31) is discussed in many textbooks, e.g. E.M. Rose [Ros61]. Due to spin-orbit coupling  $m$  and  $m_s$  are not good quantum numbers any more, and they have to be replaced by the quantum numbers  $\kappa$  and  $\mu$  (or  $j$  and  $\mu$ ), which are eigenvalues of the operators  $K$  and the z-component of the total angular momentum  $j_z$  (or the total angular momentum  $\mathbf{j}$  and  $j_z$ ) respectively.  $K$  is defined by

$$K = \beta(\boldsymbol{\sigma} \cdot \mathbf{l} + 1) \quad (3.32)$$

The solutions of (3.31) have the form

$$\Psi = \Psi_{\kappa\mu} = \begin{pmatrix} g_{\kappa}(r)\chi_{\kappa\mu} \\ if_{\kappa}(r)\chi_{-\kappa\mu} \end{pmatrix} \quad (3.33)$$

Where  $g_{\kappa}(r)$  is the large component,  $f_{\kappa}(r)$  is the small component,  $\chi_{\kappa\mu}$  and  $\chi_{-\kappa\mu}$  are spin angular functions, which are eigenfunctions of  $\mathbf{j}$ ,  $j_z$ ,  $K$  and  $\mathbf{s}^2$  with eigenvalues  $j$ ,  $\mu$ ,  $\kappa$  ( $-\kappa$ ) and  $s = 1/2$  respectively. The spin angular functions can be expanded into



a sum of products of spherical harmonics and Pauli spinors. Where the expansion coefficients are the Clebsch-Gordon coefficients. The radial functions have to satisfy the following set of coupled equations.

$$\frac{\partial}{\partial r} g_\kappa(r) = -\frac{\kappa+1}{r} g_\kappa(r) + 2Mc f_\kappa(r) \quad (3.34)$$

$$\frac{\partial}{\partial r} f_\kappa(r) = \frac{1}{c}(V(r) - E)g_\kappa(r) + \frac{\kappa-1}{r} f_\kappa(r) \quad (3.35)$$

with

$$M = m + \frac{1}{2c^2}(E - V(r)) \quad (3.36)$$

This can be written in matrix form.

$$\begin{pmatrix} -\frac{\kappa+1}{r} - \frac{\partial}{\partial r} & 2Mc \\ \frac{1}{c}(V(r) - E) & \frac{\kappa-1}{r} - \frac{\partial}{\partial r} \end{pmatrix} \begin{pmatrix} g_\kappa(r) \\ f_\kappa(r) \end{pmatrix} = 0 \quad (3.37)$$

To derive the scalar relativistic approximation D.D. Koelling and B.N. Harmon [KH77] introduce the following transformation.

$$\begin{pmatrix} g_\kappa(r) \\ \phi_\kappa(r) \end{pmatrix} = \begin{pmatrix} 1 & 0 \\ \frac{1}{2Mc} \frac{\kappa+1}{r} & 1 \end{pmatrix} \begin{pmatrix} g_\kappa(r) \\ f_\kappa(r) \end{pmatrix} \quad (3.38)$$

Using this transformation (3.37) becomes

$$\begin{pmatrix} -\frac{\partial}{\partial r} & 2Mc \\ \frac{1}{2Mc} \frac{\kappa(\kappa+1)}{r^2} + \frac{1}{c}(V(r) - E) - \frac{1}{2Mc} \frac{\kappa+1}{r} \left( \frac{\partial}{\partial r} - \frac{M'}{M} \right) & \frac{\kappa-1}{r} - \frac{\partial}{\partial r} \end{pmatrix} \begin{pmatrix} g_\kappa(r) \\ \phi_\kappa(r) \end{pmatrix} = 0 \quad (3.39)$$

Where  $M'$  denotes the derivative of  $M$  with respect to  $r$  ( $\partial M/\partial r$ ). Multiplying the first line in (3.39) by  $(\kappa+1)/2Mc r$  and subtracting it from the second yields

$$\begin{pmatrix} -\frac{\partial}{\partial r} & 2Mc \\ \frac{1}{2Mc} \frac{l(l+1)}{r^2} + \frac{1}{c}(V(r) - E) + \frac{\kappa+1}{r} \frac{M'}{2M^2 c} & -\frac{2}{r} - \frac{\partial}{\partial r} \end{pmatrix} \begin{pmatrix} g_\kappa(r) \\ \phi_\kappa(r) \end{pmatrix} = 0 \quad (3.40)$$

Where the identity  $\kappa(\kappa+1) = l(l+1)$  has been used. Recalling, that  $\kappa$  is the eigenvalue of  $K = \beta(\boldsymbol{\sigma} \cdot \mathbf{l} + 1)$  the term  $(\kappa+1)M'/2M^2 c r$  can be identified as the spin-orbit

term. This term is dropped in the scalar relativistic approximation, because it is the only one, that causes coupling of spin up and spin down contributions. In the original paper this is interpreted as an average over all states for the two possible values of  $\kappa$ ,  $\kappa = l, (j = l - 1/2)$  and  $\kappa = -(l + 1), (j = l + 1/2)$ . The radial functions  $g_l(r)$  and  $\phi_l(r)$  (the index  $\kappa$  has been replaced by  $l$ ) can now be calculated from the following set of differential equations.

$$\frac{\partial}{\partial r} g_l(r) = 2Mc\phi_l(r) \quad (3.41)$$

$$\frac{\partial}{\partial r} \phi_l(r) = \left( \frac{1}{2Mc} \frac{l(l+1)}{r^2} + \frac{1}{c}(V(r) - E) \right) g_l(r) - \frac{2}{r} \phi_l(r) \quad (3.42)$$

Deriving these equations with respect to the energy yields a set of equations for  $\dot{g}_l(r)$  and  $\dot{\phi}_l(r)$ , which are the relativistic analog of  $\dot{u}_l(r)$ .

$$\frac{\partial}{\partial r} \dot{g}_l(r) = 2Mc\dot{\phi}_l(r) + 2\dot{M}c\phi_l(r) \quad (3.43)$$

$$\begin{aligned} \frac{\partial}{\partial r} \dot{\phi}_l(r) &= \left( \frac{1}{2Mc} \frac{l(l+1)}{r^2} + \frac{1}{c}(V(r) - E) \right) \dot{g}_l(r) \\ &\quad - \left( \frac{\dot{M}}{2M^2c} \frac{l(l+1)}{r^2} + \frac{1}{c} \right) g_l(r) - \frac{2}{r} \dot{\phi}_l(r) \end{aligned} \quad (3.44)$$

For numerical reasons the functions  $g_l(r)$  and  $\phi_l(r)$  are replaced by  $p(r) = rg_l(r)$  and  $q(r) = cr\phi_l(r)$ . Thus, equations (3.41) – (3.44) become

$$\frac{\partial}{\partial r} p(r) = 2 \left( 1 + \frac{1}{2c^2}(E - V(r)) \right) q(r) + \frac{p(r)}{r} \quad (3.45)$$

$$\frac{\partial}{\partial r} q(r) = \left( \frac{l(l+1)}{2 \left( 1 + \frac{1}{2c^2}(E - V(r)) \right) r^2} + V(r) - E \right) p(r) - \frac{q(r)}{r} \quad (3.46)$$

$$\frac{\partial}{\partial r} \dot{p}(r) = 2 \left( \left( 1 + \frac{1}{2c^2}(E - V(r)) \right) \dot{q}(r) + \frac{1}{2c^2} q(r) \right) + \frac{\dot{p}(r)}{r} \quad (3.47)$$

$$\begin{aligned} \frac{\partial}{\partial r} \dot{q}(r) &= \left( \frac{l(l+1)}{2 \left( 1 + \frac{1}{2c^2}(E - V(r)) \right) r^2} + V(r) - E \right) \dot{p}(r) \\ &\quad - \left( \frac{l(l+1)}{4c^2 \left( 1 + \frac{1}{2c^2}(E - V(r)) \right) r^2} + 1 \right) p(r) - \frac{\dot{q}(r)}{r} \end{aligned} \quad (3.48)$$

This formulae have been obtained using the definition of  $M$  (3.36),  $\dot{M} = 1/2c^2$  and the fact that  $m = 1$  in Hartree units. In our implementation of FLAPW the radial wavefunctions are normalized according to

$$\left\langle \begin{pmatrix} g_l \\ \phi_l \end{pmatrix} \middle| \begin{pmatrix} g_l \\ \phi_l \end{pmatrix} \right\rangle = \int_0^{R_{MT}} (g_l^2(r) + \phi_l^2(r)) r^2 dr = 1 \quad (3.49)$$

However,  $g_l^2(r) + \phi_l^2(r)$  is not the charge density. The radial charge density is defined by

$$\rho_l(r) = \left\langle \left( \begin{array}{c} g_l \\ f_l \end{array} \right) \middle| \left( \begin{array}{c} g_l \\ f_l \end{array} \right) \right\rangle = \int_0^{R_{MT}} (g_l^2(r) + f_l^2(r)) r^2 dr \quad (3.50)$$

The energy derivatives of the radial functions have to be made orthogonal to the radial functions (comp. section(3.1.2)).

$$\left\langle \left( \begin{array}{c} g_l \\ \phi_l \end{array} \right) \middle| \left( \begin{array}{c} \dot{g}_l \\ \dot{\phi}_l \end{array} \right) \right\rangle = 0 \quad (3.51)$$

Thus, the scalar relativistic FLAPW basis set is

$$\varphi_{\mathbf{G}_{\parallel} \mathbf{G}_{\perp}}(\mathbf{r}) = \begin{cases} \frac{1}{\sqrt{\Omega}} e^{i(\mathbf{G}_{\parallel} + \mathbf{k}_{\parallel}) \cdot \mathbf{r}_{\parallel}} e^{i \mathbf{G}_{\perp} \cdot \mathbf{z}} & Int. \\ \{A_{\mathbf{G}_{\parallel} \mathbf{G}_{\perp}} u_{\mathbf{G}_{\parallel}}(z) + B_{\mathbf{G}_{\parallel} \mathbf{G}_{\perp}} \dot{u}_{\mathbf{G}_{\parallel}}(z)\} e^{i(\mathbf{G}_{\parallel} + \mathbf{k}_{\parallel}) \cdot \mathbf{r}_{\parallel}} & Vac. \\ \sum_{lm}^{\alpha} A_{lm}^{\alpha \mathbf{G} \mathbf{k}} \begin{pmatrix} g_l(r) \\ \phi_l(r) \end{pmatrix} Y_{lm}(\hat{\mathbf{r}}) + B_{lm}^{\alpha \mathbf{G} \mathbf{k}} \begin{pmatrix} \dot{g}_l(r) \\ \dot{\phi}_l(r) \end{pmatrix} Y_{lm}(\hat{\mathbf{r}}) & MT \end{cases} \quad (3.52)$$

Note, that the Pauli-spinors have been omitted, since the spin up and down problems are solved independently within the scalar relativistic approximation. Rewriting (3.40)

$$\mathcal{H}_{SP} \begin{pmatrix} g_l(r) \\ \phi_l(r) \end{pmatrix} = E \begin{pmatrix} g_l(r) \\ \phi_l(r) \end{pmatrix} \quad (3.53)$$

with

$$\mathcal{H}_{SP} = \begin{pmatrix} \frac{1}{2M} \frac{l(l+1)}{r^2} + V(r) & -\frac{2c}{r} - c \frac{\partial}{\partial r} \\ c \frac{\partial}{\partial r} & -2mc^2 + V(r) \end{pmatrix} \quad (3.54)$$

a matrix expression for the scalar relativistic Hamiltonian including only the spherically averaged part of the potential can be obtained.

### 3.3 Construction of the Hamiltonian Matrix

The FLAPW Hamiltonian and overlap matrices consist of three contributions from the three regions into which space is divided.

$$\mathbf{H} = \mathbf{H}_I + \mathbf{H}_{MT} + \mathbf{H}_V \quad (3.55)$$

$$\mathbf{S} = \mathbf{S}_I + \mathbf{S}_{MT} + \mathbf{S}_V \quad (3.56)$$

All three contributions have to be computed separately. Let's begin with the muffin-tin spheres.

### 3.3.1 Contribution of the Muffin-Tins

The contribution of the muffin-tin to the Hamiltonian matrix and the overlap matrix is given by:

$$H_{MT}^{\mathbf{G}'\mathbf{G}}(\mathbf{k}) = \sum_{\mu} \int_{MT^{\mu}} \left( \sum_{L'} A_{L'}^{\mu\mathbf{G}'}(\mathbf{k}) \varphi_{L'}^{\alpha}(\mathbf{r}) + B_{L'}^{\mu\mathbf{G}'}(\mathbf{k}) \dot{\varphi}_{L'}^{\alpha}(\mathbf{r}) \right)^* \mathcal{H}_{MT^{\alpha}} \left( \sum_L A_L^{\mu\mathbf{G}}(\mathbf{k}) \varphi_L^{\alpha}(\mathbf{r}) + B_L^{\mu\mathbf{G}}(\mathbf{k}) \dot{\varphi}_L^{\alpha}(\mathbf{r}) \right) d^3r \quad (3.57)$$

$$S_{MT}^{\mathbf{G}'\mathbf{G}}(\mathbf{k}) = \sum_{\mu} \int_{MT^{\mu}} \left( \sum_{L'} A_{L'}^{\mu\mathbf{G}'}(\mathbf{k}) \varphi_{L'}^{\alpha}(\mathbf{r}) + B_{L'}^{\mu\mathbf{G}'}(\mathbf{k}) \dot{\varphi}_{L'}^{\alpha}(\mathbf{r}) \right)^* \left( \sum_L A_L^{\mu\mathbf{G}}(\mathbf{k}) \varphi_L^{\alpha}(\mathbf{r}) + B_L^{\mu\mathbf{G}}(\mathbf{k}) \dot{\varphi}_L^{\alpha}(\mathbf{r}) \right) d^3r \quad (3.58)$$

with

$$\varphi_L^{\alpha}(\mathbf{r}) = \begin{pmatrix} g_l(r) \\ \phi_l(r) \end{pmatrix} Y_L(\hat{\mathbf{r}}), \quad \dot{\varphi}_L^{\alpha}(\mathbf{r}) = \begin{pmatrix} \dot{g}_l(r) \\ \dot{\phi}_l(r) \end{pmatrix} Y_L(\hat{\mathbf{r}}) \quad (3.59)$$

Where we distinguish between the atom index  $\mu$  and the atom type index  $\alpha(\mu)$ . In most application the are symmetry equivalent atom in the unit cell, i.e. some atoms can be mapped onto each other by space group operations. Clearly, these atom must possess the same physical properties, e.g. the potential has to be equal. As a consequence, the Hamiltonian and the basis functions  $\varphi_L^{\alpha}(\mathbf{r})$  do not differ among the atoms of the same type. This fact is exploited in that the muffin-tin potential of an atom type is only stored once for the representative atom, and the matrices 3.61–3.64 is also calculated for the representative only.  $\mathcal{H}_{MT^{\alpha}}$  is the scalar relativistic Hamiltonian operator. It can be split up into two parts, the spherical Hamiltonian  $\mathcal{H}_{sp}$  (3.54) and the nonspherical contributions to the potential  $V_{ns}$ .

$$\mathcal{H}_{MT^{\alpha}} = \mathcal{H}_{sp}^{\alpha} + V_{ns}^{\alpha} \quad (3.60)$$

The above integrations contain the following matrix elements.

$$t_{L'L}^{\alpha\varphi\varphi} = \int_{MT^{\alpha}} \varphi_{L'}^{\alpha}(\mathbf{r}) \mathcal{H}_{MT^{\alpha}} \varphi_L^{\alpha}(\mathbf{r}) d^3r \quad (3.61)$$

$$t_{L'L}^{\alpha\varphi\dot{\varphi}} = \int_{MT^{\alpha}} \varphi_{L'}^{\alpha}(\mathbf{r}) \mathcal{H}_{MT^{\alpha}} \dot{\varphi}_L^{\alpha}(\mathbf{r}) d^3r \quad (3.62)$$

$$t_{L'L}^{\alpha\dot{\varphi}\varphi} = \int_{MT^{\alpha}} \dot{\varphi}_{L'}^{\alpha}(\mathbf{r}) \mathcal{H}_{MT^{\alpha}} \varphi_L^{\alpha}(\mathbf{r}) d^3r \quad (3.63)$$

$$t_{L'L}^{\alpha\dot{\varphi}\dot{\varphi}} = \int_{MT^{\alpha}} \dot{\varphi}_{L'}^{\alpha}(\mathbf{r}) \mathcal{H}_{MT^{\alpha}} \dot{\varphi}_L^{\alpha}(\mathbf{r}) d^3r \quad (3.64)$$

These matrix elements do not depend on the  $A_L^{\mu\mathbf{G}}(\mathbf{k})$  and  $B_L^{\mu\mathbf{G}}(\mathbf{k})$  coefficients. Thus, they are independent of the Bloch vector and need to be calculated only once per

iteration. The functions  $\varphi_L^\alpha$  and  $\dot{\varphi}_L^\alpha$  have been constructed to diagonalize the spherical part  $\mathcal{H}_{sp}^\alpha$  of the muffin-tin Hamiltonian  $\mathcal{H}_{MT^\alpha}$ .

$$\mathcal{H}_{sp}^\alpha \varphi_L^\alpha = E_l \varphi_L^\alpha \quad (3.65)$$

$$\mathcal{H}_{sp}^\alpha \dot{\varphi}_L^\alpha + \dot{\mathcal{H}}_{sp}^\alpha \varphi_L^\alpha = E_l \dot{\varphi}_L^\alpha + \varphi_L^\alpha \quad (3.66)$$

However,  $\dot{\mathcal{H}}_{sp}^\alpha$  is smaller than  $\mathcal{H}_{sp}^\alpha$ , by a factor of  $1/c^2$  and is therefore neglected.

$$\mathcal{H}_{sp}^\alpha \dot{\varphi}_L^\alpha = E_l \dot{\varphi}_L^\alpha + \varphi_L^\alpha \quad (3.67)$$

Multiplying these equations with  $\varphi_{L'}^\alpha(\mathbf{r})$  and  $\dot{\varphi}_{L'}^\alpha(\mathbf{r})$  respectively and integrating over the muffin-tins gives

$$\langle \varphi_{L'}^\alpha | \mathcal{H}_{sp}^\alpha \varphi_L^\alpha \rangle_{MT^\alpha} = \delta_{l'l'} \delta_{mm'} E_l \quad (3.68)$$

$$\langle \varphi_{L'}^\alpha | \mathcal{H}_{sp}^\alpha \dot{\varphi}_L^\alpha \rangle_{MT^\alpha} = \delta_{l'l'} \delta_{mm'} \quad (3.69)$$

$$\langle \dot{\varphi}_{L'}^\alpha | \mathcal{H}_{sp}^\alpha \varphi_L^\alpha \rangle_{MT^\alpha} = 0 \quad (3.70)$$

$$\langle \dot{\varphi}_{L'}^\alpha | \mathcal{H}_{sp}^\alpha \dot{\varphi}_L^\alpha \rangle_{MT^\alpha} = \delta_{l'l'} \delta_{mm'} E_l \langle \dot{\varphi}_L^\alpha | \dot{\varphi}_L^\alpha \rangle_{MT^\alpha} \quad (3.71)$$

Where the normalization condition for  $\varphi_L^\alpha$  has been used. So, only the expectation values of the nonspherical part of the potential are left to be determined. Since the potential is also expanded into a product of radial functions and spherical harmonics, the corresponding integrals consist of product of a radial integrals and an angular integrals over three spherical harmonics, the so-called gaunt coefficients.

$$V^\alpha(\mathbf{r}) = \sum_{L''} V_{L''}^\alpha(r) Y_{L''}(\hat{\mathbf{r}}) \quad (3.72)$$

$$t_{L'L}^{\alpha\varphi\varphi} = \sum_{l''} I_{l'l''}^{\alpha\varphi\varphi} G_{l'l''}^{m'mm''} + \delta_{l'l'} \delta_{mm'} E_l \quad (3.73)$$

$$t_{L'L}^{\alpha\varphi\dot{\varphi}} = \sum_{l''} I_{l'l''}^{\alpha\varphi\dot{\varphi}} G_{l'l''}^{m'mm''} + \delta_{l'l'} \delta_{mm'} \quad (3.74)$$

$$t_{L'L}^{\alpha\dot{\varphi}\varphi} = \sum_{l''} I_{l'l''}^{\alpha\dot{\varphi}\varphi} G_{l'l''}^{m'mm''} \quad (3.75)$$

$$t_{L'L}^{\alpha\dot{\varphi}\dot{\varphi}} = \sum_{l''} I_{l'l''}^{\alpha\dot{\varphi}\dot{\varphi}} G_{l'l''}^{m'mm''} + \delta_{l'l'} \delta_{mm'} E_l \langle \dot{\varphi}_{lm}^\alpha | \dot{\varphi}_{lm}^\alpha \rangle_{MT^\alpha} \quad (3.76)$$

with

$$I_{l'l''}^{\alpha\varphi\varphi} = \int (g_{l''}^\alpha(r) g_l^\alpha(r) + \phi_{l''}^\alpha(r) \phi_l^\alpha(r)) V_{l''}^\alpha(r) r^2 dr \quad (3.77)$$

$$I_{l'l''}^{\alpha\varphi\dot{\varphi}} = \int (g_{l''}^\alpha(r) \dot{g}_l^\alpha(r) + \phi_{l''}^\alpha(r) \dot{\phi}_l^\alpha(r)) V_{l''}^\alpha(r) r^2 dr \quad (3.78)$$

$$I_{l'l''}^{\alpha\dot{\varphi}\varphi} = \int (\dot{g}_{l''}^\alpha(r) g_l^\alpha(r) + \dot{\phi}_{l''}^\alpha(r) \phi_l^\alpha(r)) V_{l''}^\alpha(r) r^2 dr \quad (3.79)$$

$$I_{l'l''}^{\alpha\dot{\varphi}\dot{\varphi}} = \int (\dot{g}_{l''}^\alpha(r) \dot{g}_l^\alpha(r) + \dot{\phi}_{l''}^\alpha(r) \dot{\phi}_l^\alpha(r)) V_{l''}^\alpha(r) r^2 dr \quad (3.80)$$

and

$$G_{l'l''}^{mm'm''} = \int Y_{lm}^* Y_{l'm'} Y_{l''m''} d\Omega \quad (3.81)$$

The  $I$  matrices contain the radial integrals. Finally, the Hamiltonian and overlap matrix elements become

$$\begin{aligned} H_{MT}^{\mathbf{G}'\mathbf{G}}(\mathbf{k}) &= \sum_{\mu} \sum_{L'L} (A_{L'}^{\mu\mathbf{G}'}(\mathbf{k}))^* t_{L'L}^{\alpha\varphi\varphi} A_L^{\mu\mathbf{G}}(\mathbf{k}) + (B_{L'}^{\mu\mathbf{G}'}(\mathbf{k}))^* t_{L'L}^{\alpha\dot{\varphi}\dot{\varphi}} B_L^{\mu\mathbf{G}}(\mathbf{k}) \\ &\quad + (A_{L'}^{\mu\mathbf{G}'}(\mathbf{k}))^* t_{L'L}^{\alpha\varphi\dot{\varphi}} B_L^{\mu\mathbf{G}}(\mathbf{k}) + (B_{L'}^{\mu\mathbf{G}'}(\mathbf{k}))^* t_{L'L}^{\alpha\dot{\varphi}\varphi} A_L^{\mu\mathbf{G}}(\mathbf{k}) \end{aligned} \quad (3.82)$$

$$S_{MT}^{\mathbf{G}'\mathbf{G}}(\mathbf{k}) = \sum_{\mu} \sum_L (A_L^{\mu\mathbf{G}'}(\mathbf{k}))^* A_L^{\mu\mathbf{G}}(\mathbf{k}) + (B_L^{\mu\mathbf{G}'}(\mathbf{k}))^* B_L^{\mu\mathbf{G}}(\mathbf{k}) \langle \dot{\varphi}_L^{\alpha} | \dot{\varphi}_L^{\alpha} \rangle_{MT\mu} \quad (3.83)$$

### 3.3.2 The Vacuum Contribution

The vacuum contributions to the Hamiltonian and overlap matrix are.

$$\begin{aligned} H_V^{\mathbf{G}'\mathbf{G}}(\mathbf{k}_{\parallel}) &= \int_V \left( \{ A_{\mathbf{G}'_{\parallel}\mathbf{G}'_{\perp}}(\mathbf{k}_{\parallel}) u_{\mathbf{G}'_{\parallel}}(\mathbf{k}_{\parallel}, z) + B_{\mathbf{G}'_{\parallel}\mathbf{G}'_{\perp}}(\mathbf{k}_{\parallel}) \dot{u}_{\mathbf{G}'_{\parallel}}(\mathbf{k}_{\parallel}, z) \} e^{i(\mathbf{G}'_{\parallel} + \mathbf{k}_{\parallel})\mathbf{r}_{\parallel}} \right)^* \\ &\quad \mathcal{H}_V \left( \{ A_{\mathbf{G}_{\parallel}\mathbf{G}_{\perp}}(\mathbf{k}_{\parallel}) u_{\mathbf{G}_{\parallel}}(\mathbf{k}_{\parallel}, z) + B_{\mathbf{G}_{\parallel}\mathbf{G}_{\perp}}(\mathbf{k}_{\parallel}) \dot{u}_{\mathbf{G}_{\parallel}}(\mathbf{k}_{\parallel}, z) \} e^{i(\mathbf{G}_{\parallel} + \mathbf{k}_{\parallel})\mathbf{r}_{\parallel}} \right) d^3r \\ S_V^{\mathbf{G}'\mathbf{G}}(\mathbf{k}_{\parallel}) &= \int_V \left( \{ A_{\mathbf{G}'_{\parallel}\mathbf{G}'_{\perp}}(\mathbf{k}_{\parallel}) u_{\mathbf{G}'_{\parallel}}(\mathbf{k}_{\parallel}, z) + B_{\mathbf{G}'_{\parallel}\mathbf{G}'_{\perp}}(\mathbf{k}_{\parallel}) \dot{u}_{\mathbf{G}'_{\parallel}}(\mathbf{k}_{\parallel}, z) \} e^{i(\mathbf{G}'_{\parallel} + \mathbf{k}_{\parallel})\mathbf{r}_{\parallel}} \right)^* \\ &\quad \left( \{ A_{\mathbf{G}_{\parallel}\mathbf{G}_{\perp}}(\mathbf{k}_{\parallel}) u_{\mathbf{G}_{\parallel}}(\mathbf{k}_{\parallel}, z) + B_{\mathbf{G}_{\parallel}\mathbf{G}_{\perp}}(\mathbf{k}_{\parallel}) \dot{u}_{\mathbf{G}_{\parallel}}(\mathbf{k}_{\parallel}, z) \} e^{i(\mathbf{G}_{\parallel} + \mathbf{k}_{\parallel})\mathbf{r}_{\parallel}} \right) d^3r \end{aligned} \quad (3.84)$$

The treatment of the vacuum region in FLAPW is in many way similar to the treatment of the muffin-tins. As in the muffin-tins the basis functions are constructed to diagonalize only a certain part of the Hamiltonian. Here this part of the Hamiltonian includes only the non-corrugated planar averaged part of the potential ( $V_{nc}(z)$ ), that depends only on  $z$ .

$$\mathcal{H}_V = \mathcal{H}_{nc} + V_{co}(\mathbf{r}) \quad (3.85)$$

The t-matrices can be defined in the same way as inside the muffin-tin spheres ((3.61) – (3.64)).

$$t_{\mathbf{G}'_{\parallel}\mathbf{G}_{\parallel}}^{uu}(\mathbf{k}_{\parallel}) = \langle \varphi_{\mathbf{G}'_{\parallel}}(\mathbf{k}_{\parallel}) | \mathcal{H}_V \varphi_{\mathbf{G}_{\parallel}}(\mathbf{k}_{\parallel}) \rangle_V \quad (3.86)$$

$$t_{\mathbf{G}'_{\parallel}\mathbf{G}_{\parallel}}^{ui}(\mathbf{k}_{\parallel}) = \langle \varphi_{\mathbf{G}'_{\parallel}}(\mathbf{k}_{\parallel}) | \mathcal{H}_V \dot{\varphi}_{\mathbf{G}_{\parallel}}(\mathbf{k}_{\parallel}) \rangle_V \quad (3.87)$$

$$t_{\mathbf{G}'_{\parallel}\mathbf{G}_{\parallel}}^{iu}(\mathbf{k}_{\parallel}) = \langle \dot{\varphi}_{\mathbf{G}'_{\parallel}}(\mathbf{k}_{\parallel}) | \mathcal{H}_V \varphi_{\mathbf{G}_{\parallel}}(\mathbf{k}_{\parallel}) \rangle_V \quad (3.88)$$

$$t_{\mathbf{G}'_{\parallel}\mathbf{G}_{\parallel}}^{ii}(\mathbf{k}_{\parallel}) = \langle \dot{\varphi}_{\mathbf{G}'_{\parallel}}(\mathbf{k}_{\parallel}) | \mathcal{H}_V \dot{\varphi}_{\mathbf{G}_{\parallel}}(\mathbf{k}_{\parallel}) \rangle_V \quad (3.89)$$

The contribution to these matrices from  $\mathcal{H}_{nc}$ , are given by the analog of equations (3.68) – (3.71). The non-corrugated potential is expanded into  $z$ -dependent functions

and planewaves in the x-y-plane.

$$V_{\infty}(\mathbf{r}) = \sum_{\mathbf{G}''_{\parallel}} V_{\mathbf{G}''_{\parallel}}(z) e^{i\mathbf{G}''_{\parallel}\mathbf{r}} \quad (3.90)$$

The contribution due to the expectation values of  $V_{CO}(\mathbf{r})$  consists of a z-dependent integral and an integral in the x-y-plane of the following form.

$$\int e^{-i\mathbf{G}'_{\parallel}\mathbf{r}} e^{i\mathbf{G}''_{\parallel}\mathbf{r}} e^{i\mathbf{G}_{\parallel}\mathbf{r}} dx dy = \delta_{\mathbf{G}'_{\parallel}(\mathbf{G}_{\parallel}+\mathbf{G}''_{\parallel})} \quad (3.91)$$

Thus, the t-matrices are given by

$$t_{\mathbf{G}'_{\parallel}\mathbf{G}_{\parallel}}^{uu}(\mathbf{k}_{\parallel}) = I_{\mathbf{G}'_{\parallel}\mathbf{G}_{\parallel}(\mathbf{G}'_{\parallel}-\mathbf{G}_{\parallel})}^{uu}(\mathbf{k}_{\parallel}) + \delta_{\mathbf{G}'_{\parallel}\mathbf{G}_{\parallel}} E_{vac} \quad (3.92)$$

$$t_{\mathbf{G}'_{\parallel}\mathbf{G}_{\parallel}}^{ui}(\mathbf{k}_{\parallel}) = I_{\mathbf{G}'_{\parallel}\mathbf{G}_{\parallel}(\mathbf{G}'_{\parallel}-\mathbf{G}_{\parallel})}^{ui}(\mathbf{k}_{\parallel}) + \delta_{\mathbf{G}'_{\parallel}\mathbf{G}_{\parallel}} \quad (3.93)$$

$$t_{\mathbf{G}'_{\parallel}\mathbf{G}_{\parallel}}^{iu}(\mathbf{k}_{\parallel}) = I_{\mathbf{G}'_{\parallel}\mathbf{G}_{\parallel}(\mathbf{G}'_{\parallel}-\mathbf{G}_{\parallel})}^{iu}(\mathbf{k}_{\parallel}) \quad (3.94)$$

$$t_{\mathbf{G}'_{\parallel}\mathbf{G}_{\parallel}}^{ii}(\mathbf{k}_{\parallel}) = I_{\mathbf{G}'_{\parallel}\mathbf{G}_{\parallel}(\mathbf{G}'_{\parallel}-\mathbf{G}_{\parallel})}^{ii}(\mathbf{k}_{\parallel}) + \delta_{\mathbf{G}'_{\parallel}\mathbf{G}_{\parallel}} E_{vac} \langle \dot{u}_{\mathbf{G}_{\parallel}}(\mathbf{k}_{\parallel}) | \dot{u}_{\mathbf{G}_{\parallel}}(\mathbf{k}_{\parallel}) \rangle_V \quad (3.95)$$

Where the  $I$  matrices abbreviate the z-dependent integrals including  $V_{(\mathbf{G}'_{\parallel}-\mathbf{G}_{\parallel})}(z)$ .

$$I_{\mathbf{G}'_{\parallel}\mathbf{G}_{\parallel}\mathbf{G}''_{\parallel}}^{uu}(\mathbf{k}_{\parallel}) = \int u_{\mathbf{G}'_{\parallel}}(\mathbf{k}_{\parallel}) u_{\mathbf{G}_{\parallel}}(\mathbf{k}_{\parallel}) V_{\mathbf{G}''_{\parallel}}(z) dz \quad (3.96)$$

$$I_{\mathbf{G}'_{\parallel}\mathbf{G}_{\parallel}\mathbf{G}''_{\parallel}}^{ui}(\mathbf{k}_{\parallel}) = \int u_{\mathbf{G}'_{\parallel}}(\mathbf{k}_{\parallel}) \dot{u}_{\mathbf{G}_{\parallel}}(\mathbf{k}_{\parallel}) V_{\mathbf{G}''_{\parallel}}(z) dz \quad (3.97)$$

$$I_{\mathbf{G}'_{\parallel}\mathbf{G}_{\parallel}\mathbf{G}''_{\parallel}}^{iu}(\mathbf{k}_{\parallel}) = \int \dot{u}_{\mathbf{G}'_{\parallel}}(\mathbf{k}_{\parallel}) u_{\mathbf{G}_{\parallel}}(\mathbf{k}_{\parallel}) V_{\mathbf{G}''_{\parallel}}(z) dz \quad (3.98)$$

$$I_{\mathbf{G}'_{\parallel}\mathbf{G}_{\parallel}\mathbf{G}''_{\parallel}}^{ii}(\mathbf{k}_{\parallel}) = \int \dot{u}_{\mathbf{G}'_{\parallel}}(\mathbf{k}_{\parallel}) \dot{u}_{\mathbf{G}_{\parallel}}(\mathbf{k}_{\parallel}) V_{\mathbf{G}''_{\parallel}}(z) dz \quad (3.99)$$

The Hamiltonian and overlap matrix elements are calculated according to

$$\begin{aligned} H_V^{\mathbf{G}'\mathbf{G}}(\mathbf{k}_{\parallel}) &= (A_{\mathbf{G}'_{\parallel}\mathbf{G}'_{\perp}}(\mathbf{k}_{\parallel}))^* t_{\mathbf{G}'_{\parallel}\mathbf{G}_{\parallel}}^{uu}(\mathbf{k}_{\parallel}) A_{\mathbf{G}_{\parallel}\mathbf{G}_{\perp}}(\mathbf{k}_{\parallel}) \\ &\quad + (A_{\mathbf{G}'_{\parallel}\mathbf{G}'_{\perp}}(\mathbf{k}_{\parallel}))^* t_{\mathbf{G}'_{\parallel}\mathbf{G}_{\parallel}}^{ui}(\mathbf{k}_{\parallel}) B_{\mathbf{G}_{\parallel}\mathbf{G}_{\perp}}(\mathbf{k}_{\parallel}) \\ &\quad + (B_{\mathbf{G}'_{\parallel}\mathbf{G}'_{\perp}}(\mathbf{k}_{\parallel}))^* t_{\mathbf{G}'_{\parallel}\mathbf{G}_{\parallel}}^{iu}(\mathbf{k}_{\parallel}) A_{\mathbf{G}_{\parallel}\mathbf{G}_{\perp}}(\mathbf{k}_{\parallel}) \\ &\quad + (B_{\mathbf{G}'_{\parallel}\mathbf{G}'_{\perp}}(\mathbf{k}_{\parallel}))^* t_{\mathbf{G}'_{\parallel}\mathbf{G}_{\parallel}}^{ii}(\mathbf{k}_{\parallel}) B_{\mathbf{G}_{\parallel}\mathbf{G}_{\perp}}(\mathbf{k}_{\parallel}) \end{aligned} \quad (3.100)$$

$$\begin{aligned} S_V^{\mathbf{G}'\mathbf{G}}(\mathbf{k}_{\parallel}) &= (A_{\mathbf{G}'_{\parallel}\mathbf{G}'_{\perp}}(\mathbf{k}_{\parallel}))^* A_{\mathbf{G}_{\parallel}\mathbf{G}_{\perp}}(\mathbf{k}_{\parallel}) \delta_{\mathbf{G}'_{\parallel}\mathbf{G}_{\parallel}} \\ &\quad + (B_{\mathbf{G}'_{\parallel}\mathbf{G}'_{\perp}}(\mathbf{k}_{\parallel}))^* B_{\mathbf{G}_{\parallel}\mathbf{G}_{\perp}}(\mathbf{k}_{\parallel}) \langle \dot{u}_{\mathbf{G}_{\parallel}}(\mathbf{k}_{\parallel}) | \dot{u}_{\mathbf{G}_{\parallel}}(\mathbf{k}_{\parallel}) \rangle_V \delta_{\mathbf{G}'_{\parallel}\mathbf{G}_{\parallel}} \end{aligned} \quad (3.101)$$

### 3.3.3 The Interstitial Contribution

The interstitial contributions to the Hamiltonian and overlap matrix have the following form.

$$H_I^{\mathbf{G}\mathbf{G}'}(\mathbf{k}) = \frac{1}{\Omega} \int_I e^{-i(\mathbf{G}+\mathbf{k})\mathbf{r}} \left( -\frac{\hbar^2}{2m} \Delta + V(\mathbf{r}) \right) e^{i(\mathbf{G}'+\mathbf{k})\mathbf{r}} d^3r \quad (3.102)$$

$$S_I^{\mathbf{G}\mathbf{G}'} = \frac{1}{\Omega} \int_I e^{-i(\mathbf{G}+\mathbf{k})\mathbf{r}} e^{i(\mathbf{G}'+\mathbf{k})\mathbf{r}} d^3r \quad (3.103)$$

The potential is also expanded into planewaves in the interstitial region.

$$V(\mathbf{r}) = \sum_{\mathbf{G}'} V_{\mathbf{G}'} e^{-i\mathbf{G}'\mathbf{r}} \quad (3.104)$$

Without the existence of the muffin-tin spheres the integration would stretch over the entire unit cell and the integration becomes rather simple. The kinetic energy is diagonal in momentum space and the potential is local, diagonal in real space and of convolution form in momentum space.

$$H_I^{\mathbf{G}\mathbf{G}'}(\mathbf{k}) = \frac{\hbar^2}{2m} |\mathbf{G} + \mathbf{k}|^2 \delta_{\mathbf{G}\mathbf{G}'} + V_{(\mathbf{G}-\mathbf{G}')}$$

$$S_I^{\mathbf{G}\mathbf{G}'} = \delta_{\mathbf{G}\mathbf{G}'}$$

However, these matrix elements are not as straightforward to calculate as they appear at first glance, because of the complicated structure of the interstitial region. The integrations have to be performed only in between the muffin-tins. Therefore, a step function  $\Theta(\mathbf{r})$  has to be introduced, that cuts out the muffin-tins.

$$\Theta(\mathbf{r}) = \begin{cases} 1 & \text{interstitial region} \\ 0 & \text{muffin-tins} \end{cases} \quad (3.105)$$

In film calculations the region between  $D/2$  and  $\tilde{D}/2$  has to be cut out too, but to keep it simple we will discuss the only the bulk case in this section. Using the step function the matrix elements can be written:

$$\begin{aligned} H_{INT}^{\mathbf{G}\mathbf{G}'}(\mathbf{k}) &= \frac{1}{\Omega} \int_{cell} e^{-i(\mathbf{G}-\mathbf{G}')\mathbf{r}} V(\mathbf{r}) \Theta(\mathbf{r}) d^3r \\ &+ \frac{1}{2} (\mathbf{G}' + \mathbf{k})^2 \frac{1}{\Omega} \int_{cell} e^{-i(\mathbf{G}-\mathbf{G}')\mathbf{r}} \Theta(\mathbf{r}) d^3r \end{aligned} \quad (3.106)$$

$$S_{INT}^{\mathbf{G}\mathbf{G}'} = \frac{1}{\Omega} \int_{cell} e^{-i(\mathbf{G}-\mathbf{G}')\mathbf{r}} \Theta(\mathbf{r}) d^3r \quad (3.107)$$

In momentum space 3.106 becomes:

$$\Rightarrow H_{INT}^{\mathbf{G}\mathbf{G}'}(\mathbf{k}) = (V\Theta)_{(\mathbf{G}-\mathbf{G}')} + \frac{\hbar^2}{2m} (\mathbf{G}' + \mathbf{k})^2 \Theta_{(\mathbf{G}-\mathbf{G}')} \quad (3.108)$$

$$S_{INT}^{\mathbf{G}\mathbf{G}'} = \Theta_{(\mathbf{G}-\mathbf{G}')} \quad (3.109)$$

Where  $\Theta_{\mathbf{G}}$  and  $(V\Theta)_{\mathbf{G}}$  are the Fourier coefficients of  $\Theta(\mathbf{r})$  and  $V(\mathbf{r})\Theta(\mathbf{r})$  respectively. Apparently these coefficients are needed up to a cut-off of  $2G_{max}$ . The step function can be Fourier transformed analytically.

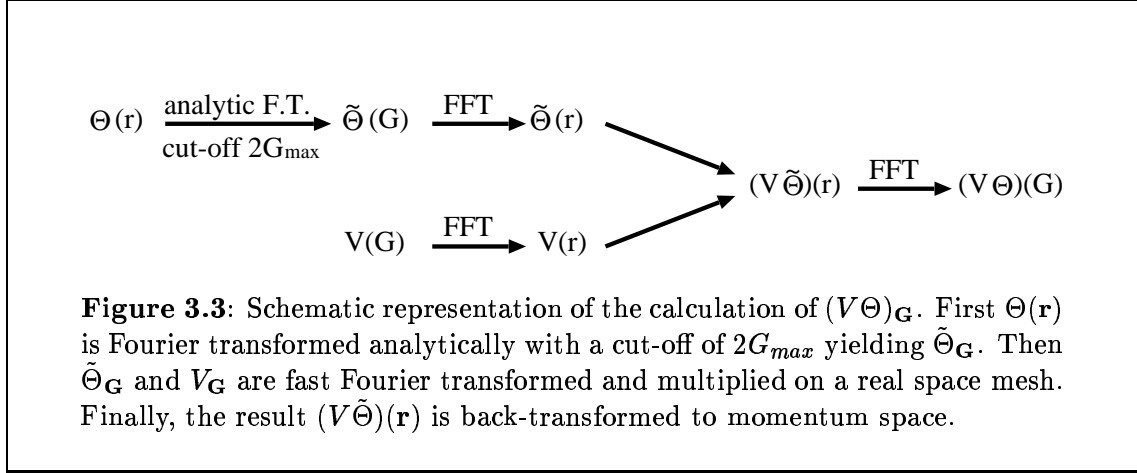
$$\Theta_{\mathbf{G}} = \delta_{\mathbf{G},\mathbf{0}} - \sum_{\mu} e^{-i\mathbf{G}\mathbf{p}^{\mu}} \frac{4\pi(R_{MT}^{\alpha})^3}{\Omega} \frac{j_1(GR_{MT}^{\alpha})}{GR_{MT}^{\alpha}}$$



The Fourier transform of the product of  $V(\mathbf{r})$  and  $\Theta(\mathbf{r})$  is given by a convolution in momentum space.

$$(V\Theta)_{\mathbf{G}} = \sum_{\mathbf{G}'} V_{\mathbf{G}'} \Theta_{(\mathbf{G}-\mathbf{G}')}$$

This convolution depends on both,  $\mathbf{G}$  and  $\mathbf{G}'$ , therefore the numerical effort increases like  $(G_{max})^6$ . However,  $(V\Theta)_{\mathbf{G}}$  can be determined more efficiently, using Fast-Fourier-Transform (FFT). In fig. 3.3 it is shown schematically how  $(V\Theta)_{\mathbf{G}}$  can be obtained using FFT. Using this scheme the numerical effort increases like  $(G_{max})^3 \ln((G_{max})^3)$  with  $G_{max}$ .

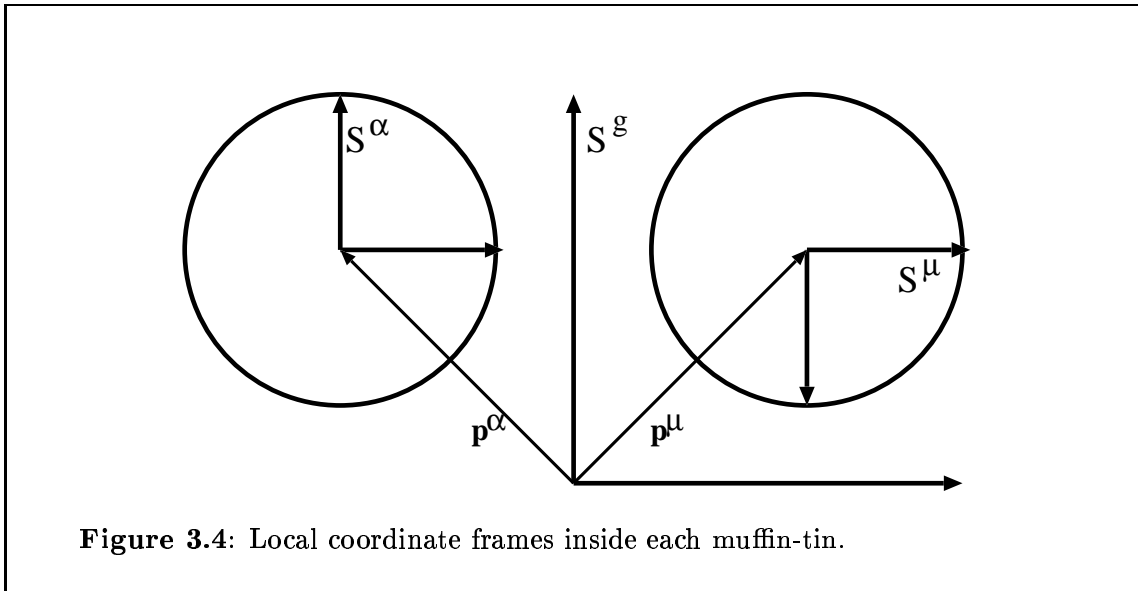


### 3.3.4 The Muffin-Tin A- and B-Coefficients

Within FLAPW the electron wavefunctions are expanded differently in the interstitial region and the muffin-tins. Each basis function consists of a planewave in the interstitial, which is matched to the radial functions and spherical harmonics in the muffin-tins. The coefficients of the function inside the spheres are determined from the requirement, that the basis functions and their derivatives are continuous at the sphere boundaries. These coefficients play an important role. In this section we will therefore discuss how the matching conditions can be solved and what properties they induce.

In many systems that the FLAPW method can be applied to some atom are symmetry equivalent, i.e. these atoms can be mapped onto each other by a space group operation  $\{\mathbf{R}|\boldsymbol{\tau}\}$ . Such a group of atoms is called an atom type, represented by one of the atoms. Let  $\{\mathbf{R}^{\mu}|\boldsymbol{\tau}^{\mu}\}$  the operation that maps the atom  $\mu$  onto its representative. This atom can now be assigned a local coordinate frame  $S^{\mu}$  (cf. fig. 3.4), where the origin of  $S^{\mu}$  is at the atoms position<sup>3</sup>  $\mathbf{p}^{\mu}$ . The local frame is chosen such that the unit vectors of the local frame  $S^{\mu}$  are mapped onto those of the

<sup>3</sup>The atom position is very frequently denoted by  $\boldsymbol{\tau}^{\mu}$ , which would clearly cause some confusion in this context.



global frame by  $\mathbf{R}^g$  ( $\mathbf{R}^\mu S^\mu = S^g$ ). The local frame of the representative atom  $S^\alpha$  is only translated with respect to the global frame, i.e. the same rotation  $\mathbf{R}^\mu$  maps  $S^\mu$  onto  $S^\alpha$ . The potential (and other quantities) inside the muffin-tins can now be written in terms of the local coordinate system. Due to the symmetry we find  $V_{MT^\alpha}(\mathbf{r}^\alpha) = V_{MT^\mu}(\mathbf{r}^\mu)$ , where  $\mathbf{r}^\alpha$  and  $\mathbf{r}^\mu$  are expanded in terms of the local frames  $S^\alpha$  and  $S^\mu$  respectively. As a consequence the radial functions<sup>4</sup>  $u_l(r)$  and the t-matrices are the same for all atoms of the same type. This way symmetry is exploited to save memory and computer time (during the calculation of the t-matrices).

Any plane wave can be expanded into spherical harmonics via the Rayleigh expansion.

$$e^{i\mathbf{K}\mathbf{r}} = 4\pi \sum_L i^l j_l(rK) Y_L^*(\hat{\mathbf{K}}) Y_L(\hat{\mathbf{r}}) \quad (3.110)$$

Where  $r = |\mathbf{r}|$ ,  $K = |\mathbf{K}|$  and  $\mathbf{K}$  abbreviates  $(\mathbf{G} + \mathbf{k})$ . Looked at from the local frame  $\mathbf{K}$  and  $\mathbf{p}^\mu$  appear rotated, besides the origin of the local frame is shifted. Therefore, the plane wave has the following form in the local frame:

$$e^{i(\mathbf{R}^\mu \mathbf{K})(\mathbf{r} + \mathbf{R}^\mu \mathbf{p}^\mu)} \quad (3.111)$$

Thus, the Rayleigh expansion of the plane wave in the local frame is given by:

$$e^{i\mathbf{K}\mathbf{p}^\mu} 4\pi \sum_L i^l j_l(rK) Y_L^*(\mathbf{R}^\mu \hat{\mathbf{K}}) Y_L(\hat{\mathbf{r}}) \quad (3.112)$$

The requirement of continuity of the wavefunctions at the sphere boundary leads to the equation:

$$\sum_L A_L^{\mu\mathbf{G}}(\mathbf{k}) u_l(R_{MT^\alpha}) Y_L(\hat{\mathbf{r}}) + B_L^{\mu\mathbf{G}}(\mathbf{k}) \dot{u}_l(R_{MT^\alpha}) Y_L(\hat{\mathbf{r}})$$

<sup>4</sup>Within this section the radial functions are denoted by  $u_l(r)$  for simplicity, though in scalar relativistic calculating the large component  $g_l(r)$  is used instead of  $u_l(r)$ .

$$= e^{i\mathbf{K}\mathbf{p}^\mu} 4\pi \sum_L i^l j_l(rK) Y_L^*(\mathbf{R}^\mu \hat{\mathbf{K}}) Y_L(\hat{\mathbf{r}}) \quad (3.113)$$

Where  $R_{MT^\alpha}$  is the muffin-tin radius of the atom type  $\alpha$ . The second requirement is, that the derivative with respect to  $r$ , denoted by  $\partial/\partial r = '$ , is also continuous.

$$\begin{aligned} & \sum_L A_L^{\mu\mathbf{G}}(\mathbf{k}) u_l'(R_{MT^\alpha}) Y_L(\hat{\mathbf{r}}) + B_L^{\mu\mathbf{G}}(\mathbf{k}) \dot{u}_l'(R_{MT^\alpha}) Y_L(\hat{\mathbf{r}}) \\ &= e^{i\mathbf{K}\mathbf{p}^\mu} 4\pi \sum_L i^l K j_l'(rK) Y_L^*(\mathbf{R}^\mu \hat{\mathbf{K}}) Y_L(\hat{\mathbf{r}}) \end{aligned} \quad (3.114)$$

These conditions can only be satisfied, if the coefficients of each spherical harmonic  $Y_L(\hat{\mathbf{r}})$  are equal. Solving the resulting equations for  $A_L^{\mu\mathbf{G}}(\mathbf{k})$  and  $B_L^{\mu\mathbf{G}}(\mathbf{k})$  yields:

$$\begin{aligned} A_L^{\mu\mathbf{G}}(\mathbf{k}) &= e^{i\mathbf{K}\mathbf{p}^\mu} 4\pi \frac{1}{W} i^l Y_L^*(\mathbf{R}^\mu \hat{\mathbf{K}}) \\ & \quad [\dot{u}_l(R_{MT^\alpha}) K j_l'(R_{MT^\alpha} K) - u_l'(R_{MT^\alpha}) j_l(R_{MT^\alpha} K)] \\ B_L^{\mu\mathbf{G}}(\mathbf{k}) &= e^{i\mathbf{K}\mathbf{p}^\mu} 4\pi \frac{1}{W} i^l Y_L^*(\mathbf{R}^\mu \hat{\mathbf{K}}) \\ & \quad [u_l'(R_{MT^\alpha}) j_l(R_{MT^\alpha} K) - u_l(R_{MT^\alpha}) K j_l'(R_{MT^\alpha} K)] \end{aligned} \quad (3.115)$$

The Wronskian  $W$  is given by:

$$W = [\dot{u}_l(R_{MT^\alpha}) u_l'(R_{MT^\alpha}) - u_l(R_{MT^\alpha}) \dot{u}_l'(R_{MT^\alpha})] \quad (3.116)$$

### Transformation of the FLAPW basis functions in systems that possess inversion symmetry

Planewaves transform in a very simple way under the operation  $\mathbf{r} \rightarrow -\mathbf{r}$ . Let  $\mathcal{I}$  be the inversion operator:

$$\mathcal{I} e^{i\mathbf{K}\mathbf{r}} = e^{-i\mathbf{K}\mathbf{r}} = (e^{i\mathbf{K}\mathbf{r}})^* \quad (3.117)$$

The FLAPW basis functions still have this property, i.e.  $\varphi_{\mathbf{G}}(\mathbf{k}, -\mathbf{r}) = \varphi_{\mathbf{G}}^*(\mathbf{k}, \mathbf{r})$ . Clearly, the system must possess inversion symmetry, because only if there is an equivalent atom at the position  $-\mathbf{p}^\mu$  to each atom  $\mu$  at position  $\mathbf{p}^\mu$ , the basis functions inside the corresponding spheres can be complex conjugates. The value of the basis function  $\varphi_{\mathbf{G}}(\mathbf{k}, \mathbf{r})$  inside the muffin-tin  $\mu$  is give by:

$$\varphi_{\mathbf{G}}(\mathbf{k}, \mathbf{r}) = \sum_L A_L^{\mu\mathbf{G}}(\mathbf{k}) u_l(r) Y_L(\hat{\mathbf{r}}) + B_L^{\mu\mathbf{G}}(\mathbf{k}) \dot{u}_l(r) Y_L(\hat{\mathbf{r}}) \quad (3.118)$$

The vector  $-\mathbf{r}$  lies in the opposite muffin-tin at the position  $-\mathbf{p}^\mu$ . Let's denote this atom by  $-\mu$ . Thus, we find:

$$\varphi_{\mathbf{G}}(\mathbf{k}, -\mathbf{r}) = \sum_L A_L^{-\mu\mathbf{G}}(\mathbf{k}) u_l(r) Y_L(\hat{\mathbf{r}}) + B_L^{-\mu\mathbf{G}}(\mathbf{k}) \dot{u}_l(r) Y_L(\hat{\mathbf{r}}) \quad (3.119)$$

The argument of the spherical harmonic is  $\hat{\mathbf{r}}$  rather than  $-\hat{\mathbf{r}}$ , because the vector is expanded in the local frame of the atom  $-\mu$ . Substituting the explicit form of  $A_L^{-\mu\mathbf{G}}(\mathbf{k})$  and  $B_L^{-\mu\mathbf{G}}(\mathbf{k})$  from (3.115), yields:

$$\varphi_{\mathbf{G}}(\mathbf{k}, -\mathbf{r}) = \sum_L e^{i\mathbf{K}(-\mathbf{p}^\mu)} i^l Y_L^*(-\mathbf{R}^\mu \hat{\mathbf{K}}) Y_L(\hat{\mathbf{r}}) \{Au_l(r) + B\dot{u}_l(r)\} \quad (3.120)$$

Where it has been used, that  $\mathbf{p}^{-\mu} = -\mathbf{p}^\mu$  and  $\mathbf{R}^{-\mu} = -\mathbf{R}^\mu$ ,  $A$  and  $B$  abbreviates all terms in (3.115) that are real and do not depend on  $r$  or  $\hat{\mathbf{r}}$ . Using that  $Y_L(\hat{\mathbf{r}}) = (-1)^l Y_L(\hat{\mathbf{r}})$  (3.120) becomes:

$$\varphi_{\mathbf{G}}(\mathbf{k}, -\mathbf{r}) = \sum_L e^{-i\mathbf{K}(\mathbf{p}^\mu)} (-i)^l Y_L^*(\mathbf{R}^\mu \hat{\mathbf{K}}) Y_L(\hat{\mathbf{r}}) \{Au_l(r) + B\dot{u}_l(r)\} \quad (3.121)$$

In the last step it can be exploited that  $Y_{l-m}(\hat{\mathbf{r}}) = (-1)^m Y_{lm}^*(\hat{\mathbf{r}})$ . Substituting  $m' = -m$  (3.121) becomes:

$$\varphi_{\mathbf{G}}(\mathbf{k}, -\mathbf{r}) = \sum_{lm'} e^{-i\mathbf{K}(\mathbf{p}^\mu)} (-i)^l Y_{lm'}(\mathbf{R}^\mu \hat{\mathbf{K}}) Y_{lm'}^*(\hat{\mathbf{r}}) \{Au_l(r) + B\dot{u}_l(r)\} \quad (3.122)$$

Hence, we have shown, that the FLAPW basis functions transform according to

$$\varphi_{\mathbf{G}}(\mathbf{k}, -\mathbf{r}) = \varphi_{\mathbf{G}}^*(\mathbf{k}, \mathbf{r}) \quad (3.123)$$

in the interstitial region and the muffin-tins, if the system possesses inversion symmetry.

### The Hamiltonian Matrix of Systems with Inversion Symmetry

The property of the FLAPW basis functions derived in the previous section leads to property of the Hamiltonian and overlap matrix. In systems that possess inversion symmetry these two matrices are real symmetric rather than complex hermitian. The Hamiltonian depends explicitly on  $\mathbf{r}$  via the potential. The matrix elements are given by:

$$H^{\mathbf{G}'\mathbf{G}}(\mathbf{k}) = \int \varphi_{\mathbf{G}'}^*(\mathbf{k}, \mathbf{r}) \mathcal{H}(\mathbf{r}) \varphi_{\mathbf{G}}(\mathbf{k}, \mathbf{r}) d^3r \quad (3.124)$$

Substituting  $\mathbf{r}' = -\mathbf{r}$  yields:

$$H^{\mathbf{G}'\mathbf{G}}(\mathbf{k}) = \int \varphi_{\mathbf{G}'}(\mathbf{k}, \mathbf{r}') \mathcal{H}(\mathbf{r}') \varphi_{\mathbf{G}}^*(\mathbf{k}, \mathbf{r}') d^3r \quad (3.125)$$

Where (3.123) and  $\mathcal{H}(\mathbf{r}) = \mathcal{H}(-\mathbf{r})$  have been used. In addition the Hamiltonian operator is real, i.e.  $\mathcal{H}(\mathbf{r}) = \mathcal{H}^*(\mathbf{r})$ . Thus, we finally obtain:

$$\begin{aligned} H^{\mathbf{G}'\mathbf{G}}(\mathbf{k}) &= \int \varphi_{\mathbf{G}'}(\mathbf{k}, \mathbf{r}') \mathcal{H}^*(\mathbf{r}') \varphi_{\mathbf{G}}^*(\mathbf{k}, \mathbf{r}') d^3r \\ &= \left( H^{\mathbf{G}'\mathbf{G}}(\mathbf{k}) \right)^* \end{aligned} \quad (3.126)$$

Apparently, the same relation holds for the overlap matrix. The fact, that the two matrices are real means a great simplification in actual calculation. In principle, the diagonalization of a hermitian matrix is no more difficult than in the real case. However, one complex multiplication contains four real multiplication, and therefore the complex problem is far more “expensive” than the real, and the diagonalization needs the biggest part of the computer-time in each iteration.

### 3.4 Brillouin Zone Integration and Fermi Energy

If density functional theory is applied to infinite periodic solids, quantities that are given by integrals of functions that depend on the band and the Bloch vector over the Brillouin zone have to be determined. These integrations stretch only over the occupied part of the band, i.e. over the region of the Brillouin zone where the band energy  $\epsilon_\nu(\mathbf{k})$  ( $\nu$  is the band index) is smaller than the Fermi energy. Hence, the integrals are of the form

$$\frac{1}{V_{BZ}} \int_{BZ} \sum_{\nu, \epsilon_\nu(\mathbf{k}) < E_F} f_\nu(\mathbf{k}) d^3k, \quad (3.127)$$

where  $f$  is the function to be integrated. Example of such quantities are the number of electrons per unit cell

$$N = \frac{1}{V_{BZ}} \int_{BZ} \sum_{\nu, \epsilon_\nu(\mathbf{k}) < E_F} 1 d^3k, \quad (3.128)$$

the electron (charge) density (cf. section 3.6) and the eigenvalue sum

$$\frac{1}{V_{BZ}} \int_{BZ} \sum_{\nu, \epsilon_\nu(\mathbf{k}) < E_F} \epsilon_\nu(\mathbf{k}) d^3k. \quad (3.129)$$

Numerically, these integrations are performed on a discrete mesh in the Brillouin zone. In fact, only the irreducible part can be used to save computer time. There are different methods, that can be used to perform the integration, e.g. the special points method [CC73, Cun74] and the tetrahedron method [JA71, LT72, BJA94]. The special points method is a method to integrate smoothly varying periodic functions of  $\mathbf{k}$ . The function to be integrated has to be calculated a set of special points in the (irreducible) Brillouin zone, each of which is assigned a weight. Thus, the Brillouin zone integration is transformed into a sum over a set of  $\mathbf{k}$ -points. However, these weights do not take into account, that the integration stretches only over the occupied part of the bands. This problem is solved by including only those bands into the summation that have an energy below the Fermi energy at the  $\mathbf{k}$ -point under consideration. Thus, the integrals become:

$$\frac{1}{V_{BZ}} \int_{BZ} \sum_{\nu, \epsilon_\nu(\mathbf{k}) < E_F} f_\nu(\mathbf{k}) d^3k \longrightarrow \sum_{\mathbf{k}} \sum_{\nu, \epsilon_\nu(\mathbf{k}) < E_F} f_\nu(\mathbf{k}) w(\mathbf{k}) \quad (3.130)$$

Alternatively, this integration can be viewed as an integration over the whole Brillouin zone, where the function to be integrated is given by a product of the function  $f$  with a step function that cuts out the region of the Brillouin zone, where the band energy is above the Fermi energy. Clearly, the resulting function does not satisfy the condition of being smoothly varying. Therefore, the special k-points method does not converge very quickly, and rather many k-points are needed to obtain accurate results. On

the other hand this method is simple to implement, because the weights depend only on  $\mathbf{k}$  and the band energy (via the step function) at each  $\mathbf{k}$ -point. Another problem arises from this “sharp” differentiation between occupied and empty bands (parts of bands). Let’s consider a band that is very close to the Fermi energy at a certain  $\mathbf{k}$ -point. During the iterations the energy of this band might rise above or drop below the Fermi energy. This leads to sudden changes in the charge density, which can slow down or even prevent the convergence of the density. These sudden changes are clearly a result of the discretization in momentum space. To avoid this problem, the sharp edges of the step function have to be removed. This can be done, e.g. by using the Fermi function  $(e^{(\epsilon - E_F)/k_B T} + 1)^{-1}$  rather than the step function. In other words, the function to be integrated is artificially made smoothly varying. The temperature  $T$  can then be adjusted to obtain the best convergence. This method is called temperature broadening.

In the current implementation of the FLAPW method the Fermi energy is determined in two steps. First the bands are occupied (at all  $\mathbf{k}$ -points simultaneously), starting from the lowest energy, until the sum of their weights equals the total number of electrons per unit cell, i.e. the discretized equivalent of (3.128) is solved at  $T = 0$ . Then the step function is replaced by the Fermi and the Fermi energy is determined from the requirement that:

$$N = \sum_{\mathbf{k}} \sum_{\nu} w(\mathbf{k}, \epsilon_{\nu}(\mathbf{k}) - E_F) \quad (3.131)$$

Where the weights are given by:

$$w(\mathbf{k}, \epsilon_{\nu}(\mathbf{k}) - E_F) = w(\mathbf{k}) \frac{1}{e^{(\epsilon_{\nu}(\mathbf{k}) - E_F)/k_B T} + 1} \quad (3.132)$$

The weights  $w(\mathbf{k}, \epsilon_{\nu}(\mathbf{k}) - E_F)$  are stored to be used for later Brillouin zone integrations.

## 3.5 Representation of the Density and the Potential

The expansion of the charge density  $\rho$ <sup>5</sup> and the potential is very similar to expansion of the wavefunction. In the interstitial-region the two quantities are expanded into three-dimensional planewave, inside the muffin-tins they are represented by spherical harmonics and radial functions, which are store on an exponential mesh and in the vacuum they are expanded into two-dimensional planewave and  $z$ -depended functions, which are also given on an exponential mesh. However, the charge density is given by

$$\rho(\mathbf{r}) = \sum_i |\psi_i(\mathbf{r})|^2, \quad (3.133)$$

---

<sup>5</sup>The charge density is related to the electron density by  $\rho(\mathbf{r}) = -en(\mathbf{r})$ . However, the program is written in Hartree units, where  $e = 1$ , therefore  $\rho$  and  $n$  are equal.

which contains terms of the form  $e^{i(\mathbf{G}-\mathbf{G}')\mathbf{r}}$ . Consequently, for a consistent representation the charge density cut-off has to be twice the wavefunction cut-off  $G_{max}$ . In section 3.3.3 we explained, that the potential is also needed up to cut-off of  $2G_{max}$ . This leads to a large number of coefficients, that need to be stored. Fortunately, this number can be reduced, if the symmetry of the system is exploited.

Of course, the charge density and the potential posses the lattice symmetry. Therefore, the expansion into planewaves is more general than necessary. The Planewaves can be replaced by symmetrized planewaves, the so called stars. They are defined by:

$$\Phi_s^{3D}(\mathbf{r}) = \frac{1}{N_{op}} \sum_{op} e^{i\mathbf{R}\mathbf{G}(\mathbf{r}-\boldsymbol{\tau})} \quad (3.134)$$

where  $\{\mathbf{R}|\boldsymbol{\tau}\}$  are the symmetry operation of the lattice space group; if all the translation vectors  $\boldsymbol{\tau}$  are zero, the space group is call symmorphic. By this construction all planewaves, that are symmetry equivalent, are combined to form one star. The two-dimensional stars  $\Phi_s^{2D}(\mathbf{r})$  are defined in the same way, applying the operations of the two-dimensional space group only.

The same arguments can be applied to the expansion of the  $\rho(V)$  inside the muffin-tins. In this case the relevant symmetry group is the point group of the atom under consideration. Thus, different expansions are used at different atoms in general. The symmetrized functions are called lattice harmonics and they are linear combinations of spherical harmonics.

$$K_\nu(\hat{\mathbf{r}}) = \sum_m c_{\nu,m}^\alpha Y_L(\hat{\mathbf{r}}) \quad (3.135)$$

The lattice harmonics are real, orthonormal and invariant under the point group operations. Finally, the expansion of the the charge density has the form

$$\rho(\mathbf{r}) = \begin{cases} \sum_s \rho_s \Phi_s^{3D}(\mathbf{r}) & \mathbf{r} \in I \\ \sum_s \rho_s(z) \Phi_s^{2D}(\mathbf{r}) & \mathbf{r} \in \text{Vakuum} \\ \sum_\nu \rho_\nu^\alpha(r) K_\nu(\hat{\mathbf{r}}) & \mathbf{r} \in MT^\alpha \end{cases} \quad (3.136)$$

The Potential is expanded in exactly the same way.

## 3.6 Construction of the Electron Density

In this section we will discuss the determination of the charge density from the eigenfunctions. In density functional calculations of an infinite periodic solid the electron density is given by an integral over the Brillouin zone (cf. (2.20)).

$$n(\mathbf{r}) = \frac{1}{V_{BZ}} \int_{BZ} \sum_{\nu, \epsilon_\nu(\mathbf{k}) < E_F} |\psi_\nu(\mathbf{k}, \mathbf{r})|^2 d^3k \quad (3.137)$$

Where  $V_{BZ}$  is the volume of the Brillouin zone,  $\nu$  is the band index and  $E_F$  is the Fermi energy. In spin-polarized calculations the summation includes also the

spin-index  $\sigma$  (cf. (2.8)), while in a non-magnetic calculation a factor “2” has to be added to account for the spin-degeneracy. In the case of film calculations the three-dimensional Brillouin zone is replaced by a two-dimensional Brillouin zone. In both cases integration methods that sample eigenfunctions and the eigenvalues on discrete  $\mathbf{k}$ -point are used to compute the integrals. These methods transform the integration into a weighted sum over the  $\mathbf{k}$ -points, where the choice of  $\mathbf{k}$ -points and their weights depend on the integration method used. These weights depend not only on the  $\mathbf{k}$ -point, but also on the energy of a band, i.e. on the band (index), because each band contributes to the electron density only if its energy is below the Fermi energy.

$$n(\mathbf{r}) = \sum_{\mathbf{k}} \sum_{\nu} |\psi_{\nu}(\mathbf{k}, \mathbf{r})|^2 w(\nu, \mathbf{k}) \quad (3.138)$$

Within the FLAPW method the eigenfunctions are represented in terms of the coefficients of the augmented planewaves.

$$\psi_{\nu}(\mathbf{k}, \mathbf{r}) = \sum_{\mathbf{G}} c_{\nu}^{\mathbf{G}}(\mathbf{k}) \varphi_{\mathbf{G}}(\mathbf{k}, \mathbf{r}) \quad (3.139)$$

Inside the muffin-tin spheres each planewave is coupled to a sum of spherical harmonics and radial functions. Hence, in a sphere  $\mu$  an eigenfunction is given by:

$$\psi_{\nu}^{\mu}(\mathbf{k}, \mathbf{r}) = \sum_{\mathbf{G}} c_{\nu}^{\mathbf{G}}(\mathbf{k}) \sum_L A_L^{\mu\mathbf{G}}(\mathbf{k}) u_l^{\alpha}(r) Y_L(\hat{\mathbf{r}}) + B_L^{\mu\mathbf{G}}(\mathbf{k}) \dot{u}_l^{\alpha}(r) Y_L(\hat{\mathbf{r}}) \quad (3.140)$$

The  $A_L^{\mu\mathbf{G}}(\mathbf{k})$  and  $B_L^{\mu\mathbf{G}}(\mathbf{k})$  coefficients can be replaced by band dependent A- and B-coefficients, obtained by performing the contraction over the planewaves:

$$\psi_{\nu}^{\mu}(\mathbf{k}, \mathbf{r}) = \sum_L A_{L,\nu}^{\mu}(\mathbf{k}) u_l^{\alpha}(r) Y_L(\hat{\mathbf{r}}) + B_{L,\nu}^{\mu}(\mathbf{k}) \dot{u}_l^{\alpha}(r) Y_L(\hat{\mathbf{r}}), \quad (3.141)$$

where

$$A_{L,\nu}^{\mu}(\mathbf{k}) = \sum_{\mathbf{G}} c_{\nu}^{\mathbf{G}}(\mathbf{k}) A_L^{\mu\mathbf{G}}(\mathbf{k}), \quad B_{L,\nu}^{\mu}(\mathbf{k}) = \sum_{\mathbf{G}} c_{\nu}^{\mathbf{G}}(\mathbf{k}) B_L^{\mu\mathbf{G}}(\mathbf{k}). \quad (3.142)$$

### 3.6.1 “ $l$ -like” Charge

Since the wavefunctions are expanded into spherical harmonics inside the muffin-tin spheres, they can be split up into contributions with a certain  $l$ -character.

$$\psi_{\nu}^{\mu}(\mathbf{k}, \mathbf{r}) = \sum_l \psi_{\nu,l}^{\mu}(\mathbf{k}, \mathbf{r}) \quad (3.143)$$

The particle density of a certain state depends on the square of the wavefunction. Therefore, it contains cross-terms with a mixture of different  $l$ 's.

$$n_{\nu}^{\mu}(\mathbf{r}) = \frac{1}{V_{BZ}} \int_{BZ} \sum_l |\psi_{\nu,l}^{\mu}(\mathbf{k}, \mathbf{r})|^2 + \sum_{l'l} 2 \left( \psi_{\nu,l'}^{\mu}(\mathbf{k}, \mathbf{r}) \right)^* \psi_{\nu,l}^{\mu}(\mathbf{k}, \mathbf{r}) d^3 k \quad (3.144)$$



If, however, the density is integrated over the muffin-tin, the cross-terms vanish because of the orthogonality of the spherical harmonics. Thus, the total electron density inside a sphere can be written as a sum over contributions with definite l-character.

$$n_\nu^\mu = \sum_l n_{\nu,l}^\mu, \quad n_{\nu,l}^\mu = \frac{1}{V_{BZ}} \int_{BZ} \int_{MT^\mu} |\psi_{\nu,l}^\mu(\mathbf{k}, \mathbf{r})|^2 d^3r d^3k \quad (3.145)$$

Where  $n_{\nu,l}^\mu$  is called ‘‘l-like’’ charge. We can also define a k-dependent l-like charge by:

$$n_{\nu,l}^\mu(\mathbf{k}) = \int_{MT^\mu} |\psi_{\nu,l}^\mu(\mathbf{k}, \mathbf{r})|^2 d^3r \quad (3.146)$$

Substituting (3.141) yields:

$$n_{\nu,l}^\mu(\mathbf{k}) = \sum_{m=-l}^l |A_{L,\nu}^\mu(\mathbf{k})|^2 + |B_{L,\nu}^\mu(\mathbf{k})|^2 \dot{N}_l^\alpha \quad (3.147)$$

Where

$$\dot{N}_l^\alpha = \int_0^{R_{MT^\alpha}} (\dot{u}_l^\alpha(r))^2 r^2 dr \quad (3.148)$$

and the orthogonality of the spherical harmonics, the normalization of  $u_l^\alpha$  and the orthogonality of  $u_l^\alpha$  and  $\dot{u}_l^\alpha$  have been used.

### 3.6.2 Determination of the Optimal Energy Parameter

In order to minimize the linearization error, the energy parameters should be chosen as close to the band energies as possible. However, the band energies  $\epsilon_\nu(\mathbf{k})$  depend on  $\mathbf{k}$  whereas the energy parameters  $E_l^\alpha$  are constants. In addition, the radial functions contribute to the eigenfunctions of different band with different energies. Therefore, deviations between  $\epsilon_\nu(\mathbf{k})$  and  $E_l^\alpha$  have to be accepted. An optimal choice can be obtained from the requirement, that the energy parameters minimize

$$\int_{BZ} \sum_{\nu, \epsilon_\nu(\mathbf{k}) < E_F} (\epsilon_\nu(\mathbf{k}) - E_l^\alpha)^2 n_{\nu,l}^\mu(\mathbf{k}) d^3k, \quad (3.149)$$

which is the quadratic error weighted with the amount of charge that each band contributes to the l-like charge with the l-character of the energy parameter. Setting the derivative ( $\partial/\partial E_l^\alpha$ ) equal to zero yields the optimal energy parameter:

$$E_l^\alpha = \left( \int_{BZ} \sum_{\nu, \epsilon_\nu(\mathbf{k}) < E_F} \epsilon_\nu(\mathbf{k}) n_{\nu,l}^\mu(\mathbf{k}) d^3k \right) / \left( \int_{BZ} \sum_{\nu, \epsilon_\nu(\mathbf{k}) < E_F} n_{\nu,l}^\mu(\mathbf{k}) d^3k \right) \quad (3.150)$$

The Brillouin zone integration methods transform this into a sum over a discrete k-point set.

$$E_l^\alpha = \left( \sum_{\mathbf{k}} \sum_{\nu} \epsilon_\nu(\mathbf{k}) n_{\nu,l}^\mu(\mathbf{k}) w(\nu, \mathbf{k}) \right) / \left( \sum_{\mathbf{k}} \sum_{\nu} n_{\nu,l}^\mu(\mathbf{k}) w(\nu, \mathbf{k}) \right) \quad (3.151)$$

### 3.6.3 Construction of the Electron Density in the Muffin-Tins

Substituting (3.141) into (3.137) yields the electron density in the muffin-tin spheres.

$$n^\mu(\mathbf{r}) = \frac{1}{V_{BZ}} \int_{BZ} \sum_{\nu, \epsilon_\nu(\mathbf{k}) < E_F} \sum_{L'} \left( A_{L', \nu}^\mu(\mathbf{k}) u_{l'}^\alpha(r) + B_{L', \nu}^\mu(\mathbf{k}) \dot{u}_{l'}^\alpha(r) \right)^* Y_{L'}^*(\hat{\mathbf{r}}) \sum_L \left( A_{L, \nu}^\mu(\mathbf{k}) u_l^\alpha(r) + B_{L, \nu}^\mu(\mathbf{k}) \dot{u}_l^\alpha(r) \right) Y_L(\hat{\mathbf{r}}) d^3k \quad (3.152)$$

The particle density inside the muffin-tins is also expanded into spherical harmonics.

$$n^\mu(\mathbf{r}) = \sum_L C_L^\mu(r) Y_L(\hat{\mathbf{r}}) \quad (3.153)$$

The coefficients  $C_{L'}^\mu(r)$  can be determined by multiplying (3.152) with  $\int d\Omega Y_{L''}(\hat{\mathbf{r}})$ .

$$C_{L''}^\mu(r) = \frac{1}{V_{BZ}} \int_{BZ} \sum_{\nu, \epsilon_\nu(\mathbf{k}) < E_F} \sum_{L'} \left( A_{L', \nu}^\mu(\mathbf{k}) u_{l'}^\alpha(r) + B_{L', \nu}^\mu(\mathbf{k}) \dot{u}_{l'}^\alpha(r) \right)^* \sum_L \left( A_{L, \nu}^\mu(\mathbf{k}) u_l^\alpha(r) + B_{L, \nu}^\mu(\mathbf{k}) \dot{u}_l^\alpha(r) \right) G_{l'l''}^{mm'm''} d^3k \quad (3.154)$$

with

$$G_{l'l''}^{mm'm''} = \int Y_{lm}^* Y_{l'm'} Y_{l''m''} d\Omega \quad (3.155)$$

where it has been used, that the gaunt coefficients are real, i.e.

$$\int Y_{lm} Y_{l'm'}^* Y_{l''m''} d\Omega = \int Y_{lm}^* Y_{l'm'} Y_{l''m''} d\Omega \quad (3.156)$$

Finally, applying a Brillouin zone integration method yields:

$$\begin{aligned} C_{L''}^\mu(r) &= \sum_{l'l} \left( \sum_{\mathbf{k}} \sum_{\nu} \sum_{m'm} \left( A_{L', \nu}^\mu(\mathbf{k}) \right)^* A_{L, \nu}^\mu(\mathbf{k}) G_{l'l''}^{mm'm''} w(\nu, \mathbf{k}) \right) u_{l'}^\alpha(r) u_l^\alpha(r) \\ &+ \sum_{l'l} \left( \sum_{\mathbf{k}} \sum_{\nu} \sum_{m'm} \left( A_{L', \nu}^\mu(\mathbf{k}) \right)^* B_{L, \nu}^\mu(\mathbf{k}) G_{l'l''}^{mm'm''} w(\nu, \mathbf{k}) \right) u_{l'}^\alpha(r) \dot{u}_l^\alpha(r) \\ &+ \sum_{l'l} \left( \sum_{\mathbf{k}} \sum_{\nu} \sum_{m'm} \left( B_{L', \nu}^\mu(\mathbf{k}) \right)^* A_{L, \nu}^\mu(\mathbf{k}) G_{l'l''}^{mm'm''} w(\nu, \mathbf{k}) \right) \dot{u}_{l'}^\alpha(r) u_l^\alpha(r) \\ &+ \sum_{l'l} \left( \sum_{\mathbf{k}} \sum_{\nu} \sum_{m'm} \left( B_{L', \nu}^\mu(\mathbf{k}) \right)^* B_{L, \nu}^\mu(\mathbf{k}) G_{l'l''}^{mm'm''} w(\nu, \mathbf{k}) \right) \dot{u}_{l'}^\alpha(r) \dot{u}_l^\alpha(r) \end{aligned} \quad (3.157)$$

### 3.6.4 Construction of the Electron Density in the Interstitial Region

In the interstitial region the wavefunctions are represented in the following form.

$$\psi_\nu(\mathbf{k}, \mathbf{r}) = \sum_{\mathbf{G}} c_\nu^{\mathbf{G}}(\mathbf{k}) e^{i(\mathbf{G}+\mathbf{k})\mathbf{r}} \quad (3.158)$$

Starting from (2.8) the electron density is given by:

$$n(\mathbf{r}) = \frac{1}{V_{BZ}} \int_{BZ} \sum_{\nu, \epsilon_\nu(\mathbf{k}) < E_F} \sum_{\mathbf{G}' \mathbf{G}''} \left( c_\nu^{\mathbf{G}'}(\mathbf{k}) \right)^* c_\nu^{\mathbf{G}''}(\mathbf{k}) d^3k e^{i(\mathbf{G}'' - \mathbf{G}') \mathbf{r}} \quad (3.159)$$

The electron density in the interstitial region is also expanded into planewaves.

$$n(\mathbf{r}) = \sum_{\mathbf{G}} n^{\mathbf{G}} e^{i\mathbf{G}\mathbf{r}} \quad (3.160)$$

Hence, the planewave coefficients of the electron density are:

$$n^{\mathbf{G}} = \frac{1}{V_{BZ}} \int_{BZ} \sum_{\nu, \epsilon_\nu(\mathbf{k}) < E_F} \sum_{\substack{\mathbf{G}' \mathbf{G}'' \\ \mathbf{G}'' - \mathbf{G}' = \mathbf{G}}} \left( c_\nu^{\mathbf{G}'}(\mathbf{k}) \right)^* c_\nu^{\mathbf{G}''}(\mathbf{k}) d^3k \quad (3.161)$$

Apparently, the planewave cut-off of the particle density has to be twice the cut-off of the wavefunction expansion ( $G_{max}$ ) to allow an accurate description. The  $\mathbf{k}$  and state dependent density

$$n_\nu^{\mathbf{G}}(\mathbf{k}) = \sum_{\substack{\mathbf{G}' \mathbf{G}'' \\ \mathbf{G}'' - \mathbf{G}' = \mathbf{G}}} \left( c_\nu^{\mathbf{G}'}(\mathbf{k}) \right)^* c_\nu^{\mathbf{G}''}(\mathbf{k}) = \sum_{\mathbf{G}'} \left( c_\nu^{\mathbf{G}'}(\mathbf{k}) \right)^* c_\nu^{(\mathbf{G} + \mathbf{G}')}(\mathbf{k}) \quad (3.162)$$

is given by a convolution in momentum space. For each coefficient a sum over  $\mathbf{G}$  has to be performed. Consequently, the numerical effort put into the determination of  $n_\nu^{\mathbf{G}}(\mathbf{k})$  scales proportional to the number of  $G$ -vectors squared, i.e. proportional to  $(G_{max})^6$ . However,  $n_\nu^{\mathbf{G}}(\mathbf{k})$  can be calculated more efficiently using the fast Fourier transform (FFT). First,  $c_\nu^{\mathbf{G}}(\mathbf{k})$  is Fourier transformed to real space, where it is squared on a real space mesh yielding  $n_\nu(\mathbf{k}, \mathbf{r})$ , then all states are summed up and finally the resulting particle density is back-transformed to momentum space.

$$c_\nu^{\mathbf{G}}(\mathbf{k}) \xrightarrow{FFT} \psi_\nu(\mathbf{k}, \mathbf{r}) \xrightarrow{square} n_\nu(\mathbf{k}, \mathbf{r}) \xrightarrow{\sum_\nu} n(\mathbf{k}, \mathbf{r}) \xrightarrow{FFT^{-1}} n^{\mathbf{G}}(\mathbf{k})$$

With this scheme the numerical effort increases proportional to  $(G_{max})^3 \ln((G_{max})^3)$ , which is a major improvement for large systems. In a last step the planewaves have to be combined to form the three-dimensional stars.

### 3.6.5 Construction of the Electron Density in the Vacuum Region

In the vacuum region the wavefunctions are expanded into two-dimensional plane-waves parallel to the surface and z-dependent functions perpendicular to the surface.

$$\psi_\nu(\mathbf{k}_\parallel, \mathbf{r}) = \sum_{\mathbf{G}_\parallel \mathbf{G}_\perp} c_\nu^{\mathbf{G}_\parallel \mathbf{G}_\perp}(\mathbf{k}_\parallel) \left( A_{\mathbf{G}_\parallel \mathbf{G}_\perp}(\mathbf{k}_\parallel) u_{\mathbf{G}_\parallel}(\mathbf{k}_\parallel, z) + B_{\mathbf{G}_\parallel \mathbf{G}_\perp}(\mathbf{k}_\parallel) \dot{u}_{\mathbf{G}_\parallel}(\mathbf{k}_\parallel, z) \right) e^{i(\mathbf{G}_\parallel + \mathbf{k}_\parallel) \mathbf{r}_\parallel} \quad (3.163)$$

Hence, the electron density is given by:

$$\begin{aligned}
n(\mathbf{r}) = & \frac{1}{V_{BZ}} \int_{BZ} \sum_{\nu, \epsilon_{\nu}(\mathbf{k}) < E_F} \sum_{\mathbf{G}'_{\parallel} \mathbf{G}'_{\perp}} \sum_{\mathbf{G}''_{\parallel} \mathbf{G}''_{\perp}} \\
& \left( c_{\nu}^{\mathbf{G}'_{\parallel} \mathbf{G}'_{\perp}}(\mathbf{k}_{\parallel}) \left( A_{\mathbf{G}'_{\parallel} \mathbf{G}'_{\perp}}(\mathbf{k}_{\parallel}) u_{\mathbf{G}'_{\parallel}}(\mathbf{k}_{\parallel}, z) + B_{\mathbf{G}'_{\parallel} \mathbf{G}'_{\perp}}(\mathbf{k}_{\parallel}) \dot{u}_{\mathbf{G}'_{\parallel}}(\mathbf{k}_{\parallel}, z) \right) \right)^* \\
& \left( c_{\nu}^{\mathbf{G}''_{\parallel} \mathbf{G}''_{\perp}}(\mathbf{k}_{\parallel}) \left( A_{\mathbf{G}''_{\parallel} \mathbf{G}''_{\perp}}(\mathbf{k}_{\parallel}) u_{\mathbf{G}''_{\parallel}}(\mathbf{k}_{\parallel}, z) + B_{\mathbf{G}''_{\parallel} \mathbf{G}''_{\perp}}(\mathbf{k}_{\parallel}) \dot{u}_{\mathbf{G}''_{\parallel}}(\mathbf{k}_{\parallel}, z) \right) \right) d^3 k \\
& e^{i(\mathbf{G}''_{\parallel} - \mathbf{G}'_{\parallel}) \mathbf{r}_{\parallel}} \tag{3.164}
\end{aligned}$$

The particle density in the vacuum is represented in the following form.

$$n(\mathbf{r}) = \sum_{\mathbf{G}_{\parallel}} n^{\mathbf{G}_{\parallel}}(z) e^{i\mathbf{G}_{\parallel} \mathbf{r}_{\parallel}} \tag{3.165}$$

Performing the Brillouin zone integration on a discrete  $\mathbf{k}_{\parallel}$ -mesh and carrying out the summation over  $\mathbf{G}'_{\perp}$  and  $\mathbf{G}''_{\perp}$  we find that the coefficients  $n^{\mathbf{G}_{\parallel}}(z)$  are:

$$\begin{aligned}
n^{\mathbf{G}_{\parallel}}(z) = & \sum_{\mathbf{k}_{\parallel}} \sum_{\nu} \sum_{\mathbf{G}'_{\parallel}} \left( A_{\mathbf{G}'_{\parallel}, \nu}(\mathbf{k}_{\parallel}) \right)^* A_{(\mathbf{G}_{\parallel} + \mathbf{G}'_{\parallel}), \nu}(\mathbf{k}_{\parallel}) w(\nu, \mathbf{k}_{\parallel}) u_{\mathbf{G}'_{\parallel}}(\mathbf{k}_{\parallel}, z) u_{(\mathbf{G}_{\parallel} + \mathbf{G}'_{\parallel})}(\mathbf{k}_{\parallel}, z) \\
& + \sum_{\mathbf{k}_{\parallel}} \sum_{\nu} \sum_{\mathbf{G}'_{\parallel}} \left( A_{\mathbf{G}'_{\parallel}, \nu}(\mathbf{k}_{\parallel}) \right)^* B_{(\mathbf{G}_{\parallel} + \mathbf{G}'_{\parallel}), \nu}(\mathbf{k}_{\parallel}) w(\nu, \mathbf{k}_{\parallel}) u_{\mathbf{G}'_{\parallel}}(\mathbf{k}_{\parallel}, z) \dot{u}_{(\mathbf{G}_{\parallel} + \mathbf{G}'_{\parallel})}(\mathbf{k}_{\parallel}, z) \\
& + \sum_{\mathbf{k}_{\parallel}} \sum_{\nu} \sum_{\mathbf{G}'_{\parallel}} \left( B_{\mathbf{G}'_{\parallel}, \nu}(\mathbf{k}_{\parallel}) \right)^* A_{(\mathbf{G}_{\parallel} + \mathbf{G}'_{\parallel}), \nu}(\mathbf{k}_{\parallel}) w(\nu, \mathbf{k}_{\parallel}) \dot{u}_{\mathbf{G}'_{\parallel}}(\mathbf{k}_{\parallel}, z) u_{(\mathbf{G}_{\parallel} + \mathbf{G}'_{\parallel})}(\mathbf{k}_{\parallel}, z) \\
& + \sum_{\mathbf{k}_{\parallel}} \sum_{\nu} \sum_{\mathbf{G}'_{\parallel}} \left( B_{\mathbf{G}'_{\parallel}, \nu}(\mathbf{k}_{\parallel}) \right)^* B_{(\mathbf{G}_{\parallel} + \mathbf{G}'_{\parallel}), \nu}(\mathbf{k}_{\parallel}) w(\nu, \mathbf{k}_{\parallel}) \dot{u}_{\mathbf{G}'_{\parallel}}(\mathbf{k}_{\parallel}, z) \dot{u}_{(\mathbf{G}_{\parallel} + \mathbf{G}'_{\parallel})}(\mathbf{k}_{\parallel}, z) \tag{3.166}
\end{aligned}$$

with

$$A_{\mathbf{G}_{\parallel}, \nu}(\mathbf{k}_{\parallel}) = \sum_{\mathbf{G}_{\perp}} c_{\nu}^{\mathbf{G}_{\parallel} \mathbf{G}_{\perp}}(\mathbf{k}_{\parallel}) A_{\mathbf{G}_{\parallel} \mathbf{G}_{\perp}}(\mathbf{k}_{\parallel}), \quad B_{\mathbf{G}_{\parallel}, \nu}(\mathbf{k}_{\parallel}) = \sum_{\mathbf{G}_{\perp}} c_{\nu}^{\mathbf{G}_{\parallel} \mathbf{G}_{\perp}}(\mathbf{k}_{\parallel}) B_{\mathbf{G}_{\parallel} \mathbf{G}_{\perp}}(\mathbf{k}_{\parallel}) \tag{3.167}$$

Here, the terms of the form

$$\sum_{\mathbf{G}'_{\parallel}} \left( A_{\mathbf{G}'_{\parallel}, \nu}(\mathbf{k}_{\parallel}) \right)^* A_{(\mathbf{G}_{\parallel} + \mathbf{G}'_{\parallel}), \nu}(\mathbf{k}_{\parallel}) u_{\mathbf{G}'_{\parallel}}(\mathbf{k}_{\parallel}, z) u_{(\mathbf{G}_{\parallel} + \mathbf{G}'_{\parallel})}(\mathbf{k}_{\parallel}, z)$$

represent convolutions in momentum space. Similar to the interstitial region these terms could be calculated more efficiently, using two-dimensional fast Fourier transform. However, there are far less two-dimensional planewaves than three-dimensional planewaves. Therefore, the possible saving of computer time is much smaller.

## 3.7 Construction of the Coulomb Potential

The Coulomb potential consists of two parts, the Hartree term  $V_H(\mathbf{r})$  and the external potential of the nuclei  $V_i(\mathbf{r})$ .

$$V_c(\mathbf{r}) = V_H(\mathbf{r}) + V_i(\mathbf{r}) \quad (3.168)$$

The Hartree potential has to be determined from the charge density via the Poisson equation.

$$\Delta V_H(\mathbf{r}) = 4\pi\rho(\mathbf{r}) \quad (3.169)$$

In real space the solution of 3.169 is given by

$$V_H(\mathbf{r}) = \int \frac{4\pi\rho(\mathbf{r}')}{|\mathbf{r} - \mathbf{r}'|} d^3\mathbf{r}'. \quad (3.170)$$

In reciprocal space, however, the Poisson equation is diagonal, as a result the solution is very simple.

$$V_H(\mathbf{G}) = \frac{4\pi\rho(\mathbf{G})}{\mathbf{G}^2} \quad (3.171)$$

Therefore, and because of the representation of the charge density and the potential in the interstitial- and vacuum-region, the solution of the Poisson equation in reciprocal space appears to be convenient. However, due to the rather localized core and valence states the charge density changes on a very small length scale near the nuclei. Therefore, the planewave expansion of  $\rho$  converges slowly, and a direct use of (3.171) is impractical, if not impossible. This difficulty can be circumvented via the pseudocharge method.

### 3.7.1 The Pseudocharge Method

The pseudocharge method, developed by Weinert [Wei81], is a very elegant technique to calculate the interstitial and vacuum Hartree potential. The underlying idea is to divide the solution of the Poisson equation into two steps. In the first step the true muffin-tin charge is replaced by a convergent pseudocharge density  $\tilde{\rho}$ , that leads to the same potential outside the muffin-tins. Then the interstitial (and vacuum) potential is calculated in reciprocal space. In the second step the muffin-tin potential is determined from the Dirichlet boundary value problem, defined by the exact muffin-tin charge and the interstitial potential on the muffin-tin sphere boundaries. The potential outside the muffin-tin spheres due to a charge distribution inside the sphere is determined completely by its multipole moments  $q_L$ .

$$V(\mathbf{r}) = \sum_{l=0}^{\infty} \sum_{m=-l}^l \frac{4\pi}{2l+1} \frac{q_L}{r^{l+1}} Y_L(\hat{\mathbf{r}}), \quad (3.172)$$

However, the multipole moments do not define the charge density uniquely. The charge density is given by:

$$\rho(\mathbf{r}) = \rho_I(\mathbf{r})\Theta(\mathbf{r} \in I) + \sum_{\alpha} \rho_{\alpha}(\mathbf{r})\Theta(\mathbf{r} \in MT^{\alpha}) \quad (3.173)$$

Of course, in film calculation there is also a vacuum charge, and we will come back to this later. 3.173 can be rewritten

$$\rho(\mathbf{r}) = \rho_I(\mathbf{r}) + \sum_{\alpha} [\rho_{\alpha}(\mathbf{r}) - \rho_I(\mathbf{r})] \Theta(\mathbf{r} \in MT^{\alpha}) \quad (3.174)$$

Thus, the interstitial charge has been extended into the muffin-tin and subtracted there again. The second term in 3.174 can now be replaced by a pseudocharge  $\tilde{\rho}^{\alpha}$ , that has the same multipole moments (s. [Wei81] for details). The resultant pseudocharge  $\tilde{\rho}$  is given by

$$\tilde{\rho}(\mathbf{r}) = \rho_I(\mathbf{r}) + \sum_{\alpha} \tilde{q}^{\alpha}(\mathbf{r}) \quad (3.175)$$

$\tilde{\rho}(\mathbf{r})$  is constructed to have a more rapidly converging Fourier expansion than the original charge density  $\rho(\mathbf{r})$ . Therefore, the Poisson equation can now be solved using (3.171).

Still, the muffin-tin potential  $V_{MT}^{\alpha}$  remains to be determined. For this step the exact muffin-tin charge  $\rho_{\alpha}$  has to be used. Since, the interstitial potential is already known at this point, the calculation of  $V_{MT}^{\alpha}$  constitutes a classical spherically symmetric Dirichlet boundary value problem, which can be solved by the Green's function method [Jac83].

$$V_{MT}^{\alpha}(\mathbf{r}) = \int_{MT^{\alpha}} \rho_{\alpha}(\mathbf{r}') G(\mathbf{r}, \mathbf{r}') d^3 r' - \frac{R_{\alpha}^2}{4\pi} \oint_{S^{\alpha}} V_I(\mathbf{r}') \frac{\partial G}{\partial n'} d\Omega' \quad (3.176)$$

The second integral is over the muffin-tin sphere boundary  $S^{\alpha}$ , and it is necessary to satisfies the boundary conditions. The Green's function is given by:

$$G^{\alpha}(\mathbf{r}, \mathbf{r}') = 4\pi \sum_{l,m} \frac{Y_L(\hat{\mathbf{r}}') Y_L(\hat{\mathbf{r}})}{2l+1} \frac{r_{<}^l}{r_{>}^{l+1}} \left( 1 - \left( \frac{r_{>}}{R_{MT^{\alpha}}} \right)^{2l+1} \right) \quad (3.177)$$

where  $r_{>} = \max\{|\mathbf{r}|, |\mathbf{r}'|\}$ ,  $r_{<} = \min\{|\mathbf{r}|, |\mathbf{r}'|\}$ . Finally, the muffin-tin potential has to be expanded into lattice harmonics  $K_{\nu}(\hat{\mathbf{r}})$ .

$$V_{MT}^{\alpha}(\mathbf{r}) = \sum_{\nu} V_{MT,\nu}^{\alpha}(r) K_{\nu}(\hat{\mathbf{r}}) \quad (3.178)$$

The potential of the nuclei  $V_i^{\alpha}(\mathbf{r}) = \frac{eZ^{\alpha}}{|\mathbf{r}|}$  is added to the spherical ( $l=0$ ) component of the potential  $V_{MT,0}^{\alpha}(r)$ .

The muffin-tin potential is computed in the same way for both, bulk and film calculations. Apparently, the interstitial and the vacuum have to be treated differently in the two cases, due to the different boundary conditions and the different representation of the vacuum potential. Therefore, in the next two sections the solution of the Poisson equation will be outlined separately for these cases in.

### 3.7.2 Determination of the interstitial Coulomb Potential in Bulk Calculations

In the case of bulk calculations we have periodic boundary conditions in three dimensions. Therefore, the solution of the Poisson equation,

$$\mathbf{G}^2 V(\mathbf{G}) = 4\pi \tilde{\rho}(\mathbf{G}) \quad (3.179)$$

is very simple. Obviously, this equation can only be solved, if  $\tilde{\rho}(0) = 0$ . Since  $\tilde{\rho}(0)$  is the average charge density, this means, that charge neutrality is essential. Still,  $V(0)$  remains undetermined by 3.179, i.e. one has the freedom to shift the potential by a constant. This is a consequence of the periodic boundary conditions, because they do not fix the reference of the potential. Usually  $V(0)$  is chosen to be zero, hence the Coulomb potential in the interstitial-region is given by:

$$V_I(\mathbf{r}) = \sum_{\mathbf{G} \neq 0} \frac{4\pi \tilde{\rho}(\mathbf{G})}{\mathbf{G}^2} e^{i\mathbf{G}\mathbf{r}} = \sum_{s \neq 0} \frac{4\pi \tilde{\rho}_s}{\mathbf{G}_s^2} \Phi_s^{3D}(\mathbf{r}) \quad (3.180)$$

where the first summation is expressed in terms of  $G$ -vectors and the second in terms of stars.

### 3.7.3 Determination of the interstitial and vacuum Coulomb Potential in Film Calculations

In a film the translational symmetry in  $z$ -direction is lost. Accordingly, the boundary conditions are periodic in two dimensions only. In  $z$ -direction the periodic boundary conditions are replaced by the requirement, that the potential approaches zero at infinity. The latter condition defines the absolute reference of the potential. As a consequence of the symmetry breaking, the following expansion of  $V$  and  $\rho$  is most suitable to solve the Poisson equation:

$$V(\mathbf{r}) = V_0(z) + \sum_{\mathbf{G}_{\parallel} \neq 0} V_{G_{\parallel}}(z) e^{i\mathbf{G}_{\parallel}\mathbf{r}} \quad (3.181)$$

$$\rho(\mathbf{r}) = \rho_0(z) + \sum_{\mathbf{G}_{\parallel} \neq 0} \rho_{G_{\parallel}}(z) e^{i\mathbf{G}_{\parallel}\mathbf{r}} \quad (3.182)$$

Substituting this into the Poisson equations yields:

$$\left( \frac{d^2}{dz^2} - G_{\parallel}^2 \right) V_{G_{\parallel}}(z) = -4\pi \rho_{G_{\parallel}}(z) \quad (3.183)$$

This equation is treated differently for  $G_{\parallel} = 0$  and  $G_{\parallel} \neq 0$ .

### The $G_{\parallel} = 0$ Component of the Potential

For the  $G_{\parallel} = 0$  component of the potential the Poisson equation has the form

$$\frac{d^2}{dz^2} V_0(z) = -4\pi\rho_0(z) \quad (3.184)$$

The  $G_{\parallel} = 0$  component of the pseudocharge density is given by:

$$\rho_0(z) = \begin{cases} \rho_I^{0,0} + \sum_{G_{\perp}} \rho_I^{0,G_{\perp}} e^{iG_{\perp}z} & |z| \leq \frac{D}{2} \\ \rho_V^0(z) & |z| > \frac{D}{2} \end{cases} \quad (3.185)$$

The Poisson equation for the  $G_{\parallel} = 0$  can be integrated directly. The result in the vacuum region is given by:

$$V_V^0(z) = -4\pi \int_z^{\infty} \sigma_V(z') dz', \quad (3.186)$$

with

$$\sigma_V(z) = \int_{\frac{D}{2}}^z \rho_V^0(z') dz' + \bar{\rho}_I \frac{D}{2} \quad (3.187)$$

where the average interstitial charge density  $\bar{\rho}_I$  is given by:

$$\bar{\rho}_I = \sum_{G_{\perp}} \rho_I^{0,G_{\perp}} j_0(G_{\perp} D). \quad (3.188)$$

Here  $\bar{\rho}_I$  does not equal  $\rho_I^{0,0}$ , because the  $G_{\perp}$  are defined in terms of  $\tilde{D}$  rather than  $D$ , i.e. the period of the  $z$ -dependent planewaves does not equal the integration interval.

In the interstitial region the solution to (3.184) is

$$V_I^0(z) = -2\pi\rho_I^{0,0} \left( z^2 - \frac{D^2}{4} \right) - 4\pi \sum_{G_{\perp}} \frac{\rho_I^{0,G_{\perp}}}{G_{\perp}^2} \left( e^{iG_{\perp}z} - e^{iG_{\perp}\frac{D}{2}} \right) - 4\pi \int_{\frac{D}{2}}^{\infty} \sigma_V(z') dz' \quad (3.189)$$

### The $G_{\parallel} \neq 0$ Component of the Potential

In the case  $G_{\parallel} \neq 0$  the Poisson equation is solved via the Green's function method.

$$V_{G_{\parallel}}(z) = \int_{-\infty}^{\infty} \rho_{G_{\parallel}}(z) G_{G_{\parallel}}(z - z') dz' \quad (3.190)$$

Where the Green's function is given by:

$$G_{G_{\parallel}}(z - z') = \frac{2\pi}{G_{\parallel}} e^{|G_{\parallel}||z-z'|} \quad (3.191)$$



This leads to the following solution in the vacuum-region

$$\begin{aligned}
V_V^{G_{\parallel}}(z) &= \frac{2\pi}{G_{\parallel}} e^{G_{\parallel}z} \int_{-\infty}^z \rho_V^{G_{\parallel}}(z') e^{-G_{\parallel}z'} dz' \\
&\quad + \frac{2\pi}{G_{\parallel}} e^{-G_{\parallel}z} \int_z^{-\frac{D}{2}} \rho_V^{G_{\parallel}}(z') e^{G_{\parallel}z'} dz' \\
&\quad + \frac{2\pi}{G_{\parallel}} e^{-G_{\parallel}z} \sum_{G_{\perp}} \frac{\rho_I^{G_{\parallel}, G_{\perp}}}{G_{\parallel} + iG_{\perp}} \left( e^{(G_{\parallel} + iG_{\perp})z} - e^{-(G_{\parallel} + iG_{\perp})z} \right)
\end{aligned} \tag{3.192}$$

and in the interstitial-region

$$\begin{aligned}
V_I^{G_{\parallel}}(z) &= 4\pi \sum_n \frac{\rho_I^{G_{\parallel}, G_{\perp}}}{G^2} e^{iG_{\perp}z} \\
&\quad + \frac{2\pi}{G_{\parallel}} \sum_{G_{\perp}} \frac{\rho_I^{G_{\parallel}, G_{\perp}}}{G^2} \left[ e^{G_{\parallel}z} (G_{\parallel} + iG_{\perp}) e^{-(G_{\parallel} - iG_{\perp})\frac{D}{2}} \right. \\
&\quad \left. + e^{-G_{\parallel}z} (G_{\parallel} - iG_{\perp}) e^{-(G_{\parallel} + iG_{\perp})\frac{D}{2}} \right] + \\
&\quad + \frac{2\pi}{G_{\parallel}} \left[ e^{G_{\parallel}z} \int_{-\frac{D}{2}}^{\infty} \rho_V^{G_{\parallel}}(z) e^{-G_{\parallel}z'} dz' + e^{-G_{\parallel}z} \int_{-\infty}^{\frac{D}{2}} \rho_V^{G_{\parallel}}(z) e^{G_{\parallel}z'} dz' \right]
\end{aligned} \tag{3.193}$$

## 3.8 Computation of the Exchange Correlation Potential

The problem of the determination of the exchange correlation potential is quite different from the Coulomb potential. On one hand,  $V_{xc}^{\sigma}$  is a local quantity, i.e.  $V_{xc}^{\sigma}(\mathbf{r})$  depends only on  $n_{\uparrow}(\mathbf{r})$  and  $n_{\downarrow}(\mathbf{r})$  at the same position  $\mathbf{r}$ . Thus, the muffin-tins, the interstitial- and vacuum-region can be treated independently. On the other hand,  $V_{xc}^{\sigma}$  and  $\epsilon_{xc}^{\sigma}$  are non-linear functions of  $n_{\uparrow}$  and  $n_{\downarrow}$ . Therefore,  $V_{xc}^{\sigma}$  and  $\epsilon_{xc}^{\sigma}$  have to be calculated in real space.  $V_{xc}^{\sigma}$  and  $\epsilon_{xc}^{\sigma}$  are determined in the same way. First,  $n_{\uparrow}$  and  $n_{\downarrow}$  are transformed to real space, where  $V_{xc}^{\sigma}$  and  $\epsilon_{xc}^{\sigma}$  are calculated. Then  $V_{xc}^{\sigma}$  and  $\epsilon_{xc}^{\sigma}$  are back-transformed. Then,  $V_{xc}^{\sigma}$  is added to the Coulomb potential, yielding the spin-dependent potential  $V_{\uparrow}$  and  $V_{\downarrow}$ .  $\epsilon_{xc}^{\sigma}$  is needed for the determination of the total energy.

### 3.8.1 Calculation of $\epsilon_{xc}^{\sigma}$ and $V_{xc}^{\sigma}$ in the Interstitial-Region

In the interstitial-region the charge density is expanded into three-dimensional stars with coefficients  $n_s^{\sigma}$ . Multiplying these by  $e^{i\mathbf{R}\mathbf{G}\cdot\boldsymbol{\tau}}$  yields the planewave coefficients  $n_G^{\sigma}$ . If the space group is symmorphic the star and planewave coefficients are identical. However, due to numerical inaccuracy, the calculated coefficients of symmetry equivalent planewaves are not exactly equal, and the corresponding star coefficient

is obtained from the average of the planewave coefficients. In the next step a three-dimensional Fast-Fourier transform is carried out. Then the exchange correlation potential is calculated on a real space mesh  $\mathbf{r}_i$ . Finally,  $V_{xc}^\sigma$  is back-transformed, and the star coefficients are computed.

$$n_s^\sigma \longrightarrow n_G^\sigma \xrightarrow{FFT} n^\sigma(\mathbf{r}_i) \longrightarrow V_{xc}^\sigma(\mathbf{r}_i) \xrightarrow{FFT^{-1}} V_{xc}^{\sigma,G} \longrightarrow V_{xc}^{\sigma,s}.$$

### 3.8.2 Calculation of $\epsilon_{xc}^\sigma$ and $V_{xc}^\sigma$ in the Vacuum-Region

The vacuum charge density is stored in terms of two-dimensional stars and a  $z$ -dependent exponential mesh  $z_i$ . The  $G_{\parallel} = 0$  component reaches further into the vacuum than the  $G_{\parallel} \neq 0$  components. In the so called warping region the planewave coefficients on each mesh point are determined by a multiplication with the phase factor  $e^{i\mathbf{R}\mathbf{G}_{\parallel}\tau}$ . Then, for each grid point  $z_i$  along the  $z$ -axis, the two-dimensional charge density is Fourier transformed to a real space grid  $(\mathbf{r}_{\parallel}, z_i)$ , where  $V_{xc}^\sigma$  is calculated. Afterwards,  $V_{xc}^\sigma$  is back-transformed and the star coefficients are computed.

$$\begin{aligned} n^\sigma(\Phi_s^{2D}, z_i) &\longrightarrow n^\sigma(\mathbf{G}_{\parallel}, z_i) \xrightarrow{2DFFT} n^\sigma(\mathbf{r}_{\parallel}, z_i) \longrightarrow V_{xc}^\sigma(\mathbf{r}_{\parallel}, z_i) \\ &\xrightarrow{2DFFT^{-1}} V_{xc}^\sigma(\mathbf{G}_{\parallel}, z_i) \longrightarrow V_{xc}^\sigma(\Phi_s^{2D}, z_i) \end{aligned}$$

Beyond the warping region the exchange correlation potential is calculated directly on the  $z$ -dependent mesh.

### 3.8.3 Calculation of $\epsilon_{xc}^\sigma$ and $V_{xc}^\sigma$ in the Muffin-Tin Spheres

The muffin-tin charge is expanded into lattice harmonics and radial functions. The radial functions are stored on a discrete real-space mesh. Thus, the transform to real space affects only the angular part. The charge density is calculated on a set of special angular points  $\hat{\mathbf{r}}_i = (\theta_i, \phi_i)$ . Again, the exchange correlation potential is calculated in real space. Thereafter, the result  $V_{xc}^\sigma(\mathbf{r})$  is expanded into spherical harmonics  $Y_L$ . The  $Y_L$  are orthonormal, therefore the coefficients can be obtained from

$$v_{xc,L}^\sigma(r) = \int Y_L(\hat{\mathbf{r}}) V_{xc}^\sigma(r, \hat{\mathbf{r}}) d\Omega. \quad (3.194)$$

The choice of the points  $\hat{\mathbf{r}}_i = (\theta_i, \phi_i)$ , on which  $n^\sigma(\mathbf{r})$  and  $V_{xc}^\sigma(\mathbf{r})$  are calculated, depends on the integration method, that is used to perform the angular integration. In the current implementation (3.194) is computed via a Gauß-Legendre integration and the angular points are chosen such, that the orthonormality condition of the  $Y_L$  holds also for the angular mesh  $\hat{\mathbf{r}}_i$ .

## 3.9 Minimization of the Energy Functional

The aim of electronic structure calculations is to minimize the energy functional with respect to the electron density. Within density functional theory this minimization

is performed implicitly, by the determination of a selfconsistent density  $n(\mathbf{r})$ . In the previous sections we described, how an effective Potential can be calculated from a charge density, how the Kohn-Sham equations including this potential can be solved and how a new electron density can be calculated from the resulting single particle wavefunctions. Combining these steps defines a map:

$$n'(\mathbf{r}) = F\{n(\mathbf{r})\} \quad (3.195)$$

The electron density that minimizes the energy functional  $n_0(\mathbf{r})$  is a fix-point of  $F\{n(\mathbf{r})\}$ , i.e. it solves

$$\mathcal{F}\{n_0(\mathbf{r})\} = 0, \quad \text{with } \mathcal{F}\{n(\mathbf{r})\} = F\{n(\mathbf{r})\} - n(\mathbf{r}). \quad (3.196)$$

The density is expanded into a large set of basis functions. Therefore, in actual calculations, the charge density is a coefficient vector of dimension  $n$ , where  $n$  is typically of the order of  $10^4$ . Thus, (3.196) constitutes a system of  $n$  nonlinear equations, which can be solved by iteration:

$$n^{m+1}(\mathbf{r}) = F\{n^m(\mathbf{r})\} \quad (3.197)$$

A starting density can be constructed by a superposition of atomic densities. However, this scheme is in general divergent. To achieve convergence the output density has to be mixed with the input density. Different mixing schemes are discussed in the following.

### 3.9.1 “simple mixing”

The slowest method is the “simple mixing”, which converges only linearly.

$$\frac{|\delta n^{(m+1)}|}{|\delta n^{(m)}|} \leq \text{const.} \quad (3.198)$$

Where  $\delta n^{(m)}$  is the difference of the density of the  $m^{\text{th}}$  iteration and the unknown fix-point,  $\delta n^{(m)} = n^{(m)} - n_0$ . The density for the next iteration is constructed as a linear combination of  $n^{(m)}$  and  $F\{n^m\}$  according to:

$$\begin{aligned} n^{(m+1)} &= (1 - \alpha)n^{(m)} + \alpha F\{n^m\} \\ &= n^{(m)} + \alpha \mathcal{F}\{n^{(m)}\} \end{aligned} \quad (3.199)$$

$\alpha$  is the so-called mixing parameter. If it is chosen small enough the iteration converges and is very stable. In spin-polarized calculations different mixing parameters can be used for the charge and the magnetization density. Usually, the spin mixing parameter can be chosen far larger than the parameter for the charge density. However, for the type of systems we are interested in  $\alpha$  is very small, requiring many hundreds of iterations.

### 3.9.2 The Newton-Raphson Method

In the Newton-Raphson method the functional  $\mathcal{F}\{n\}$  is linearized around the approximate solution  $n^{(m)}$ .

$$\mathcal{F}\{n\} \approx \mathcal{F}\{n^{(m)}\} + \mathcal{J}\{n^{(m)}\}(n - n^{(m)}) \quad (3.200)$$

Where the Jacobian is defined by:

$$\mathcal{J}\{n^{(m)}(\mathbf{r})\} = \left. \frac{\partial \mathcal{F}\{n(\mathbf{r})\}}{\partial n(\mathbf{r}')} \right|_{n^{(m)}(\mathbf{r})} \quad (3.201)$$

In actual calculations the Jacobian is a  $n \times n$  matrix. Similar to the well known Newton method for one dimensional functions, the next approximation to  $n_0$ ,  $n^{(m+1)}$ , is determined from the requirement, that the linearized functional in (3.200) vanishes at  $n^{(m+1)}$ . Thus,  $n^{(m+1)}$  is given by:

$$n^{(m+1)} = n^{(m)} - [\mathcal{J}\{n^{(m)}\}]^{-1} \mathcal{F}\{n^{(m)}\} \quad (3.202)$$

The Newton-Raphson method converges quadratically:

$$\frac{|\delta n^{(m+1)}|}{|\delta n^{(m)}|^2} \leq \text{const.} \quad (3.203)$$

The major drawback of this method is the difficulty to evaluate the Jacobian. Even if the functional  $\mathcal{F}\{n\}$  was known, the evaluation would be cumbersome due to the enormous size of  $\mathcal{J}\{n\}$ . In addition, the Jacobian has to be inverted where the amount of calculation scales with cube of the dimension. A further problem is that the convergence radius is rather small so that the method can only be used if  $n^{(m)}$  is already very close to  $n_0$ .

### 3.9.3 Quasi-Newton Methods

With the development of the Quasi-Newton methods it became possible to exploit the advantages of the Newton-Raphson method, i.e. to make use of the information that is contained in the Jacobian, for problems where the Jacobian cannot be calculated or its determination is too demanding. Rather than computing the Jacobian each iteration, an approximate Jacobian is set up and improved iteration by iteration. From the linearization of  $\mathcal{F}\{n\}$  (3.200) we find the following condition for the Jacobian, which is usually called Quasi-Newton condition:

$$\Delta n^{(m)} = [\mathcal{J}^{(m)}]^{-1} \Delta \mathcal{F}^{(m)} \quad (3.204)$$

$$\Delta n^{(m)} = n^{(m)} - n^{(m-1)}, \quad \Delta \mathcal{F}^{(m)} = \mathcal{F}\{n^{(m)}\} - \mathcal{F}\{n^{(m-1)}\}$$

Quasi-Newton methods converge super-linearly

$$\frac{|\delta n^{(m+1)}|}{|\delta n^{(m)}|} \rightarrow 0,$$

and have a larger convergence radius than the Newton-Raphson method. Since the Jacobian is build up iteration by iteration, the “history” of the previous iterations is memorized in  $\mathcal{J}$ , whereas the Jacobian of the Newton-Raphson method depends only on the previous iteration. In this sense the Newton-Raphson method is self-corrective [Blü88], it “forgets” inadequately chosen corrections. The Quasi-Newton methods sometimes need to be restarted, if the iteration converges only slowly. This can happen if the starting density is very far from  $n_0$  or when physical or numerical parameters that affect the calculations are changed during the iteration. Equation (3.204) does not determine the Jacobian uniquely, instead (3.204) constitutes a system of  $n$  equations for  $n^2$  unknowns. The various Quasi-Newton schemes differ by the ansatz how the new information is used to build the inverse Jacobian. The methods that are implemented in the FLAPW code are discussed in [Pen96].

# Chapter 4

## Non-Collinear Magnetism

As we have seen in Sec. 2.3 the energy functional of a general magnetic system can be expressed in two ways. It can be written as a functional of the charge density  $n$  and the magnetization density vector field  $\mathbf{m}$  or as a functional of the hermitian  $2 \times 2$  density matrix  $\boldsymbol{\rho}$ . The two formulations are completely equivalent. The density matrix is defined by the following equation:

$$\boldsymbol{\rho} = \frac{1}{2} n \mathbf{I}_2 + \boldsymbol{\sigma} \cdot \mathbf{m} = \frac{1}{2} \begin{pmatrix} n + m_z & m_x - im_y \\ m_x + im_y & n - m_z \end{pmatrix}. \quad (4.1)$$

We can also define the potential matrix in the same way.

$$\mathbf{V} = V \mathbf{I}_2 + \mu_B \boldsymbol{\sigma} \cdot \mathbf{B} = \begin{pmatrix} V + \mu_B B_z & \mu_B (B_x - iB_y) \\ \mu_B (B_x + iB_y) & V - \mu_B B_z \end{pmatrix} \quad (4.2)$$

Comparing (4.1) with equation 2.17 on page 12 shows that the components of the density matrix are given by a very simple relation in terms of the solutions of the Kohn-Sham equation:

$$\rho_{\alpha\beta} = \sum_{\nu=1}^N \psi_{\nu,\alpha}^* \psi_{\nu,\beta}. \quad (4.3)$$

In an actual implementation of non-collinear magnetism in a computer program these matrix quantities are very useful, though they are less intuitive than the “physical” quantities  $n$ ,  $\mathbf{m}$ ,  $V$ , and  $\mathbf{B}$ .

Using the potential matrix (4.2), the Kohn-Sham equation (Eqn. 2.18, p. 12) becomes

$$\left\{ -\frac{\hbar^2}{2m} \nabla^2 \mathbf{I}_2 + \mathbf{V} \right\} \boldsymbol{\psi}_\nu = \epsilon_\nu \boldsymbol{\psi}_\nu \quad (4.4)$$

The kinetic energy part of the Hamiltonian is diagonal in the two spin directions. It is only the off-diagonal part of the hermitian  $2 \times 2$  potential matrix, e.g.  $V_{21} = \mu_B (B_x + iB_y)$ , that couples the two components of the Pauli spinor  $\boldsymbol{\psi}_\nu$ . If the  $B$ -field is collinear, the spin coordinate frame can always be chosen such that the  $B$ -field points in the spin  $z$ -direction. In this case  $V_{21}$ , and thus the off-diagonal

part of the Hamiltonian, becomes zero, because  $B_x$  and  $B_y$  are zero. The notation  $V_\uparrow = V + \mu_B B_z$ ,  $V_\downarrow = V - \mu_B B_z$  is commonly used for the diagonal elements of  $\mathbf{V}$  in the collinear case. Since the two spin directions become completely independent, the spin-up and down problem can be solved separately in two steps. Each step can be treated like the non-magnetic problem with the appropriate potential  $V_\uparrow$  or  $V_\downarrow$ . In practice this means that extending a non-magnetic ab-initio program to collinear magnetism is rather straight forward. In addition collinear calculations are by far less costly. Since the effort required to diagonalize the Hamiltonian matrix scales with the number of basis functions to the third power, diagonalizing two small matrices for each spin is much faster than diagonalizing one matrix of twice the size. It also requires only 1/4 of the memory to store the matrix. Another advantage arises when the system has inversion symmetry. In that case the Hamiltonian and the overlap matrix become real symmetric rather than complex hermitian (cf. Sec. 3.3.4, p. 40). In a general non-collinear calculation the Hamiltonian matrix is always complex, due to the complex Pauli matrix  $\sigma_y$ , i.e. the term  $i\mu_B B_y$  in  $V_{21}$ . A third point is, that in most cases non-collinearity reduces the symmetry. The consequence is, that the area of the irreducible part of the Brillouin zone increases. The computational effort increases linearly with the number of  $k$ -points that have to be taken into account for the Brillouin zone integration. So far most magnetic calculations have been performed for collinear systems, because such calculations are more simple and significantly less time consuming.

Since the density functional theory was first proposed, different parameterizations of the exchange correlation energy  $\epsilon_{xc}$  have been suggested in the local spin density approximation (LSDA) and also in the generalized gradient approximation (GGA). These parameterizations have been developed and mostly used for collinear calculations. Due to the local character of LSDA  $\epsilon_{xc}$  depends only on the magnitude of the magnetization ( $\epsilon_{xc} = \epsilon_{xc}(n, |\mathbf{m}|)$ , cf. Sec. 2.4). The environment of a point in space does not enter into the formula for the exchange energy. Hence, there is no reference to any direction and  $\epsilon_{xc}$  can only depend on  $|\mathbf{m}|$ . Therefore, the LSDA can equally be applied to collinear and non-collinear systems. The application of the LSDA to non-collinear systems is straight forward. All that needs to be done is to locally calculate  $n$ ,  $|\mathbf{m}|$  and memorize the local direction of  $\mathbf{m}$ , since the exchange correlation  $B$ -field always has the same direction as the magnetization (cf. eq. 2.22). After this step the standard parameterizations can be applied. In contrast, in the generalized gradient approximation the environment of a point in space does enter the formula for  $\epsilon_{xc}$  through the gradients of the densities. In general the gradients of  $n$ ,  $m_x$ ,  $m_y$  and  $m_z$  have to be considered. The available parameterizations are, however, developed for collinear calculations and hence consider only the gradients of the scalar quantities  $n$  and  $m$ . Therefore, these parameterizations are in principle not applicable to a non-collinear system. In practice the GGA can be used in an approximate way, because the contribution of the gradient of  $n$  is more important than the gradients of the magnetization. There are two possible quantities to feed into the parameterization in replacement of the gradient of  $m$  of a collinear calculation: (i) the gradient of the

magnitude of the magnetization vector field, (ii) the gradient of the projection of the magnetization vector field onto the local direction of the magnetization. We have chosen the first option.

All results in the present work have been obtained within the scalar relativistic approximation, i.e. the spin-orbit coupling (SOC) is neglected. This has important consequences for the symmetry groups that have to be used. The spin-orbit coupling and the dipole interaction, which is usually treated classically, are the only terms in the Hamiltonian that couples real space and spin space. Only these parts of the Hamiltonian create a relation between the spin and the spatial coordinates. When the spin-orbit coupling and the dipole interaction (both terms are of similar size in the systems under consideration) are neglected, real space and spin space can be regarded as completely independent. For this purpose generalized groups, the spin space groups (SSG), have been introduced [BE66, San91]. The action of a SSG operator  $\{\alpha_S|\alpha_R|\mathbf{t}\}$  on a two-component spinor can be defined by

$$\{\alpha_S|\alpha_R|\mathbf{t}\}\boldsymbol{\psi}(\mathbf{r}) = \mathbf{U}(\alpha_S)\boldsymbol{\psi}(\{\alpha_R|\mathbf{t}\}^{-1}\mathbf{r}) = \mathbf{U}(\alpha_S)\boldsymbol{\psi}(\alpha_R^{-1}\mathbf{r} - \alpha_R^{-1}\mathbf{t}), \quad (4.5)$$

where  $\boldsymbol{\psi}$  is a two-component spinor,  $\mathbf{U}$  is the spin 1/2 rotation matrix (cf. appendix A),  $\alpha_S$  and  $\alpha_R$  are the spin and space rotation, respectively, and  $\mathbf{t}$  is a space translation. Under the restriction  $\alpha_S = \alpha_R$  we return to the definition of the operations of the usual space group. The operators of the space group are thus a subset of the SSG operators. The condition  $\alpha_S = \alpha_R$  implies that the spin and the space coordinates are transformed in the same way. This property is required for operations that leave the Hamiltonian invariant when SOC is taken into account. The relative angle between the lattice and the spin is important in this case. However, when SOC is neglected  $\alpha_S$  and  $\alpha_R$  can be different. This is a very important feature of the SSG and it is a prerequisite for the treatment of incommensurate spin-spirals within an ab-initio calculation. A more comprehensive discussion of this topic can be found in a review article by L. M. Sandratskii [San98].

## 4.1 Constrained magnetic moments

In general, an arbitrary magnetic configuration given by a set of local (atomic) magnetization directions are not extrema of the total energy functional  $E[n(\mathbf{r}), \mathbf{m}(\mathbf{r})]$ . The exceptions are high symmetry states, like the ferromagnetic state, the antiferromagnetic state, a certain class of spin-spiral states and also some more complex non-collinear states like the Néel state of the triangular lattice. Therefore, an generalization of the density functional theory is necessary to be able to deal with arbitrary magnetic configuration, i.e. configurations where the orientations of the local moments are constrained to non-equilibrium directions. Dederichs et al. [DBZA84] extended the density functional theory to systems that are subject to arbitrary constraints. The basic idea is to minimize the energy functional enforcing the constraint condition, i.e. to find the lowest energy state compatible with the constraint. The



constraint can be taken into account by a Lagrange parameter in the energy functional. Enforcing the constraint that the direction of the average magnetic moment of atom  $\alpha$  is fixed to  $\hat{\mathbf{e}}^\alpha$  yields the energy functional

$$\begin{aligned}
\tilde{E}[n(\mathbf{r}), \mathbf{m}(\mathbf{r})|\{\hat{\mathbf{e}}^\alpha\}] &= E[n(\mathbf{r}), \mathbf{m}(\mathbf{r})] \\
&\quad + \mu_B \sum_{\alpha} \mathbf{B}_c^\alpha \cdot \left\{ \int_{MT^\alpha} \mathbf{m}(\mathbf{r}) d^3r - \hat{\mathbf{e}}^\alpha \left( \hat{\mathbf{e}}^\alpha \cdot \int_{MT^\alpha} \mathbf{m}(\mathbf{r}) d^3r \right) \right\} \\
&= E[n(\mathbf{r}), \mathbf{m}(\mathbf{r})] + \mu_B \sum_{\alpha} \mathbf{B}_c^\alpha \cdot \{ \mathbf{M}^\alpha - \mathbf{M}_{\parallel}^\alpha \} \\
&= E[n(\mathbf{r}), \mathbf{m}(\mathbf{r})] + \mu_B \sum_{\alpha} \mathbf{B}_c^\alpha \cdot \mathbf{M}_{\perp}^\alpha, \tag{4.6}
\end{aligned}$$

where  $E[n(\mathbf{r}), \mathbf{m}(\mathbf{r})]$  is the energy functional of the unconstrained system and the local (integrated) moment  $\mathbf{M}^\alpha$  and its parallel and perpendicular components,  $\mathbf{M}_{\parallel}^\alpha$  and  $\mathbf{M}_{\perp}^\alpha$ , have been introduced. Physically, the Lagrange parameter is a magnetic field. Minimizing (4.6) with respect to the wave functions yield the Kohn-Sham equations inside the muffin-tin sphere  $\alpha$ , which contain an extra contribution.

$$\left\{ -\frac{\hbar^2}{2m} \nabla^2 + V_{eff}(\mathbf{r}) + \mu_B \boldsymbol{\sigma} \cdot \mathbf{B}_{eff}(\mathbf{r}) + \mu_B \boldsymbol{\sigma} \cdot (\mathbf{B}_c^\alpha - \hat{\mathbf{e}}^\alpha (\hat{\mathbf{e}}^\alpha \cdot \mathbf{B}_c^\alpha)) \right\} \psi_i(\mathbf{r}) = \epsilon_i \psi_i(\mathbf{r}) \tag{4.7}$$

The extra term,  $\mu_B \boldsymbol{\sigma} \cdot (\mathbf{B}_c^\alpha - \hat{\mathbf{e}}^\alpha (\hat{\mathbf{e}}^\alpha \cdot \mathbf{B}_c^\alpha))$  is always perpendicular to  $\hat{\mathbf{e}}^\alpha$  so that  $\mathbf{B}_c^\alpha$  can be assumed to be perpendicular to  $\hat{\mathbf{e}}^\alpha$  without loss of generality. By means of the Hellmann-Feynman theorem the change  $dE$  of the energy due to a directional change  $d\hat{\mathbf{e}}^\alpha$  is given by the classical result

$$dE = -\mu_B M_{\parallel}^\alpha(\hat{\mathbf{e}}^\alpha) \mathbf{B}_c^\alpha(\hat{\mathbf{e}}^\alpha) \cdot d\hat{\mathbf{e}}^\alpha. \tag{4.8}$$

$M_{\parallel}^\alpha$  is the projection of the local (integrated) moment of the muffin-tin sphere  $\alpha$  onto  $\hat{\mathbf{e}}^\alpha$ ,  $M_{\parallel}^\alpha = \hat{\mathbf{e}}^\alpha \cdot \int_{MT^\alpha} \mathbf{m}(\mathbf{r}) d^3r$ . The difference vector  $d\hat{\mathbf{e}}^\alpha$  is perpendicular to  $\hat{\mathbf{e}}^\alpha$ . The factor  $\mu_B$ , which was already present in Eqn. (4.6), appears in the Hellmann-Feynman theorem because of the definition of the magnetization density and the magnetic moment. In the context of ab-initio calculations the (z-component) of the magnetization density is commonly defined as  $m_z = n_{\uparrow} - n_{\downarrow}$ , and we define the density matrix (4.1) in that spirit. However, the standard definition of the magnetization density in electrodynamic is:  $m_z = -\mu_B(n_{\uparrow} - n_{\downarrow})$ .

Demanding that the perpendicular component of the local moment  $\mathbf{M}_{\perp}^\alpha$  vanishes is not the only way to formulate a constraint to the direction of the local moment. There are several alternatives. A formulation that differs only formally from the constraint of equation 4.6 is to require that the crossproduct  $\mathbf{M}^\alpha \times \hat{\mathbf{e}}^\alpha$  vanishes.  $\mathbf{M}^\alpha \times \hat{\mathbf{e}}^\alpha$  has the same magnitude as  $\mathbf{M}_{\perp}^\alpha$  but is perpendicular to  $\mathbf{M}_{\perp}^\alpha$ . Using this constraint the additional term in the energy functional for each atom would be  $\mathbf{B}_c^\alpha \cdot (\mathbf{M}^\alpha \times \hat{\mathbf{e}}^\alpha)$ . Applying the Hellmann-Feynman theorem we find that the change of the energy is given by  $dE = -\mu_B \mathbf{M}^\alpha \cdot (\mathbf{B}_c^\alpha \times d\hat{\mathbf{e}}^\alpha)$ . Therefore, the constraint field can be interpreted as a torque acting on the magnetic moment, in the spirit of the derivation of Antropov et

al. [AKvSH95, AKH<sup>+</sup>96]. Stocks et al. [SUW<sup>+</sup>98, UWN<sup>+</sup>99] performed constrained local moment calculation, where they used the approximation that the constraint field has the same functional form as the exchange correlation  $B$ -field, rather than being a constant. Within that approximation the constraint field can be written as the exchange correlation  $B$ -field times a scaling factor  $c$ . Of course, the direction of the constraint field  $\hat{\mathbf{e}}_{\perp}^{\alpha}$  is perpendicular to  $\mathbf{B}_{xc}^{\alpha}$ , which is parallel to the local quantization axis  $\hat{\mathbf{e}}^{\alpha}$ . They write the constraint field as  $\mathbf{B}_c^{\alpha}(\mathbf{r}) = c\hat{\mathbf{e}}_{\perp}^{\alpha}B_{xc}^{\alpha}(\mathbf{r})$ , where  $B_{xc}^{\alpha}(\mathbf{r})$  is the magnitude of the exchange correlation  $B$ -field,  $\mathbf{B}_{xc}^{\alpha}(\mathbf{r}) = \hat{\mathbf{e}}_{\parallel}^{\alpha}B_{xc}^{\alpha}(\mathbf{r})$ . A much stronger constraint condition than those discussed so far would be to demand that the magnetization density  $\mathbf{m}(\mathbf{r})$  is parallel to  $\hat{\mathbf{e}}^{\alpha}$  in every point inside a muffin-tin sphere. This constraint would result in a constraint field that depends on the position in the muffin-tin.

In an actual constrained local moment (CLM) calculation  $n(\mathbf{r})$ ,  $\mathbf{m}(\mathbf{r})$  and  $\mathbf{B}_c^{\alpha}$  have to be determined self-consistently.  $n(\mathbf{r})$  and  $\mathbf{m}(\mathbf{r})$  are calculated in the usual self-consistency cycle. At the same time the local constraint fields  $\mathbf{B}_c^{\alpha}$  have to be adjusted, until the constraint condition  $\int_{MT^{\alpha}} \mathbf{m}(\mathbf{r})d^3r - \hat{\mathbf{e}}^{\alpha}(\hat{\mathbf{e}}^{\alpha} \cdot \int_{MT^{\alpha}} \mathbf{m}(\mathbf{r})d^3r) = 0$  is fulfilled. At the end of such a calculation we obtain the self-consistent densities and a set of local constraint  $B$ -fields that make the integrated magnetization perpendicular to the local spin quantization axes  $\hat{\mathbf{e}}^{\alpha}$  vanish in each muffin-tin sphere. The total energy of the system is given by the constrained energy functional (4.6). Since  $\mathbf{B}_c^{\alpha}$  is always perpendicular to  $\hat{\mathbf{e}}^{\alpha}$  the extra contribution to the total energy is  $\int_{MT^{\alpha}} \mathbf{B}_c^{\alpha} \cdot \mathbf{m}(\mathbf{r})d^3r$ . However, the effective  $B$ -field that enters the Hamiltonian in the the muffin-tin sphere of atom  $\alpha$  is given by  $\mathbf{B}_{eff}^{\alpha}(\mathbf{r}) = \mathbf{B}_{xc}^{\alpha}(\mathbf{r}) + \mathbf{B}_{ext}^{\alpha}(\mathbf{r}) + \mathbf{B}_c^{\alpha}$ . Therefore, the above contribution to the total energy cancels with the contribution of the constraint field to the kinetic energy (2.25). Thus, the constraint field does not enter the expression for the total energy (2.28) explicitly, but it enters implicitly through the eigenvalues  $\epsilon_i$  and through the self-consistent densities.

## 4.2 Spin-Spirals

A magnetic structure with moments that are rotated by a constant angle from atom to atom along a certain direction of the crystal is called a spin-spiral. This can be described by a reciprocal lattice vector, the spin-spiral vector  $\mathbf{q}$ . The rotation angle of the magnetic moment of an atom at the position  $\mathbf{R}^n$  is then given by  $\varphi = \mathbf{q} \cdot \mathbf{R}^n$ . The magnetic moment of an atom at the position  $\mathbf{R}^n$  is given by

$$\mathbf{M}^n = M(\cos(\mathbf{q} \cdot \mathbf{R}^n) \sin \vartheta, \sin(\mathbf{q} \cdot \mathbf{R}^n) \sin \vartheta, \cos \vartheta) \quad (4.9)$$

Spin-spirals are also frequently called spin density wave, or more specific spiral spin density wave, to distinguish from the longitudinal spin density waves, or frozen magnons. The origin of the last term is that a spin-spiral looks like a “snap shot” of a single magnon at a fixed time. Spin spiral calculations can therefore be used to simulate the effect of temperature on a magnetic system. In particular at very low

temperatures, when magnons with long wavelength dominate. Without the application of the generalized Bloch theorem, which I will discuss in Sec. 4.3, the investigation of such magnetic structures requires very large unit cells. Another possible application of spin-spirals is the simulation of domain walls including the calculation of the formation energy. In general, it can be said that among all possible magnetic states, besides the high-symmetry magnetic states, i.e. ferromagnetic or antiferromagnetic configurations, the spin spirals are the next class of relevant spin states. It is believed, that they cover a large and important part of the phase space of possible spin states. Though there are many possible applications for spin-spiral calculations, it was the discovery of a spiral ground state structure in fcc iron [Tsu89] and  $4f$  and  $5f$  metals [NM00] that gave rise to many theoretical studies [MLSG91, USK92].

In addition to the spin-spiral vector  $\mathbf{q}$  there are two more parameters needed to define a spin-spiral uniquely, the rotation axis and the relative angle  $\vartheta$  between the magnetic moment and the rotation axis. Fig. 4.1 shows four examples of spin-spirals with spin-rotation axis perpendicular (upper two) and parallel (lower two) to the spin-spiral vector  $\mathbf{q}$  and different angles between the spin-rotation axis and the magnetic moment. The spin-spiral vector  $\mathbf{q}$  is a vector in the real space coordinate frame, while

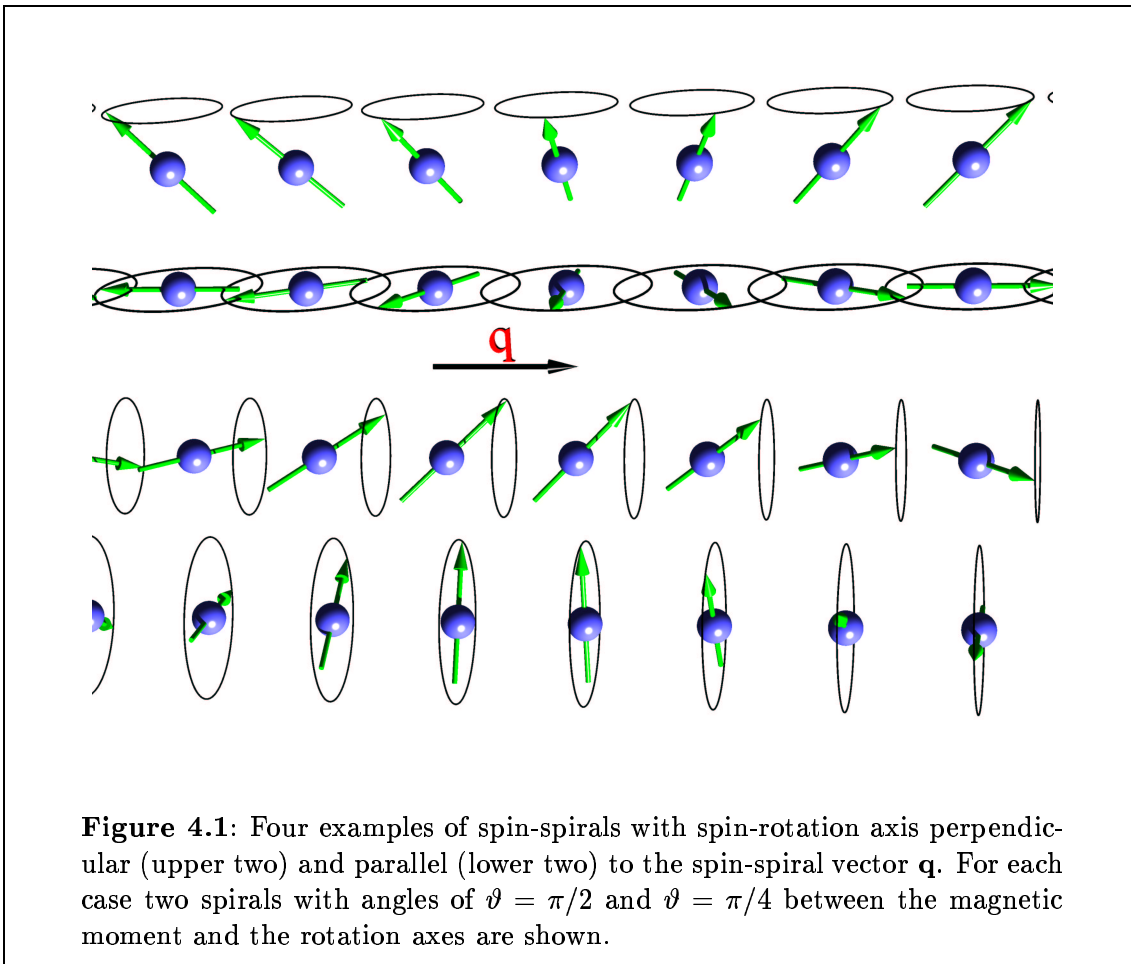


**Figure 4.1:** Four examples of spin-spirals with spin-rotation axis perpendicular (upper two) and parallel (lower two) to the spin-spiral vector  $\mathbf{q}$ . For each case two spirals with angles of  $\vartheta = \pi/2$  and  $\vartheta = \pi/4$  between the magnetic moment and the rotation axes are shown.

the spin-rotation axis is a direction (vector) in the spin-coordinate frame. Since these two coordinate frames become totally independent when spin-orbit coupling is neglected, the angle between the spin-spiral vector  $\mathbf{q}$  and the spin-rotation axis becomes meaningless. In that case the two spirals at the top and the two spirals at the bottom of Fig. 4.1 become completely equivalent. However, the spin spirals with different  $\vartheta$  do not become equivalent.  $\vartheta$  is still a well defined quantity, if SOC is neglected, because the rotation axis is a vector (direction) in spin space. In the next section it will be shown that a very elegant treatment of spin-spirals by first-principle calculations is possible when a generalized Bloch theorem [Her66, San86] is applied, that will be discussed in the next section. However, this theorem can only be proven, when SOC is neglected. For this reason the spin-rotation axis will always be considered as parallel to the z-axis of the spin-coordinate frame. Thus, only the  $m_x$  and  $m_y$  components are rotated, while  $m_z$  does not change.

### 4.3 Generalized Bloch Theorem

In the case of an incommensurate spin-spiral the periodicity with respect to lattice translations along the direction of  $\mathbf{q}$  is lost. This is a major problem for ab-initio methods that rely on the translational periodicity. However, when spin-orbit coupling is neglected all atoms of the spiral structure are equivalent. The magnitude of the magnetic moment of each atom is the same and they all “see” the same local environment, i.e. the relative angles between the local moment and the moments of the neighbors are equal. Only the angle between the local moment and the lattice changes from site to site, but that is only significant in the presence of SOC. This leads to a generalization of the Bloch Theorem[Her66, San86].

Let us consider a spin-spiral structure in a crystal without an external magnetic field and take the rotation angle  $\varphi = \mathbf{q} \cdot \mathbf{R}^n$  to be counterclockwise. The only term of the Hamiltonian that changes from site to site is the exchange correlation B-field  $\mathbf{B}_{xc}$ , i.e. the matrix potential  $\mathbf{V} = V\mathbf{I}_2 + \mu_B \boldsymbol{\sigma} \cdot \mathbf{B}_{xc}$ . Hence, the Hamiltonian satisfies the relation

$$\mathcal{H}(\mathbf{r} + \mathbf{R}^n) = \mathbf{U}(\mathbf{q}\mathbf{R}^n)\mathcal{H}(\mathbf{r})\mathbf{U}^\dagger(\mathbf{q}\mathbf{R}^n). \quad (4.10)$$

As pointed out in the previous section the rotation axis can always be taken to be along the spin z-axis. Thus, the spin 1/2 rotation matrix (cf. appendix A) has the form

$$\mathbf{U}(\mathbf{q}\mathbf{R}^n) = \begin{pmatrix} e^{-i\varphi/2} & 0 \\ 0 & e^{i\varphi/2} \end{pmatrix}, \quad \varphi = \mathbf{q} \cdot \mathbf{R}^n. \quad (4.11)$$

Keeping these properties of the Hamiltonian in mind we can define a generalized translation,  $\mathcal{T}_n = \{-\mathbf{q}\mathbf{R}^n | \epsilon | \mathbf{R}^n\}$ , that combines a lattice translation and a spin rotation. Here  $\epsilon$  denotes the identity operation. These translations are members of the SSG but not of the usual space group, since the rotation in spin space differs from the rotation in real space. Applying a generalized translation to  $\mathcal{H}\psi$  yields

$$\mathcal{T}_n \mathcal{H}(\mathbf{r})\psi(\mathbf{r}) = \mathbf{U}(-\mathbf{q}\mathbf{R}^n)\mathcal{H}(\mathbf{r} + \mathbf{R}^n)\mathbf{U}^\dagger(-\mathbf{q}\mathbf{R}^n)\mathbf{U}(-\mathbf{q}\mathbf{R}^n)\psi(\mathbf{r} + \mathbf{R}^n)$$

$$= \mathcal{H}(\mathbf{r})\mathbf{U}(-\mathbf{q}\mathbf{R}^n)\psi(\mathbf{r} + \mathbf{R}^n). \quad (4.12)$$

Thus, the generalized translation commutes with the Hamiltonian:

$$\mathcal{T}_n\mathcal{H} = \mathcal{H}\mathcal{T}_n \quad (4.13)$$

It can be shown that the generalized translation operations satisfy the relation

$$\mathcal{T}_n\mathcal{T}_m = \mathcal{T}_m\mathcal{T}_n = \mathcal{T}_{n+m} \quad (4.14)$$

In analogy with the proof of Bloch's theorem in the textbook by Ashcroft and Mermin [AM76] it follows that the eigenstates can be chosen such that

$$\mathcal{T}_n\psi(\mathbf{k}, \mathbf{r}) = \mathbf{U}(-\mathbf{q}\mathbf{R}^n)\psi(\mathbf{k}, \mathbf{r} + \mathbf{R}^n) = e^{i\mathbf{k}\cdot\mathbf{R}^n}\psi(\mathbf{k}, \mathbf{r}). \quad (4.15)$$

This formulation of the generalized Bloch Theorem is equivalent to the statement that the eigenstates of the Hamiltonian can be written in the form

$$\psi(\mathbf{k}, \mathbf{r}) = e^{i\mathbf{k}\cdot\mathbf{r}} \begin{pmatrix} e^{-i\mathbf{q}\cdot\mathbf{r}/2}\alpha(\mathbf{k}, \mathbf{r}) \\ e^{+i\mathbf{q}\cdot\mathbf{r}/2}\beta(\mathbf{k}, \mathbf{r}) \end{pmatrix}, \quad (4.16)$$

where  $\alpha(\mathbf{k}, \mathbf{r})$  and  $\beta(\mathbf{k}, \mathbf{r})$  are functions with translational periodicity, e.g.  $\alpha(\mathbf{k}, \mathbf{r}) = \alpha(\mathbf{k}, \mathbf{r} + \mathbf{R}^n)$ . We will prove the equivalence of (4.15) and (4.16) in two steps.

(i) (4.16)  $\Rightarrow$  (4.15)

$$\begin{aligned} \mathcal{T}_n\psi(\mathbf{k}, \mathbf{r}) &= \begin{pmatrix} e^{i\mathbf{q}\cdot\mathbf{R}^n/2} & 0 \\ 0 & e^{-i\mathbf{q}\cdot\mathbf{R}^n/2} \end{pmatrix} e^{i\mathbf{k}\cdot(\mathbf{r}+\mathbf{R}^n)} \begin{pmatrix} e^{-i\mathbf{q}\cdot(\mathbf{r}+\mathbf{R}^n)/2}\alpha(\mathbf{k}, \mathbf{r} + \mathbf{R}^n) \\ e^{+i\mathbf{q}\cdot(\mathbf{r}+\mathbf{R}^n)/2}\beta(\mathbf{k}, \mathbf{r} + \mathbf{R}^n) \end{pmatrix} \\ &= e^{i\mathbf{k}\cdot\mathbf{R}^n}\psi(\mathbf{k}, \mathbf{r}) \end{aligned} \quad (4.17)$$

(ii) (4.15)  $\Rightarrow$  (4.16)  $\alpha$  and  $\beta$  can always be defined to be

$$\alpha(\mathbf{k}, \mathbf{r}) = \frac{\psi_1(\mathbf{k}, \mathbf{r})}{e^{i(\mathbf{k}-\mathbf{q}/2)\cdot\mathbf{r}}}, \quad \beta(\mathbf{k}, \mathbf{r}) = \frac{\psi_2(\mathbf{k}, \mathbf{r})}{e^{i(\mathbf{k}+\mathbf{q}/2)\cdot\mathbf{r}}}, \quad (4.18)$$

where  $\psi_1$  and  $\psi_2$  are the two components of the spinor  $\psi$ . Now it remains to be proven that  $\alpha$  and  $\beta$  are periodic. Starting from (4.15) we find

$$\begin{aligned} &\begin{pmatrix} e^{i\mathbf{q}\cdot\mathbf{R}^n/2} & 0 \\ 0 & e^{-i\mathbf{q}\cdot\mathbf{R}^n/2} \end{pmatrix} \begin{pmatrix} e^{i(\mathbf{k}-\mathbf{q}/2)\cdot(\mathbf{r}+\mathbf{R}^n)}\alpha(\mathbf{k}, \mathbf{r} + \mathbf{R}^n) \\ e^{i(\mathbf{k}+\mathbf{q}/2)\cdot(\mathbf{r}+\mathbf{R}^n)}\beta(\mathbf{k}, \mathbf{r} + \mathbf{R}^n) \end{pmatrix} = \\ &e^{i\mathbf{k}\cdot\mathbf{R}^n} \begin{pmatrix} e^{i(\mathbf{k}-\mathbf{q}/2)\cdot\mathbf{r}}\alpha(\mathbf{k}, \mathbf{r} + \mathbf{R}^n) \\ e^{i(\mathbf{k}+\mathbf{q}/2)\cdot\mathbf{r}}\beta(\mathbf{k}, \mathbf{r} + \mathbf{R}^n) \end{pmatrix} \\ \Rightarrow &e^{i\mathbf{k}\cdot\mathbf{R}^n} \begin{pmatrix} e^{i(\mathbf{k}-\mathbf{q}/2)\cdot\mathbf{r}}\alpha(\mathbf{k}, \mathbf{r} + \mathbf{R}^n) \\ e^{i(\mathbf{k}+\mathbf{q}/2)\cdot\mathbf{r}}\beta(\mathbf{k}, \mathbf{r} + \mathbf{R}^n) \end{pmatrix} = e^{i\mathbf{k}\cdot\mathbf{R}^n} \begin{pmatrix} e^{i(\mathbf{k}-\mathbf{q}/2)\cdot\mathbf{r}}\alpha(\mathbf{k}, \mathbf{r}) \\ e^{i(\mathbf{k}+\mathbf{q}/2)\cdot\mathbf{r}}\beta(\mathbf{k}, \mathbf{r}) \end{pmatrix} \\ \Rightarrow &\alpha(\mathbf{k}, \mathbf{r} + \mathbf{R}^n) = \alpha(\mathbf{k}, \mathbf{r}), \quad \beta(\mathbf{k}, \mathbf{r} + \mathbf{R}^n) = \beta(\mathbf{k}, \mathbf{r}). \end{aligned} \quad (4.19)$$

The fact that  $\alpha$  and  $\beta$  are periodic functions is very important for the implementation of the spin-spiral into the FLAPW method. The FLAPW method relies on plane wave expansions and Fourier Transforms. Therefore, it is necessary to formulate the theory in terms of periodic functions.

## Chapter 5

# Implementation of Non-Collinear Magnetism into FLAPW

The first non-collinear ab-initio calculations for a periodic solid were performed using the Korringa-Kohn-Rostoker (KKR) method [SG86, SG89] and the Augmented Spherical Wave (ASW) methods [KHSW88a, KHSW88b, SHK89]. Later calculations used the Linear Muffin Tin Orbital (LMTO) [MLSG91, MLSG92] method. All of these methods have one common feature, they use cells (spheres) around each atom. Every point in space can thus be associated uniquely with an atom. The implementation of non-collinear magnetism is done in a way that allows only one direction of magnetization per atom, i.e. the direction of the magnetization density  $\mathbf{m}$  is not allowed to change within one sphere, but varies only from sphere to sphere. Nevertheless, the magnitude of the magnetization density can change within a cell.

$$\mathbf{m}(\mathbf{r}) = m(\mathbf{r} - \mathbf{p}^\alpha)\hat{\mathbf{e}}^\alpha \quad (5.1)$$

Here  $\mathbf{p}^\alpha$  is the position of the atom  $\alpha$  and  $\hat{\mathbf{e}}^\alpha$  is the direction of the local magnetization. We call this the atomic sphere approximation for the direction of magnetization. It agrees with the intuitive picture that each atom carries a magnetic moment and these moments differ between the atoms. Such methods describe only the inter-atomic non-collinearity. However, in general the direction of the magnetization changes continuously from site to site, though, in many cases, the deviations from the main atomic direction are only significant in a region between the atom, where the magnitude of the magnetization is rather small. The first calculation that treated the magnetization as a continuous vector quantity was published by Nordström et al. [NS96]. They followed the most general approach allowing the magnetization to change magnitude and direction continuously, i.e. even within an atom. Thus, their implementation, that is based on the FLAPW method, allows them to also investigate the intra-atomic non-collinearity.

We are interested in the non-collinear magnetism of  $3d$  transition metals at surfaces and in open structures. The intra-atomic non-collinearity is expected to be small for these systems and we are mainly interested in the inter-atomic non-collinear

magnetism. However, it is difficult to use a pure inter-atomic treatment of the non-collinearity in the FLAPW method due to the representation of the magnetization within the FLAPW method. In the interstitial and the vacuum region the potential and the magnetization are expanded into plane waves. Points that lie in these regions cannot be assigned to an atom uniquely. Therefore, the magnetization is treated as a continuous vector field in the interstitial and in the vacuum regions, while inside each muffin-tin sphere we only allow for one direction of magnetization. This “hybrid” approach is illustrated schematically in figure 5.1. The ratio of the volume

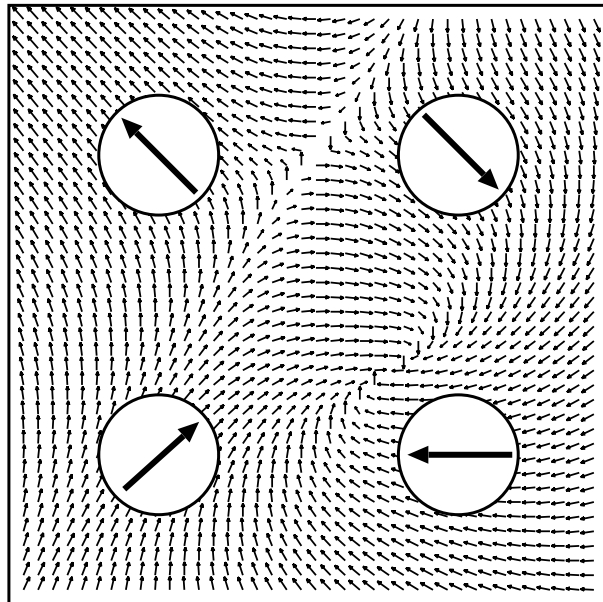


**Figure 5.1:** Schematic illustration of the representation of the non-collinear magnetization density within the present approach. The magnetization is treated as a continuous vector field in the interstitial region and in the vacuum. Within each muffin-tin the magnetization has a fixed direction and can only vary in magnitude. For a better illustration the muffin-tins have been chosen much smaller than in actual calculations.

in which the magnetization is treated as a continuous vector field and the volume of the muffin-tins, in which the atomic sphere approximation of the magnetization direction is applied, can be changed by changing the muffin-tin radius. We performed non-collinear calculations with different muffin-tin radii to investigate the validity of this approximation. The result of these test calculations are discussed in Sec. 5.4.2 (Fig. 5.4) and 6.3.3. The method can be extended to full vector field treatment of the magnetization density everywhere in space. To achieve this it would be necessary to calculate the components of the magnetization that are not parallel to the local

quantization axis of an atom and to include the corresponding components of the  $B$ -field into the Hamiltonian. If that was done the implementation would still differ from that of Nordström[NS96], because Nordström uses different basis functions in the muffin-tin.

The FLAPW method for collinear calculation uses two sets of radial basis functions inside the muffin-tin spheres, one for each spin direction. For each spin direction they are set up using the spherical part of the corresponding potential,  $V_{\uparrow}$  or  $V_{\downarrow}$ , and the corresponding energy parameter,  $E_{I\uparrow}$  or  $E_{I\downarrow}$ . It is still possible to work with  $V_{\uparrow}$  and  $V_{\downarrow}$  in the non-collinear case, since we restrict the magnetization to the local quantization axis. Therefore, a local spin-space coordinate-frame is introduced with the  $z$ -axis parallel to the local quantization axis.  $V_{\uparrow}$  and  $V_{\downarrow}$  are now spin-up and -down with respect to the local axis. Since both, the potential and the basis functions, are set up in terms of the local spin-coordinate frame, the determination of the basis functions and calculation of the integrals of these functions with the Hamiltonian inside the muffin-tins is completely unchanged. The changes come in, when the basis functions inside the muffin-tins are matched to the plane waves in the interstitial region, because the local spin-coordinate frame  $S^{\alpha}$  is rotated with respect to the global frame  $S^g$ . Finally, it is important to realize that these rotations are only applied to the direction of the magnetization, i.e. the spin space. The real space is not affected at all by the rotations. In particular, no rotation has to be applied to the coordinate  $\mathbf{r}$  or the spherical harmonics  $Y_L$ .

## 5.1 Setup of the Hamiltonian Matrix

The FLAPW method uses augmented plane waves as basis functions. Therefore, each basis function can be uniquely identified by its wave vector  $\mathbf{G}$  and the spin direction. The basis functions in the interstitial region are:

$$e^{i(\mathbf{k}+\mathbf{G})\mathbf{r}}\chi_{\sigma}^g \quad (5.2)$$

$\chi_{\sigma}^g$  is a two component spinor. The index  $g$  has been added to notify that  $\chi_{\sigma}^g$  is the representation of this spinor in the global spin frame (cf. appendix A). This representation of the basis functions is used for both collinear and non-collinear calculations. However, the potential matrix  $\mathbf{V}$ , and thus the Hamiltonian, is diagonal in the two spin directions in the collinear case. Therefore, the Hamiltonian can be set up and solved separately for the two spin directions. In the non-collinear case the off-diagonal part of  $\mathbf{V}$  is not zero anymore. Hence, the full Hamiltonian for both spin directions has to be set up and solved in a single step. In the vacuum we also use the global spin frame for the representation of the basis functions. The basis set is only changed in the muffin-tins, because we use a local spin coordinate frame, which is rotated with respect to the global frame. The consequence is that, when the plane waves are matched to the functions in the muffin tin spheres, each spin direction in the interstitial region has to be matched to both, the spin-up and -down



basis functions, in the sphere. Thus, the basis set has the following form.

$$\varphi_{\mathbf{G},\sigma}(\mathbf{k}, \mathbf{r}) = \begin{cases} e^{i(\mathbf{G}+\mathbf{k})\mathbf{r}} \chi_{\sigma}^g & \text{Int.} \\ \left( A_{\sigma}^{\mathbf{G}}(\mathbf{k}_{\parallel}) u_{\sigma}^{\mathbf{G}}(\mathbf{k}_{\parallel}, z) + B_{\sigma}^{\mathbf{G}}(\mathbf{k}_{\parallel}) \dot{u}_{\sigma}^{\mathbf{G}}(\mathbf{k}_{\parallel}, z) \right) e^{i(\mathbf{G}_{\parallel}+\mathbf{k}_{\parallel})\mathbf{r}_{\parallel}} \chi_{\sigma}^g & \text{Vac.} \\ \sum_{\sigma^{\alpha}} \sum_L \left( A_{L\sigma\sigma^{\alpha}}^{\mu\mathbf{G}}(\mathbf{k}) u_l(r) + B_{L\sigma\sigma^{\alpha}}^{\mu\mathbf{G}}(\mathbf{k}) \dot{u}_l(r) \right) Y_L(\hat{\mathbf{r}}) \chi_{\sigma^{\alpha}} & \text{MT}\mu \end{cases} \quad (5.3)$$

The sum in the muffin-tins is over the local spin directions. The  $A$ - and  $B$ -coefficients depend on the local and the global spin.

The global spin-coordinate frame  $S^g$  can be transformed into the local frame by a rotation, given by the Euler angles  $(\alpha, \beta, 0)$ . In this case, the Euler angles are equivalent to the polar angles of the local quantization axis in the global frame,  $\alpha = \varphi$ ,  $\beta = \vartheta$ . The magnetization density and the magnetic field, seen from the global frame,  $\mathbf{m}^{\alpha g}(\mathbf{r})$  and  $\mathbf{B}^{\alpha g}(\mathbf{r})$ , are related to the same quantities seen from the local frame by

$$\begin{aligned} \mathbf{m}^{\alpha g}(\mathbf{r}) &= \mathbf{R}^{\alpha g l} \mathbf{m}^{\alpha l}(\mathbf{r}) \\ \mathbf{B}^{\alpha g}(\mathbf{r}) &= \mathbf{R}^{\alpha g l} \mathbf{B}^{\alpha l}(\mathbf{r}). \end{aligned} \quad (5.4)$$

where the index  $\alpha$  indicates, that this corresponds to quantities inside the muffin-tin of atom type  $\alpha$ . The Pauli spinors transform according to

$$\chi^{\alpha g} = \mathbf{U}^{\alpha g l} \chi^{\alpha l}. \quad (5.5)$$

The matrices  $\mathbf{R}^{\alpha g l}$  and  $\mathbf{U}^{\alpha g l}$  are explained in appendix A, p. 189, on coordinate frame transformations, which also contains our definition of the Euler angles.

In the collinear case the radial functions  $u_{l\sigma}^{\alpha}$  and  $\dot{u}_{l\sigma}^{\alpha}$ <sup>1</sup> are determined as solutions of the radial Schrödinger (scalar-relativistic) Eqn. (3.2) (3.41), including the spin-dependent potential  $V_{\sigma}$ . Thus, the basis functions inside the muffin-tins are linear combinations of

$$\begin{aligned} u_{l\uparrow}^{\alpha}(r) Y_L(\hat{\mathbf{r}}) \chi_{\uparrow}^{\alpha}, & \quad \dot{u}_{l\uparrow}^{\alpha}(r) Y_L(\hat{\mathbf{r}}) \chi_{\uparrow}^{\alpha}, \\ u_{l\downarrow}^{\alpha}(r) Y_L(\hat{\mathbf{r}}) \chi_{\downarrow}^{\alpha}, & \quad \dot{u}_{l\downarrow}^{\alpha}(r) Y_L(\hat{\mathbf{r}}) \chi_{\downarrow}^{\alpha}, \end{aligned} \quad (5.6)$$

where  $L$  abbreviates  $lm$ , and

$$\chi_{\uparrow}^{\alpha l} = \begin{pmatrix} 1 \\ 0 \end{pmatrix}, \quad \chi_{\downarrow}^{\alpha l} = \begin{pmatrix} 0 \\ 1 \end{pmatrix}. \quad (5.7)$$

Afterwards, the spin-dependent  $t$ -matrices (3.61 – 3.64) are calculated. This whole procedure remains completely unchanged in the non-collinear case, with the only difference, that spin-up and -down means up and down in terms of the local quantization

---

<sup>1</sup>The radial functions are denoted  $u$  only for convenience. In the actual calculations the scalar-relativistic approximation is employed, and therefore the large component of the radial function is used here.

axis. Consequently, the muffin-tin basis set becomes

$$\begin{aligned} u_{i\uparrow}^\alpha(r) Y_L(\hat{\mathbf{r}}) \chi_{i\uparrow}^{\alpha g}, & \quad \dot{u}_{i\uparrow}^\alpha(r) Y_L(\hat{\mathbf{r}}) \chi_{i\uparrow}^{\alpha g}, \\ u_{i\downarrow}^\alpha(r) Y_L(\hat{\mathbf{r}}) \chi_{i\downarrow}^{\alpha g}, & \quad \dot{u}_{i\downarrow}^\alpha(r) Y_L(\hat{\mathbf{r}}) \chi_{i\downarrow}^{\alpha g}, \end{aligned} \quad (5.8)$$

with

$$\chi_{i\uparrow}^{\alpha g} = \mathbf{U}^{\alpha g l} \chi_{i\uparrow}^{\alpha l} = \begin{pmatrix} e^{-\frac{i\alpha}{2}} \cos(\frac{\beta}{2}) \\ e^{\frac{i\alpha}{2}} \sin(\frac{\beta}{2}) \end{pmatrix}, \quad \chi_{i\downarrow}^{\alpha g} = \mathbf{U}^{\alpha g l} \chi_{i\downarrow}^{\alpha l} = \begin{pmatrix} -e^{-\frac{i\alpha}{2}} \sin(\frac{\beta}{2}) \\ e^{\frac{i\alpha}{2}} \cos(\frac{\beta}{2}) \end{pmatrix}. \quad (5.9)$$

The next step is to connect the plane waves, representing the basis functions in the interstitial region, to the muffin-tin basis, with the aim of forming a set of continuous and differentiable basis functions. In the collinear case the plane waves with spin  $\sigma$  are connected to the muffin-tin basis functions with the same spin only. Hence, the boundary conditions that have to be satisfied on the muffin-tin sphere are:

$$e^{i(\mathbf{k}+\mathbf{G})\mathbf{r}} \chi_\sigma = \sum_L \left( A_{L\sigma}^{\mu\mathbf{G}}(\mathbf{k}) u_{l\sigma}^\alpha(r) + B_{L\sigma}^{\mu\mathbf{G}}(\mathbf{k}) \dot{u}_{l\sigma}^\alpha(r) \right) Y_L(\hat{\mathbf{r}}) \chi_\sigma \quad (5.10)$$

In the non-collinear case each function in the interstitial couples to both, spin-up and -down, in the muffin-tins. Therefore, the boundary conditions become:

$$e^{i(\mathbf{k}+\mathbf{G})\mathbf{r}} \chi_\sigma = \sum_{\sigma^\alpha} \sum_L \left( A_{L\sigma\sigma^\alpha}^{\mu\mathbf{G}}(\mathbf{k}) u_{l\sigma^\alpha}^\alpha(r) + B_{L\sigma\sigma^\alpha}^{\mu\mathbf{G}}(\mathbf{k}) \dot{u}_{l\sigma^\alpha}^\alpha(r) \right) Y_L(\hat{\mathbf{r}}) \chi_{\sigma^\alpha}^{\alpha g} \quad (5.11)$$

In order to calculate the  $A$  and  $B$ -coefficients, we multiply equation 5.11 with  $(\chi_{i\uparrow}^{\alpha g})^*$  or  $(\chi_{i\downarrow}^{\alpha g})^*$ , which yields

$$e^{i(\mathbf{k}+\mathbf{G})\mathbf{r}} (\chi_{\sigma^\alpha}^{\alpha g})^* \chi_\sigma = \sum_L \left( A_{L\sigma\sigma^\alpha}^{\mu\mathbf{G}}(\mathbf{k}) u_{l\sigma^\alpha}^\alpha(r) + B_{L\sigma\sigma^\alpha}^{\mu\mathbf{G}}(\mathbf{k}) \dot{u}_{l\sigma^\alpha}^\alpha(r) \right) Y_L(\hat{\mathbf{r}}). \quad (5.12)$$

Comparing this equation with Eqn. (5.10) shows, that the non-collinear  $A$ - and  $B$ -coefficients can be expressed in terms of the collinear coefficients.

$$\begin{aligned} A_{L\sigma\sigma^\alpha}^{\mu\mathbf{G}}(\mathbf{k}) &= (\chi_{\sigma^\alpha}^{\alpha g})^* \chi_\sigma A_{L\sigma}^{\mu\mathbf{G}}(\mathbf{k}) \\ B_{L\sigma\sigma^\alpha}^{\mu\mathbf{G}}(\mathbf{k}) &= (\chi_{\sigma^\alpha}^{\alpha g})^* \chi_\sigma B_{L\sigma}^{\mu\mathbf{G}}(\mathbf{k}) \end{aligned} \quad (5.13)$$

Similarly, the contribution of the muffin-tin of atom  $\mu$   $H_{MT^\mu}^{\mathbf{G}'\sigma'\mathbf{G}\sigma}(\mathbf{k})$  to the non-collinear Hamiltonian  $H^{\mathbf{G}'\sigma'\mathbf{G}\sigma}(\mathbf{k})$  can be expressed in term of the muffin-tin contribution  $H_{MT^\mu\sigma}^{\mathbf{G}'\mathbf{G}}(\mathbf{k})$  to the collinear spin-dependent Hamiltonian  $H_\sigma^{\mathbf{G}'\mathbf{G}}(\mathbf{k})$ .

$$\begin{aligned} H_{MT^\mu\sigma}^{\mathbf{G}'\mathbf{G}}(\mathbf{k}) &= \int_{MT^\mu} \left( \sum_{L'} \left( A_{L'\sigma}^{\mu\mathbf{G}'}(\mathbf{k}) u_{l'\sigma}^\alpha(r) + B_{L'\sigma}^{\mu\mathbf{G}'}(\mathbf{k}) \dot{u}_{l'\sigma}^\alpha(r) \right) Y_{L'}(\hat{\mathbf{r}}) \chi_\sigma \right)^* \mathcal{H}_{MT^\mu\sigma} \\ &\quad \left( \sum_L \left( A_{L\sigma}^{\mu\mathbf{G}}(\mathbf{k}) u_{l\sigma}^\alpha(r) + B_{L\sigma}^{\mu\mathbf{G}}(\mathbf{k}) \dot{u}_{l\sigma}^\alpha(r) \right) Y_L(\hat{\mathbf{r}}) \chi_\sigma \right) d^3r \end{aligned} \quad (5.14)$$

In the non-collinear case an additional summation over the local spin  $\sigma^\alpha$  has to be performed.

$$\begin{aligned}
H_{MT^\mu}^{\mathbf{G}'\sigma'\mathbf{G}\sigma}(\mathbf{k}) = & \int_{MT^\mu} \left( \sum_{\sigma^{\alpha'}} \sum_{L'} \left( A_{L'\sigma'\sigma^{\alpha'}}^{\mu\mathbf{G}'}(\mathbf{k}) u_{l'\sigma^{\alpha'}}^\alpha(r) + B_{L'\sigma'\sigma^{\alpha'}}^{\mu\mathbf{G}'}(\mathbf{k}) \dot{u}_{l'\sigma^{\alpha'}}^\alpha(r) \right) Y_{L'}(\hat{\mathbf{r}}) \chi_{\sigma^{\alpha'}}^{\alpha g} \right)^* \mathcal{H}_{MT^\mu} \\
& \left( \sum_{\sigma^\alpha} \sum_L \left( A_{L\sigma\sigma^\alpha}^{\mu\mathbf{G}}(\mathbf{k}) u_{l\sigma^\alpha}^\alpha(r) + B_{L\sigma\sigma^\alpha}^{\mu\mathbf{G}}(\mathbf{k}) \dot{u}_{l\sigma^\alpha}^\alpha(r) \right) Y_L(\hat{\mathbf{r}}) \chi_{\sigma^\alpha}^{\alpha g} \right) d^3 r \quad (5.15)
\end{aligned}$$

However,  $\mathcal{H}_{MT^\mu}$  is diagonal in  $\chi_{\sigma^\alpha}^{\alpha g}$ , and  $(\chi_{\sigma^{\alpha'}}^{\alpha g})^* \chi_{\sigma^\alpha}^{\alpha g} = \delta_{\sigma^{\alpha'}\sigma^\alpha}$ . Hence, 5.15 becomes:

$$\begin{aligned}
H_{MT^\mu}^{\mathbf{G}'\sigma'\mathbf{G}\sigma}(\mathbf{k}) = & \sum_{\sigma^\alpha} \int_{MT^\mu} \left( \sum_{L'} \left( A_{L'\sigma'\sigma^\alpha}^{\mu\mathbf{G}'}(\mathbf{k}) u_{l'\sigma^\alpha}^\alpha(r) + B_{L'\sigma'\sigma^\alpha}^{\mu\mathbf{G}'}(\mathbf{k}) \dot{u}_{l'\sigma^\alpha}^\alpha(r) \right) Y_{L'}(\hat{\mathbf{r}}) \chi_{\sigma^\alpha}^{\alpha g} \right)^* \mathcal{H}_{MT^\mu} \\
& \left( \sum_L \left( A_{L\sigma\sigma^\alpha}^{\mu\mathbf{G}}(\mathbf{k}) u_{l\sigma^\alpha}^\alpha(r) + B_{L\sigma\sigma^\alpha}^{\mu\mathbf{G}}(\mathbf{k}) \dot{u}_{l\sigma^\alpha}^\alpha(r) \right) Y_L(\hat{\mathbf{r}}) \chi_{\sigma^\alpha}^{\alpha g} \right) d^3 r \quad (5.16)
\end{aligned}$$

Using 5.13 and the fact that  $(\chi_{\sigma^\alpha}^{\alpha g})^* \mathcal{H}_{MT^\mu} \chi_{\sigma^\alpha}^{\alpha g} = H_{MT^\mu\sigma^\alpha}^{\mathbf{G}'\mathbf{G}}(\mathbf{k})$  5.16 simplifies to:

$$H_{MT^\mu}^{\mathbf{G}'\sigma'\mathbf{G}\sigma}(\mathbf{k}) = \sum_{\sigma^\alpha} ((\chi_{\sigma^\alpha}^{\alpha g})^* \chi_{\sigma'})^* (\chi_{\sigma^\alpha}^{\alpha g})^* \chi_{\sigma} H_{MT^\mu\sigma^\alpha}^{\mathbf{G}'\mathbf{G}}(\mathbf{k}) \quad (5.17)$$

In complete analogy the muffin-tin contribution to the non-collinear overlap-matrix is given by:

$$S_{MT^\mu}^{\mathbf{G}'\sigma'\mathbf{G}\sigma}(\mathbf{k}) = \sum_{\sigma^\alpha} ((\chi_{\sigma^\alpha}^{\alpha g})^* \chi_{\sigma'})^* (\chi_{\sigma^\alpha}^{\alpha g})^* \chi_{\sigma} S_{MT^\mu\sigma^\alpha}^{\mathbf{G}'\mathbf{G}}(\mathbf{k}) \quad (5.18)$$

In the interstitial and vacuum region we work within the global spin coordinate frame. Hence, the Hamiltonian matrix can be set up directly according to

$$H^{\mathbf{G}'\sigma'\mathbf{G}\sigma} = \int \varphi_{\mathbf{G},\sigma}^* \left\{ -\frac{\hbar^2}{2m} \nabla^2 \mathbf{I}_2 + \mathbf{V} \right\} \varphi_{\mathbf{G},\sigma} d^3 r \quad (5.19)$$

Because the basis functions are either pure spin-up or spin-down in the interstitial and the vacuum the contribution to the overlap matrix and the contribution of the kinetic energy term to the Hamiltonian matrix are diagonal in spin. Thus, the only quantity that needs to be calculated in a non-collinear calculation which is not needed in the collinear case is the integral of the basis function with the off-diagonal elements of the potential matrix. However, that integration can be performed in exactly the same way as the integrals including the diagonal parts of the potential matrix, with the sole difference that the off-diagonal part is in general a complex quantity.

In the interstitial region the step function that ‘‘cuts out’’ the muffin-tin spheres has to be taken into account (cf. Sec. 3.3.3). The product of the step function with the potential matrix is calculated separately for each part of the potential matrix.

The procedure of calculating  $(V\Theta)_{\mathbf{G}\sigma\sigma'}$  is precisely the same as described in Sec. 3.3.3. Once  $(V\Theta)_{\mathbf{G}\sigma\sigma'}$  is calculated the Hamiltonian and overlap matrix are given by

$$\begin{aligned} H_{INT}^{\mathbf{G}\sigma\mathbf{G}'\sigma'}(\mathbf{k}) &= (V_{\sigma\sigma'}\Theta)_{(\mathbf{G}-\mathbf{G}')} + \delta_{\sigma\sigma'} \frac{\hbar^2}{2m} (\mathbf{G}' + \mathbf{k})^2 \Theta_{(\mathbf{G}-\mathbf{G}')} \\ S_{INT}^{\mathbf{G}\sigma\mathbf{G}'\sigma'} &= \delta_{\sigma\sigma'} \Theta_{(\mathbf{G}-\mathbf{G}')} \end{aligned} \quad (5.20)$$

In contrast to the muffin-tin the vacuum basis functions couple only to one spin direction in the interstitial region, because they are set up in terms of the global spin frame. In addition to the spin diagonal parts, integrals of the form (cf. 3.96)

$$I_{\mathbf{G}_{\parallel}\mathbf{G}'_{\parallel}\mathbf{G}''_{\parallel}}^{uu\sigma\sigma'}(\mathbf{k}_{\parallel}) = \int u_{\mathbf{G}_{\parallel}\sigma}(\mathbf{k}_{\parallel}, z) u_{\mathbf{G}'_{\parallel}\sigma'}(\mathbf{k}_{\parallel}, z) V_{\mathbf{G}''_{\parallel}\sigma\sigma'}(z) dz, \quad \dots \quad (5.21)$$

that also take into account the off-diagonal part of the potential matrix have to be calculated. The t-matrices (cf. 3.92) become

$$t_{\mathbf{G}_{\parallel}\mathbf{G}'_{\parallel}}^{uu\sigma\sigma'}(\mathbf{k}_{\parallel}) = I_{\mathbf{G}_{\parallel}\mathbf{G}'_{\parallel}(\mathbf{G}_{\parallel}-\mathbf{G}'_{\parallel})}^{uu\sigma\sigma'}(\mathbf{k}_{\parallel}) + \delta_{\mathbf{G}_{\parallel}\mathbf{G}'_{\parallel}} \delta_{\sigma\sigma'} E_{vac,\sigma}, \quad \dots \quad (5.22)$$

Finally, the Hamiltonian and overlap (cf. 3.100) matrix are given by

$$\begin{aligned} H_V^{\mathbf{G}\sigma\mathbf{G}'\sigma'}(\mathbf{k}_{\parallel}) &= (A_{\mathbf{G}\sigma}(\mathbf{k}_{\parallel}))^* t_{\mathbf{G}_{\parallel}\mathbf{G}'_{\parallel}}^{uu\sigma\sigma'}(\mathbf{k}_{\parallel}) A_{\mathbf{G}'\sigma'}(\mathbf{k}_{\parallel}) + \dots \\ S_V^{\mathbf{G}\sigma\mathbf{G}'\sigma'}(\mathbf{k}_{\parallel}) &= (A_{\mathbf{G}\sigma}(\mathbf{k}_{\parallel}))^* A_{\mathbf{G}'\sigma'}(\mathbf{k}_{\parallel}) \delta_{\mathbf{G}_{\parallel}\mathbf{G}'_{\parallel}} \delta_{\sigma\sigma'} + \dots \end{aligned} \quad (5.23)$$

## 5.2 Construction of the Charge and Magnetization Density

From solving generalized eigenvalue problem (cf. Sec. 3.1.4) including the full Hamiltonian and overlap matrix for both spin direction we obtain the eigenstates of the non-collinear system. The eigenstates are given in terms of the basis functions (5.3).

$$\psi_{\nu}(\mathbf{k}, \mathbf{r}) = \sum_{\sigma} \sum_{\mathbf{G}} c_{\nu,\sigma}^{\mathbf{G}}(\mathbf{k}) \varphi_{\mathbf{G},\sigma}(\mathbf{k}, \mathbf{r}) \quad (5.24)$$

Now the density matrix has to be determined from the eigenstates. In the interstitial and vacuum region, where we work within the global spin frame, this is done according to eqn. 4.3. In addition to the diagonal elements of the density matrix that are needed in a collinear calculation we now also have to calculate the off-diagonal element  $\rho_{21} = \rho_{12}^*$ . In the interstitial region (3.162) has to be generalized to

$$\rho_{\nu,\alpha\beta}^{\mathbf{G}}(\mathbf{k}) = \sum_{\mathbf{G}'} (c_{\nu,\alpha}^{\mathbf{G}'}(\mathbf{k}))^* c_{\nu,\beta}^{(\mathbf{G}+\mathbf{G}')}(\mathbf{k}). \quad (5.25)$$

As in a collinear calculation (cf. Sec. 3.6.4) the calculation of the density matrix can be performed more efficiently using fast Fourier transform (FFT) according to the scheme

$$c_{\nu,\sigma}^{\mathbf{G}}(\mathbf{k}) \xrightarrow{FFT} \psi_{\nu,\sigma}(\mathbf{k}, \mathbf{r}) \xrightarrow{\psi_{\nu,\alpha}^* \psi_{\nu,\beta}} \rho_{\nu,\alpha\beta}(\mathbf{k}, \mathbf{r}) \xrightarrow{\sum_{\nu}} \rho_{\alpha\beta}(\mathbf{k}, \mathbf{r}) \xrightarrow{FFT^{-1}} \rho_{\alpha\beta}^{\mathbf{G}}(\mathbf{k}).$$

Similarly, in the vacuum eqn. 3.166 has to be generalized to

$$\begin{aligned} \rho_{\alpha\beta}^{\mathbf{G}_{\parallel}}(z) &= \sum_{\mathbf{k}_{\parallel}} \sum_{\nu} \sum_{\mathbf{G}'_{\parallel}} \left( A_{\nu,\alpha}^{\mathbf{G}'_{\parallel}}(\mathbf{k}_{\parallel}) \right)^* A_{\nu,\beta}^{(\mathbf{G}_{\parallel}+\mathbf{G}'_{\parallel})}(\mathbf{k}_{\parallel}) w(\nu, \mathbf{k}_{\parallel}) u_{\mathbf{G}'_{\parallel},\alpha}(\mathbf{k}_{\parallel}, z) u_{(\mathbf{G}_{\parallel},\beta+\mathbf{G}'_{\parallel})}(\mathbf{k}_{\parallel}, z) \\ &+ \dots \end{aligned} \quad (5.26)$$

Inside each muffin-tin we need to calculate only the diagonal elements of the density matrix. By neglecting the off-diagonal part we project the magnetization density onto the local quantization axis. Therefore, the changes affect only the determination of the  $A$  and  $B$ -coefficients of the local spin-up and down basis functions. In contrast to a collinear calculation each basis function  $\varphi_{\mathbf{G},\sigma}$  couples to both spin directions in the spheres. In other words, each spin direction in the global frame contributes to both spin directions in the local frame. Thus, a summation of the global spins has to be performed when the  $A$  and  $B$ -coefficients of each state (cf. 3.142) are computed.

$$A_{L,\nu\sigma\alpha}^{\mu}(\mathbf{k}) = \sum_{\sigma} \sum_{\mathbf{G}} c_{\nu,\sigma}^{\mathbf{G}}(\mathbf{k}) A_{L\sigma\sigma\alpha}^{\mu\mathbf{G}}(\mathbf{k}), \quad B_{L,\nu\sigma\alpha}^{\mu}(\mathbf{k}) = \sum_{\sigma} \sum_{\mathbf{G}} c_{\nu,\sigma}^{\mathbf{G}}(\mathbf{k}) B_{L\sigma\sigma\alpha}^{\mu\mathbf{G}}(\mathbf{k}) \quad (5.27)$$

### 5.3 Construction of the Potential Matrix

The remaining task that needs to be done in each self-consistency iteration is the determination of the potential matrix  $V$  from the density matrix  $\rho$ . The potential matrix can be split up into three contributions, the external potential, which is usually given by the atomic nuclei, the Hartree potential and the exchange correlation potential. The first two contributions depend on the atomic positions and on the electron density. They do not depend on the magnetization. Thus, we are concerned with the exchange correlation potential when generalizing the method to non-collinear magnetism. If we allowed for a general magnetization vector field everywhere in the unit cell the changes would affect all parts of space, i.e. the muffin-tins, the interstitial and the vacuum regions. However, since we use a local spin coordinate frame in the muffin-tin spheres and allow only for a collinear magnetization inside the spheres, the potential generation in the muffin-tins is unchanged compared to a collinear calculation. Hence, the changes are in the interstitial and vacuum region. In these parts of space we work within the global spin coordinate frame and the charge and magnetization densities are stored in terms of the density matrix  $\rho$ . The standard parameterizations of the exchange correlation potentials are in terms of the scalar quantities  $n$  and  $m$ . In the local density approximation this is not a major problem, as I have pointed out in the previous chapter. Due to the local character of the approximation it is possible to calculate the charge density and the magnitude of the magnetization density at each point in space and then apply the standard parameterization of the exchange correlation potential. In addition, it is necessary to calculate and store the polar angles  $\vartheta$  and  $\varphi$  of the local direction of the magnetization density, because they are also the polar angles of the exchange correlation

$B$ -field and are therefore needed later. Starting from the definition of the density matrix (4.1) we find that the quantities needed are given by:

$$\begin{aligned}
n(\mathbf{r}) &= n_{\uparrow}(\mathbf{r}) + n_{\downarrow}(\mathbf{r}) = \rho_{11}(\mathbf{r}) + \rho_{22}(\mathbf{r}) & (5.28) \\
m(\mathbf{r}) &= |\mathbf{m}(\mathbf{r})| = \sqrt{(m_x(\mathbf{r}))^2 + (m_y(\mathbf{r}))^2 + (m_z(\mathbf{r}))^2} \\
&= \sqrt{(2\text{Re}\{\rho_{21}(\mathbf{r})\})^2 + (2\text{Im}\{\rho_{21}(\mathbf{r})\})^2 + (\rho_{11}(\mathbf{r}) - \rho_{22}(\mathbf{r}))^2} \\
\tan(\varphi(\mathbf{r})) &= \frac{m_y(\mathbf{r})}{m_x(\mathbf{r})} = \frac{\text{Im}\{\rho_{21}(\mathbf{r})\}}{\text{Re}\{\rho_{21}(\mathbf{r})\}} \\
\tan(\vartheta(\mathbf{r})) &= \frac{\sqrt{(m_x(\mathbf{r}))^2 + (m_y(\mathbf{r}))^2}}{m_z(\mathbf{r})} = \frac{\sqrt{(2\text{Re}\{\rho_{21}(\mathbf{r})\})^2 + (2\text{Im}\{\rho_{21}(\mathbf{r})\})^2}}{\rho_{11}(\mathbf{r}) - \rho_{22}(\mathbf{r})}
\end{aligned}$$

$n_{\uparrow}(\mathbf{r})$  and  $n_{\downarrow}(\mathbf{r})$  are the spin-up and down densities, which are commonly used to formulate the collinear theory. Now the LDA parameterization of the exchange correlation potential can be applied yielding  $V_{xc}(\mathbf{r})$  and  $B_{xc}(\mathbf{r})$ . Using the the angles  $\varphi(\mathbf{r})$  and  $\vartheta(\mathbf{r})$  we can retrieve the vector field  $\mathbf{B}_{xc}(\mathbf{r})$ . The effective potential matrix is then given by the sum of the external potential, the Hartree potential and the exchange correlation terms (cf. also eqn. 4.2).

$$\begin{aligned}
\mathbf{V}(\mathbf{r}) &= (V_{ext}(\mathbf{r}) + V_H(\mathbf{r}) + V_{xc}(\mathbf{r}))\mathbf{I}_2 + \frac{\hbar}{2} \boldsymbol{\sigma} \cdot \mathbf{B}_{xc}(\mathbf{r}) \\
\mathbf{B}_{xc}(\mathbf{r}) &= B_{xc}(\mathbf{r}) \begin{pmatrix} \sin(\vartheta(\mathbf{r})) \cos(\varphi(\mathbf{r})) \\ \sin(\vartheta(\mathbf{r})) \sin(\varphi(\mathbf{r})) \\ \cos(\vartheta(\mathbf{r})) \end{pmatrix} & (5.29)
\end{aligned}$$

The procedure of calculating  $n$ ,  $m$  and the angles  $\varphi$ ,  $\vartheta$  is commonly formulated in an equivalent way in the literature, e.g. [San98]. The density matrix is locally diagonal in a spin coordinate system with the spin z-axis along the local direction of the magnetization. This local spin coordinate system is rotated with respect to the global system by the angles  $\varphi$  and  $\vartheta$ . Thus, calculating  $n$ ,  $m$ ,  $\varphi$  and  $\vartheta$  we have diagonalized  $\boldsymbol{\rho}(\mathbf{r})$  in each point of space by local coordinate transformation. This rotation of the coordinate system can be done with the spin 1/2 rotation matrices (A.5). Hence, the density matrix in the global frame can be expressed by the the diagonal density matrix (in the local frame) and the spin 1/2 rotation matrices (cf. appendix A).

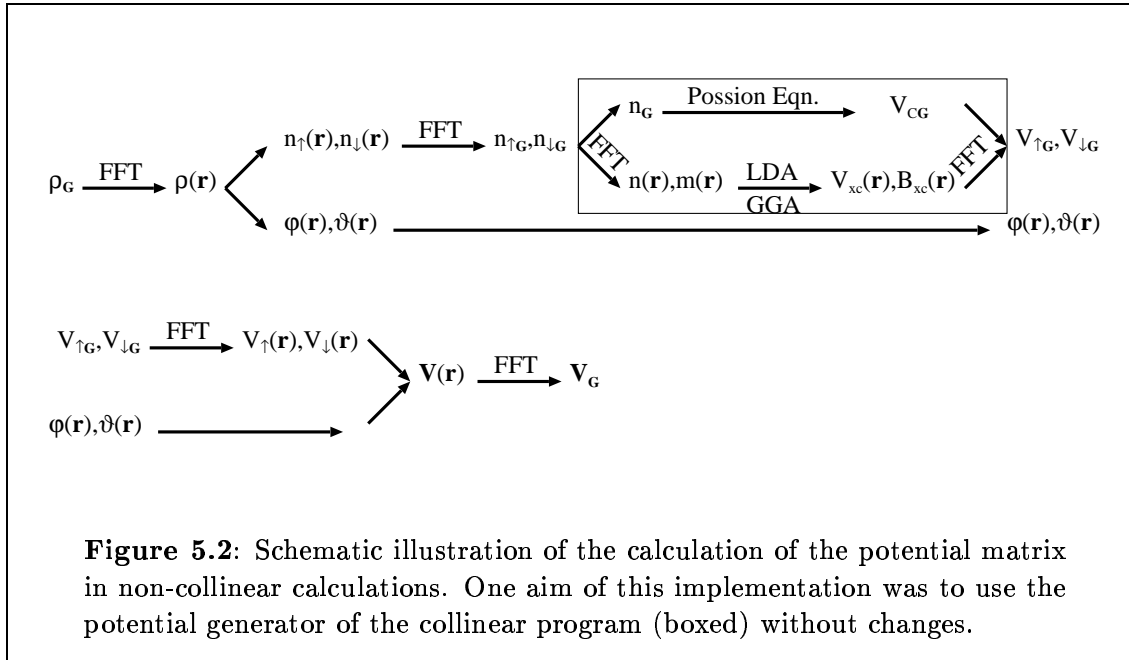
$$\boldsymbol{\rho}^{\alpha g}(\mathbf{r}) = \mathbf{U}^{\alpha g l} \begin{pmatrix} n_{\uparrow}(\mathbf{r}) & 0 \\ 0 & n_{\downarrow}(\mathbf{r}) \end{pmatrix} \mathbf{U}^{\alpha l g} & (5.30)$$

The same applies to the potential matrix.

$$\mathbf{V}^{\alpha g}(\mathbf{r}) = \mathbf{U}^{\alpha g l} \begin{pmatrix} V_{\uparrow}(\mathbf{r}) & 0 \\ 0 & V_{\downarrow}(\mathbf{r}) \end{pmatrix} \mathbf{U}^{\alpha l g} & (5.31)$$

Where  $V_{\uparrow} = V_{ext} + V_H + V_{xc} + \hbar/2B_{xc}$  and  $V_{\downarrow} = V_{ext} + V_H + V_{xc} - \hbar/2B_{xc}$  are the spin-up and -down potentials in the terminology of the collinear theory.

The procedures described above have to be carried out in real space. The rotation angles  $\varphi(\mathbf{r})$  and  $\vartheta(\mathbf{r})$  in general different for every point in space. However, the density matrix is stored in terms of three-dimensional plane waves in the interstitial region and two-dimensional plane waves in the vacuum (cf. Sec. 3.5). Therefore, the density matrix has to be Fourier transformed to a real space mesh on which the angles,  $n$  and  $m$  are calculated. The angles are kept on the mesh in order to be used later to calculate the potential matrix. The whole procedure is illustrated in Fig. 5.2. The



potential generator of the collinear program is enclosed in a box in Fig. 5.2. One aim of this implementation was to use it without any changes, i.e. to use it as a “black box”. For this reason the quantities  $n_{\uparrow}$ ,  $n_{\downarrow}$  and  $V_{\uparrow}$ ,  $V_{\downarrow}$  appear as intermediate results.

As we have seen in the previous chapter the treatment of non-collinear magnetism requires a generalization of the GGA exchange correlation potential. The currently available parameterizations do not take gradients of the off-diagonal part of the density matrix, i.e.  $m_x$  and  $m_y$ , in to account. The current implementation uses the GGA in an approximate way. The gradient of  $|\mathbf{m}(\mathbf{r})|$  is used instead of the gradient of  $m_z(\mathbf{r}) = |\mathbf{m}(\mathbf{r})|$  of the collinear problem. A second way to implement the GGA would be to use the gradient of the projection of  $\mathbf{m}(\mathbf{r})$  onto the local quantization axis in each point of space, rather than the gradient of  $|\mathbf{m}(\mathbf{r})|$ . Comparing these two approximations could give an idea of how large the contribution from the gradients of the off-diagonal part of the density matrix are. It should be kept in mind that this problem exists only in the interstitial and vacuum region, where the magnetization is rather small. Inside the muffin-tins the standard GGA potential can be applied, because of the collinear magnetization in this region. Therefore, the corrections are expected to be small.

## 5.4 Constrained local moments (CLM) in FLAPW

The implementation of non-collinear magnetism I have presented in the previous sections allows us to specify the orientation of the moment for each atom by specifying the direction of the z-axis of the local spin-coordinate frame. When constructing the magnetization density  $\mathbf{m}(\mathbf{r})$  in each self-consistency cycle the components  $m_x(\mathbf{r})$  and  $m_y(\mathbf{r})$  in the local coordinate frame are neglected, i.e. the magnetization density is projected onto the local z-direction. This can be interpreted as constraining the magnetization density along a prescribed direction. Since these components of the density are neglected in each iteration the resulting magnetization density is not a self-consistent solution of the energy functional. Thus, in general the constrained density functional theory [DBZA84] has to be applied for such calculations.

The method of constrained local moment (CLM) calculations is explained in Sec. 4.1. There it is shown how constraint is taken into account by Lagrange parameters, the local constraint  $B$ -fields, that enter the energy functional. However, up to now we have not answered the question of how the local constraint fields are determined in an actual calculation. As we have pointed out above the  $\mathbf{B}_c^\alpha$  have to be determined self-consistently in an iteration scheme. Thus, after each iteration, or set of iterations that converges  $n(\mathbf{r})$  and  $\mathbf{m}(\mathbf{r})$ , a correction to  $\mathbf{B}_c^\alpha$  needs to be determined.

$$\mathbf{B}_{c,out}^\alpha = \mathbf{B}_{c,in}^\alpha + \Delta\mathbf{B}_c^\alpha \quad (5.32)$$

Naturally, we expect  $\Delta\mathbf{B}_c^\alpha$  to be proportional to the perpendicular magnetic moment in the sphere,  $\mathbf{M}_\perp^\alpha = \int_{MT^\alpha} \mathbf{m}(\mathbf{r}) - \hat{\mathbf{e}}^\alpha(\hat{\mathbf{e}}^\alpha \cdot \mathbf{m}(\mathbf{r}))d^3r$ . The proportionality factor should be chosen such, that  $\mathbf{B}_c^\alpha$  approaches the self-consistent value quickly, but does not overshoot. In principle, we best need to know  $d\mathbf{M}_\perp^\alpha/d\mathbf{B}_c^\alpha$ , but this quantity is not easily accessible. However, if we assume that rotating  $\mathbf{B}_{eff}^\alpha$  by some angle rotates  $\mathbf{M}^\alpha$  by the same angle, we arrive at the following choice for the correction to the constraint field,

$$\Delta\mathbf{B}_c^\alpha = -|\langle\mathbf{B}_{eff}^\alpha\rangle| \frac{\mathbf{M}_\perp^\alpha}{|\mathbf{M}^\alpha|} \quad (5.33)$$

where  $\mathbf{M}^\alpha = \int_{MT^\alpha} \mathbf{m}(\mathbf{r})d^3r$  is the integrated magnetic moment in the muffin-tin and  $\langle\mathbf{B}_{eff}^\alpha\rangle$  is the average effective  $B$ -field in the sphere. All quantities on the right-hand side the output of a self-consistency iteration. To generalize this formula and to improve the convergence we can add a scaling factor  $\alpha_c$ .

$$\Delta\mathbf{B}_c^\alpha = -\alpha_c |\langle\mathbf{B}_{eff}^\alpha\rangle| \frac{\mathbf{M}_\perp^\alpha}{|\mathbf{M}^\alpha|} \quad (5.34)$$

Our test calculations show that, for systems where the size of the local moment  $|\mathbf{M}^\alpha|$  does not change much with  $\mathbf{B}_c^\alpha$ , the constraint field and the densities can be converged simultaneously, i.e. the constraint field can be improved according to (5.32) after each self-consistency iteration for  $n(\mathbf{r})$  and  $\mathbf{m}(\mathbf{r})$ . An obvious improvement to (5.32) and (5.34) would be to use a Newton scheme to find the constraint  $B$ -field that makes the perpendicular moment vanish. However, the test calculations show, that



the constraint fields converge faster than the charge and magnetization densities. In most cases a large scaling factor  $0.5 < \alpha_c < 1.0$  can be used. Hence, it does not seem to be necessary to improve the iteration scheme for  $\mathbf{B}_c^\alpha$ .

### 5.4.1 Hamiltonian setup in constrained local moment calculations

The implementation described in the previous sections is based on the atomic sphere approximation (ASA) for the spin direction inside the muffin-tin spheres, as illustrated in Fig. 5.1. Thus, the effective  $B$ -field, which is given by the exchange correlation  $B$ -field alone in all calculations presented in this thesis, is collinear and parallel to the local quantization axis,  $\mathbf{B}_{eff}^\alpha(\mathbf{r}) = B_{eff}^\alpha(\mathbf{r})\hat{\mathbf{e}}^\alpha$ . As a consequence, the Hamiltonian is diagonal in the local spin directions. Due to this property, the equations for the contributions of the muffin-tin region to the Hamiltonian and the overlap matrix (5.17, 5.18) have a rather simple form. However, the constraint  $B$ -field is perpendicular to the local quantization axis,  $\mathbf{B}_c^\alpha \perp \hat{\mathbf{e}}^\alpha$ , leading to a coupling between the local spin directions. Fortunately, the constraint field is constant, and thus spherical, inside each muffin-tin. Thus, the contribution of the constraint to the Hamiltonian is diagonal in  $l$  and  $m$ , which keeps the computational effort calculating these matrix elements moderate.

When the constraint field is added, the potential matrix, represented in the local spin-coordinate frame inside muffin-tin sphere  $\alpha$  is given by:

$$\begin{aligned} \mathbf{V}^{\alpha l}(\mathbf{r}) &= V^\alpha(\mathbf{r})\mathbf{I}_2 + \mu_B \boldsymbol{\sigma} \cdot (B_{xc}^\alpha(\mathbf{r})\hat{\mathbf{e}}^\alpha) - \mu_B \boldsymbol{\sigma} \cdot (B_{c,x}^\alpha \hat{\mathbf{e}}_x^\alpha + B_{c,y}^\alpha \hat{\mathbf{e}}_y^\alpha) \quad (5.35) \\ &= \begin{pmatrix} V^\alpha(\mathbf{r}) + \mu_B B_{xc}^\alpha(\mathbf{r}) & -\mu_B (B_{c,x}^\alpha - iB_{c,y}^\alpha) \\ -\mu_B (B_{c,x}^\alpha + iB_{c,y}^\alpha) & V^\alpha(\mathbf{r}) - \mu_B B_{xc}^\alpha(\mathbf{r}) \end{pmatrix}. \end{aligned}$$

The constraint  $B$ -field can be written as the sum of the x- and y-component in the local frame, since it is perpendicular to the local quantization ( $z$ -) axis,  $\hat{\mathbf{e}}_x^\alpha, \hat{\mathbf{e}}_y^\alpha$  represent the x- and y-axis of the local spin-coordinate frame. As I have already pointed out, the off-diagonal part of the potential matrix, and thus the Hamiltonian is given by the constraint field alone. Hence, the additional term in the Hamiltonian can be written as

$$\mathcal{H}_{MT^\mu, \text{off-d}} = \delta_{\sigma^\alpha, -\sigma^{\alpha'}} (-\mu_B (B_{c,x}^\alpha + \text{sign}(\sigma^\alpha) i B_{c,y}^\alpha)), \quad \text{sign}(\sigma^\alpha) = \begin{cases} 1, & \sigma^\alpha = \uparrow \\ -1, & \sigma^\alpha = \downarrow \end{cases}. \quad (5.36)$$

Using (5.36), in particular the fact that it is purely off-diagonal in the local spin directions, the additional contribution to the Hamiltonian matrix due to the constraint  $B$ -field is given by

$$\begin{aligned} H_{MT^\mu, \text{off-d}}^{\mathbf{G}'\sigma' \mathbf{G}\sigma}(\mathbf{k}) &= \sum_{\sigma^\alpha} (-\mu_B (B_{c,x}^\alpha + \text{sign}(\sigma^\alpha) i B_{c,y}^\alpha)) \\ &\int_{MT^\mu} \left( \sum_{L'} \left( A_{L'\sigma' - \sigma^\alpha}^{\mu \mathbf{G}'}(\mathbf{k}) u_{l' - \sigma^\alpha}^\alpha(r) + B_{L'\sigma' - \sigma^\alpha}^{\mu \mathbf{G}'}(\mathbf{k}) \hat{u}_{l' - \sigma^\alpha}^\alpha(r) \right) Y_{L'}(\hat{\mathbf{r}}) \right)^* \end{aligned}$$

$$\left( \sum_L \left( A_{L\sigma\sigma}^{\mu\mathbf{G}}(\mathbf{k}) u_{l\sigma}^\alpha(r) + B_{L\sigma\sigma}^{\mu\mathbf{G}}(\mathbf{k}) \dot{u}_{l\sigma}^\alpha(r) \right) Y_L(\hat{\mathbf{r}}) \right) d^3r. \quad (5.37)$$

Substituting (5.13) yields:

$$\begin{aligned} H_{MT^\mu, \text{off-d}}^{\mathbf{G}'\sigma'\mathbf{G}\sigma}(\mathbf{k}) &= \sum_{\sigma^\alpha} (-\mu_B(B_{c,x}^\alpha + \text{sign}(\sigma^\alpha) i B_{c,y}^\alpha)) \left[ ((\chi_{-\sigma^\alpha}^{\alpha g})^* \chi_{\sigma'})^* (\chi_{\sigma^\alpha}^{\alpha g})^* \chi_\sigma \right] \\ &\int_{MT^\mu} \left( \sum_{L'} \left( A_{L'-\sigma^\alpha}^{\mu\mathbf{G}'}(\mathbf{k}) u_{l'-\sigma^\alpha}^\alpha(r) + B_{L'-\sigma^\alpha}^{\mu\mathbf{G}'}(\mathbf{k}) \dot{u}_{l'-\sigma^\alpha}^\alpha(r) \right) Y_{L'}(\hat{\mathbf{r}}) \right)^* \\ &\left( \sum_L \left( A_{L\sigma^\alpha}^{\mu\mathbf{G}}(\mathbf{k}) u_{l\sigma^\alpha}^\alpha(r) + B_{L\sigma^\alpha}^{\mu\mathbf{G}}(\mathbf{k}) \dot{u}_{l\sigma^\alpha}^\alpha(r) \right) Y_L(\hat{\mathbf{r}}) \right) d^3r. \end{aligned} \quad (5.38)$$

The  $A$ - and  $B$ -coefficients are given by:

$$\begin{aligned} A_{L\sigma^\alpha}^{\mu\mathbf{G}}(\mathbf{k}) &= e^{i\mathbf{K}\mathbf{p}^\mu} \frac{4\pi}{\sqrt{\Omega}} i^l Y_L^*(\mathbf{R}^\mu \hat{\mathbf{K}}) \frac{F_{l\sigma^\alpha}^{\alpha G}(\mathbf{k})}{W_{l\sigma^\alpha}^\alpha} \\ B_{L\sigma^\alpha}^{\mu\mathbf{G}}(\mathbf{k}) &= e^{i\mathbf{K}\mathbf{p}^\mu} \frac{4\pi}{\sqrt{\Omega}} i^l Y_L^*(\mathbf{R}^\mu \hat{\mathbf{K}}) \frac{G_{l\sigma^\alpha}^{\alpha G}(\mathbf{k})}{W_{l\sigma^\alpha}^\alpha}, \end{aligned} \quad (5.39)$$

where  $\Omega$  is the volume of the unit cell and the Wronskian,  $F_{l\sigma^\alpha}^{\alpha G}(\mathbf{k})$  and  $G_{l\sigma^\alpha}^{\alpha G}(\mathbf{k})$  are defined as:

$$\begin{aligned} W_{l\sigma^\alpha}^\alpha &= \left[ \dot{u}_{l\sigma^\alpha}^\alpha(R_{MT^\alpha}) u_{l\sigma^\alpha}^{\alpha'}(R_{MT^\alpha}) - u_{l\sigma^\alpha}^\alpha(R_{MT^\alpha}) \dot{u}_{l\sigma^\alpha}^{\alpha'}(R_{MT^\alpha}) \right] \\ F_{l\sigma^\alpha}^{\alpha G}(\mathbf{k}) &= \left[ \dot{u}_{l\sigma^\alpha}^\alpha(R_{MT^\alpha}) K j_l'(R_{MT^\alpha} K) - \dot{u}_{l\sigma^\alpha}^{\alpha'}(R_{MT^\alpha}) j_l(R_{MT^\alpha} K) \right] \\ G_{l\sigma^\alpha}^{\alpha G}(\mathbf{k}) &= \left[ u_{l\sigma^\alpha}^{\alpha'}(R_{MT^\alpha}) j_l(R_{MT^\alpha} K) - u_{l\sigma^\alpha}^\alpha(R_{MT^\alpha}) K j_l'(R_{MT^\alpha} K) \right]. \end{aligned} \quad (5.40)$$

$j_l$  is the spherical Bessel function and a  $'$  denotes a radial derivative  $\partial/\partial r$ . Now, we can substitute (5.39) into (5.38). Using the addition theorem for the spherical harmonics:

$$P_l(\hat{\mathbf{k}}_1 \cdot \hat{\mathbf{k}}_2) = \frac{4\pi}{2l+1} \sum_{m=-l}^l Y_L(\hat{\mathbf{k}}_1) Y_L^*(\hat{\mathbf{k}}_2), \quad (5.41)$$

where  $P_l$  is the Legendre polynomial, and the fact that  $\int Y_{L'}^*(\hat{\mathbf{r}}) Y_L(\hat{\mathbf{r}}) d\Omega = \delta_{L',L}$  we obtain:

$$\begin{aligned} H_{MT^\mu, \text{off-d}}^{\mathbf{G}'\sigma'\mathbf{G}\sigma}(\mathbf{k}) &= \sum_{\sigma^\alpha} (-\mu_B(B_{c,x}^\alpha + \text{sign}(\sigma^\alpha) i B_{c,y}^\alpha)) \left[ ((\chi_{-\sigma^\alpha}^{\alpha g})^* \chi_{\sigma'})^* (\chi_{\sigma^\alpha}^{\alpha g})^* \chi_\sigma \right] \\ &\sum_l e^{i(\mathbf{G}-\mathbf{G}')\mathbf{p}^\mu} \frac{(4\pi)^2}{\Omega} \frac{1}{W_{l-\sigma^\alpha}^\alpha W_{l\sigma^\alpha}^\alpha} \frac{2l+1}{4\pi} P_l(\mathbf{K} \cdot \mathbf{K}') \\ &\left( F_{l-\sigma^\alpha}^{\alpha G'}(\mathbf{k}) F_{l\sigma^\alpha}^{\alpha G}(\mathbf{k}) \int u_{l-\sigma^\alpha}^\alpha(r) u_{l\sigma^\alpha}^\alpha(r) r^2 dr + F_{l-\sigma^\alpha}^{\alpha G'}(\mathbf{k}) G_{l\sigma^\alpha}^{\alpha G}(\mathbf{k}) \int u_{l-\sigma^\alpha}^\alpha(r) \dot{u}_{l\sigma^\alpha}^\alpha(r) r^2 dr \right. \\ &\left. G_{l-\sigma^\alpha}^{\alpha G'}(\mathbf{k}) F_{l\sigma^\alpha}^{\alpha G}(\mathbf{k}) \int \dot{u}_{l-\sigma^\alpha}^\alpha(r) u_{l\sigma^\alpha}^\alpha(r) r^2 dr + G_{l-\sigma^\alpha}^{\alpha G'}(\mathbf{k}) G_{l\sigma^\alpha}^{\alpha G}(\mathbf{k}) \int \dot{u}_{l-\sigma^\alpha}^\alpha(r) \dot{u}_{l\sigma^\alpha}^\alpha(r) r^2 dr \right). \end{aligned} \quad (5.42)$$

The task to calculate these matrix elements can be compared to the determination of the overlap matrix elements in a non-collinear calculation. The principal differences

are: i) The constant pre-factor  $(-\mu_B(B_{c,x}^\alpha + \text{sign}(\sigma^\alpha)iB_{c,y}^\alpha))$  given by the constraint  $B$ -field and ii) the fact that all terms are cross-terms of the two local spin directions  $\sigma^\alpha$  and  $-\sigma^\alpha$ . Consequently, the radial overlap integrals that appear in (5.42) are the overlap of the radial basis functions with different local spin character.

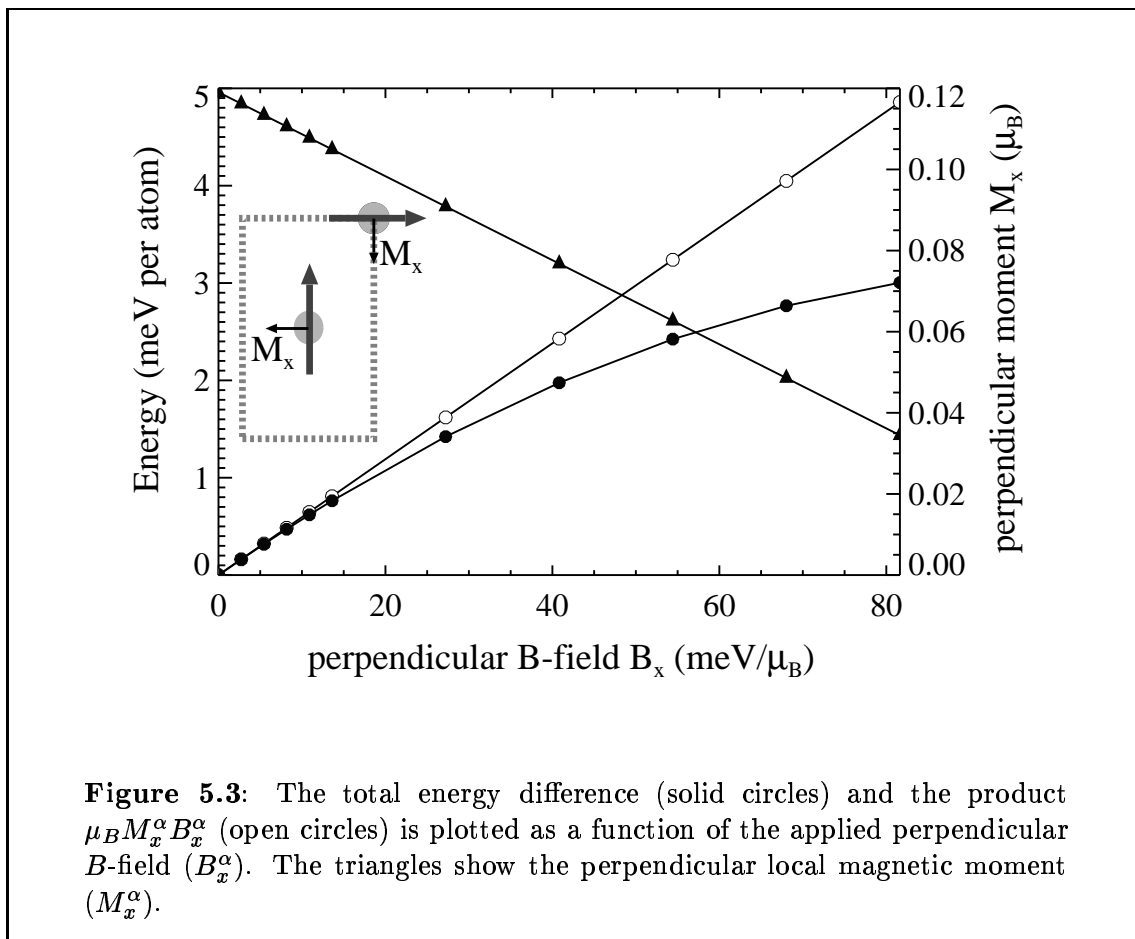
### 5.4.2 Test calculations

As a first test of the implementation of the constrained local moment method we compared the change of the total energy for small constraint  $B$ -fields with the energy calculated in first order perturbation theory. We performed non-self-consistent calculations, setting the constraint field to different values manually, rather than calculating it self-consistently. In other words, we applied small perpendicular  $B$ -fields inside each muffin-tin, using the implementation for constrained local moment calculations. We tried fields with different magnitudes, which were smaller than the constraint field necessary to make the perpendicular moment in the respective muffin-tin sphere vanish. Such fields represent a small perturbation of the system. In first order perturbation theory the energy difference between the unperturbed and the perturbed system is given by the sum over the expectation values of all occupied states of the unperturbed system with the perturbation term of the Hamiltonian. If we write the contribution to the Hamiltonian due to the perpendicular field within the local spin-coordinate frame as in (5.36), we find that the energy difference is given by:

$$\begin{aligned} \Delta E &= \sum_{\nu} \sum_{\mu} \int_{MT^{\mu}} \psi_{\nu}^*(\mathbf{r}) \left( -\mu_B (\sigma_x B_x^{\alpha} + \sigma_y B_y^{\alpha}) \right) \psi_{\nu}(\mathbf{r}) d^3r \quad (5.43) \\ &= -\mu_B \sum_{\mu} M_x^{\alpha} B_x^{\alpha} + M_y^{\alpha} B_y^{\alpha}. \end{aligned}$$

We performed the test for an unsupported monolayer (UML) of Cr with the symmetry and the lattice constant of a monolayer on the Ag(111) surface. We used a unit cell containing two atoms according to the inset of Fig. 5.3. The magnetic moments of the two atoms are aligned at  $90^\circ$ , so that the configuration consists of alternating rows of atoms with moments pointing in  $z$ - and  $x$ -direction respectively. We chose the theoretical LDA Ag lattice constant of 7.79 a.u. The  $k$ -point set that we employed corresponds to 180 points in the full two-dimensional Brillouin zone, the planewave cutoff was set to  $K_{max} = 3.3 \text{ a.u.}^{-1}$  leading to a basis set with about 130 basis function per atom and the muffin-tin radius was chosen as large as possible,  $R_{MT} = 2.75 \text{ a.u.}$  We applied the LDA parameterization according to Moruzzi, Janak and Williams [MJW78].

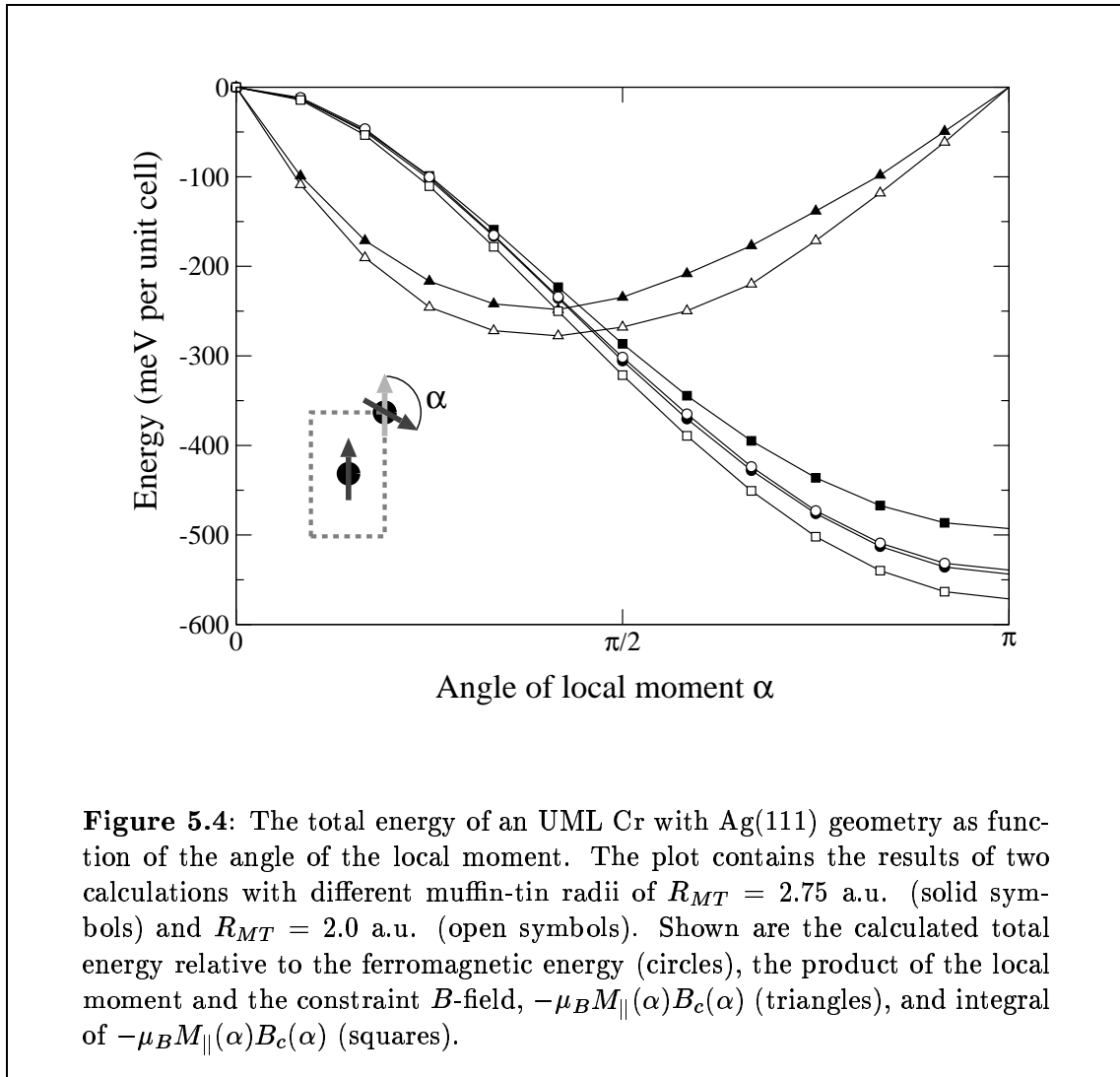
From a self-consistent calculation without a constraint field we obtained small perpendicular moments of about  $0.12 \mu_B$  inside the muffin-tin spheres. The direction of the perpendicular moments is shown in the inset of Fig. 5.3, indicating the tendency of the system to evolve into a state of alternating antiferromagnetic rows. The local spin-coordinate frames of each atoms was chosen such that the perpendicular moments point along the  $x$ -axis of the local frame. Starting from the



self-consistent charge and magnetization densities we performed non-self-consistent calculations where we applied a perpendicular field also in  $x$ -direction and with the same magnitude in each muffin-tin. Fig. 5.3 shows the change of the energy as a function of the applied perpendicular  $B$ -field (solid circles). For very small fields this energy difference is in excellent agreement with the energy difference calculated in first order perturbation theory (open circles) according to Eqn. (5.43). But already for field as small as  $20 \text{ meV}/\mu_B^2$  the calculated energy starts to deviate from the result of the perturbation theory. In first order perturbation theory the effect of the change of the eigenfunctions due to the perturbation is neglected. As a measure for that change we can take the output perpendicular moment of the calculation, which is also shown in Fig. 5.3 (solid triangles). It can be seen that  $M_x^\alpha$  decreases linearly with increasing field. At a field of about  $60 \text{ meV}/\mu_B$  it has already decreased to half its original size. Hence, the result, that first order perturbation theory is only accurate for very small  $B$ -fields, is not surprising.

As a second test we compared the calculated total energy to the energy obtained

<sup>2</sup>For comparison: the average exchange correlation  $B$ -field is about  $2500 \text{ meV}/\mu_B$  inside the muffin-tins.



from the constraint  $B$ -fields using the Hellmann-Feynman theorem. Eqn. (4.8) can be used to calculate the energy difference between two magnetic states by an integration over a path of magnetic configuration that connects the two states. This method has been used by Oswald et al. [OZD85] to calculate the magnetic energy of  $3d$ -impurity pairs in Cu, Ag and Pd. We chose the same system, the UML Cr/Ag(111), as in the previous paragraphs, using the same computational parameters. As starting and final states we consider the ferromagnetic and a row-wise antiferromagnetic configuration. Rotating one of the two atoms in the unit cell, as illustrated in the inset of Fig. 5.4, yields a path connecting the two magnetic states. This path is described by a single parameter, the angle  $\alpha$ . If  $\alpha$  is changed by an infinitesimal step  $d\alpha$ , the change of the direction of the local moment  $d\hat{e}$  is always parallel to the local constraint field  $\mathbf{B}_c^\alpha$  in such a configuration. Now the Hellmann-Feynman theorem (4.8) can be integrated, yielding an equation for the energy difference between the ferromagnetic state and a

state with angle  $\alpha$  between the magnetic moments:

$$E(\alpha) - E(\alpha = 0) = \int_0^\alpha -\mu_B M_{\parallel}(\alpha) B_c(\alpha) d\alpha. \quad (5.44)$$

The result of the test calculation is shown in Fig. 5.4. The graph shows the calculated energy difference (solid circles), the product  $-\mu_B M_{\parallel}(\alpha) B_c(\alpha)$  (solid triangles) and the integral of the latter quantity (solid squares). The energy decreases with increasing angle. It shows a cosine like behavior as expected from the nearest neighbor Heisenberg model for an antiferromagnetic material. The shape of the  $-\mu_B M_{\parallel}(\alpha) B_c(\alpha)$  curve is dominated by  $B_c(\alpha)$ .  $M_{\parallel}(\alpha)$  is almost constant. It changes only within a range of  $4.1 \mu_B - 4.2 \mu_B$ .  $M_{\parallel}(\alpha)$  also changes very little (less than 1 %) from a calculation with the constraint field switched off to a constraint calculation. The symmetric magnetic states, ferromagnetic and antiferromagnetic, represent extrema of the total energy. Hence, they are stable magnetic solutions. Consequently, the constraint field, and thus  $-\mu_B M_{\parallel}(\alpha) B_c(\alpha)$  is zero for  $\alpha = 0$  and  $\alpha = \pi$ .  $-\mu_B M_{\parallel}(\alpha) B_c(\alpha)$  is a continuous function, that reaches a maximum at an intermediate angle slightly smaller than  $\pi/2$ .

The integral of  $-\mu_B M_{\parallel}(\alpha) B_c(\alpha)$  exhibits the same behavior as the total energy, but has a slightly smaller magnitude than the calculated total energy difference. At the final (antiferromagnetic) state the two curves differ by about 9 %. We have not completely understood the origin of the deviation. We suspect that it might be due to incomplete-basis-set corrections. The Hellmann-Feynman theorem is based on the fact that the functional derivative of the total energy with respect to the (components) of the density (-matrix) vanishes,  $\delta E/\delta \rho = 0$ , because  $\rho$  is already the groundstate density and minimizes  $E$ . Therefore, only the explicit dependence of the energy on an external parameter has to be taken into account when differentiating the energy with respect to the parameter. In our case this parameter is the direction of the local moment. However, in methods like the FLAPW method the basis set depends on the external parameters. The corresponding corrections are called the incomplete-basis-set corrections. Such corrections play an important role in the calculation of the atomic forces [YSK91]. In fact, in atomic force calculations the incomplete-basis-set corrections are usually even larger than the Hellmann-Feynman force. Recently, Grotheer and Fahnle have derived an expression for the incomplete-basis-set corrections to the torque acting on the localized magnetic moments [GF98]. They have performed calculations similar to that presented in Fig. 5.4 on bcc Fe and found that the corrections are about 2 % of the size of the Hellmann-Feynman torque.

The basis function of the FLAPW method in the interstitial region are plane-waves. Thus, the basis set is independent of the local quantization axis  $\hat{e}^\alpha$  in that region. Hence, changing the muffin-tin radii  $R_{MT}^\alpha$  should have an effect on the size the incomplete-basis-set corrections. To gain an indication whether the incomplete-basis-set corrections are the cause of the difference between the calculated total energy difference and the energy difference obtained from the Hellmann-Feynman theorem, we have repeated the calculation with a much smaller muffin-tin radius of  $R_{MT} = 2.00$  a.u. With this choice the volume covered by the muffin-tin spheres is

reduced by more than 60 %. The result of this second calculation is also shown in Fig. 5.4 by the open symbols. The product  $-\mu_B M_{\parallel}(\alpha) B_c(\alpha)$  is changed considerably. The energy difference calculated from the Hellmann-Feynman theorem is now about 6 % to large, i.e. the deviation has changed the sign and its magnitude has become smaller. This result supports the idea that the deviation is due to the incomplete-basis-set corrections. However, to definitely settle this point, calculations including these corrections would be necessary. Such calculations remain a future project.

Stocks et al. [SUW<sup>+</sup>98, UWN<sup>+</sup>99] chose bcc Fe to test their implementation of constrained local moment calculations. Also Grotheer and Fähnle [GF98] used the same test system for their implementation of the incomplete-basis-set corrections to the Hellmann-Feynman torque on the magnetic moments. Therefore, we repeated the test for bcc Fe using the same geometry as Stocks et al. In particular, we used the same LDA lattice constant of  $a_0 = 5.27$  a.u. Our  $k$ -point set corresponds to 2016  $k$ -points in the full three-dimensional Brillouin zone. The planewave cutoff was set to  $K_{max} = 4.0$  a.u.<sup>-1</sup> leading to a basis set with about 80 basis functions per atom. We chose a muffin-tin radius of  $R_{MT} = 2.25$  a.u. To compare with the result of Stocks et al. we started with an unconstrained calculation. In such a calculation the magnetization density is projected onto the local quantization axis  $\hat{e}^\alpha$  inside the muffin-tins after each iteration, i.e. the perpendicular magnetic moment  $\mathbf{M}_\perp^\alpha$  is neglected. Although these calculations can be converged to a stable solutions, the result is not self-consistent in the sense that the direction of the output magnetic moment is not equal the direction of the input moment,  $\hat{e}_{out}^\alpha \neq \hat{e}_{in}^\alpha = \hat{e}^\alpha$ .

The results of the bcc Fe calculations are presented in Fig. 5.5. Panel b) contains the parallel magnetic moment  $M_{\parallel}(\alpha)$  (open diamonds) and the perpendicular (output) moment  $M_\perp(\alpha)$  (open triangles). Our results are not in agreement with those of Stocks et al. In particular, we find that the moment decreases strongly, by more than 50 %, when it is rotated towards the antiferromagnetic state. Stocks et al. obtain a very similar magnetic moment for the ferromagnetic state. However, in their study the moment varies only within a range of  $1.9 \mu_B - 2.2 \mu_B$  with the rotation. Other authors also found a strong reduction of the moment in the antiferromagnetic state. For example, Kübler [Küb81] found a moment that is even slightly below  $1 \mu_B$  in the antiferromagnetic configuration for the same lattice constant. Moruzzi and Marcus [MM90] obtain a reduction from  $2.34 \mu_B$  (ferromagnetic) to  $1.75 \mu_B$  (antiferromagnetic). Their moments are larger in both configurations, because they used the experimental lattice constant of  $a_0 = 5.48$  a.u.

Another difference between our results and those of Stocks et al. is the size of  $M_\perp(\alpha)$ . Stocks et al. specify the difference between the input and the output angle of the local moment rather than  $M_\perp$ . They find a maximum difference of about  $25^\circ$ . The size of the magnetic moment for that angle is about  $2 \mu_B$ , which means that  $M_\perp$  must be about  $0.9 \mu_B$ . This value much larger compared to the maximum  $M_\perp$  of  $0.37 \mu_B$  that we found. Finally, Stocks et al. obtain a maximum constraint field of about  $0.23 Ry/\mu_B$  at  $90^\circ$ . We also find the maximum at  $90^\circ$  but the our value of  $0.029 Ry/\mu_B$  is almost a factor of 10 smaller. However, Fig. 5.5 shows that the energy

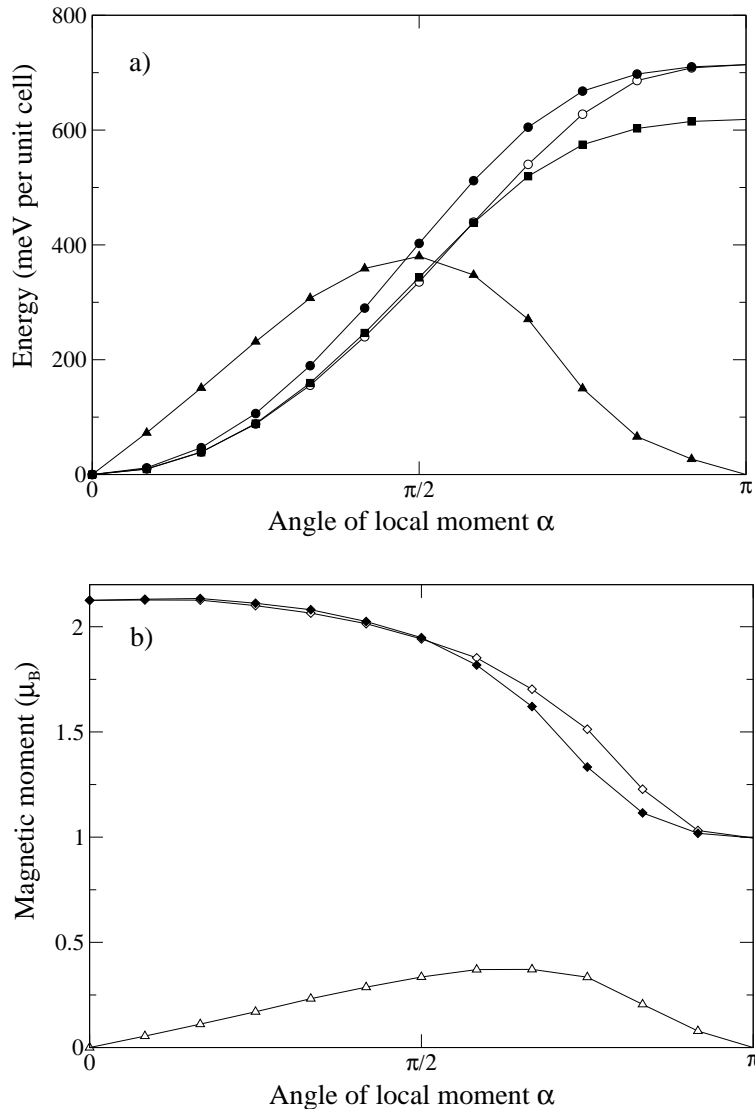
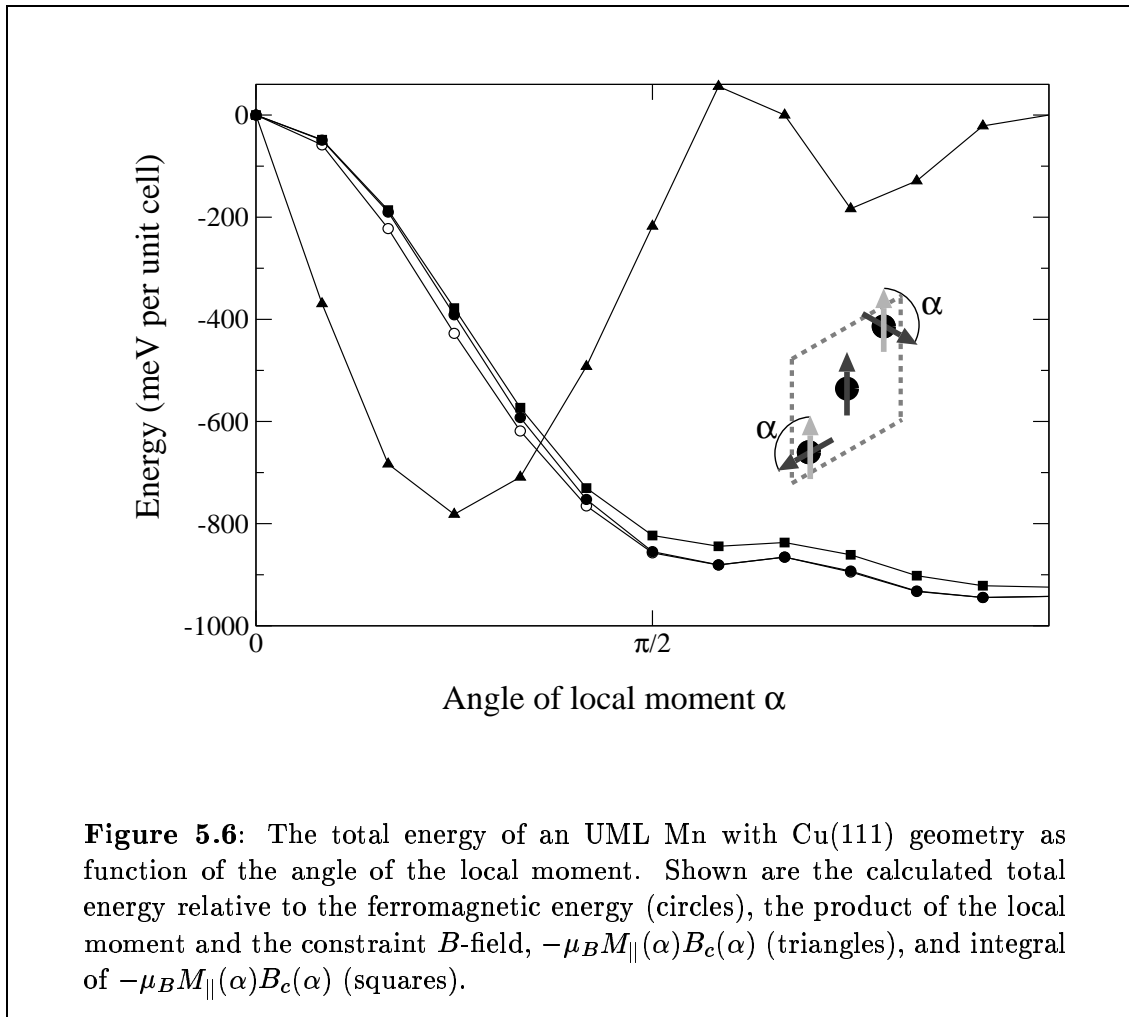


**Figure 5.5:** Panel a): The total energy of bcc Fe as function of the angle of the local moment. Shown are the calculated total energy relative to the ferromagnetic energy (circles), the product of the local moment and the constraint  $B$ -field,  $-\mu_B M_{\parallel}(\alpha) B_c(\alpha)$  (triangles), and integral of  $-\mu_B M_{\parallel}(\alpha) B_c(\alpha)$  (squares). Panel b): Shown are the parallel magnetic moment  $M_{\parallel}(\alpha)$  (diamonds) and the perpendicular moment  $M_{\perp}(\alpha)$  (triangles). Both panels contain results of constrained (solid symbols) and unconstrained calculations (open symbols).

difference calculated from the Hellmann-Feynman theorem using  $B_c(\alpha)$  (panel a) solid squares) is in fair agreement with the calculated total energy difference (panel a) solid circles). The Hellmann-Feynman result underestimates the energy difference



between the ferromagnetic and the antiferromagnetic state by about 13 %. Panel a) also contains the calculated total energy of the unconstrained calculation (open circles). Naturally, the energies calculated with and without constraint are equal for the ferromagnetic and the antiferromagnetic configuration, where the constraint  $B$ -field vanishes. For the intermediate angles the energy calculated with constraint is always larger. We obtained the largest difference of 98 meV at an angle of  $105^\circ$ . Compared to the other test systems this value is uncommonly large, e.g. for the Cr UML we found a maximum difference of only 7.4 meV. Another effect of the constraint can be seen in panel b) of Fig. 5.5. In the region where the magnetic moment decrease rapidly with changing angle the moment of the constrained calculation (solid diamonds) is reduced even more strongly compared to the unconstrained moment (open diamonds). Other results showed that this seems to be a general trend. In situations where the magnetic moments become unstable, the constraint tends to reduce the moment further, while in most calculations the effect of the constraint on the size of the moment is negligible.



As the final test system we chose another unsupported monolayer (UML) of Mn with the geometry of the Cu(111) surface ( $a_{0,Cu} = 6.65$  a.u.). In contrast to the previous two test systems the unit cell of this example contains three atoms. During the computation the moment of two atoms was rotated into opposite directions as illustrated in the inset of Fig. 5.6. Since two atoms are rotated the integral of Eqn. (5.44) has to be multiplied by a factor of two, to obtain the corresponding equation for this configuration. When the angle  $\alpha$  is changed from  $0^\circ$  to  $180^\circ$  the path of magnetic configuration goes through three high-symmetry states, the ferromagnetic state ( $\alpha = 0^\circ$ ), the Néel state ( $\alpha = 120^\circ$ ), and a collinear antiferromagnetic state ( $\alpha = 180^\circ$ ). In the Néel state the magnetic moments of all nearest neighbors of each atom are aligned at  $120^\circ$ . The antiferromagnetic state has a net moment, because the magnetic moments of two atoms are parallel and only one atom has an anti-parallel moment. This state will be denoted the  $180^\circ$  configuration in the following. In Fig. 5.6 it can be seen that  $B_c$ , and thus  $\mu_B M_{\parallel}(\alpha) B_c(\alpha)$  (solid triangles), becomes zero at the three high symmetry configurations. The calculated total energy and the energy obtained from the Hellmann-Feynman theorem are in good agreement. The two energy curves have a very similar shape and in the  $180^\circ$  configuration the energies differ by only about 2 %. At  $120^\circ$  the energy exhibits a local maximum. The quantity  $\mu_B M_{\parallel}(\alpha) B_c(\alpha)$ , which is proportional to the slope of  $E(\alpha)$  according to the Hellmann-Feynman theorem (cf. eqn. 5.44), changes sign at this point. The plot also shows that the difference between the calculated energies with and without constraint (open circles) is rather small. This difference reaches its maximum value of 36 meV at  $45^\circ$ .

In summary, the outcome of the test calculation can be condensed in three main points. The first test, presented in Fig. 5.3, shows that the constraint  $B$ -fields necessary to force the magnetic moment into a prescribed direction, are to larger to be dealt with in perturbation theory. Our results show further that the accuracy of the Hellmann-Feynman theorem is limited to about 10 %. We suspect that the reason for this limitation are the incomplete-basis-set corrections. However, calculations that take these corrections into account are necessary to prove this hypothesis. A consequence of this result is that if an interpretation of the constraint field as a force (or torque) on the magnetic moment with high accuracy is desired, the incomplete-basis-set corrections can not be neglected. Finally, in all calculations we have performed, also those presented in later chapters, the dependence of the energy on the magnetic configuration does not change qualitatively when the constraint is switched on. In most cases the difference between the total energy calculated with and without constraint is only a few percent ( $< 5$  %) of the difference between, for example, the ferromagnetic and the antiferromagnetic state.

## 5.5 Spin-Spirals in FLAPW

The FLAPW method relies on plane wave expansions for quantities like the charge density, the potential, and the wave functions. It is therefore necessary to formulate

the basic equations in terms of periodic quantities that can be Fourier transformed. However, in an incommensurate spiral magnetic structure the magnetization density, the  $B$ -field and the eigenfunctions are no longer periodic. They have to be replaced by periodic quantities. For the wave functions the corresponding periodic quantities,  $\alpha(\mathbf{r})$  and  $\beta(\mathbf{r})$ , have already been introduced in Sec. 4.3. Choosing the rotation axis along the spin  $z$ -axis is only  $m_x$ ,  $m_y$ ,  $B_x$ , and  $B_y$  that are affected by the spin rotation. The magnetization and the  $B$ -field are rotated by  $\varphi = \mathbf{q} \cdot \mathbf{r}$  counter clockwise in the  $x$ - $y$ -plane, i.e.  $(m_x(\mathbf{r}) + im_y(\mathbf{r}))$  and  $(B_x(\mathbf{r}) + iB_y(\mathbf{r}))$  are complex quantities that rotate like  $e^{i\mathbf{q}\cdot\mathbf{r}}$  in the complex plane. Accordingly, we have to apply a rotation in the opposite direction to obtain the periodic quantities. These quantities are thus given by  $e^{-i\mathbf{q}\cdot\mathbf{r}}(m_x(\mathbf{r}) + im_y(\mathbf{r}))$  and  $e^{-i\mathbf{q}\cdot\mathbf{r}}(B_x(\mathbf{r}) + iB_y(\mathbf{r}))$ . According to the definitions of the density and potential matrix (eqn. 4.1 and 4.2)  $(m_x + im_y)$  and  $(B_x + iB_y)$  are the off-diagonal part of these matrices and the above substitution yields the corresponding periodic matrices  $\tilde{\rho}$  and  $\tilde{V}$ . These relations can also be expressed in terms of the the spin 1/2 rotation matrix (4.11):

$$\begin{aligned}\tilde{\rho} &= \mathbf{U}^\dagger \rho \mathbf{U} \\ \tilde{V} &= \mathbf{U}^\dagger \mathbf{V} \mathbf{U}.\end{aligned}\tag{5.45}$$

As suggested by Eqn. (4.16) a plane wave basis set is used for the periodic quantities  $\alpha(\mathbf{r})$  and  $\beta(\mathbf{r})$  in the interstitial region. Hence, the interstitial basis functions are given by

$$\varphi_{\mathbf{G},\sigma}(\mathbf{k}, \mathbf{r}) = e^{i(\mathbf{G}+\mathbf{k}\mp\mathbf{q}/2)\cdot\mathbf{r}} \chi_\sigma,\tag{5.46}$$

where the  $-$  sign in  $\mp\mathbf{q}/2$  holds for spin-up and the  $+$  sign hold for spin-down. If we multiply  $\varphi_{\mathbf{G},\sigma}$  by  $\mathbf{U}^\dagger$ , we obtain the function  $\tilde{\varphi}_{\mathbf{G},\sigma} = e^{i(\mathbf{G}+\mathbf{k})\cdot\mathbf{r}} \chi_\sigma$  that has exactly the same form as the basis functions of a normal magnetic basis set,

$$\tilde{\varphi}_{\mathbf{G},\sigma}(\mathbf{k}, \mathbf{r}) = \mathbf{U}^\dagger \varphi_{\mathbf{G},\sigma}(\mathbf{k}, \mathbf{r}).\tag{5.47}$$

In film calculations the spin-spiral vector  $\mathbf{q}$  is always parallel to the surface and the two-dimensional plane wave expansion that corresponds to (5.47) is used for the basis functions.

Due to the term  $e^{\mp\mathbf{q}\cdot\mathbf{r}/2}$  term, the basis functions are now different for the two spin directions. Before the basis functions differed only due to the spinor  $\chi_\sigma$ . This is not a fundamental problem, but as a practical consequence changes required to the computer program are rather involved. There is another technical point I would like to mention. In an conventional collinear or non-collinear calculation the plane wave cutoff for the basis functions is enforced according to  $|\mathbf{K}| = |\mathbf{G} + \mathbf{k}| \leq K_{max}$ . The obvious generalization is to use  $|\mathbf{G} + \mathbf{k} \mp \mathbf{q}/2| \leq K_{max}$  as the cutoff condition. The consequence is that we find different sets of  $\mathbf{G}$ 's for the two spin directions. In fact, even the number of basis functions is in general different for spin-up and -down. In order to save programming work we first tried keeping the old cutoff condition  $|\mathbf{G} + \mathbf{k}| \leq K_{max}$ . In this case the sphere of  $\mathbf{G}$ 's is not centered around  $\mathbf{k} \mp \mathbf{q}/2$  but around  $\mathbf{k}$ . In other words, the average of  $|\mathbf{G} + \mathbf{k} \mp \mathbf{q}/2|^2$  over all basis functions is

larger than it would be if we took  $|\mathbf{G} + \mathbf{k} \mp \mathbf{q}/2| \leq K_{max}$  as the cutoff condition, i.e. on average the basis functions have a larger kinetic energy matrix elements. In the limit of large cutoffs this is not a problem, but for small cutoffs that are used in actual calculations, this can cause a significant contribution to the total energy. The calculated energies for configurations with large spin-spiral vectors are relatively larger than for small  $q$ -vectors, e.g. the energy of a spin-spiral with  $\mathbf{q}$  equal to a reciprocal lattice vector is larger than that of a spiral with  $\mathbf{q} = 0$ , though both configurations are ferromagnetic. To retain the required accuracy it is necessary to go to larger cutoffs and the method becomes less efficient. Therefore, we have changed the program again enforcing the cutoff according to  $|\mathbf{G} + \mathbf{k} \mp \mathbf{q}/2| \leq K_{max}$ . This effect and the difference between the two cutoff conditions is illustrated for the example of Fe in Sec. 5.5.4.

On the other hand representing the matrix density and potential by  $\tilde{\varphi}$  and  $\tilde{\mathbf{V}}$  respectively has a very convenient feature. When the Hamiltonian matrix is calculated, we need to determine the matrix elements of the basis functions with the potential matrix. Thus we have to calculate integrals of the form

$$\int \varphi_{\mathbf{G},\sigma}^* \mathbf{V} \varphi_{\mathbf{G},\sigma} d^3r = \int \tilde{\varphi}_{\mathbf{G},\sigma}^* \mathbf{U} \mathbf{U}^\dagger \tilde{\mathbf{V}} \mathbf{U} \mathbf{U}^\dagger \tilde{\varphi}_{\mathbf{G},\sigma} d^3r = \int \tilde{\varphi}_{\mathbf{G},\sigma}^* \tilde{\mathbf{V}} \tilde{\varphi}_{\mathbf{G},\sigma} d^3r. \quad (5.48)$$

Hence, if we work with  $\tilde{\varphi}$  and  $\tilde{\mathbf{V}}$ , the form of these integrals does not change. This means that the corresponding part of the computer program does not need to be modified. Inside of the muffin-tins the basis functions are set up as in a conventional calculation. However, they have to be matched to the new interstitial basis functions. Due to the term  $e^{\mp \mathbf{q} \cdot \mathbf{r}/2}$ , the value of the plane wave at the sphere boundary is now different for the two interstitial spin directions. Consequently, Eqn. (5.13) that relates the non-collinear  $A$  and  $B$ -coefficients to their collinear counterparts does not hold anymore.

### 5.5.1 Setup of the Hamiltonian Matrix

In contrast to a non-spin-spiral calculation the extra term  $\mp \mathbf{q}/2$  appears in the exponent of the plane waves of the spin-spiral basis set. This term has to be taken into account when the Hamiltonian matrix elements are calculated in the interstitial region. The overlap matrix elements remain unchanged, which becomes obvious when (5.47) is substituted into the integral equation for the overlap matrix elements.

$$S_{INT}^{\mathbf{G}\sigma\mathbf{G}'\sigma'} = \int \varphi_{\mathbf{G},\sigma}^* \varphi_{\mathbf{G}',\sigma'} d^3r = \int \tilde{\varphi}_{\mathbf{G},\sigma}^* \mathbf{U}^\dagger \mathbf{U} \tilde{\varphi}_{\mathbf{G}',\sigma'} d^3r = \delta_{\sigma\sigma'} \Theta_{(\mathbf{G}-\mathbf{G}')} \quad (5.49)$$

We have already shown that the contribution to the Hamiltonian due to the potential matrix does not change, because we work with  $\tilde{\mathbf{V}}$  (5.48). Yet, the term  $\mp \mathbf{q}/2$  contributes to the kinetic energy and the Hamiltonian matrix elements are given by

$$H_{INT}^{\mathbf{G}\sigma\mathbf{G}'\sigma'}(\mathbf{k}) = (\tilde{V}_{\sigma\sigma'} \Theta)_{(\mathbf{G}-\mathbf{G}')} + \delta_{\sigma\sigma'} \frac{\hbar^2}{2m} (\mathbf{G}' + \mathbf{k} \mp \mathbf{q}/2)^2 \Theta_{(\mathbf{G}-\mathbf{G}')} \quad (5.50)$$

The changes in the vacuum are very similar to those in the interstitial region. The basic difference to a non-spin-spiral calculation is the extra contribution to the kinetic energy. However, in the vacuum the extra term enters in to the setup of the z-dependent functions. As a consequence the  $A$  and  $B$ -coefficients, the overlap matrix elements and the contribution to the Hamiltonian from the potential matrix are affected. Nevertheless, these changes are only indirect through the change of  $u_{\mathbf{G}_{\parallel\sigma}}$  and  $\dot{u}_{\mathbf{G}_{\parallel\sigma}}$ . To take the extra contribution to the kinetic energy into account the 1-dimensional Schrödinger equation for the z-dependent functions (3.24) has to be replaced by

$$\left\{ -\frac{\hbar^2}{2m} \frac{\partial^2}{\partial z^2} + \tilde{V}_{0\sigma\sigma}(z) - E_{vac,\sigma} + \frac{\hbar^2}{2m} (\mathbf{G}_{\parallel} + \mathbf{k}_{\parallel} \mp \mathbf{q}_{\parallel}/2)^2 \right\} u_{\mathbf{G}_{\parallel\sigma}}(\mathbf{k}_{\parallel}, z) = 0. \quad (5.51)$$

The equation for the energy derivative  $\dot{u}_{\mathbf{G}_{\parallel\sigma}}$  (3.25) has to be changed correspondingly. Once the z-depending functions have been setup including the extra term  $\mp \mathbf{q}_{\parallel}/2$  the rest of the matrix setup, e.g. Eqn. (5.21) – (5.23), remains unchanged provided that  $\mathbf{V}$  is replace by  $\tilde{\mathbf{V}}$  (5.21).

Inside of the muffin-tins the change to the plane waves do not play a role, instead spherical harmonics and radial functions are used. Therefore, the quantities  $\boldsymbol{\rho}$  and  $\mathbf{V}$  can still be used and do not need to be replaced by  $\tilde{\boldsymbol{\rho}}$  and  $\tilde{\mathbf{V}}$  in spin-spiral calculations. The changes to the basis set enter only through the boundary conditions, since the functions inside the spheres need to be matched to the plane waves in the interstitial including the extra term  $\mp \mathbf{q}/2$  now. By replacing  $e^{i(\mathbf{G}+\mathbf{k})\mathbf{r}}$  by  $e^{i(\mathbf{G}+\mathbf{k}\mp\mathbf{q}/2)\mathbf{r}}$  in (5.10) we find that the  $A$  and  $B$ -coefficients of a spin-spiral calculation can be expressed in terms of the corresponding coefficients of a collinear calculation.

$$\begin{aligned} A_{L\sigma\sigma\alpha}^{\mu\mathbf{G}}(\mathbf{k}, \mathbf{q}) &= (\chi_{\sigma\alpha}^{\alpha g})^* \chi_{\sigma} A_{L\sigma}^{\mu\mathbf{G}}(\mathbf{k} \mp \mathbf{q}/2) \\ B_{L\sigma\sigma\alpha}^{\mu\mathbf{G}}(\mathbf{k}, \mathbf{q}) &= (\chi_{\sigma\alpha}^{\alpha g})^* \chi_{\sigma} B_{L\sigma}^{\mu\mathbf{G}}(\mathbf{k} \mp \mathbf{q}/2) \end{aligned} \quad (5.52)$$

In contrast to an ordinary non-collinear calculation the coefficients for the two interstitial spin directions differ by more than a complex pre-factor in the spin-spiral case. Therefore, the very simple relations for the Hamiltonian and overlap matrix elements (5.17) and (5.18) do not hold anymore. Instead, the Hamiltonian matrix elements have to be calculated directly from Eqn. (5.16). As a consequence, the numerical effort setting up the contribution to the Hamiltonian and overlap matrix from the muffin-tins is increased compared to an ordinary non-collinear calculation.

### 5.5.2 Construction of the Charge and Magnetization Density

Due to plane wave expansion of the density matrix in the interstitial and vacuum region it is necessary to work exclusively with the periodic quantity  $\tilde{\boldsymbol{\rho}}$  rather than  $\boldsymbol{\rho}$  in these two regions. Starting from Eqn. (4.1) and substituting the representation of the eigenfunctions (5.24) we find that the contribution from a point  $\mathbf{K}$  in the Brillouin zone is given by

$$\rho_{\sigma\sigma'}(\mathbf{k}, \mathbf{r}) = \sum_{\nu} \sum_{\mathbf{G}} \sum_{\mathbf{G}'} \left( c_{\nu,\sigma}^{\mathbf{G}}(\mathbf{k}) \varphi_{\mathbf{G}\sigma}(\mathbf{k}, \mathbf{r}) \right)^* c_{\nu,\sigma'}^{\mathbf{G}'}(\mathbf{k}) \varphi_{\mathbf{G}'\sigma'}(\mathbf{k}, \mathbf{r}), \quad (5.53)$$

with the spin-spiral basis functions (5.46). To obtain an equation for  $\tilde{\rho}$  (5.53) has to be multiplied from the left and from the right by  $\mathbf{U}^\dagger$  and  $\mathbf{U}$  respectively.

$$\tilde{\rho}_{\sigma\sigma'}(\mathbf{k}, \mathbf{r}) = \sum_{\nu} \sum_{\mathbf{G}} \sum_{\mathbf{G}'} \left( c_{\nu,\sigma}^{\mathbf{G}}(\mathbf{k}) \tilde{\varphi}_{\mathbf{G}\sigma}(\mathbf{k}, \mathbf{r}) \right)^* c_{\nu,\sigma'}^{\mathbf{G}'}(\mathbf{k}) \tilde{\varphi}_{\mathbf{G}'\sigma'}(\mathbf{k}, \mathbf{r}), \quad (5.54)$$

Since the  $\tilde{\varphi}$  have exactly the same form as the plane waves in an ordinary calculation we can immediately write down the expression for the plane wave coefficients of  $\tilde{\rho}$  (cf. eqn. 5.25).

$$\tilde{\rho}_{\nu,\sigma\sigma'}^{\mathbf{G}}(\mathbf{k}) = \sum_{\mathbf{G}'} \left( c_{\nu,\sigma}^{\mathbf{G}'}(\mathbf{k}) \right)^* c_{\nu,\sigma'}^{\mathbf{G}+\mathbf{G}'}(\mathbf{k}). \quad (5.55)$$

The equation for  $\tilde{\rho}$  of a spin-spiral calculation has exactly the same form as the equation for  $\rho$  in a non-spin-spiral calculation (5.25), which means that no changes to the computer program are necessary.

The situation in the vacuum is very similar. Eqn. (5.26) has to be changed to

$$\begin{aligned} \tilde{\rho}_{\alpha\beta}^{\mathbf{G}_{\parallel}}(z) &= \sum_{\mathbf{k}_{\parallel}} \sum_{\nu} \sum_{\mathbf{G}'_{\parallel}} \left( A_{\nu,\alpha}^{\mathbf{G}'_{\parallel}}(\mathbf{k}_{\parallel}) \right)^* A_{\nu,\beta}^{\mathbf{G}_{\parallel}+\mathbf{G}'_{\parallel}}(\mathbf{k}_{\parallel}) w(\nu, \mathbf{k}_{\parallel}) u_{\mathbf{G}'_{\parallel},\alpha}(\mathbf{k}_{\parallel}, z) u_{\mathbf{G}_{\parallel},\beta+\mathbf{G}'_{\parallel}}(\mathbf{k}_{\parallel}, z) \\ &+ \dots \end{aligned} \quad (5.56)$$

Where the z-dependent functions have to be setup according to (5.51), taking into account the extra contribution to the kinetic energy.

In the muffin-tin spheres the only change are the different boundary conditions, i.e. the changed  $A$  and  $B$ -coefficients, since we do not need to work with  $\tilde{\rho}$  in the spheres as pointed out in the previous section.

### 5.5.3 Construction of the Potential Matrix

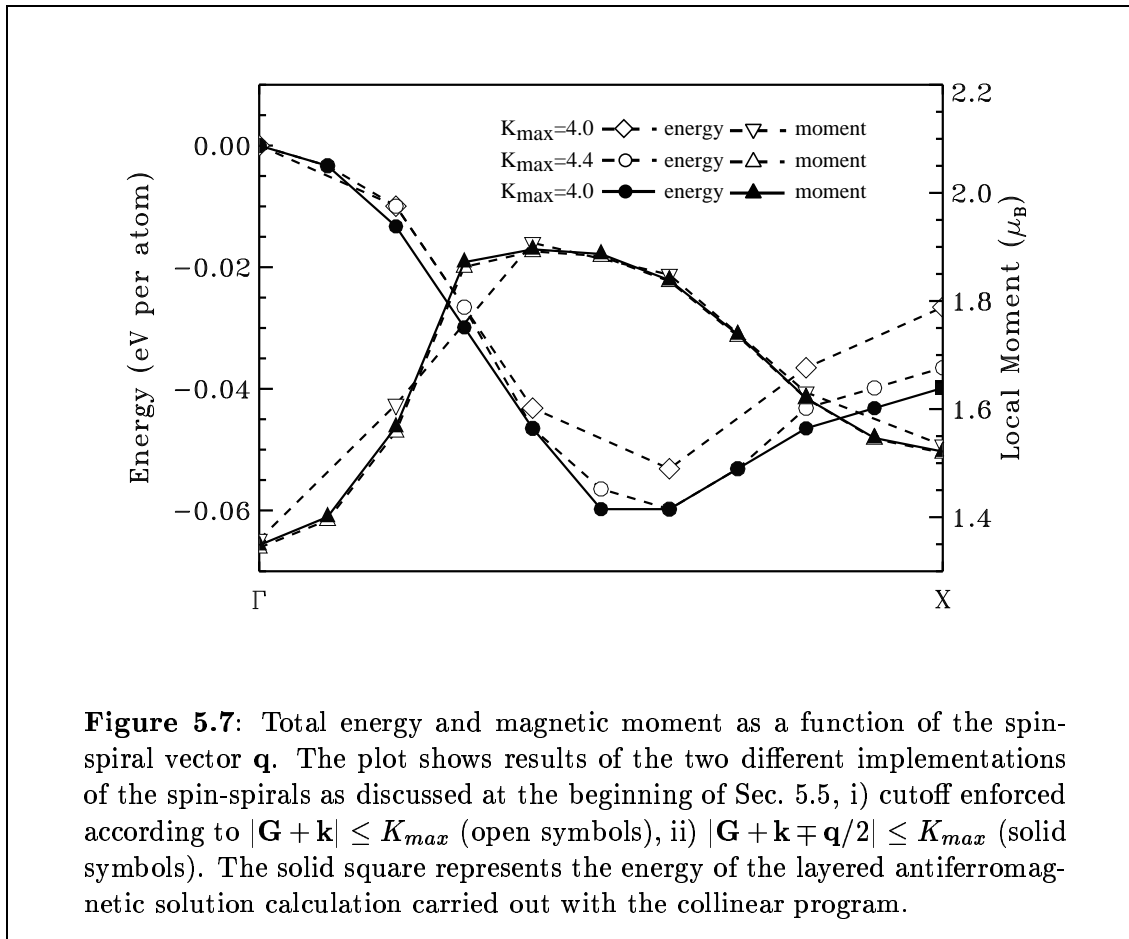
In a spin-spiral calculation the task of the potential generation involves determining  $\tilde{\mathbf{V}}$  from  $\tilde{\rho}$ . Starting from eqn. 5.30 and 5.31 the corresponding equations for  $\tilde{\rho}$  and  $\tilde{\mathbf{V}}$  are obtained by multiplying with  $\mathbf{U}(\mathbf{q} \cdot \mathbf{r}, 0, 0)$  and  $\mathbf{U}^\dagger(\mathbf{q} \cdot \mathbf{r}, 0, 0)$  from the right and from the left respectively. As a result we find that  $\tilde{\rho}$  and  $\tilde{\mathbf{V}}$  are diagonalized by  $\mathbf{U}(\tilde{\varphi}(\mathbf{r}), \vartheta(\mathbf{r}), 0)$ , where  $\tilde{\varphi}$  is given by  $\tilde{\varphi}(\mathbf{r}) = \varphi(\mathbf{r}) - \mathbf{q} \cdot \mathbf{r}$ . Thus, exactly the same scheme that is illustrated in Fig. 5.2 can be used in a spin-spiral calculation, with the only change that the quantities  $\rho$ ,  $\mathbf{V}$  and  $\varphi$  have to be replaced by their counterparts  $\tilde{\rho}$ ,  $\tilde{\mathbf{V}}$  and  $\tilde{\varphi}$ .

### 5.5.4 Test Calculations on fcc Iron

In order to test the spin-spiral implementation we have performed calculations on the  $\gamma$ -Fe (fcc Fe) system.  $\gamma$ -Fe has been extensively studied for many years. One of the reasons for the large experimental and theoretical attention this system attracted are the Invar properties of alloys based on  $\gamma$ -Fe. This interest has been renewed by neutron diffraction experiments by Tsunoda [Tsu89], who found that the ground

state of  $\gamma$ -Fe most likely consist of a non-collinear, spiral magnetic structure. This discovery stimulated many non-collinear ab-initio investigations by different authors [MLSG91, CBL91, MSLG92, USK92, USK94, MFL96, KE96]. The large amount of ab-initio data on  $\gamma$ -Fe spin-spirals make this an ideal test system for a spin-spiral implementation.

We have used the experimental Cu lattice constant of 6.82 a.u., since the  $\gamma$ -Fe has been found for Fe in a Cu matrix. Our  $k$ -point set corresponds to 1120  $k$ -points in the full three-dimensional Brillouin zone. Our unit cell contains two atoms and we have performed the calculation with two different plane wave cutoffs,  $K_{max} = 4.0$  a.u.<sup>-1</sup> and 4.4 a.u.<sup>-1</sup> corresponding to 85 and 115 basis functions per atom, respectively. The calculated total energies and magnetic moments for spin-spirals with  $q$ -vectors on the line  $\Gamma$ - $X$  are shown in Fig. 5.7. A spin-spiral with a  $q$ -vector at  $X$  corresponds to a layered antiferromagnetic configuration. The results agree with those of previous



calculations. We find the minimal energy for a  $q$ -vector of about  $\mathbf{q} \approx 0.55\bar{X}$ . The minimal  $q$ -vector, the shape of the energy curve and, in particular, the magnetic moment of  $\gamma$ -Fe varies strongly with the lattice parameter. Uhl et al. [USK92] found a low-spin ferromagnetic solution for Wigner-Seitz radii of 2.66 a.u. ( $a = 6.81$  a.u.) and

smaller, using a spin-spiral method. For Wigner-Seitz radii of 2.67 a.u. ( $a = 6.83$  a.u.) and larger they found a high-spin solution. The magnetic moments were about  $0.6 \mu_B$  for the low- and  $2.5 \mu_B$  for the high-spin state. Other authors [MLSG92] report a ferromagnetic moment of about  $0.9 \mu_B$  at a Wigner-Seitz radius of  $R_{WS} = 2.66$  a.u. We have found a moment of  $1.3 \mu_B$ , which lies within that range.

As I have explained at the beginning of Sec. 5.5 we have tested two slightly different implementations of the spin-spirals, that use different cutoff conditions for the basis functions: i)  $|\mathbf{G} + \mathbf{k}| \leq K_{max}$  and ii)  $|\mathbf{G} + \mathbf{k} \mp \mathbf{q}/2| \leq K_{max}$ . Fig. 5.7 presents results for both implementations. Implementation i) is expected to yield less accurate energies, they are generally too large for large  $\mathbf{q}$ . This can very clearly be seen from Fig. 5.7. Even for the larger cutoff of  $4.4 \text{ a.u.}^{-1}$  implementation i) deviates from implementation ii). In particular, implementation i) gives larger total energies. The accuracy of this improved implementation can be appreciated from the fact that the result for a  $q$ -vector of  $\mathbf{q} = \bar{X}$  coincides with that of a collinear antiferromagnetic calculation (solid square at the right-hand side of the plot). To achieve the same accuracy with implementation i) it would be necessary to go to even higher plane wave cutoffs. However, increasing  $K_{max}$  from  $4.0 \text{ a.u.}^{-1}$  to  $4.4 \text{ a.u.}^{-1}$  already means to use 115 basis functions per atom rather than 85, which makes the calculation much more time consuming, since the effort of setting up and diagonalizing the matrix scales with the number of basis functions to the third power.





## Chapter 6

# Magnetism of 3d-monolayers on Cu and Ag (111)

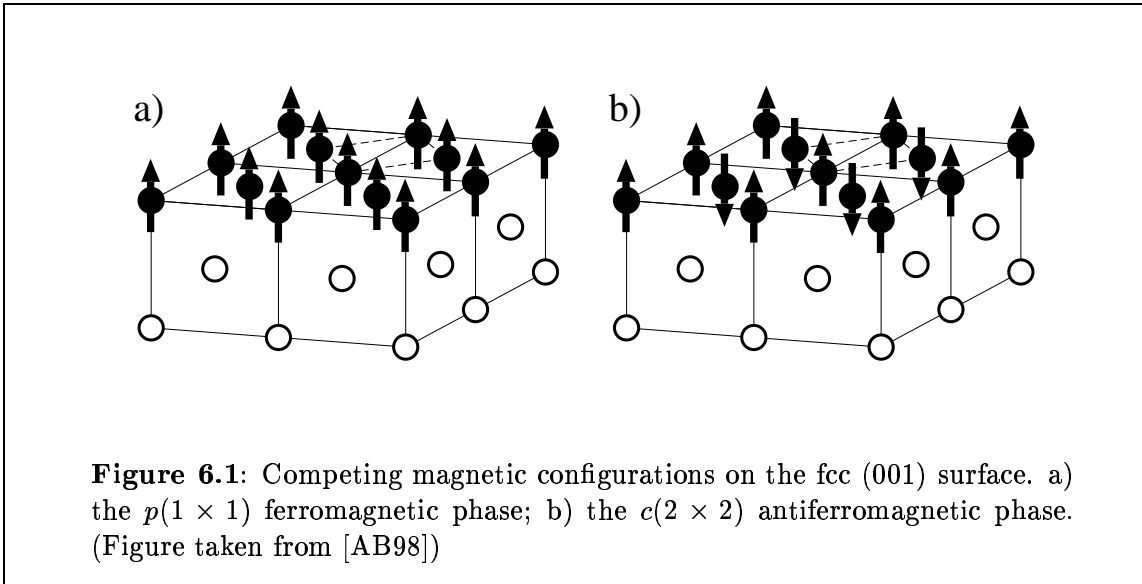
In the frontier field of nano-magnetism understanding the effect of frustration on the magnetic properties is one of the current key issues. Exchange bias [NS99], for example, is a technologically important effect for the magnetic recording industry and the magnetoelectronics, for which frustration plays an important role. In magnetic systems the term frustration refers to the inability to satisfy the competing exchange interactions to neighboring atoms. Frustration is known to be responsible for a number of diverse phenomena such as spin-glass behavior, non-collinear and incommensurate magnetic order and unusual critical properties. Frustration is very common in low dimensional systems like for example small (antiferro-) magnetic cluster in the gas phase [IA99], deposited on surfaces [UUD99] or included in biological molecules. A further example are step edges at interfaces between a ferromagnet and an antiferromagnet, e.g. Fe and Cr [SG93, SG95, VSDD95, BF97, BHB<sup>+</sup>98]. But magnetic frustration also appears in the bulk phase, e.g. in the alloys of FeMn [KHSW88a, KK63, EI71], RhMn<sub>3</sub> [KK65, KKPS67] and PtMn<sub>3</sub> [KKP<sup>+</sup>68]. One of the most evident examples of frustration is the so-called geometric frustration of an antiferromagnet on a triangular lattice. In fact, triangular antiferromagnets can be crystallized e.g. in form of stacked antiferromagnets. Typical compounds are RbNiCl<sub>3</sub>, VCl<sub>2</sub>, or CuCrO<sub>2</sub> [Kaw98, CP97] and they are localized spin systems. The magnetic properties of these triangular antiferromagnets are almost exclusively described within the framework of model Hamiltonians the simplest of which is the classical Heisenberg model.

Another physical realization of antiferromagnetism on the triangular lattice are antiferromagnetic monolayers grown on the (0001) surface of an hcp crystal or the (111) surface of an fcc crystal of a non-magnetic or ferromagnetic substrate. In the recent years the epitaxial growth of such ultra-thin films has been studied intensively by various experimental techniques. In particular, Mn films on the (111) surface of fcc Pd [TLW<sup>+</sup>92], Ir [AFM<sup>+</sup>96], Cu [TBJ92, GW97, GWH<sup>+</sup>98] and MgO [GSFW99] and on the (0001) surface of Ru [AHP<sup>+</sup>87] and Co [OVH<sup>+</sup>94] have been prepared and

analyzed. But also other ultra-thin hexagonal films, e.g. Cr and V on Pt (111) and Ru (0001) [ZKD97, APW<sup>+</sup>98, SG99], have been investigated. A triangular lattice can also be provided by pseudo-hexagonal growth on non-hexagonal substrates as for example by the  $c(8 \times 2)$  reconstruction of Mn on Cu(001) [FW92].

During the recent years, a particular interest has developed in 3d transition metal films on noble metal substrates. They represent very interesting physical systems, both experimentally and theoretically [FPB<sup>+</sup>90, Sie92, LF85, FFO85, Ter87, BDZD89, FW91, WB93, Blü95]. Due to filled  $d$ -bands of the noble metals the  $3d$ - $3d$  hybridization between the overlayer and the substrate is small, which leads to a narrowing of the  $d$ -bands in the monolayer compared to the bulk transition-metals. As a consequence, magnetism is enhanced and the magnetic moments become larger (cf. Fig. 6.2 top panel). Moreover, there is a possibility of new magnetic materials, which are non-magnetic as bulk metals and may become magnetic in low dimensions, e.g. V.

So far most of the work has been done on overlayers grown on the (100) oriented substrates, where the atoms of the monolayer are arranged on a square lattice. In these monolayers, there is a competition between two magnetic configurations, the  $p(1 \times 1)$  ferromagnetic (Fig. 6.1 a) and the  $c(2 \times 2)$  antiferromagnetic phase (Fig. 6.1 b). The energy difference between the two magnetic configuration has been



calculated on different (001) oriented substrates [BWD88, BD89, Blü96]. The results of these calculations for the Cu (001) and the Ag (001) substrate are shown in Fig. 6.2 (lower panel). It turns out, that the early transition-metals, V, Cr and Mn, were predicted to order  $c(2 \times 2)$  antiferromagnetically, while Fe, Co and Ni prefer the  $p(1 \times 1)$  ferromagnetic configuration. Currently, huge experimental efforts are being undertaken to spatially determine the microscopic structure of the antiferromagnetic thin film [SSL<sup>+</sup>00]. Very recently, it has been shown that it is possible to image the magnetism of antiferromagnetic thin films using the spin-polarized scanning tunnel

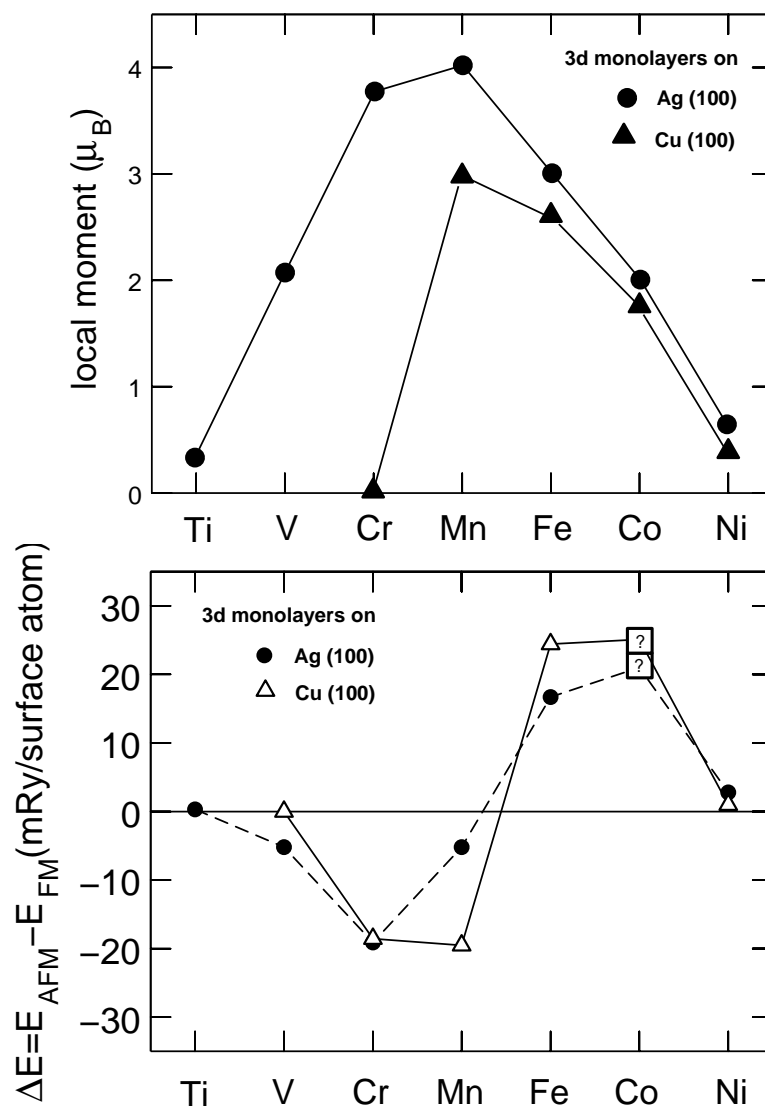


**Figure 6.2:** Magnetic moments (for the ferromagnetic configuration, top panel) and total energy difference per  $3d$  atom between the  $p(1 \times 1)$  ferromagnetic and the  $c(2 \times 2)$  antiferromagnetic phase (lower panel) for  $3d$  transition metal monolayers on Cu and Ag(100). A negative energy difference means, that the antiferromagnetic configuration is more stable than the ferromagnetic one. (Figure taken from [Blü96])

microscope (STM) on the atomic scale [HBK<sup>+</sup>00]. With this technique it is possible to distinguish atoms with different spin orientations in an antiferromagnetic surface. For the example of a mono-atomic layer of Mn on the W (110) surface, these experiments verify the theoretical predictions.

Not only the magnetic, but also the structural ground states of  $3d$  monolayers on noble metal substrates have been investigated. The stability of Mn/Cu(001) films

against clustering and interdiffusion and in particular the formation of Mn/Cu surface alloys has been investigated [Blü96]. In a series of experimental investigations Wuttig et al. have studied such alloys formed after deposition of Mn on Cu(001) [FW92, WT93, WFF95]. Several recent experiments confirmed the formation of these surface alloys as well as the formation of large magnetic moments [OZT93, OT94, HPW95, SRCE96, RGC<sup>+</sup>97]. But the interest is not limited to the Mn/Cu system: In search of an understanding of the correlation between volume, magnetism and surface alloy formation, Mn deposited on Pd(100) [TLJ90] and Ag(100) [SKHG97, SKHG98] has been investigated experimentally as well as theoretically [KKO<sup>+</sup>98, AB98].

While 3d metal films grown on fcc (001) oriented noble metal surfaces are well investigated both experimentally and theoretically, little theoretical work has been done on (111) oriented substrate. Recently, Krüger et al. [KTMA00] studied 3d transition metal monolayers on Cu(111) and Ag(111). Bihlmayer et al. investigated the Mn/Cu(111) system [BKB00], concentrating on the stability of surface alloys and mono-atomic films against interdiffusion and clustering in different magnetic configurations, including also non-collinear magnetic states. We have also investigated the non-collinear magnetism of monolayers of Cr and Mn on Cu(111) [KBB00]. Spišák and Hafner [SH00] investigated the magnetic structure of the same system. However, they come to a different conclusion than we do.

In this chapter we present results of ab-initio calculations for monolayers of the early 3d transition metals V, Cr, Mn and Fe on the Cu(111) and the Ag(111) surface, with the aim to find the magnetic ground state configuration, taking into account collinear, non-collinear and also incommensurate magnetic structures. Until now, there have been hardly any investigations of two-dimensional antiferromagnets on a triangular lattice beyond model Hamiltonians. In contrast to the stacked triangular antiferromagnets, like RbNiCl<sub>3</sub>, VCl<sub>2</sub>, or CuCrO<sub>2</sub>, which are localized spin systems, in itinerant magnets, the electrons that are responsible for the formation of the magnetic state do participate in the formation of the Fermi-surface and hop across the lattice. Thus, it is by no means clear how far a short-ranged n.n. interaction or even how far the Heisenberg model can go in giving a sufficiently good description of the physics of itinerant magnets on a triangular lattice.

Since non-collinear calculations are computationally extremely demanding, we started our study using unsupported monolayers as model systems for the monolayers on the substrate. Because of the small 3d-3d hybridization between the overlayers and the substrate, neglecting the substrate is a reasonable approximation. Hence, the UMLs represent a good starting point to investigate the magnetism of the monolayer systems. In Sec. 6.1 we investigate the change of the total energy and the magnetic moment upon the rotation of the local moment in real space in different magnetic unit cells. We find surprising results, which cannot be explained in terms of the nearest neighbor Heisenberg model. Therefore, in Sec. 6.2 we present a comprehensive study the Heisenberg model on the triangular lattice beyond the nearest neighbor interaction. We develop a  $T = 0$  phase diagram of possible spin-structures and discuss also the relevant higher order spin interactions. In the light of these results

we investigate in Sec. 6.3 the magnetism of unsupported monolayers, but this time in reciprocal space in terms of spin-spirals for spin-spiral  $q$ -vectors along the high symmetry lines in the two-dimensional Brillouin zone. Particular multiple spin-wave states have been taken into consideration. The accuracy of our results with respect to the computational parameters is discussed in detail. From the results of Sec. 6.1 and Sec. 6.3 exchange parameters are estimated in Sec. 6.4 and the results are classified and discussed on the basis of these parameters. From this discussion we conclude the existence of spin-spiral ground states for MnFe alloy films. Results of  $3d$  metal monolayers on actual Cu(111) and Ag(111) substrates including test of the accuracy are presented and discussed in Sec. 6.5. In Sec. 6.6 we suggest spin-polarized scanning tunneling microscopy experiments to unravel the complex spin structures with fully compensated magnetic moments in the unit cell of chemically identical atoms.

## 6.1 Unsupported monolayers: Rotation in real space

We have performed self-consistent calculations of hexagonal unsupported monolayers (UMLs) of  $3d$  transition metals. These UMLs have the same geometry as monolayers (MLs) on an (111) oriented fcc substrate and we used the lattice constant of Cu and Ag respectively. In order to find possible candidates for (non-collinear) ground state configurations we investigate first the Heisenberg model. Localized spin systems are well described by restricting the magnetic exchange interaction to nearest neighbors (n.n.). In this approximation the minimum energy configuration of a material with antiferromagnetic exchange in this geometry is a two-dimensional non-collinear structure, where the moments of the individual atoms are aligned at  $120^\circ$  with respect to each other (cf. Sec. 6.2). This state is called the Néel state and is shown in Fig. 6.3 b. The unit cell of the Néel state contains three atoms and is of  $(\sqrt{3} \times \sqrt{3})R30^\circ$  structure (Fig. 6.3 d). Each atom forms a sublattice on which the magnetic moments are ferromagnetically aligned. It has the same shape as the  $p(1 \times 1)$  unit cell of the ferromagnetic (FM) state, but it is rotated by  $30^\circ$  and the lattice constant is by a factor of  $\sqrt{3}$  larger. In addition we considered a collinear row-wise antiferromagnetic (RW-AFM) structure, which is shown in Fig. 6.3 a. The unit cell of this magnetic configuration (Fig. 6.3 c) contains two atoms. We change the angle of the local moments in small steps on continuous paths connecting the high symmetry states in both unit cells. In the unit cell with two atoms we rotated one atom from the FM state to the RW-AFM state according to Fig. 6.3 c. In the unit cell containing three atoms we rotated two atoms by the same angle  $\alpha$  but in opposite directions. Thus, starting from the FM state the moments are rotated towards the Néel structure ( $\alpha = 120^\circ$ ) and finally into a collinear ferrimagnetic (FI) state ( $\alpha = 180^\circ$ ). The latter state has a net magnetic moment, since two atoms have parallel moments and only one atom points into the opposite direction.

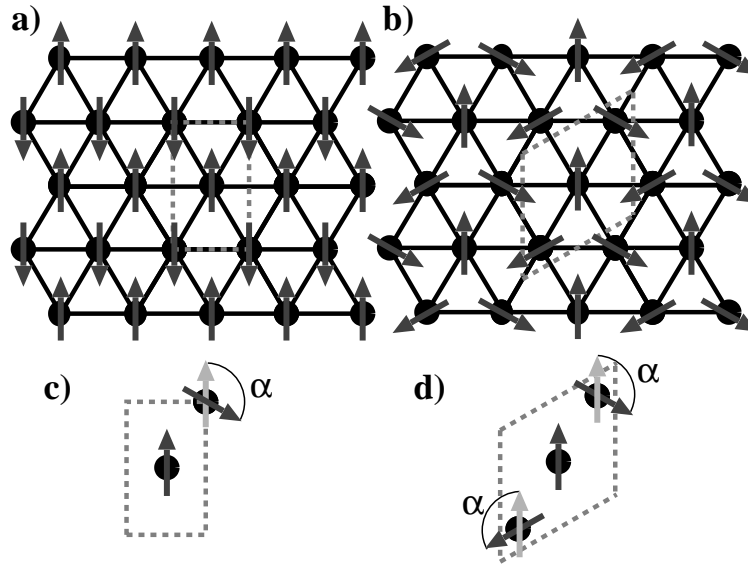


**Figure 6.3:** (a) The row-wise antiferromagnetic structure (RW-AFM). (b) The non-collinear Néel state. The ferromagnetic structure can be transformed by a continuous rotation into structure (a) via path (c) and into structure (b) via path (d). Since the calculations have been performed within the scalar-relativistic approximation, which neglects spin-orbit coupling, the direction of the magnetic moments with respect to the lattice is undetermined. They are drawn in plane only for better illustration.

### 6.1.1 Computational details

We performed self-consistent constrained local moment (CLM, cf. Sec. 4.1 and 5.4) calculations in the local density approximation (LDA) applying the parameterization according to Moruzzi, Janak and Williams [MJW78]. We chose the theoretical Cu and Ag lattice constants,  $a_{Cu} = 6.65$  a.u. and  $a_{Ag} = 7.79$  a.u. [MJW78]. The planewave cutoff for the basis functions was set to  $K_{max} = 3.7$  a.u.<sup>-1</sup> for the UMLs with Cu(111) geometry and  $K_{max} = 3.3$  a.u.<sup>-1</sup> for the UMLs with Ag(111) geometry. This corresponds to about 110 and 125 basis functions per atom for Cu(111) and Ag(111), respectively. The charge density and the potential were expanded up to a cutoff  $G_{max} = 9.0$  a.u.<sup>-1</sup> in both cases. The muffin-tin radii of the 3d transition metals was chosen as  $R_{MT} = 2.35$  a.u. and  $R_{MT} = 2.75$  a.u. for Cu and Ag, respectively. The wave functions as well as the density and the potential were expanded up to  $l_{max} = 8$  inside the muffin-tin spheres. For the unit cell with two atoms we used 135  $k$ -points in the irreducible wedge of the two-dimensional Brillouin zone (IBZ) corresponding to 540  $k$ -points in the full two-dimensional Brillouin zone. In the unit

cell containing three atoms we used 70  $k$ -points in the IBZ corresponding to 361  $k$ -points in full Brillouin zone. Both  $k$ -point set correspond to slightly more than 1000  $k$ -points in the  $p(1 \times 1)$  unit cell. With these  $k$ -point sets it is guaranteed that the total energies of different unit cells are absolutely converged and directly comparable.

## 6.1.2 Results for the real-space rotation

The moments and the total energy of the UMLs on Cu(111) are presented in Fig. 6.5. It can be seen that the magnetic moments of Cr, Mn and Fe are very large (cf. also Tab. 6.1). Due to the symmetry the size of the local moments of two atoms is equal for

UML	Cr	Mn	Fe
FM	–	3.06 $\mu_B$	2.75 $\mu_B$
RW-AFM	2.62 $\mu_B$	3.08 $\mu_B$	2.58 $\mu_B$
Néel	2.58 $\mu_B$	3.06 $\mu_B$	2.54 $\mu_B$

**Table 6.1:** Magnetic moment of different magnetic states inside the muffin-tin spheres for the UMLs Cu(111).

all angles along the rotation path according to Fig. 6.3 c. Similarly, during the second rotation (Fig. 6.3 d), the size of the two outer atoms (down-triangles) that are rotated is equal, but is generally different from the size of the third atom at the center of the unit cell (up-triangles). Only in the FM state and the Néel state, where all three atoms are equivalent, all moments have the same size. Mn shows the largest moment in agreement with Hund’s first rule. This effect is well known from the work of the past years. The moments calculated for the UMLs are in reasonable agreement with our results including the substrate and also with earlier results of monolayers on the (001) surface [Blü96], even though the substrate has been neglected here. This shows the influence of the substrate on the size of the moments is not severe, since the magnetic moments are already close to saturation. It should be noted that care is needed when comparing the moments with other results, in particular comparing FLAPW results with other methods. Unless stated otherwise, all local moments presented in this work are moments inside the muffin-tin sphere. Hence, these moments are always slightly smaller than the total moments per atom, since the contributions from the interstitial region and the vacuum region are missing. As a consequence, the moments calculated with the FLAPW method always depend on the choice of the muffin-tin radii. To clarify the size of this difference, we present in Tab. 6.2 a comparison between the muffin-tin moments and the total moments per atom for Mn and Fe in the FM state. The comparison reveals that the difference between the total moment and the muffin-tin moment depends strongly on the chemical element. For Mn this difference is about 10%, while it is less than 2% for Fe. This is explained by the different localization of the  $3d$  wave functions. The localization decreases with decreasing nuclear number, which reduces the ratio of  $d$ -charge inside the muffin-tin



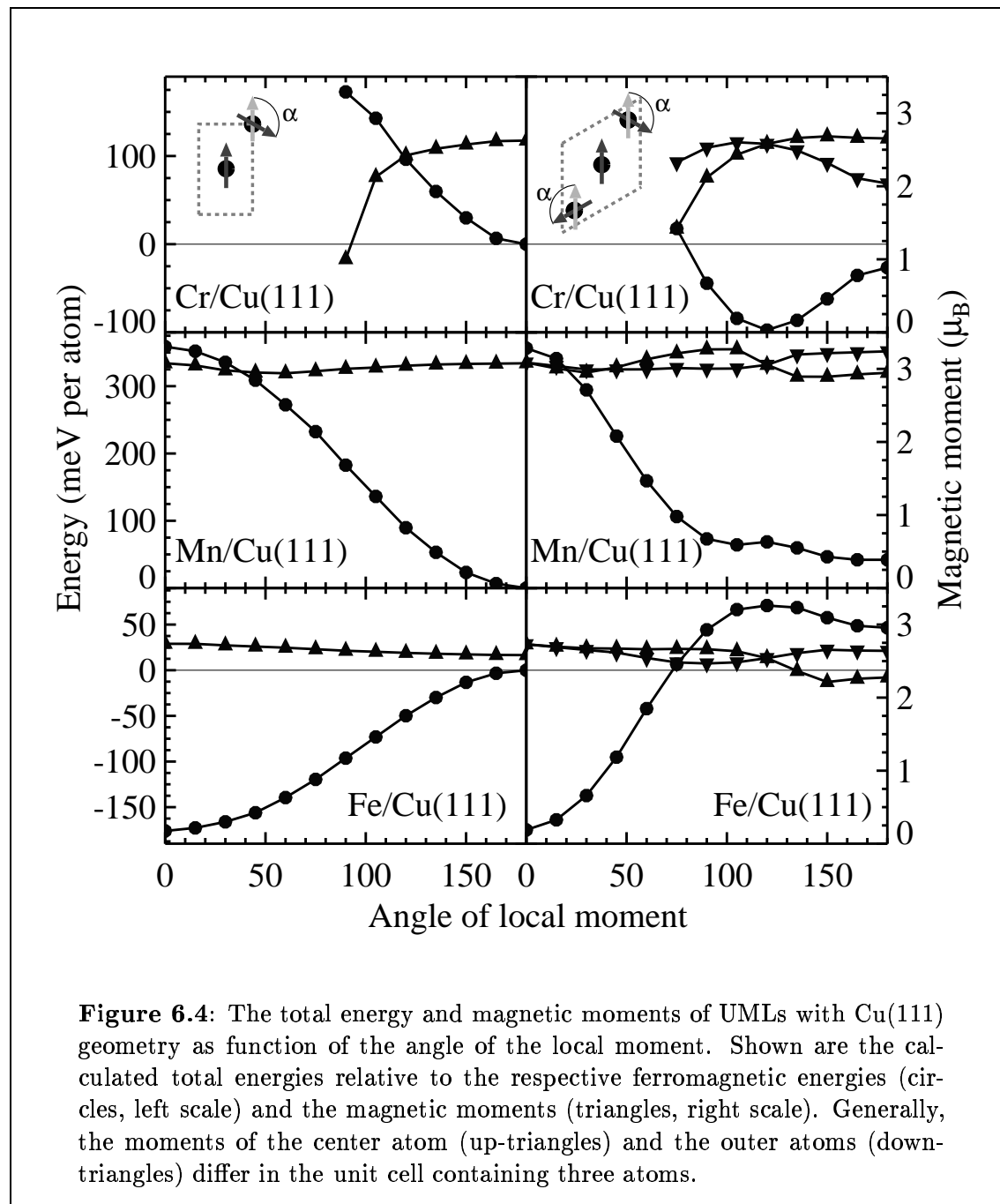


**Figure 6.4:** The total energy and magnetic moments of UMLs with Cu(111) geometry as function of the angle of the local moment. Shown are the calculated total energies relative to the respective ferromagnetic energies (circles, left scale) and the magnetic moments (triangles, right scale). Generally, the moments of the center atom (up-triangles) and the outer atoms (down-triangles) differ in the unit cell containing three atoms.

sphere, and thus the ratio of the magnetic moment, which is mainly produced by the  $d$ -electrons. We expect the same effect for other magnetic configurations. However, in the antiferromagnetic and non-collinear configurations the contributions of different atoms to the interstitial magnetization cancel partly or completely (RW-AFM Néel). Thus, the total magnetic moment has to be estimated from the muffin-tin moment.

Coming back to Fig. 6.4, consider first Cr. In contrast to Mn and Fe the local

UML	Mn	Fe
MT	3.06 $\mu_B$	2.75 $\mu_B$
total	3.40 $\mu_B$	2.80 $\mu_B$

**Table 6.2:** Comparison between the magnetic moments inside the muffin-tin sphere (MT) and the total magnetic moment per atom in the FM state for the UML Cu(111).

moment of Cr depends very strongly on the angle. In fact, a ferromagnetic solution does not exist. Starting from the row-wise antiferromagnetic solution (upper left panel,  $\alpha = 180^\circ$ ) and rotating towards the ferromagnetic structure the magnetic moment decreases rapidly and finally disappears at  $\alpha \approx 80^\circ$ . Although the moment changes drastically, the energy shows a cosine-like behavior in the region where a magnetic solution exists, as the nearest neighbor (n.n.) Heisenberg model predicts for an antiferromagnet. The total energy along the rotation path in the unit cell of Fig. 6.3 d (upper right panel of Fig. 6.4) reveals a pronounced minimum at  $120^\circ$ . This minimum and the shape of the energy curve matches the expectation from the n.n. Heisenberg model with antiferromagnetic exchange interaction very well. It is clearly visible that the  $120^\circ$  configuration is the lowest energy configuration among all configurations studied here. Thus, for Cr(111) UML the Néel state is the magnetic ground state predicted by the present investigation.

Now turning to Mn and comparing the results in the two-atom unit-cell (center left panel of Fig. 6.4) with those of Cr we found that the behavior of Mn and Cr is similar, i.e. the energy curve is also cosine-like and Mn prefers to be antiferromagnetic. However, in contrast to Cr the ferromagnetic state exists and the magnetic moments change only within a narrow range, ( $2.9 \mu_B - 3.05 \mu_B$ ), of the rotation. However, the result of the rotation in the three-atom unit-cell is unexpected. The dependence of the energy on the rotation angle  $E(\alpha)$  reveals two surprises: First, the lowest energy configuration among all magnetic structures investigated so far, is the row-wise antiferromagnetic configuration. Secondly, the total energy of the Mn system with 3 atoms per unit cell does not exhibit a minimum at  $120^\circ$ , as predicted by the n.n. Heisenberg model, but a local maximum instead. Both results are clearly in disagreement with the n.n. Heisenberg model.

Fe behaves completely different from Cr and Mn. Obviously, the FM state has the lowest energy. Along the rotation path according to Fig. 6.3 c (lower left panel)  $E(\alpha)$  has a cosine-like shape, but the energy increases from the ferromagnetic configuration to the antiferromagnetic one. Also the result for the second rotation (lower right panel) is in agreement with the n.n. Heisenberg model with ferromagnetic coupling.  $E(\alpha)$  has the form of the mirror image of the energy of Cr (where a magnetic solution exists): at  $120^\circ$  the energy goes through a maximum. During the rotation the local moments vary in a range from  $2.3 \mu_B$  to  $2.7 \mu_B$ .

The results for the unsupported monolayers with the Ag lattice constant are

presented in Fig. 6.5. The local moments we found are even larger than those of the UMLs with Cu(111) geometry (cf. also Tab. 6.3). Cr, which does not have a

UML	V	Cr	Mn	Fe
FM	2.78 $\mu_B$	4.15 $\mu_B$	4.19 $\mu_B$	3.18 $\mu_B$
RW-AFM	2.63 $\mu_B$	4.09 $\mu_B$	4.17 $\mu_B$	3.23 $\mu_B$
Néel	2.56 $\mu_B$	4.00 $\mu_B$	4.22 $\mu_B$	3.24 $\mu_B$

**Table 6.3:** Magnetic moment of different magnetic states inside the muffin-tin spheres for the UMLs Ag(111).

ferromagnetic solution on the Cu lattice constant, has a ferromagnetic solution at the Ag lattice constant. Even V, for which we did not find any magnetic solution in the Cu(111) geometry, becomes magnetic in the Ag(111) geometry. The reason for this is the larger lattice constant of Ag, which leads to weaker  $d$ - $d$  hybridization, and thus to a further narrowing of the  $d$ -bands. The moments of Mn and Fe are in reasonable agreement with the results including the substrate. However, Cr and V are more sensitive to their local environment. In particular, the effect of the substrate on V is very strong. The moment of the V UML is much larger than that of the ML on the Ag(111) substrate (cf. tab. 6.12). A comparison between the muffin-tin moments and the total moment (Tab. 6.4) of the ferromagnetic UMLs reveals two trends. First, considering Mn and Fe, we found that the difference between the

UML	V	Cr	Mn	Fe
MT	2.78 $\mu_B$	4.15 $\mu_B$	4.19 $\mu_B$	3.18 $\mu_B$
total	3.32 $\mu_B$	4.61 $\mu_B$	4.44 $\mu_B$	3.19 $\mu_B$
%	83.7	90.0	94.4	99.6

**Table 6.4:** Comparison between the magnetic moments inside the muffin-tin (MT) and the total magnetic moment per atom in the FM state.

total and the muffin-tin moment is less than 6% for Mn and less than 0.5% for Fe. This difference is smaller than what we found on the Cu lattice constant. This is probably due to the larger muffin-tin radius we used on the Ag lattice constant. A larger fraction of the  $d$ -wave functions is inside the muffin-tin sphere, and thus the polarization in the interstitial region is smaller. Secondly, the further we move to the right in the transition metal series, i.e. from V to Fe, the more the magnetization is confined inside the muffin-tins. The reason is that with increasing nuclear number the  $d$ -wave functions become more localized, in fact the whole atom shrinks.

Coming back to Fig. 6.5, the result of the V/Ag calculation is quite unexpected. In both unit cells the shape of  $E(\alpha)$  is very unlike the other materials. In the two-atom unit-cell the energy shows a maximum around  $60^\circ$  and also in the three-atom unit-cell a tendency towards a local maximum around  $40^\circ$  is visible. The shape of the

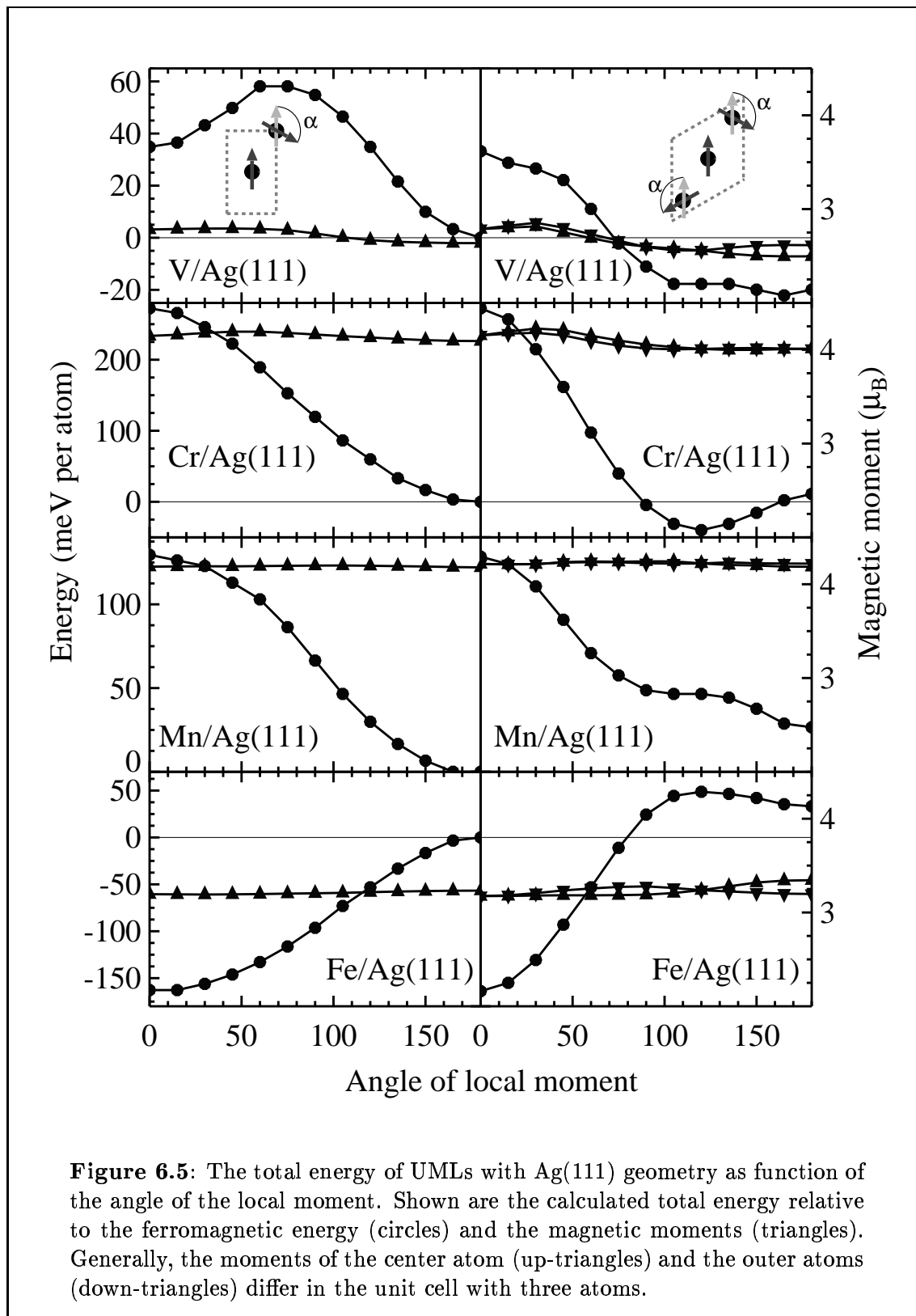


**Figure 6.5:** The total energy of UMLs with Ag(111) geometry as function of the angle of the local moment. Shown are the calculated total energy relative to the ferromagnetic energy (circles) and the magnetic moments (triangles). Generally, the moments of the center atom (up-triangles) and the outer atoms (down-triangles) differ in the unit cell with three atoms.

energy curve in the two-atom unit-cell can be reproduced by a superposition of a  $\cos \alpha$  and a  $\cos 2\alpha$  term. However, a  $\cos 2\alpha$  term cannot be provided by the Heisenberg model. Only higher order contributions beyond the Heisenberg model can explain this behavior.

Apart from the fact, that the Cr moment is larger than on the Cu lattice constant and varies only in a range from  $4.0 \mu_B$  to  $4.2 \mu_B$ , the result for the Cr UML with Ag(111) geometry is very similar to that with Cu(111) geometry in the region of angles, where a magnetic solutions exists on the Cu lattice constant.  $E(\alpha)$  has a cosine-like shape in the two-atom unit-cell and also in the three-atom unit-cell.  $E(\alpha)$  is in good agreement with the n.n. Heisenberg model, showing a pronounced minimum at  $120^\circ$ . As on the Cu lattice constant, the Néel state is the lowest energy configuration. The only qualitative difference to the result of the Cr/Cu(111) UML is that in the case of Cr/Cu(111) the FI state has a lower energy than the RW-AFM state, while for Ag/Cu(111) the energy of the FI state is slightly higher.

For the Mn UML with Ag(111) geometry we found that the moments hardly change with the rotation ( $4.18 \mu_B - 4.24 \mu_B$ ). Also for Mn the result for Ag(111) UML is in qualitative agreement with the Cu(111) UML. However, the total energy difference between FM and RW-AFM is about a factor of three smaller than for the UML Mn/Cu(111), while the energy differences between the Néel state, the FI state and the RW-AFM state are only reduced by 30 – 40%. Again, the result is in disagreement with the n.n. Heisenberg model, since the RW-AFM state has the lowest total energy and  $E(\alpha)$  has a local maximum at  $120^\circ$  when the moments are rotated in the unit cell with three atoms.

In line with the findings for the other UMLs on the Ag lattice constant the magnetic moments of Fe vary only within a small range ( $3.17 \mu_B - 3.34 \mu_B$ ). The behavior of the total energy,  $E(\alpha)$ , is extremely similar to the result of the Fe UML with the Cu(111) lattice constant.

In summary, we found that the behavior of the UMLs of Cr and Fe on both, the Cu and the Ag lattice constant, can be understood in terms of the nearest neighbor Heisenberg model with an antiferromagnetic and ferromagnetic nearest-neighbor exchange constant, respectively. However, the result of the Mn UMLs is in clear disagreement with this widely used model. Though Mn prefers to be antiferromagnetic, we do not find a minimum of the energy for the Néel state, but instead the row-wise antiferromagnetic configuration has the lowest energy on both lattice constants. In particular, the shape of the energy curve in the three atom unit cell,  $E(\alpha)$ , cannot be explained within the Heisenberg model, even if terms beyond the nearest-neighbor interaction are included. Considering a magnetic configuration characterized by an angle  $\alpha$  in the three-atom unit cell on the path according to Fig. 6.3 d, it is obvious that the moments of any pair of atoms in the monolayer span an angle of either  $\alpha$  or  $2\alpha$ . Hence, irrespective of how many neighbors are included in the Heisenberg model, the functional dependence of the energy on the angle contains only terms proportional to  $\cos \alpha$  or  $\cos 2\alpha$ . However, to reproduce the shape of  $E(\alpha)$  for Mn is necessary to include at least a term proportional to  $\cos 3\alpha$ , which cannot be derived from the

Heisenberg model. Thus, higher order interactions, that go beyond the Heisenberg model, like the 4-spin interaction, have to be taken into account to explain the Mn result.

## 6.2 Model Hamiltonians: Heisenberg model and beyond

In the past magnetic properties of antiferromagnets on the triangular lattice have almost exclusively been discussed within the framework of model Hamiltonians, e.g. [Wan50]. A very active research field is taking the quantum nature of the spin into account, in particular within the framework of the Heisenberg model [LJNL86, CP97, Kaw98, CTS99, CCT<sup>+</sup>99]. Since we are investigating 3d-metals, which are itinerant magnets, on the triangular lattice, it is not a priori clear in how far the Heisenberg model can give a good description of these systems. To investigate this point we start with the classical Heisenberg Hamiltonian

$$H = \sum_{i,j} -J_{ij} \mathbf{S}_i \cdot \mathbf{S}_j, \quad (6.1)$$

where the double sum is over all (magnetic) atoms in the system. We consider the spins localized on the lattice sites as classical vectors, using the assumption that the spins on all lattice sites have the same magnitude  $S$ :

$$\mathbf{S}_i^2 = S^2, \text{ for all } i. \quad (6.2)$$

In a second step we include higher order corrections and investigate whether the resulting model can account for the results of the ab-initio calculations.

### 6.2.1 The Heisenberg model on a Bravais lattice

Since we investigate the magnetism on a periodic lattice it is very convenient to express the quantities in terms of their Fourier components. We assume periodic boundary conditions. The number of lattice sites in the crystal will be denoted  $N$ . Thus, the spins on lattice sites can be written in terms of their discrete Fourier components by:

$$\mathbf{S}_i = \sum_{\mathbf{q}} \mathbf{S}_{\mathbf{q}} e^{i\mathbf{q}\mathbf{R}_i}, \quad (6.3)$$

where the sum is over the reciprocal lattice vectors  $\mathbf{q}$  and  $\mathbf{R}_i$  is the real-space coordinate of lattice site  $i$ . The inverse Fourier transform is given by:

$$\mathbf{S}_{\mathbf{q}} = \frac{1}{N} \sum_i \mathbf{S}_i e^{-i\mathbf{q}\mathbf{R}_i}. \quad (6.4)$$

Since the spins  $\mathbf{S}_i$  are real quantities we can immediately conclude from Eqn. (6.4) that the Fourier components of the spins fulfill the relation

$$\mathbf{S}_{\mathbf{q}} = \mathbf{S}_{-\mathbf{q}}^*. \quad (6.5)$$

Replacing the localized spin  $\mathbf{S}_i$  by their Fourier components in the Heisenberg Hamiltonian, Eqn. (6.1), yields

$$\begin{aligned} H &= \sum_{i,j} -J_{ij} \sum_{\mathbf{q}\mathbf{q}'} \mathbf{S}_{\mathbf{q}} \cdot \mathbf{S}_{\mathbf{q}'} e^{i\mathbf{q}\mathbf{R}_i} e^{i\mathbf{q}'\mathbf{R}_j} \\ &= \sum_{i,j} -J_{ij} \sum_{\mathbf{q}\mathbf{q}'} \mathbf{S}_{\mathbf{q}} \cdot \mathbf{S}_{\mathbf{q}'} e^{i(\mathbf{q}+\mathbf{q}')\mathbf{R}_i} e^{i\mathbf{q}'(\mathbf{R}_j-\mathbf{R}_i)} \\ &= -N \sum_{\mathbf{q}} \mathbf{S}_{\mathbf{q}} \cdot \mathbf{S}_{-\mathbf{q}} \left( \sum_{\delta} J_{0\delta} e^{-i\mathbf{q}\mathbf{R}_{\delta}} \right). \end{aligned} \quad (6.6)$$

Here, the fact that the relation  $\sum_i e^{i(\mathbf{q}+\mathbf{q}')\mathbf{R}_i} = N\delta_{\mathbf{q},-\mathbf{q}'}$  holds for a sum over all lattice sites and the definition  $\mathbf{R}_{\delta} = \mathbf{R}_j - \mathbf{R}_i$  have been used. The Fourier transform of the exchange constants are defined by:

$$J(\mathbf{q}) = \sum_{\delta} J_{0\delta} e^{-i\mathbf{q}\mathbf{R}_{\delta}} = J(-\mathbf{q}) = J(\mathbf{q})^*. \quad (6.7)$$

They are real quantities. Here it has been used that  $J_{0\delta} = J_{0-\delta}$ , which is a consequence of the translational symmetry and the fact that the interaction is symmetric,  $J_{ij} = J_{ji}$ . With  $J(\mathbf{q})$  the Hamiltonian can be written in the simple form

$$H = -N \sum_{\mathbf{q}} J(\mathbf{q}) \mathbf{S}_{\mathbf{q}} \cdot \mathbf{S}_{-\mathbf{q}}. \quad (6.8)$$

In order to find the magnetic ground state, the energy (6.8) has to be minimized under the condition (6.2). This equation represents a system of  $N$  independent equations, which is equivalent to a system of  $N$  equations for the Fourier components of the spins:

$$\sum_{\mathbf{q}} \mathbf{S}_{\mathbf{q}} \cdot \mathbf{S}_{-\mathbf{q}} = S^2 \quad (6.9)$$

$$\sum_{\mathbf{q}} \mathbf{S}_{\mathbf{q}} \cdot \mathbf{S}_{\mathbf{q}'-\mathbf{q}} = 0, \quad \mathbf{q}' \neq 0. \quad (6.10)$$

Clearly, the solutions are such that all  $\mathbf{S}_{\mathbf{q}}$  vanish, except for  $\mathbf{S}_{\mathbf{Q}}$  and  $\mathbf{S}_{-\mathbf{Q}}$ , where  $\pm\mathbf{Q}$  are the values of  $\mathbf{q}$  that maximize  $J(\mathbf{q})$ . The lowest energy is then given by

$$E = -NS^2 J(\mathbf{Q}). \quad (6.11)$$

In order to recover the spin structure that corresponds to  $\mathbf{S}_{\mathbf{Q}}$  and  $\mathbf{S}_{-\mathbf{Q}}$  we introduce the real and imaginary part of  $\mathbf{S}_{\mathbf{Q}}$ ,  $\mathbf{R}_{\mathbf{Q}}$  and  $\mathbf{I}_{\mathbf{Q}}$ , to express  $\mathbf{S}_{\mathbf{Q}}$  as

$$\mathbf{S}_{\mathbf{Q}} = \mathbf{R}_{\mathbf{Q}} + i\mathbf{I}_{\mathbf{Q}}, \quad \mathbf{S}_{-\mathbf{Q}} = \mathbf{R}_{\mathbf{Q}} - i\mathbf{I}_{\mathbf{Q}}. \quad (6.12)$$

From the condition (6.9) and (6.10) we obtain

$$\mathbf{S}_{\mathbf{Q}} \cdot \mathbf{S}_{-\mathbf{Q}} = \mathbf{R}_{\mathbf{Q}}^2 + \mathbf{I}_{\mathbf{Q}}^2 = S^2 \quad (6.13)$$

$$\mathbf{S}_{\mathbf{Q}} \cdot \mathbf{S}_{\mathbf{Q}} = \mathbf{R}_{\mathbf{Q}}^2 - \mathbf{I}_{\mathbf{Q}}^2 + 2i\mathbf{R}_{\mathbf{Q}} \cdot \mathbf{I}_{\mathbf{Q}} = 0. \quad (6.14)$$

The second equation shows that  $\mathbf{R}_{\mathbf{Q}}$  and  $\mathbf{I}_{\mathbf{Q}}$  are perpendicular and have the same magnitude. Thus, we finally obtain

$$\begin{aligned}\mathbf{R}_{\mathbf{Q}}^2 = \mathbf{I}_{\mathbf{Q}}^2 &= S^2/2 \\ \mathbf{R}_{\mathbf{Q}} \cdot \mathbf{I}_{\mathbf{Q}} &= 0\end{aligned}\quad (6.15)$$

Substituting this into Eqn. (6.3) yields the spins on the lattice sites:

$$\mathbf{S}_i = 2\left(\mathbf{R}_{\mathbf{Q}} \cos(\mathbf{Q} \cdot \mathbf{R}_i) - \mathbf{I}_{\mathbf{Q}} \sin(\mathbf{Q} \cdot \mathbf{R}_i)\right). \quad (6.16)$$

Hence, the fundamental solutions of the Heisenberg model on a Bravais lattice are helical spin structures. Since no spin-orbit terms are included in the Hamiltonian, we can assume the plane spanned by the two vectors  $\mathbf{R}_{\mathbf{Q}}$  and  $\mathbf{I}_{\mathbf{Q}}$  to be the xy-plane. With that choice, the spins of the helix rotate around the z-axis in the xy-plane as one moves from lattice plane to lattice plane in the direction of  $\mathbf{Q}$ . This helical spin structure can be easily identified as a special case of what we have introduced as spin-spirals in Sec. 4.2. It is a special case, because the angle between the rotation axis and the magnetic moment,  $\theta$ , is always  $90^\circ$ . It should be mentioned that for crystal structures having more than two magnetic atoms per unit cell, it is difficult to give a general prescription how to determine the spin structure. A good introduction to the Heisenberg model can be found in the textbook by Yosida [Yos96].

In order to find magnetic structures that are possible candidates for the ground state we have to search the Brillouin zone of the two-dimensional hexagonal lattice for the vector  $\mathbf{Q}$  that maximizes  $J(\mathbf{Q})$ .

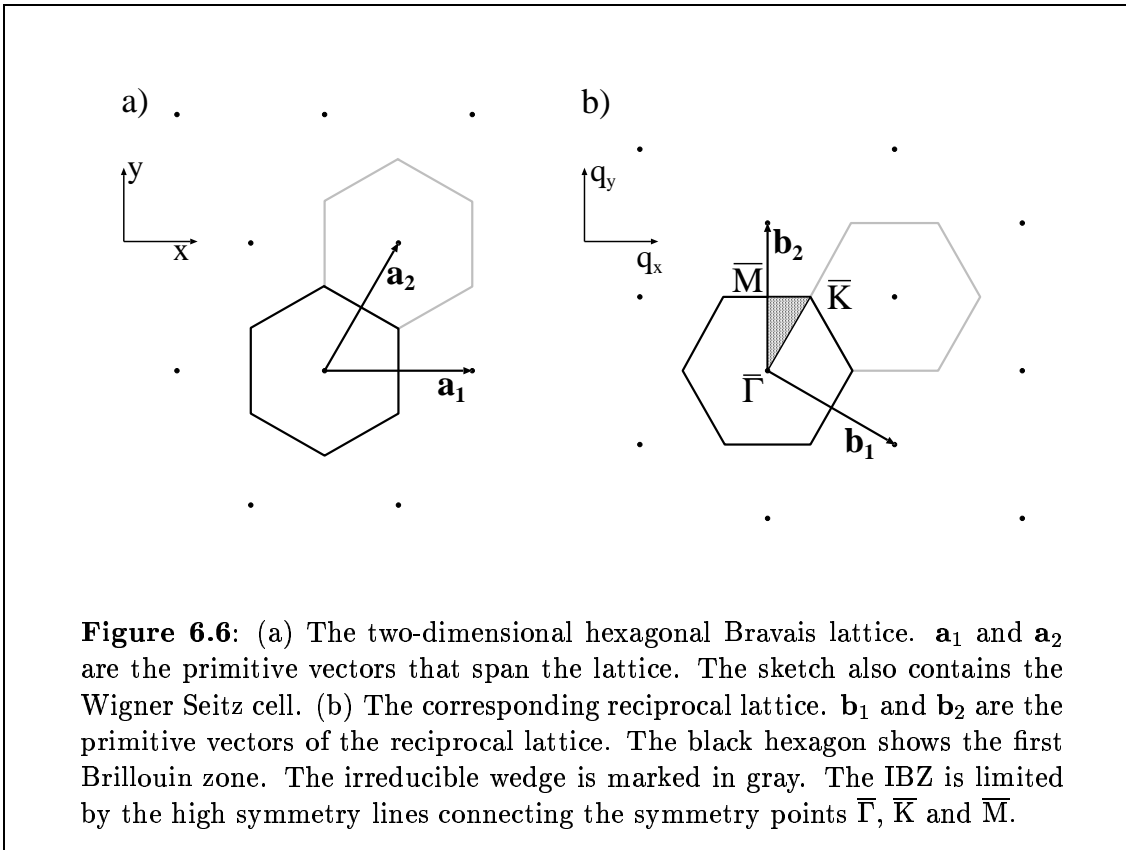
### 6.2.2 The Heisenberg model on the 2D hexagonal lattice

Before we start to search the Brillouin zone of the triangular lattice for the  $q$ -vectors that minimize the Heisenberg Hamiltonian, it is helpful to briefly review the geometry of the two-dimensional triangular (hexagonal) lattice. Fig. 6.6 contains an image of both, the real-space (a) and the reciprocal lattice (b). In the figure the primitive vectors of the lattice  $\mathbf{a}_1$  and  $\mathbf{a}_2$  as well as the primitive vectors of the reciprocal lattice  $\mathbf{b}_1$  and  $\mathbf{b}_2$  are indicated. There are two options to choose the primitive vectors either with an angle of  $60^\circ$  or  $120^\circ$  between the two vectors. Here, we have chosen the first option. As a consequence, the primitive vectors of the reciprocal lattice span an angle of  $120^\circ$ . According to the coordinate frames shown in Fig. 6.6 the primitive vectors of the (reciprocal) lattice are given in terms of cartesian coordinates by

$$\begin{aligned}\mathbf{a}_1 &= a(1, 0), & \mathbf{a}_2 &= a\left(\frac{1}{2}, \frac{\sqrt{3}}{2}\right) \\ \mathbf{b}_1 &= \frac{2\pi}{a}\left(1, \frac{-1}{\sqrt{3}}\right), & \mathbf{b}_2 &= \frac{2\pi}{a}\left(0, \frac{2}{\sqrt{3}}\right),\end{aligned}\quad (6.17)$$

where  $a$  is the lattice constant, which is equal to the nearest-neighbor distance. The figure also contains the Wigner Seitz cell (real space) and the two-dimensional Brillouin zone (reciprocal space). The irreducible part of the Brillouin zone (IBZ) is marked in gray. The corner points of the IBZ are the high symmetry points  $\bar{\Gamma}$ ,  $\bar{K}$





and  $\bar{M}$ . In the Brillouin zone we find six  $\bar{M}$ -points on the centers of the sides of the zone boundary and six  $\bar{K}$ -points at the corners of the zone boundary. However, some of these points are separated by reciprocal lattice vectors. Hence, they do not give rise to distinct spin structures. The cartesian coordinates of the symmetry points are given in Tab. 6.5.

From this knowledge of the two-dimensional Brillouin zone of the triangular lattice it is possible to construct the magnetic states that correspond to high symmetry points. Let us begin with the most simple case, the  $\bar{\Gamma}$ -point. This point always corresponds to the ferromagnetic solution. Since the vector  $\mathbf{Q}$  is  $(0,0)$  we obtain from Eqn. (6.16) that the spins on all lattice sites are given by  $\mathbf{S}_i = 2\mathbf{R}_{\mathbf{Q}}$ , i.e. all spins have the same direction. The direction of the spin  $\mathbf{R}_{\mathbf{Q}}$  with respect to the lattice remains undetermined, because no spin-orbit term is included in the model.

At the  $\bar{K}$ -point we choose for example  $\mathbf{Q} = \frac{2\pi}{a}(2/3, 0)$ ,  $-\mathbf{Q} = \frac{2\pi}{a}(-2/3, 0)$ . This leads to three distinct kinds of lattice sites, e.g.  $a(1,0)$ ,  $a(2,0)$  and  $a(3,0)$ . For these atoms the spins are given by  $\mathbf{S}_1 = 2(\mathbf{R}_{\mathbf{Q}} \cos(4\pi/3) - \mathbf{I}_{\mathbf{Q}} \sin(4\pi/3))$ ,  $\mathbf{S}_2 = 2(\mathbf{R}_{\mathbf{Q}} \cos(8\pi/3) - \mathbf{I}_{\mathbf{Q}} \sin(8\pi/3))$  and  $\mathbf{S}_3 = 2(\mathbf{R}_{\mathbf{Q}} \cos(12\pi/3) - \mathbf{I}_{\mathbf{Q}} \sin(12\pi/3))$ , respectively. The relative angle between the spins on the different sites is always  $120^\circ$ . Hence, the magnetic structure that corresponds to the  $\bar{K}$ -point is the  $120^\circ$  Néel state. As in the ferromagnetic case, the direction of  $\mathbf{R}_{\mathbf{Q}}$  and  $\mathbf{I}_{\mathbf{Q}}$  is not determined, only the condition (6.15) has to be satisfied.

symmetry point	cart. coordinate (units of $\frac{2\pi}{a}$ )
$\bar{\Gamma}$	(0, 0)
$\bar{K}$	(2/3, 0), (1/3, 1/√3), (1/3, -1/√3) (-2/3, 0), (-1/3, -1/√3), (-1/3, 1/√3)
$\bar{M}$	(0, 1/√3), (0, -1/√3) (1/2, 1/(2√3)), (-1/2, -1/(2√3)) (1/2, -1/(2√3)), (-1/2, 1/(2√3))

**Table 6.5:** The high symmetry points of the two-dimensional hexagonal lattice and the cartesian coordinates in units of  $\frac{2\pi}{a}$ . Points which are separated by reciprocal lattice vectors are grouped together in one line.

At the  $\bar{M}$ -point the situation is more involved, since there are three pairs of  $\mathbf{Q}$ -vectors that give rise to three distinct spin structures. The general solution can be a linear combination of the three  $\mathbf{Q}$ -vectors, which satisfies the conditions (6.9) and (6.10). In the case of the  $\bar{K}$ -point there are also two sets of  $\mathbf{Q}$ -vectors, but they do not give rise to separate solutions, because the condition (6.5) has to be fulfilled and  $\mathbf{q}$  and  $-\mathbf{q}$  are in different sets. To construct the magnetic structure we have the three  $\mathbf{Q}$ -vectors  $\mathbf{Q}_1 = \frac{2\pi}{a}(0, 1/\sqrt{3})$ ,  $\mathbf{Q}_2 = \frac{2\pi}{a}(1/2, 1/(2\sqrt{3}))$  and  $\mathbf{Q}_3 = \frac{2\pi}{a}(1/2, -1/(2\sqrt{3}))$ .  $\mathbf{Q}_i$  and  $-\mathbf{Q}_i$  ( $i = 1, 2, 3$ ) differ by a reciprocal lattice vector. Therefore, it follows from Eqn. (6.5) that the  $\mathbf{S}_{\mathbf{Q}_i}$  are real. At all lattice sites the product of  $\mathbf{Q}_i \cdot \mathbf{R}_j$  is a multiple of  $\pi$ . Hence, the exponential of  $i\mathbf{Q}_i \cdot \mathbf{R}_j$  takes only the value  $\pm 1$ , and thus the spin on lattice site  $j$  can be written

$$\mathbf{S}_j = \mathbf{R}_{\mathbf{Q}_1} e^{i\mathbf{Q}_1 \cdot \mathbf{R}_j} + \mathbf{R}_{\mathbf{Q}_2} e^{i\mathbf{Q}_2 \cdot \mathbf{R}_j} + \mathbf{R}_{\mathbf{Q}_3} e^{i\mathbf{Q}_3 \cdot \mathbf{R}_j}. \quad (6.18)$$

From the conditions (6.9) and (6.10) it follows that the  $\mathbf{R}_{\mathbf{Q}_i}$  are mutually orthogonal and that  $\mathbf{R}_{\mathbf{Q}_1}^2 + \mathbf{R}_{\mathbf{Q}_2}^2 + \mathbf{R}_{\mathbf{Q}_3}^2 = S^2$ . Choosing for example  $\mathbf{R}_{\mathbf{Q}_1}^2 = S^2$  and  $\mathbf{R}_{\mathbf{Q}_2} = \mathbf{R}_{\mathbf{Q}_3} = 0$  leads to a structure with two distinct lattice sites with spin  $\pm \mathbf{R}_{\mathbf{Q}_1}$ . This is the row-wise antiferromagnetic configuration as shown in Fig. 6.3 a. When all three  $\mathbf{R}_{\mathbf{Q}_i}$  are non-zero we obtain a structure with four distinct lattice sites. Let us choose the direction of the  $\mathbf{R}_{\mathbf{Q}_i}$  along the axis of the spin-coordinate frame,  $\mathbf{R}_{\mathbf{Q}_1} = A\hat{x}$ ,  $\mathbf{R}_{\mathbf{Q}_2} = B\hat{y}$  and  $\mathbf{R}_{\mathbf{Q}_3} = C\hat{z}$ . With this choice these lattice sites have a spin of  $(A, B, C)$ ,  $(A, -B, -C)$ ,  $(-A, -B, C)$  and  $(-A, B, -C)$  respectively ( $A^2 + B^2 + C^2 = S^2$ ). A particular highly symmetric state is obtained for the special case  $A = B = C = S/\sqrt{3}$ . This state, which is presented in Fig. 6.7, is called the triple-Q (3Q) state because of the three  $\mathbf{Q}$ -vectors involved. Similarly, the RW-AFM state is commonly referred to as the single-Q (1Q) state. The triple-Q (3Q) state represents a three-dimensional spin structure on the two-dimensional triangular lattice. The relative angle between all nearest-neighbor spins is the tetrahedron angle of  $109.47^\circ$ . For completeness we would like to add that there is also a double-Q (2Q) state. This is a particular high symmetry state similar to the 3Q state but constructed from only two vectors  $\mathbf{R}_{\mathbf{Q}_i}$ .

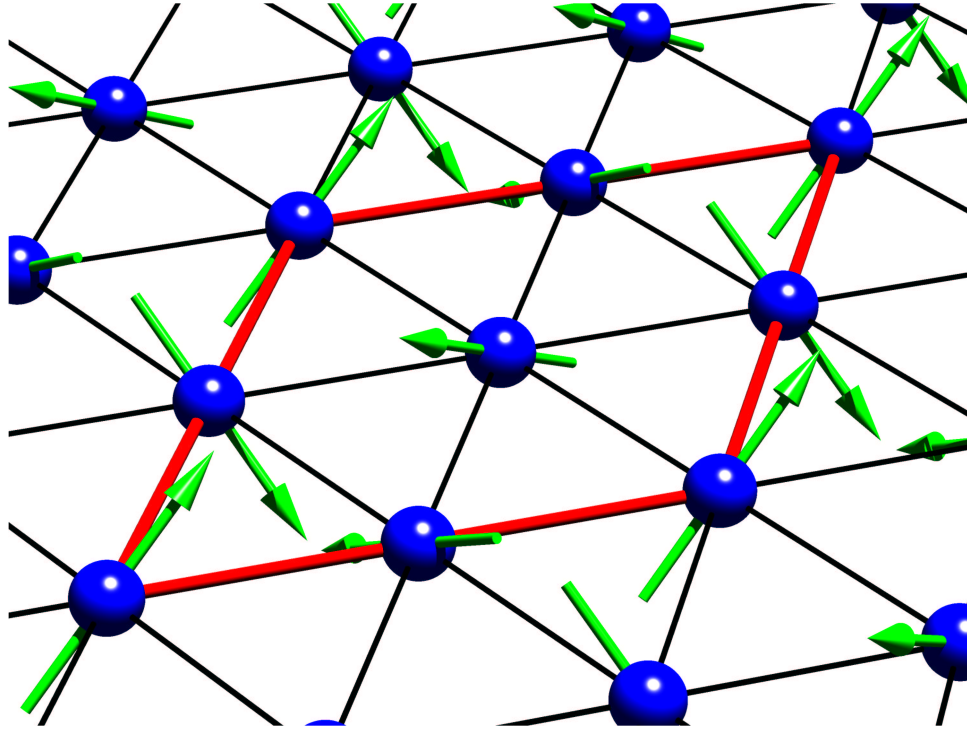


**Figure 6.7:** The triple-Q (3Q) state represents a three-dimensional spin structure on the two-dimensional triangular lattice. It is energetically degenerate with the RW-AFM state (Fig. 6.3 a) within the Heisenberg model. The relative angle between nearest-neighbor spins is the tetrahedron angle. The net moment per unit cell is zero. This structure differs from that shown at the beginning of this thesis by a rigid rotation of all spins with respect to the lattice. Hence, when spin-orbit coupling is neglected, the two structures are equal.

according to Eqn. (6.18). With the direction of  $\mathbf{R}_{\mathbf{Q}_1}$  as chosen for the 3Q state and assuming without loss of generality that  $\mathbf{R}_{\mathbf{Q}_3} = 0$  we find that the 2Q structure also has four distinct lattice sites. But in difference to the 3Q state, the 2Q state is a two-dimensional (coplanar) magnetic structure. The four lattice sites have spins of  $(A, B, 0)$ ,  $(A, -B, 0)$ ,  $(-A, -B, 0)$  and  $(-A, B, 0)$ , respectively, with  $A = B = S/\sqrt{2}$ . The net moment per unit cell of the 1Q, 2Q and 3Q state is zero. Since, all three states originate from the same  $\mathbf{Q}$ -vectors, they are degenerate within the Heisenberg model. However, this degeneracy is lifted, when higher order interactions are taken into account. As we will show below, they favor either the 1Q or the 3Q state.

### 6.2.3 Energetics of high symmetry states on the triangular lattice within the Heisenberg model

In this section we discuss the energetics of the most important magnetic states on the two-dimensional hexagonal lattice within the Heisenberg model up to the third nearest-neighbor interaction, i.e. including the exchange constants  $J_1$ ,  $J_2$  and  $J_3$ . As we have seen in the previous sections the crucial quantity for the description of the energetics within the Heisenberg model is the Fourier transform of the exchange constants  $J(\mathbf{q})$  (cf. Eqn. (6.7)). Expanding the vector  $\mathbf{q}$  into the primitive vectors of the reciprocal lattice, according to  $\mathbf{q} = q_1 \mathbf{b}_1 + q_2 \mathbf{b}_2$ ,  $J(\mathbf{q})$  is given by

$$\begin{aligned} J(\mathbf{q}) &= J_1 2 \left[ \cos(2\pi(q_1 + q_2)) + \cos(2\pi q_1) + \cos(2\pi q_2) \right] \\ &+ J_2 2 \left[ \cos(2\pi(2q_1 - q_2)) + \cos(2\pi(q_1 + q_2)) + \cos(2\pi(-q_1 + 2q_2)) \right] \\ &+ J_3 2 \left[ \cos(2\pi 2q_1) + \cos(2\pi 2q_2) + \cos(2\pi(-2q_1 + 2q_2)) \right]. \end{aligned} \quad (6.19)$$

Expressed in cartesian coordinates this becomes

$$\begin{aligned} J(\mathbf{q}) &= J_1 \left[ 2 \cos(aq_x) + 4 \cos\left(a\frac{1}{2}q_x\right) \cos\left(a\frac{\sqrt{3}}{2}q_y\right) \right] \\ &+ J_2 \left[ 4 \cos\left(a\frac{3}{2}q_x\right) \cos\left(a\frac{\sqrt{3}}{2}q_y\right) + 2 \cos(a\sqrt{3}q_y) \right] \\ &+ J_3 \left[ 2 \cos(a2q_x) + 4 \cos(aq_x) \cos(a\sqrt{3}q_y) \right]. \end{aligned} \quad (6.20)$$

As we have said before the maximum of  $J(\mathbf{q})$  determines the minimum of  $E(\mathbf{q})$ , and thus, the ground state magnetic structure. Due to their symmetry, the high symmetry points in the Brillouin zone are either local extrema or saddle points of  $E(\mathbf{q})$ . Hence, the magnetic states that correspond to the high symmetry points are very likely candidates for the the magnetic ground state. Using Eqn. (6.19) or (6.20) the energy of the magnetic states, that correspond to the three high symmetry points in the Brillouin zone of the two-dimensional triangular lattice, discussed in the previous section can directly be calculated from Eqn. (6.11). The results are given in Tab. 6.6. From these results it can be seen that, if all exchange constants are positive or if the

mag. state	sym. p.	Heisenberg energy
FM	$\bar{\Gamma}$	$-S^2(6J_1 + 6J_2 + 6J_3)$
Néel	$\bar{K}$	$-S^2(-3J_1 + 6J_2 - 3J_3)$
RW-AFM, 3Q	$\bar{M}$	$-S^2(-2J_1 - 2J_2 + 6J_3)$

**Table 6.6:** The energy per atom within the Heisenberg model of magnetic states that originate from high symmetry  $\mathbf{Q}$ -vectors in the Brillouin zone.

nearest-neighbor coupling is dominant and positive, the ground state of the Heisenberg model is ferromagnetic. On the other hand, if the interaction is dominated by a

negative  $J_1$ , the Néel state has the lowest energy. In the nearest-neighbor approximation only these two solutions are possible. However, when exchange integrals beyond  $J_1$  become important, other magnetic configurations, like the RW-AFM state, can become the ground state of the system. But before we continue with this discussion we need to include other relevant magnetic structures into our analysis.

As a next class of magnetic states we will discuss helical spin structures (spin-spirals) with  $q$ -vectors on the high symmetry lines in the Brillouin zone. We begin with the lines  $\bar{\Gamma}$ - $\bar{K}$  and  $\bar{K}$ - $\bar{M}$ . From Fig. 6.6 it can be seen that, if we follow the symmetry line from  $\bar{\Gamma}$  to  $\bar{K}$  and continue in this direction beyond the  $\bar{K}$ -point, we end up on the line  $\bar{K}$ - $\bar{M}$  of the next Brillouin zone. It is therefore convenient to discuss these two lines together. The  $q$ -vectors on this line can be parameterized by  $\mathbf{q} = (q_x, 0)$ , with  $0 \leq q_x \leq 2\pi/a$  ( $q_x = 4\pi/3a$  corresponds to the  $\bar{K}$ -point). The dependence of the energy (per atom) on the  $q$ -vector can directly be calculated from Eqn. (6.20).

$$E(\mathbf{q}) = -S^2 \left\{ \begin{aligned} & J_1 \left[ 2 \cos(aq_x) + 4 \cos\left(a\frac{1}{2}q_x\right) \right] \\ & + J_2 \left[ 4 \cos\left(a\frac{3}{2}q_x\right) + 2 \right] \\ & + J_3 \left[ 2 \cos(a2q_x) + 4 \cos(aq_x) \right] \end{aligned} \right\} \quad (6.21)$$

The  $q$ -vectors on the line  $\bar{\Gamma}$ - $\bar{M}$  can be parameterized by  $\mathbf{q} = (0, q_y)$ , with  $0 \leq q_y \leq 2\pi/\sqrt{3}a$ . In that case the energy per atom is given by

$$E(\mathbf{q}) = -S^2 \left\{ \begin{aligned} & J_1 \left[ 2 + 4 \cos\left(a\frac{\sqrt{3}}{2}q_y\right) \right] \\ & + J_2 \left[ 4 \cos\left(a\frac{\sqrt{3}}{2}q_y\right) + 2 \cos(a\sqrt{3}q_y) \right] \\ & + J_3 \left[ 2 + 4 \cos(a\sqrt{3}q_y) \right] \end{aligned} \right\}. \quad (6.22)$$

The contributions from the different  $J_i$  are shown in Fig. 6.8. All  $J_i$  are assumed to be negative, since we are mainly interested in antiferromagnets. From Fig. 6.8 the large variety of possible ground states depending on the sign and the magnitude of the  $J_i$  can be observed. If only  $J_1$  is present the  $\bar{K}$ -point, i.e. the Néel state becomes the minimum of the energy for antiferromagnetic materials. If, however,  $J_2$  is large enough the  $\bar{M}$ -point can become lower, corresponding to the RW-AFM state. If  $J_2$  or  $J_3$  or both are large there is a possibility of spin-spirals on the lines  $\bar{\Gamma}$ - $\bar{K}$  and  $\bar{\Gamma}$ - $\bar{M}$ . The same is true, if, for example,  $J_1$  is positive (ferromagnetic) and  $J_2$  is negative.

Having determined the energy of all the high symmetry magnetic states we are able to develop the zero temperature magnetic phase diagram in the  $(J_1, J_2, J_3)$  parameter space of the Heisenberg model on the two-dimensional hexagonal lattice. Cuts through the three-dimensional phase diagram presented in Fig. 6.9. The phase diagram in the  $J_1$ - $J_2$  plane,  $J_3 = 0$ , (Fig. 6.9 a) can be calculated analytically. All

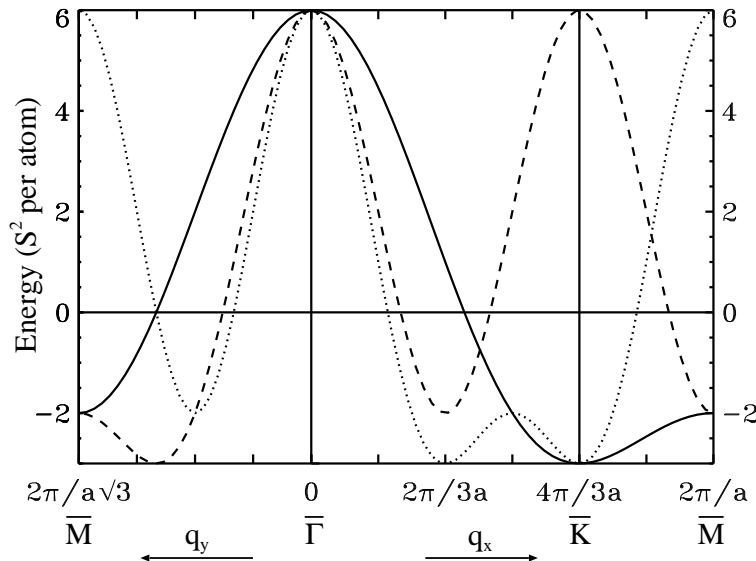


**Figure 6.8:** Contributions of the different exchange constants up to the third nearest-neighbor interaction ( $J_1$  solid line,  $J_2$  dashed line and  $J_3$  dotted line) to the Heisenberg energy per atom for spin-spirals along high symmetry lines. Since we are mainly interested in antiferromagnets all exchange integrals are assumed to be negative ( $J_1 = J_2 = J_3 = -1$ ).

the phase boundaries are straight lines. When  $J_2$  is positive the magnetic ground state is either the FM state for positive  $J_1$  or the Néel state for negative  $J_1$ . For negative  $J_2$  with a magnitude above a certain threshold a spin-spiral with  $q$ -vector on the line  $\bar{\Gamma}$ - $\bar{m}$  or the RW-AFM state can become the ground state. The phase diagram in the  $J_2$ - $J_3$  plane (Fig. 6.9 b and c) has first been calculated numerically by searching for the lowest energy configuration on a mesh in the  $J_2$ - $J_3$  plane. In a second step we investigated all the relevant phase boundaries analytically. For non-vanishing  $J_3$  another possible ground state, a spin-spiral on the line  $\bar{\Gamma}$ - $\bar{K}$ , is found. Again all phase boundaries are lines except for the boundary between the Néel state and the spin-spiral state on the line  $\bar{\Gamma}$ - $\bar{K}$ . This phase boundary has been determined numerically. When  $J_1$  is positive the phase diagram is dominated by the FM state. The Néel state and the RW-AFM state only become the magnetic ground state for rather larger values of  $J_3$  and  $J_2$ , respectively. When  $J_1$  is negative this picture is reversed. The FM configuration can only become the ground state, when both,  $J_2$  and  $J_3$  are large compared to  $J_1$  and the phase diagram is dominated by the Néel state and also the RW-AFM state.

It is very instructive to discuss the phase diagram in terms of the separate contributions of  $J_1$ ,  $J_2$  and  $J_3$  respectively (cf. Fig. 6.8). Let us begin with the case that  $J_3$

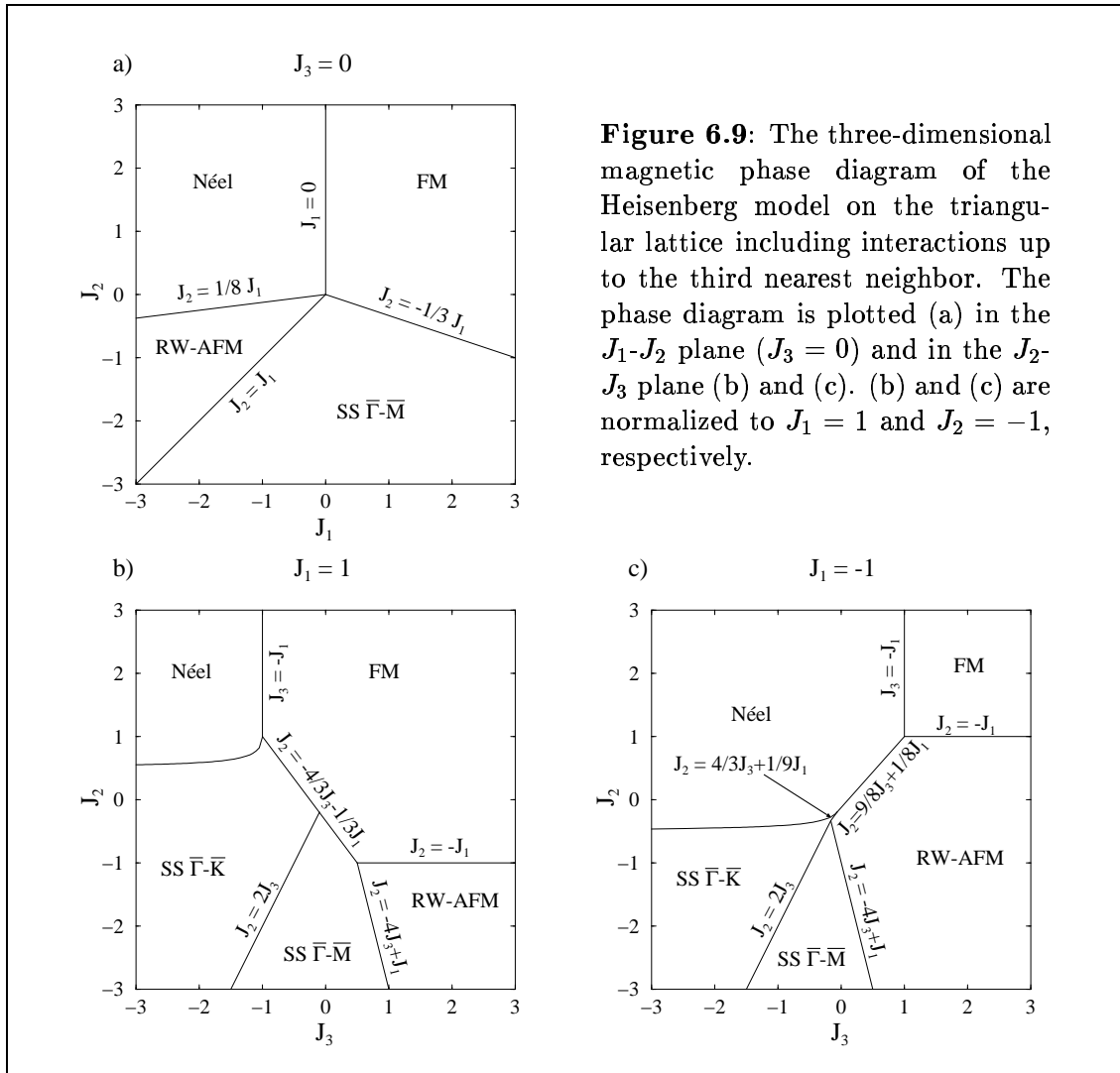


**Figure 6.9:** The three-dimensional magnetic phase diagram of the Heisenberg model on the triangular lattice including interactions up to the third nearest neighbor. The phase diagram is plotted (a) in the  $J_1$ - $J_2$  plane ( $J_3 = 0$ ) and in the  $J_2$ - $J_3$  plane (b) and (c). (b) and (c) are normalized to  $J_1 = 1$  and  $J_2 = -1$ , respectively.

is being neglected (Fig. 6.9 a). When  $J_2$  is positive (opposite sign as in Fig. 6.8) the corresponding contribution to the energy has two minima at the  $\bar{\Gamma}$ -point and at the  $\bar{K}$ -point. Thus, it favors the FM or the Néel state. In this case, the magnetic ground state is determined by  $J_1$ . However, small negative values of  $J_2$  of  $1/3$  or  $1/8$  of the size of  $J_1$  are enough to change the magnetic ground state. When  $J_2$  is negative, it disfavors the  $\bar{\Gamma}$  and the  $\bar{K}$ -point and either the  $\bar{M}$ -point (RW-AFM or 3Q state) or a spin-spiral on the line  $\bar{\Gamma}$ - $\bar{M}$  can become minimal. The latter state is stabilized by a minimum of the energy contribution of  $J_2$  on that symmetry line.

The most prominent change when  $J_3$  is present is the appearance of an additional possible ground state, a spin-spiral on the symmetry line  $\bar{\Gamma}$ - $\bar{K}$ . When  $J_3$  is negative, the corresponding contribution to the energy possesses two minima, at  $\bar{K}$  and another one in the middle of the line  $\bar{\Gamma}$ - $\bar{K}$ . The second minimum leads to the stabilization of the new spin-spiral ground state over a large region of the phase space. The minimum at  $\bar{K}$  stabilizes the Néel state, which can now be the ground state also if  $J_1$  is positive.

On the other hand, when  $J_3$  is positive, the third nearest-neighbor interaction energy becomes minimal at the  $\bar{\Gamma}$  and the  $\bar{M}$ -point. This can result in a stabilization of the RW-AFM or 3Q state even if  $J_1$  is positive, or stabilize the FM state when  $J_1$  is negative.

Finally, we need to investigate the dependence of the Heisenberg energy on the angle  $\alpha$  for the real-space rotation that we have performed in Sec. 6.1. In this case the energy per atom can be calculated directly from the Heisenberg Hamiltonian in real space (Eqn. (6.1)) by summing over all atoms in the unit cell and calculating  $\mathbf{S}_i \cdot \mathbf{S}_j$  for the 1<sup>st</sup>, 2<sup>nd</sup> and 3<sup>rd</sup> nearest neighbors of each atom and dividing by the number of atoms in the unit cell. Applying this procedure to the rotation with two atoms per unit cell according to Fig. 6.3 c we obtain

$$E_{2\text{at}}(\alpha) = -S^2 \left\{ (J_1 + J_2)(2 + 4 \cos \alpha) + 6J_3 \right\} \quad (6.23)$$

for the energy per atom. Similarly, for the rotation with three atoms per unit cell according to Fig. 6.3 d the energy per atom is given by

$$E_{3\text{at}}(\alpha) = -S^2 \left\{ (J_1 + J_3)(4 \cos \alpha + 2 \cos 2\alpha) + 6J_2 \right\}. \quad (6.24)$$

As we have pointed out before the results we obtained from our ab-initio calculations for the unsupported monolayers of Mn are in disagreement with the shape of  $E_{3\text{at}}(\alpha)$ . A term proportional to  $\cos 3\alpha$ , which cannot be provided by the Heisenberg model, is needed to fit the result for Mn. Such a term can only be provided by high order interactions.

#### 6.2.4 The four-spin and the biquadratic interaction

Exchange interactions beyond the Heisenberg model can be obtained from a perturbation expansion of the Hubbard model. Assuming that the intra-atomic Coulomb repulsion  $U$  is large compared to the transfer integrals between the sites  $t_{ij}$ , a perturbative treatment in the limit of small transfer integrals can be applied. Up to the second order such a perturbation expansion reproduces the Heisenberg model with a Hamiltonian proportional to  $\mathbf{S}_i \cdot \mathbf{S}_j$ . However, going beyond the second order yields more complicated spin interactions. In addition to terms that are proportional to  $\mathbf{S}_i \cdot \mathbf{S}_j$ , which can be incorporated into the Heisenberg model, the fourth order perturbation treatment yields two terms that have a different form. One is the four-spin exchange interaction (4-spin):

$$H_{4\text{-spin}} = - \sum_{ijkl} K_{ijkl} [(\mathbf{S}_i \mathbf{S}_j)(\mathbf{S}_k \mathbf{S}_l) + (\mathbf{S}_j \mathbf{S}_k)(\mathbf{S}_l \mathbf{S}_i) - (\mathbf{S}_i \mathbf{S}_k)(\mathbf{S}_j \mathbf{S}_l)]. \quad (6.25)$$

The 4-spin interaction arises from the hopping of electrons over four sites, i.e. the process  $1 \rightarrow 2 \rightarrow 3 \rightarrow 4 \rightarrow 1$ . The other term is the biquadratic exchange:

$$H_{\text{biquadr}} = - \sum_{ij} B_{ij} (\mathbf{S}_i \cdot \mathbf{S}_j)^2. \quad (6.26)$$



In this section we investigate how these two terms contribute to the energy of the magnetic states that we have introduced in the previous sections. In both cases we restrict ourselves to the nearest-neighbor approximation.

In the case of the 4-spin interaction nearest-neighbor approximation means that the four sites  $i, j, k$  and  $l$  involved form a minimal diamond. Such a nearest-neighbor diamond is a parallelogram, where each side is a line connecting two nearest-neighbor atoms. Two examples of minimal diamond clusters are shown in Fig. 6.10. Let us

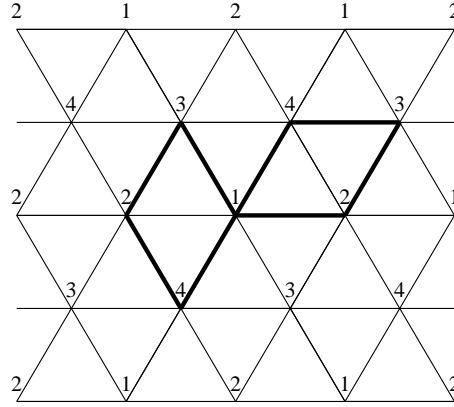


**Figure 6.10:** Minimal diamond clusters on the triangular lattice.

consider the atom at the center of Fig. 6.10, which is labeled 1. There are 12 minimal diamond clusters that contain this atom site. Hence, to calculate the contribution of the 4-spin interaction to the energy of a magnetic configuration according to Eqn. (6.25) we have to sum over the 12 diamonds and repeat that calculation for all atoms in the magnetic unit cell. We start with the largest class of magnetic states discussed so far, i.e. the states that can be described by a single vector  $\mathbf{Q}$  according to Eqn. (6.16). This includes the spin-spirals but also the FM, the RW-AFM and the Néel state. Using Eqn. (6.15) and (6.16) the product of a pair of spins is given by

$$\begin{aligned} \mathbf{S}_i \cdot \mathbf{S}_j &= S^2 \left[ \cos(\mathbf{Q} \cdot \mathbf{R}_i) \cos(\mathbf{Q} \cdot \mathbf{R}_j) + \sin(\mathbf{Q} \cdot \mathbf{R}_i) \sin(\mathbf{Q} \cdot \mathbf{R}_j) \right] \\ &= S^2 \cos(\mathbf{Q} \cdot (\mathbf{R}_i - \mathbf{R}_j)). \end{aligned} \quad (6.27)$$

Next we consider the contribution of a single diamond cluster and simplify it:

$$\begin{aligned} &(\mathbf{S}_i \mathbf{S}_j)(\mathbf{S}_k \mathbf{S}_l) + (\mathbf{S}_j \mathbf{S}_k)(\mathbf{S}_l \mathbf{S}_i) - (\mathbf{S}_i \mathbf{S}_k)(\mathbf{S}_j \mathbf{S}_l) \\ &= S^4 \left[ \cos(\mathbf{Q} \cdot (\mathbf{R}_i - \mathbf{R}_j)) \cos(\mathbf{Q} \cdot (\mathbf{R}_k - \mathbf{R}_l)) \right. \\ &\quad + \cos(\mathbf{Q} \cdot (\mathbf{R}_j - \mathbf{R}_k)) \cos(\mathbf{Q} \cdot (\mathbf{R}_l - \mathbf{R}_i)) \\ &\quad \left. - \cos(\mathbf{Q} \cdot (\mathbf{R}_i - \mathbf{R}_k)) \cos(\mathbf{Q} \cdot (\mathbf{R}_j - \mathbf{R}_l)) \right] \end{aligned}$$

$$\begin{aligned}
&= S^4 \left[ \cos(\mathbf{Q} \cdot (\mathbf{R}_i - \mathbf{R}_j)) \cos(\mathbf{Q} \cdot (\mathbf{R}_k - \mathbf{R}_l)) \right. \\
&\quad + \cos(\mathbf{Q} \cdot (\mathbf{R}_j - \mathbf{R}_k)) \cos(\mathbf{Q} \cdot (\mathbf{R}_l - \mathbf{R}_k + \mathbf{R}_k - \mathbf{R}_i)) \\
&\quad \left. - \cos(\mathbf{Q} \cdot (\mathbf{R}_i - \mathbf{R}_k)) \cos(\mathbf{Q} \cdot (\mathbf{R}_j - \mathbf{R}_k + \mathbf{R}_k - \mathbf{R}_l)) \right]. \quad (6.28)
\end{aligned}$$

Applying the the addition theorems for sin and cos three times this expression can be simplified and we finally obtain

$$(\mathbf{S}_i \mathbf{S}_j)(\mathbf{S}_k \mathbf{S}_l) + (\mathbf{S}_j \mathbf{S}_k)(\mathbf{S}_l \mathbf{S}_i) - (\mathbf{S}_i \mathbf{S}_k)(\mathbf{S}_j \mathbf{S}_l) = S^4 \cos(\mathbf{Q} \cdot (\mathbf{R}_i - \mathbf{R}_j + \mathbf{R}_k - \mathbf{R}_l)) = S^4, \quad (6.29)$$

i.e. all minimal diamond clusters add the same contribution to the magnetic energy. For every two-dimensional Bravais lattice the four atom nearest-neighbor clusters that have to be considered to calculate the 4-spin interactions are parallelograms and  $\mathbf{R}_i - \mathbf{R}_j + \mathbf{R}_k - \mathbf{R}_l = 0$ . Hence, the result, that the contribution of each nearest-neighbor cluster to the energy is  $K_1 S^4$ , is valid for any two-dimensional Bravais lattice. On the triangular lattice there are 12 minimal diamond clusters for each atom. Thus, the 4-spin contribution to the energy of all magnetic states that are represented by a single vector  $\mathbf{Q}$  is given by

$$E_{4\text{-spin},1Q} = -12 K_1 S^4, \quad (6.30)$$

where  $K_1$  is the nearest-neighbor 4-spin interaction constant. This result implies that the 4-spin interaction does not change the energy of any of the states characterized by a single  $Q$ -vector relative to each other. In particular, the energy difference between spin-spirals with different  $q$ -vectors is not changed, i.e. the functional form of  $E(\mathbf{q})$  is not changed by the 4-spin interaction.

Next we turn to the 3Q state. The magnetic states that are generated by (superposition of)  $Q$ -vectors that correspond to the  $\bar{M}$ -point have been discussed in Sec. 6.2.2. There it has been shown that the 3Q state is formed out of four distinct lattice sites. The four sites are labeled 1-4 in Fig. 6.10. Starting with site 1, e.g. the atom at the center of the figure, and performing the summation over the twelve minimal diamonds yields the contribution from this site to the energy due to the 4-spin interaction:

$$-4K_1 [(\mathbf{S}_1 \mathbf{S}_4)(\mathbf{S}_2 \mathbf{S}_3) + (\mathbf{S}_1 \mathbf{S}_2)(\mathbf{S}_3 \mathbf{S}_4) - (\mathbf{S}_1 \mathbf{S}_3)(\mathbf{S}_2 \mathbf{S}_4)]. \quad (6.31)$$

The other three atoms in the unit cell give exactly the same contribution. Using that the spins of the four sites are given by  $\mathbf{S}_1 = (A, B, C)$ ,  $\mathbf{S}_2 = (-A, -B, C)$ ,  $\mathbf{S}_3 = (A, -B, -C)$  and  $\mathbf{S}_4 = (-A, B, -C)$  (cf. Sec. 6.2.2) the energy per atom due to the 4-spin interaction can be written

$$-4K_1 [4(A^4 + B^4 + C^4) - S^4]. \quad (6.32)$$

For the RW-AFM state, where  $A^2 = S^2$ ,  $B = C = 0$ , Eqn. (6.32) reproduces the result of Eqn. (6.30)  $E = -12 K_1 S^4$ . The 3Q state is obtained for  $A = B = C = S/\sqrt{3}$ . Thus, the 4-spin contribution to the energy of the 3Q state is

$$E_{4\text{-spin},3Q} = -\frac{4}{3} K_1 S^4. \quad (6.33)$$

For completeness we also state the 4-spin contribution to the energy of the the 2Q state, which is obtained for  $A = B = S/\sqrt{2}$ :

$$E_{4\text{-spin},2Q} = -4 K_1 S^4. \quad (6.34)$$

The 4-spin contribution to the energy of real-space rotations is calculated by the same procedure, taking into account that the relative angle between two nearest-neighbor spins is 0 or  $\alpha$  in the two atom unit cell and  $\alpha$  or  $2\alpha$  in the three atom unit cell. For the rotation in the two atom unit cell according to Fig. 6.3 c we obtain

$$E_{4\text{-spin},2at}(\alpha) = -K_1 S^4(8 + 4 \cos 2\alpha) \quad (6.35)$$

and for the rotation in the three atom unit cell according to Fig. 6.3 d we find

$$E_{4\text{-spin},3at}(\alpha) = -K_1 S^4(4 + 8 \cos 3\alpha). \quad (6.36)$$

Here  $E(\alpha)$  is the energy per atom. In both cases we find a functional dependence of the energy on the angle  $\alpha$  that can not be explained within the Heisenberg model irrespective of how many neighbors are taken into account. In particular the term proportional to  $\cos 3\alpha$  is the unit cell with three atoms is very important, since it allows a much better description of the Mn results. This implies that the inclusion of the 4-spin interaction allows a better modeling of the results from the ab-initio calculations.

The calculation of the energy due to the biquadratic exchange involves pairs of spin. Consequently, the meaning of the nearest-neighbor approximation is exactly same as in the Heisenberg model. Also the procedure determining the energy of the magnetic states is less complicated as in the case of the 4-spin interaction. The energy is computed straight forwardly from Eqn. (6.26) by summing over the six nearest neighbors of each atom in the unit cell. For spin-spirals with  $q$ -vectors along the symmetry line  $\bar{\Gamma}\text{-}\bar{M}$  ( $\mathbf{q} = (0, q_y)$ ) the energy due to biquadratic exchange amounts to

$$E_{\text{biquadr}}(\mathbf{q}) = -B_1 S^4 \left( 2 + 4 \cos^2 \left( a \frac{\sqrt{3}}{2} q_y \right) \right) = -B_1 S^4 \left( 4 + 2 \cos \left( a \sqrt{3} q_y \right) \right), \quad (6.37)$$

where  $B_1$  is the biquadratic nearest-neighbor exchange constant. On the line  $\bar{\Gamma}\text{-}\bar{K}$  ( $\mathbf{q} = (q_x, 0)$ ) we have

$$\begin{aligned} E_{\text{biquadr}}(\mathbf{q}) &= -B_1 S^4 \left( 4 \cos^2 \left( a \frac{1}{2} q_x \right) + 2 \cos^2 (a q_x) \right) \\ &= -B_1 S^4 (3 + 2 \cos (a q_x) + \cos (a 2 q_x)). \end{aligned} \quad (6.38)$$

The energy of the FM state, the Néel state and the RW-AFM state can be obtained from Eqn. (6.38) by substituting  $q_x = 0$ ,  $q_x = 4\pi/3a$  and  $q_x = 2\pi/a$ , respectively. Of course, the FM state and the RW-AFM state can be calculated from Eqn. (6.37) by substituting  $q_y = 0$  and  $q_y = 2\pi/\sqrt{3}a$ , respectively, which gives the same result. The

energy of the 3Q state has to be calculated directly from Eqn. (6.26). The results are listed below:

$$\begin{aligned}
E_{\text{biquadr,FM}} &= -6B_1S^4 & (6.39) \\
E_{\text{biquadr,Néel}} &= -\frac{3}{2}B_1S^4 \\
E_{\text{biquadr,RW-AFM}} &= -6B_1S^4 \\
E_{\text{biquadr,2Q}} &= -2B_1S^4. \\
E_{\text{biquadr,3Q}} &= -\frac{2}{3}B_1S^4.
\end{aligned}$$

For the rotations with two and three atoms per unit cell we obtain:

$$\begin{aligned}
E_{\text{biquadr,2at}}(\alpha) &= -B_1 S^4(2 + 4 \cos^2 \alpha) = -B_1 S^4(4 + 2 \cos 2\alpha) & (6.40) \\
E_{\text{biquadr,3at}}(\alpha) &= -B_1 S^4(4 \cos^2 \alpha + 2 \cos^2 2\alpha) = -B_1 S^4(3 + 2 \cos 2\alpha + \cos 4\alpha).
\end{aligned}$$

At the end of this section we summarize the energies of all relevant magnetic states within the Heisenberg model up to the third nearest-neighbor interaction including in addition the contributions due to the 4-spin interaction and biquadratic exchange.

$$\begin{aligned}
E_{\text{FM}} &= -S^2 \{6J_1 + 6J_2 + 6J_3\} - S^4 \{12K_1 + 6B_1\} & (6.41) \\
E_{\text{Néel}} &= -S^2 \{-3J_1 + 6J_2 - 3J_3\} - S^4 \{12K_1 + \frac{3}{2}B_1\} \\
E_{\text{RW-AFM}} &= -S^2 \{-2J_1 - 2J_2 + 6J_3\} - S^4 \{12K_1 + 6B_1\} \\
E_{\text{3Q}} &= -S^2 \{-2J_1 - 2J_2 + 6J_3\} - S^4 \{\frac{4}{3}K_1 + \frac{2}{3}B_1\} \\
E_{\text{SS } \bar{\Gamma}\text{-}\bar{M}}(\mathbf{q}) &= -S^2 \{J_1(2 + 4 \cos(a\frac{\sqrt{3}}{2}q_y)) + J_2(4 \cos(a\frac{\sqrt{3}}{2}q_y) + 2 \cos(a\sqrt{3}q_y)) \\
&\quad + J_3(2 + 4 \cos(a\sqrt{3}q_y))\} \\
&\quad - S^4 \{12K_1 + B_1(4 + 2 \cos(a\sqrt{3}q_y))\} \\
E_{\text{SS } \bar{\Gamma}\text{-}\bar{K}}(\mathbf{q}) &= -S^2 \{J_1(2 \cos(aq_x) + 4 \cos(a\frac{1}{2}q_x)) + J_2(4 \cos(a\frac{3}{2}q_x) + 2) \\
&\quad + J_3(2 \cos(a2q_x) + 4 \cos(aq_x))\} \\
&\quad - S^4 \{12K_1 + B_1(3 + 2 \cos(aq_x) + \cos(a2q_x))\} \\
E_{\text{2at}}(\alpha) &= -S^2 \{(J_1 + J_2)(2 + 4 \cos \alpha) + 6J_3\} - S^4 \{(2K_1 + B_1)(4 + 2 \cos 2\alpha)\} \\
E_{\text{3at}}(\alpha) &= -S^2 \{(J_1 + J_3)(4 \cos \alpha + 2 \cos 2\alpha) + 6J_2\} \\
&\quad - S^4 \{K_1(4 + 8 \cos 3\alpha) + B_1(3 + 2 \cos 2\alpha + \cos 4\alpha)\}
\end{aligned}$$

## 6.3 Unsupported monolayers: Spin-spirals and the 3Q-state

In Sec. 6.1 we presented the results of self-consistent non-collinear calculations, where we rotated the magnetic moments in real space on paths that connect high symmetry magnetic states, i.e. the ferromagnetic (FM) state, the row-wise antiferromagnetic (RW-AFM) state and the Néel state. The results that we obtained from the ab-initio calculations were surprising, in particular for the case of Mn, and cannot be understood within the framework of the nearest neighbor Heisenberg model. The investigation of the Heisenberg model in the previous Sec. (6.2) up to the third nearest-neighbor interaction and also higher order exchange interactions, i.e. the four-spin interaction and the biquadratic exchange, showed that, in order to gain a thorough understanding of itinerant magnetic materials and to predict the magnetic ground state of such materials on the triangular lattice, it is necessary to take further magnetic configurations into account that we omitted in Sec. 6.1. The additional magnetic states that need to be investigated are spin-spirals (SS) with  $q$ -vectors along the high symmetry lines of the Brillouin zone and the triple-Q (3Q) state. From our previous analysis of the 4-spin interaction and the biquadratic exchange, the 2Q state can be excluded. The 3Q state is particularly important in the case of Mn, because the calculations of Sec. 6.1 show that the RW-AFM state has the lowest energy among all magnetic states investigated for the unsupported monolayers (UMLs) Mn/Cu(111) and Mn/Ag(111). Within the Heisenberg model the RW-AFM state and the 3Q state are degenerate, and therefore the 3Q state is a possible candidate for the ground state of these systems.

In this section we present the results of self-consistent ab-initio calculations of spin-spirals with  $q$ -vectors on the three high symmetry lines,  $\bar{\Gamma}$ - $\bar{M}$ ,  $\bar{\Gamma}$ - $\bar{K}$  and  $\bar{K}$ - $\bar{M}$ , in the Brillouin zone of the two-dimensional hexagonal lattice. We also present calculations for the 3Q state, in particular comparing the energy to that of the RW-AFM state.

### 6.3.1 Computational details

Both the spin-spiral calculations and the calculation of the 3Q state were performed self-consistently in the local density approximation. The exchange correlation potential and a computational parameter were chosen as described in Sec. 6.1.1. Only the  $k$ -point sets differ from those described in Sec. 6.1.1 because of the different unit cells used. The spin-spiral calculations were carried out using the implementation explained in Sec. 5.5. At this point we would like to remind the reader that due to the existence of the  $q$ -vector in spin-spiral calculations the symmetry is reduced and the  $k$ -points have to be distributed in the full Brillouin zone. The  $p(1 \times 1)$  unit cell of the spin-spiral calculation contains only one atom. We checked the  $k$ -point convergence for each system separately and found that the size of the  $k$ -point set necessary to converge the energy differences between the magnetic configuration is quite different for the different systems. To obtain converged energy differences we needed 256

$k$ -points in the full Brillouin zone for Cr/Ag, 529  $k$ -points for Cr/Cu, Mn/Cu and Fe/Ag and 1024  $k$ -points for V/Ag, Mn/Ag and Fe/Cu. With these  $k$ -point sets it is also guaranteed that the energy differences obtained from the spin-spiral calculation between for example the FM and the RW-AFM state or the FM and the Néel state agree with the corresponding energy difference calculated in real space with two and three atoms per unit cell. The unit cell of the 3Q state contains four atoms and we used a  $k$ -point set that corresponded to 256  $k$ -points in the full Brillouin zone. Once more this  $k$ -point set allows a direct comparison with the energies calculated in other unit cells.

### 6.3.2 Results for the spin-spirals

In Fig. 6.11 the local magnetic moment and the total energy of the UMLs with the Cu lattice constant are shown as function of the spin-spiral  $q$ -vector. The top panel contains the result of the Cr/Cu(111) UML. From the rotations in real space we know that the ferromagnetic solution does not exist for this system. Thus, we expect to find no magnetic solutions with spin-spiral  $q$ -vectors close to the  $\bar{\Gamma}$ -point. The calculations confirm this conjecture. It can clearly be seen that the magnetic moment decreases and finally disappears when the  $q$ -vector approaches the  $\bar{\Gamma}$ -point on the symmetry line  $\bar{\Gamma}$ - $\bar{M}$  or  $\bar{\Gamma}$ - $\bar{K}$ . In the region where a magnetic solution exists the energy is in agreement with the expectation from the nearest neighbor Heisenberg model, though a comparison with the Heisenberg model is difficult to justify because of the strong change in the magnetic moment. The energy has a pronounced minimum at the  $\bar{K}$ -point. The  $\bar{K}$ -point corresponds to the  $120^\circ$  Néel state, which we have already found to have the lowest energy among the configurations we calculated for the real-space rotations.

In the case of Mn we find stable magnetic solutions over the whole range of  $q$ -vectors. In fact, the magnetic moment is almost independent of the  $q$ -vectors. As we know already from the calculation rotating the magnetic moments in real space, the energy at the  $\bar{M}$ -point, which corresponds to the RW-AFM state, is lower than the energy at the  $\bar{K}$ -point, which corresponds to the Néel state. A feature of  $E(\mathbf{q})$  that cannot be anticipated from the results in real space is the surprising local minimum of the energy between  $\bar{\Gamma}$  and  $\bar{K}$ . This corresponds to a spin-spiral state with a  $q$ -vector of  $\mathbf{q} \approx 0.7\bar{K}$ . The energy of this minimum is only about 21 meV higher than that of the RW-AFM state. A reason for this feature could be a strongly negative second nearest-neighbor exchange integral  $J_2$  (cf. Fig. 6.8), which would also explain that  $E(\mathbf{q})$  shows a local maximum at the  $\bar{K}$ -point.

The magnetic moment of Fe is slightly smaller than that of Mn and not as stable. Still, the variation is almost negligible. The range of the variation is smaller than for example during the rotation with three atoms per unit cell. This is also true for Mn/Cu. This could possibly be a consequence of the fact that the spin-spirals are highly symmetric states, while the intermediate states of the real-space rotation have a lower symmetry. An indication of the lower symmetry are the different local

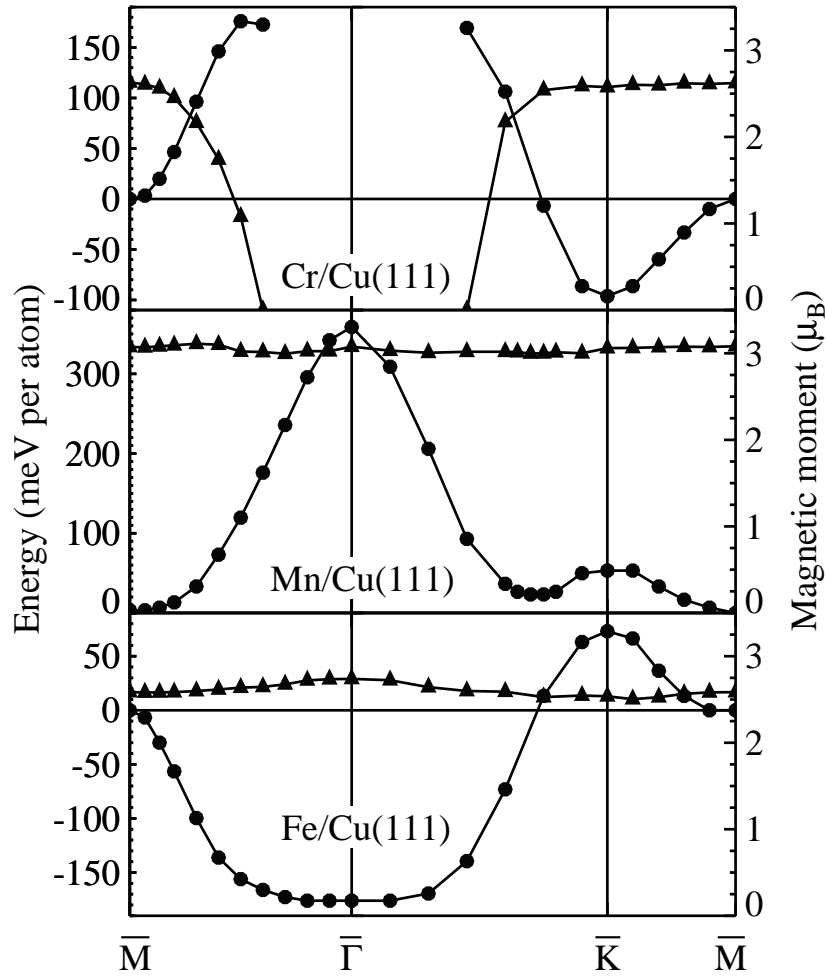


**Figure 6.11:** The total energy and magnetic moment of 3d-UMLs with Cu(111) geometry as function of the spin spiral  $q$ -vector. Shown are the calculated total energy relative to the RW-AFM energy (circles, left scale) and the magnetic moments (triangles, right scale).

moments of the atoms in the three-atom unit cell. The shape of the energy curve of Fe/Cu seems to be dominated by a ferromagnetic nearest-neighbor coupling, showing a minimum at the  $\bar{\Gamma}$ -point and a maximum at the  $\bar{K}$ -point. A very interesting aspect of the Fe/Cu system is the shape of  $E(\mathbf{q})$  in the region around the  $\bar{\Gamma}$ -point. In that region  $E(\mathbf{q})$  is almost independent of the  $q$ -vector. One consequence of the energy curve having such a flat shape could be an instability of the Fe film against magnetic fluctuations. In terms of the Heisenberg model this shape of  $E(\mathbf{q})$  can be accounted for by a negative  $J_2$  and/or  $J_3$ . A negative  $J_2$  can also explain the pronounced

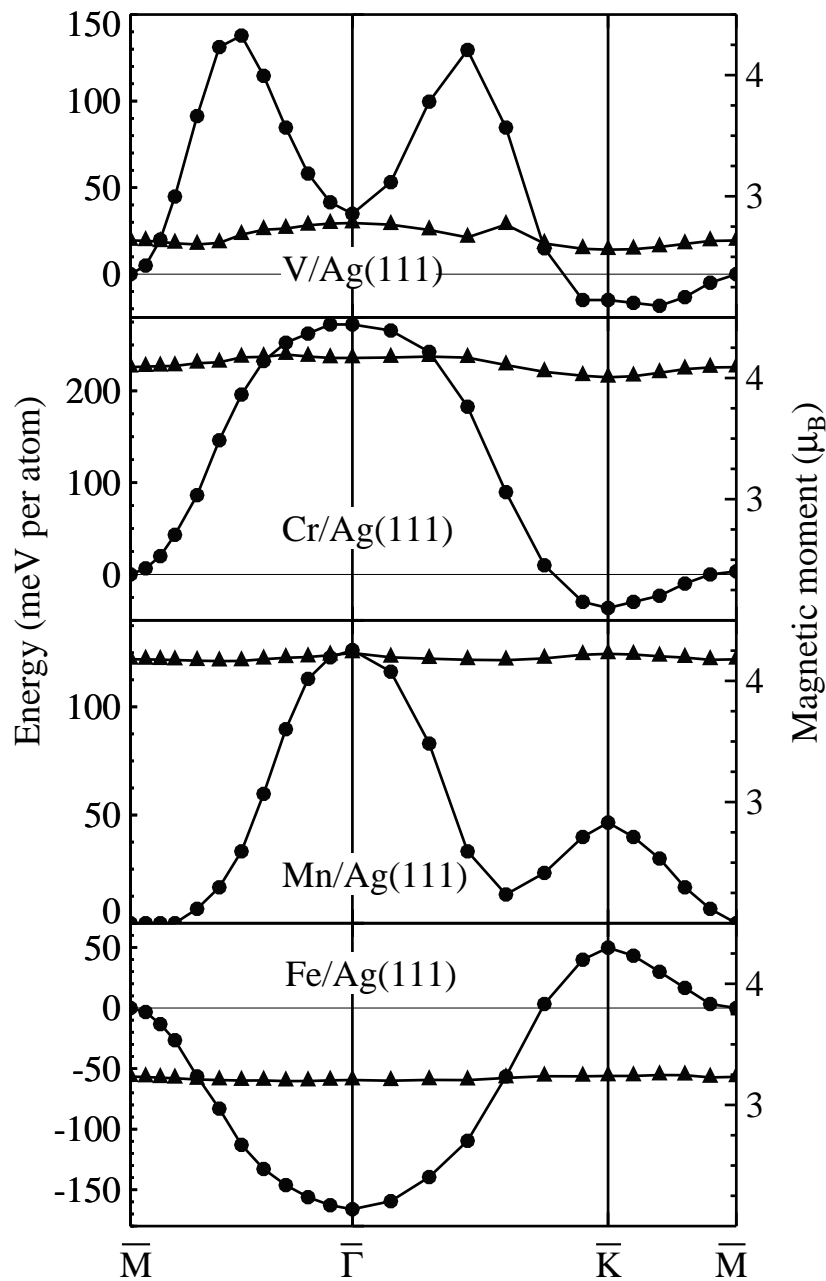


**Figure 6.12:** The total energy and magnetic moments of 3d-UMLs with Ag(111) geometry as function of the spin spiral  $q$ -vector. Shown are the calculated total energy relative to the RW-AFM energy (circles, left scale) and the magnetic moments (triangles, right scale).



maximum at the  $\bar{K}$ -point (cf. Fig. 6.8).

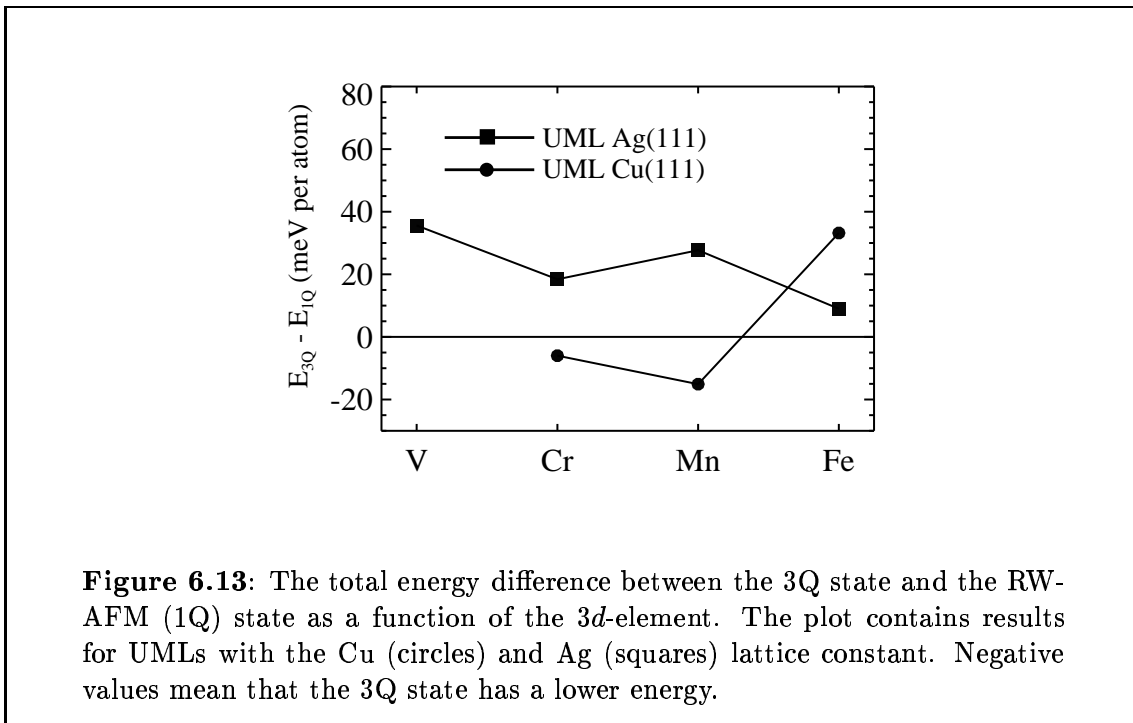
The results of the UMLs with the Ag lattice constant are presented in Fig. 6.12. All materials, V, Cr, Mn and Fe, have stable magnetic solutions for all  $q$ -vectors along the high symmetry lines and the local magnetic moments vary only within a very small range. Only V shows a slightly stronger variation of the moment in a range of about  $2.6 - 2.8 \mu_B$ . This result is not unexpected, since the variations of the moments of the UMLs with the Ag lattice constant during the real-space rotation are also small.

At first glance the result of the spin-spiral calculation for V looks surprising. However, the unusual form of the energy curve can be reproduced by the Heisenberg model, if  $J_1$  is negative and  $J_2$  and/or  $J_3$  are positive and about the same order of magnitude as  $J_1$ . The energetics of Cr appear to be dominated by the nearest-neighbor coupling.  $E(\mathbf{q})$  is extremely similar to the contribution of  $J_1$  (in Fig. 6.8). The minimum at the  $\bar{K}$ -point is not as pronounced as on the Cu lattice constant. The result for the Mn UML with the Ag lattice constant is similar to that on the Cu lattice constant. The local maximum at the  $\bar{K}$ -point and the local minimum at  $\mathbf{q} \approx 0.6\bar{K}$  on the line  $\bar{\Gamma}-\bar{K}$  appear more pronounced. However,  $E(\mathbf{q})$  varies in a much smaller energy range than in the case of Mn/Cu(111). This means, that increasing the lattice constant from Cu to Ag reduces  $J_1$  more strongly than  $J_2$ . The opposite seems to be the case for Fe. The influence of exchange beyond nearest neighbor is reduced with the Ag lattice constant. As a consequence, the maximum at the  $\bar{K}$ -point is not as clear-cut as in the case of Fe/Cu(111) and  $E(\mathbf{q})$  has a much larger curvature around the  $\bar{\Gamma}$ -point.

As a last magnetic configuration we consider the 3Q state (cf. Fig. 6.7). In particular, we consider the energy difference between the 3Q state and the RW-AFM state. This energy difference has a special significance, because the two magnetic configurations are degenerate within the Heisenberg model irrespective of how many nearest neighbor shells of atoms are taken in to account. This energy difference is purely due to higher order spin interactions. According to Eqn. (6.41) the energy difference per atom is given by

$$E_{3Q} - E_{RW-AFM} = \frac{16}{3} S^4 \{2K_1 + B_1\}. \quad (6.42)$$

$E_{3Q} - E_{RW-AFM}$  per atom is plotted as a function of the 3d-element in Fig. 6.13. First of all, it can be seen that the difference between the 3Q state and the RW-AFM state is in the order of 20 meV and thus generally smaller than the difference between the FM state and the RW-AFM state. That means that the energy differences due to higher order interactions are roughly one order of magnitude smaller than the first order effects for the system investigated here. At the Ag lattice constant the energy difference  $E_{3Q} - E_{RW-AFM}$  is positive for all UMLs, which means that the RW-AFM state is preferred over the 3Q state. The size of the energy difference depends strongly on the material. The largest value of 36 meV is found for V and the smallest value of 9 meV is found for Fe. On the Cu lattice constant the 3Q state has a lower energy for Cr and Mn, but a higher energy for Fe. In the case of Cr this does not have any



consequence for the magnetic ground state of the system, since the energy of the Néel state is clearly lower than that of both, the 3Q and the RW-AFM state. However, for Mn the RW-AFM state has the lowest energy of all configurations investigated so far. Since  $E_{3Q} - E_{RW-AFM}$  is negative, the 3Q state has the lowest energy among all magnetic configurations. Thus, the 3Q state is the magnetic ground state of the Mn/Cu(111) system. The calculated magnetic moments in the RW-AFM and 3Q state are almost identical for all materials.

UML	FM	FI	SS	Néel	3Q	ground state
Cr/Cu	-	-26	-	-97	-6	Néel
Mn/Cu	358	44	21	68	-15	3Q
Fe/Cu	-174	47	-	73	33	FM
V/Ag	35	-16	-	-16	36	FI or Néel
Cr/Ag	273	10	-	-39	18	Néel
Mn/Ag	128	26	15	48	28	RW-AFM
Fe/Ag	-164	35	-	49	9	FM

**Table 6.7:** Energies of the different magnetic configurations relative to the energy of antiferromagnetic (1Q) configuration in meV. The Cr/Cu system does not have a stable ferromagnetic solution.

The energies of all relevant magnetic states of the unsupported monolayers are summarized in Tab. 6.7. The energies are relative to the energy of the RW-AFM

state. Thus, negative values mean that the corresponding magnetic configuration has a lower energy than the RW-AFM state. If all energies listed are positive, as for Mn/Ag, the RW-AFM state has the absolutely lowest energy and is the ground state of the system. In the case of Mn we found a local minimum of the energy for spin-spirals with  $q$ -vectors on the line  $\bar{\Gamma}$ - $\bar{K}$ . The energy of this configuration is provided in the column denoted SS and was calculated only for Mn. The corresponding  $q$ -vectors are  $\mathbf{q} \approx 0.7\bar{K}$  for the UML Mn/Cu(111) and  $\mathbf{q} \approx 0.6\bar{K}$  for the UML Mn/Ag(111) (cf. Fig. 6.11 and 6.12).

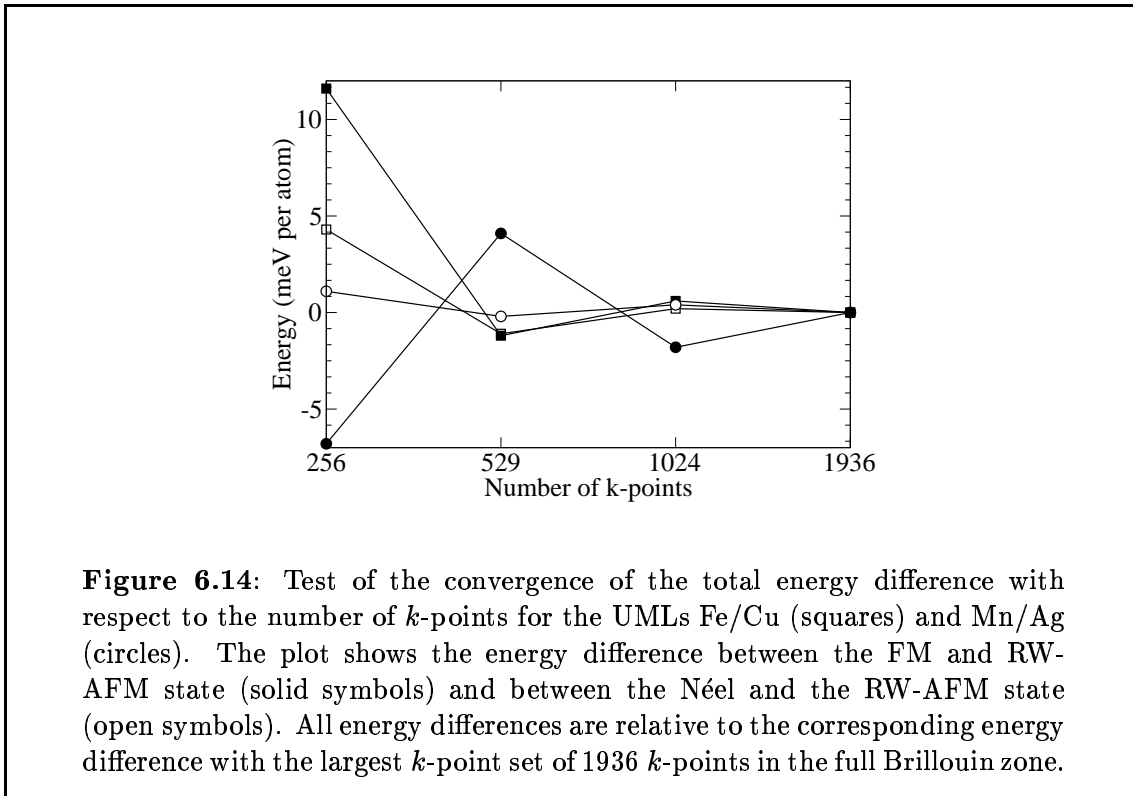
An amazing characteristic of these results is the large variety of predicted ground states, including the FM, the RW-AFM, the 120° Néel, the 3Q and possibly (in the case of V) the FI state. The UMLs of Cr reach their lowest energy in the Néel state on both, the Cu and the Ag, lattice constants. The Néel state is generated by  $q$ -vectors from the  $\bar{K}$ -point. In the case of Mn the energy becomes minimal for the 3Q state (Mn/Cu) and the RW-AFM state (Mn/Ag), respectively. Both configurations correspond to the  $\bar{M}$ -point in the Brillouin zone. The Fe UML are ferromagnetic on both lattice constants, i.e.  $J(\mathbf{Q})$  becomes maximal at the  $\bar{\Gamma}$ -point. Thus, the ground states of these three systems already cover all high symmetry points in the two-dimensional Brillouin zone. For the UML V/Ag the magnetic ground state can not be predicted with certainty, because two states, the ferrimagnetic (FI) state and the Néel state, are very close. The accuracy of the calculation does not allow to decide which of the two states has the lower energy.

### 6.3.3 Tests of the convergence with respect to numerical cut-offs

The two most important numerical parameters, which also have the strongest influence on the computer time needed for a calculation, are the number of basis functions controlled by the the planewave cutoff  $k_{\max}$  and the number of  $k$ -points used for the Brillouin zone sampling. Our aim was to achieve an accuracy of about 1 – 2 meV/atom of the calculated total energy differences. The biggest absolute variations of the total energy differences are of course expected between those states, for which the total energy difference is largest. Between those states the required absolute accuracy of 1 – 2 meV/atom corresponds to the smallest relative error. Therefore, we decided to consider the energy difference between the FM and the RW-AFM state, for most of our convergence tests. For the convergence tests with respect to the  $k$ -point set and the planewave cutoff for the basis functions we have also included the energy difference between the Néel state and the RW-AFM state. As expected, the changes of the latter energy difference with respect to the computational parameters were always smaller than that of  $E_{\text{FM}} - E_{\text{RW-AFM}}$ .

We performed systematic tests of the  $k$ -point convergence for the spin-spiral calculations. These calculations have the smallest unit cell and cover a large variety of magnetic states. In fact, most of the energies presented in Tab. 6.7, except the energies of the 3Q and FI state, are obtained from spin-spiral calculations. We calculated

$E_{\text{FM}} - E_{\text{RW-AFM}}$  for different  $k$ -point sets and increased the number of  $k$ -points until the desired accuracy was reached. Fig. 6.14 shows the energy difference as a function of the number  $k$ -points in the full Brillouin zone for two examples. We have chosen



the UMLs Fe/Cu and Mn/Ag, as they are two examples for the systems that required the largest  $k$ -point sets (cf. Sec. 6.3.1). The energy differences in Fig. 6.14 are normalized to the value obtained with the largest  $k$ -point set (1936  $k$ -points), i.e. we actually plotted the quantity  $\Delta E(N_{\text{kpt}}) - \Delta E(1936)$ , where  $N_{\text{kpt}}$  is the number of  $k$ -points. It can be seen that  $E_{\text{Néel}} - E_{\text{RW-AFM}}$  converges faster than  $E_{\text{FM}} - E_{\text{RW-AFM}}$ . For both cases we have used the  $k$ -point set with 1024  $k$ -points for all further calculations.

In order to test the convergence of the energy differences with respect to the planewave cutoff we have increased  $k_{\text{max}}$  from 3.7 a.u.<sup>-1</sup> to 4.1 a.u.<sup>-1</sup> (from 115 to 160 basis functions per atom) for the UMLs with the Cu lattice constant and from 3.3 a.u.<sup>-1</sup> to 3.7 a.u.<sup>-1</sup> (from 125 to 180 basis functions per atom) for the UMLs with the Ag lattice constant. The change of the energy difference was always clearly smaller than 0.5 meV per atom. Only for the Mn/Cu system we found a change of 0.8 meV per atom for both  $E_{\text{FM}} - E_{\text{RW-AFM}}$  and  $E_{\text{Néel}} - E_{\text{RW-AFM}}$ .

For some selected systems we have also increased the planewave cutoff for the expansion of the density  $G_{\text{max}}$  and the number of the radial mesh points for the representation of the radial basis functions inside the muffin-tin sphere. In all tested cases the changes were negligible.

Due to the approximation of a collinear magnetization inside the muffin-tin

spheres (cf. Chap. 5 and Fig. 5.1) it is very important to investigate how a change of the muffin-tin radius  $R_{\text{MT}}$  affects the results of a non-collinear calculation. Such a test has already been presented in Sec. 5.4.2 where we have tested the implementation of the constrained local moment method. We used the real-space rotation of a Cr/Ag(111) UML in the unit cell with two atoms. The calculation was performed with two different muffin-tin radii, 2.75 a.u. and 2.00 a.u. In Sec. 5.4.2 we focused on the change of the constraint field and the total (parallel) magnetic moment in the muffin-tin. Here we are mainly interested in the change of the calculated total energy. The total energy is shown in Fig. 5.4. Let us consider the energy difference between the ferromagnetic state and the antiferromagnetic state,  $E_{\text{FM}} - E_{\text{RW-AFM}}$ , and between the ferromagnetic state and the configuration where the angle  $\alpha$  between the rows of magnetic atoms is  $90^\circ$ ,  $E_{\text{FM}} - E_{90^\circ}$ . Setting the muffin-tin radius to 2.75 a.u. we obtain  $E_{\text{FM}} - E_{\text{RW-AFM}} = 272$  meV/atom and  $E_{\text{FM}} - E_{90^\circ} = 153$  meV/atom. When  $R_{\text{MT}}$  is reduced to 2.0 a.u. these energy differences change by 2.3 and 1.9 meV/atom respectively. It should be noted, that reducing  $R_{\text{MT}}$  from 2.75 to 2.00 a.u. means a radical change, because the volume of the spheres is reduced by a factor 2.6. And, in addition, the planewave cutoff  $k_{\text{max}}$  has to be increased, when  $R_{\text{MT}}$  is decreased. A remarkable consequence of this result is that apparently for the 3d transition metals the approximation of a collinear magnetization in the muffin-tin spheres does not introduce a significant error for a total energy calculation. The FM and the RW-AFM state are collinear magnetic configurations, i.e. the magnetization of the Cr UML is exactly collinear everywhere in space. Only the  $90^\circ$  state is non-collinear and replacing the magnetization inside the sphere by a collinear one is an actual approximation. However, the change of the energy differences  $E_{\text{FM}} - E_{\text{RW-AFM}}$  and  $E_{\text{FM}} - E_{90^\circ}$  has almost the same size. Hence, the approximation of a collinear magnetization in the muffin-tin spheres is not crucial for the systems considered here.

## 6.4 Discussion of the results for the unsupported monolayers

In this section we will discuss the result all ab-initio calculations for the unsupported monolayers, the real-space rotations of the magnetic moments (Sec. 6.1) as well as the spin-spiral calculation and the 3Q state (Sec. 6.3). We will first determine estimates of the exchange integrals by fitting the results to the Heisenberg model. Afterwards we will discuss the trends for the different 3d elements in term of the magnetic phase diagram of the Heisenberg model.

### 6.4.1 Estimate of exchange parameters

In order to gain a better understanding of the results of our ab-initio calculations we fitted the data using the functional dependence of the energy within the Heisenberg model. The equations for the energy as a function of the spin-spiral vector and the

angle  $\alpha$ , respectively, in the Heisenberg model including higher order terms have were in Sec. 6.2 (Eqn. (6.41)). The aim of the fitting procedure was to obtain only an estimate of the parameters of the model Hamiltonian  $J_1$ ,  $J_2$ ,  $J_3$ ,  $K_1$  and  $B_1$ . To achieve this with simplest possible fitting procedure we chose  $E_{3\text{at}}(\alpha)$  and  $E_{\text{SS } \bar{\Gamma}\text{-}\bar{K}}(\mathbf{q})$  for our fits, because the fit to  $E_{3\text{at}}(\alpha)$  allows the determination of  $S^2(J_1 + J_3)$ ,  $S^4K_1$  and  $S^4B_1$  and the fit to  $E_{\text{SS } \bar{\Gamma}\text{-}\bar{K}}(\mathbf{q})$  allows us to calculate  $S^2J_1$ ,  $S^2J_2$  and  $(2S^2J_3 + S^4B_1)$ . In contrast, fits to  $E_{2\text{at}}(\alpha)$  and  $E_{\text{SS } \bar{\Gamma}\text{-}\bar{M}}(\mathbf{q})$  only allow the determination of two independent parameters.

UML	$S^2(J_1 + J_3)$	$S^4K_1$	$S^4B_1$	$E_{3\text{Q}} - E_{\text{RW-AFM}}$
Mn/Cu	-34.6	-2.6	3.7	-8.0
Fe/Cu	28.1	-0.2	-1.0	-7.5
V/Ag	-6.8	0.1	2.6	14.9
Cr/Ag	-33.3	0.3	-2.6	-10.7
Mn/Ag	-10.6	-1.1	3.2	5.3
Fe/Ag	24.9	-0.1	-2.5	-14.4

**Table 6.8:** Exchange constants including  $K_1$  and  $B_1$  as obtained from a fit to  $E_{3\text{at}}(\alpha)$ . The last column contains the energy difference between the 3Q and the RW-AFM state as calculated from the fitted values of  $K_1$  and  $B_1$  according to  $E_{3\text{Q}} - E_{\text{RW-AFM}} = 16/3S^4\{2K_1 + B_1\}$ .

The parameters obtained from the fit of  $E_{3\text{at}}(\alpha)$  are presented in Tab. 6.8. We did not perform a fit for the Cr UML with the Cu lattice constant, because of the strong change of the magnetic moment. The Heisenberg exchange parameters are much larger than the exchange parameters of the higher order spin interactions in agreement with the results obtained for the energy difference between the 3Q and the RW-AFM state. The magnitude of  $K_1$  is mostly very small. Only the values computed for the Mn UMLs stand out. The 4-spin interaction provides a term proportional to  $\cos 3\alpha$  in  $E_{3\text{at}}(\alpha)$ . Thus, the size of  $K_1$  is the origin of the local maximum at  $\alpha = 120^\circ$  found for the Mn UMLs.

UML	$S^2J_1$	$S^2J_2$	$(2S^2J_3 + S^4B_1)$
Mn/Cu	-31.2	-13.9	-6.3
Fe/Cu	29.8	-8.8	-5.1
V/Ag	-14.4	9.9	17.1
Cr/Ag	-38.7	4.4	7.9
Mn/Ag	-9.6	-7.0	-0.3
Fe/Ag	25.1	-4.9	-3.6

**Table 6.9:** Exchange constants including  $B_1$  as obtained from a fit to  $E_{\text{SS } \bar{\Gamma}\text{-}\bar{K}}(\mathbf{q})$ .

Tab. 6.9 contains the parameters determined from a second fit to  $E_{\text{SS } \bar{\Gamma}-\bar{K}}(\mathbf{q})$ . This fit allows a direct calculation of  $J_1$  and  $J_2$ . It can be seen that, though  $J_1$  represents the largest parameter in all cases, the contribution of  $J_2$  is substantial.  $J_2$  is clearly larger than the terms due to higher order spin interactions. Taking the results of the two fits together we can also calculate the missing parameter  $J_3$ , e.g. from  $J_1$  and  $(J_1 + J_3)$ . It is of course also possible to use  $S^4 B_1$  and  $(2S^2 J_3 + S^4 B_1)$  instead. All parameters including  $J_3$  are summarized in Tab. 6.10.

UML	$S^2 J_1$	$S^2 J_2$	$S^2 J_3$	$S^4 K_1$	$S^4 B_1$	$E_{3\text{Q}} - E_{\text{RW-AFM}}$
Mn/Cu	-31.2	-13.9	-3.4	-2.6	0.5	-25.1
Fe/Cu	29.8	-8.8	-1.7	-0.2	-1.7	-11.2
V/Ag	-14.4	9.9	7.6	0.1	1.9	11.2
Cr/Ag	-38.7	4.4	5.4	0.3	-2.9	-12.3
Mn/Ag	-9.6	-7.0	-1.0	-1.1	1.7	-2.7
Fe/Ag	25.1	-4.9	-0.2	-0.1	-3.2	18.1

**Table 6.10:** Exchange constants calculated from 6.8 and 6.9.  $S^2 J_3$  has been calculated according to  $S^2 J_3 = S^2(J_1 + J_3) - S^2 J_1$  taking the values of  $S^2(J_1 + J_3)$  and  $S^2 J_1$  from tables and 6.8 and 6.9, respectively. Similarly,  $S^4 B_1$  has been calculated according to  $S^4 B_1 = (2S^2 J_3 + S^4 B_1) - 2S^2 J_3$ , in addition to the direct determination from a fit in Tab. 6.8. The last column contains the energy difference between the 3Q and the RW-AFM state as calculated from the fitted values of  $K_1$  and  $B_1$  according to  $E_{3\text{Q}} - E_{\text{RW-AFM}} = 16/3 S^4 \{2K_1 + B_1\}$  using the new value of  $S^4 B_1$ .

In Tab. 6.8 and 6.10 we present two different values of  $B_1$ . The values in table 6.8 have been directly determined from the fit of  $E_{3\text{at}}(\alpha)$ , while the values in Tab. 6.10 have been calculated indirectly from  $(2S^2 J_3 + S^4 B_1)$  and  $2S^2 J_3$ , which itself has been calculated indirectly (cf. Fig. 6.10). Therefore, we expect the values in Tab. 6.8 to be more accurate, since the second values of  $B_1$  determined in Tab. 6.10 accumulate the errors of  $J_1$ ,  $J_1 + J_3$  and  $(2S^2 J_3 + S^4 B_1)$ . The comparison of the two results for  $B_1$  can serve as test for the applicability of the fit procedure. In all cases the sign of the two calculated values of  $B_1$  agrees, but the size of  $B_1$  differs significantly. In particular for Mn/Cu, but also Mn/Ag, this difference is very large. A different check of the quality of the calculated values of  $B_1$  and  $K_1$  is a comparison with the total energy difference between the 3Q and RW-AFM state. This energy difference is given in terms of the higher order exchange parameters by  $E_{3\text{Q}} - E_{\text{RW-AFM}} = 16/3 S^4 \{2K_1 + B_1\}$ , i.e.  $E_{3\text{Q}} - E_{\text{RW-AFM}}$  can be calculated from  $K_1$  and  $B_1$  and are directly comparable to the total energy differences presented in Tab.6.7. The values of  $E_{3\text{Q}} - E_{\text{RW-AFM}}$  that correspond to  $K_1$  and  $B_1$  obtained from the fits, using the two results for  $B_1$  given in Tab 6.8 and 6.10, are presented in the last column of Tab. 6.8 and 6.10, respectively. The outcome is rather disappointing. Only half the values of  $E_{3\text{Q}} - E_{\text{RW-AFM}}$  obtained from  $K_1$  and  $B_1$  have the correct sign, and even when the sign is correct, the magnitude is usually quite far off. The reason for this

inconsistency of the results could be the neglect of further exchange integrals,  $J_4, J_5, \dots$ , but also higher order terms like  $K_2, B_2, \dots$ . If such terms contribute to  $E_{3\text{at}}(\alpha)$  and  $E_{\text{SS } \bar{\Gamma}-\bar{K}}(\mathbf{q})$  in a similar way like  $J_{1-3}, K_1$  and  $B_1$  the outcome of the fit might be inaccurate. Looking at  $J_{1-3}$ ,  $S^2 J_4$  can be expected to be comparable to  $S^4 K_1$  and  $S^4 B_1$ . On the other hand, the contribution of  $K_1$  to  $E_{3\text{at}}(\alpha)$  is proportional to  $\cos 3\alpha$ , which cannot be provided by any  $J_i$ . Thus, the values of  $K_1$  are probably more reliable than  $B_1$ .

In conclusion we can say that the parameter  $B_1$ , but also  $K_1$ , were not determined consistently and sufficiently reliably by our calculations. In order to determine these parameter more accurately it is probably necessary to include further exchange parameters  $J_4, J_5, \dots$  and perhaps also  $K_2, B_2, \dots$  into the study. It might also be helpful to choose real-space spin rotations or spin-spirals specifically selected to determine certain model parameters. However, we can say with certainty that higher order terms, i.e.  $K_1$  and  $B_1$ , play an important role for the  $3d$ -metals, since their magnitude is comparable to  $J_2, J_3, \dots$ . This last statement is independent of the fits to  $E_{3\text{at}}(\alpha)$  and  $E_{\text{SS } \bar{\Gamma}-\bar{K}}(\mathbf{q})$ . The importance of the higher order terms can be appreciated directly from the energy difference between the 3Q and the RW-AFM state, because the two states are degenerate within the Heisenberg model irrespective of how many nearest neighbors are taken into account. To stress once more, it is not our total energy calculations which are in question, but the quality of the fit to the exchange parameters due to an insufficient data set of self-consistent calculations.

### 6.4.2 Discussion and classification of the results in terms of the exchange parameters

For fcc and bcc bulk transition metals it is well know [THOA82] that the exchange integrals are rapidly oscillating functions of the band filling. Since we have not performed calculations for all elements of the  $3d$  transition metal series, we cannot discuss in detail this dependence of exchange parameter  $J_1$  to  $J_3, K_1$  and  $B_1$  for the (111) oriented UMLs. From Ref. [THOA82] we conclude that the exchange parameters  $J_n$  have at least  $2n$  zeros as function of the band filling, ignoring zero and full band filling.  $K_1$  and  $B_1$  are expected to behave similar to  $J_2$ . Despite the deficiencies of the fit of  $J_1$  to  $J_3$  and in particular  $K_1$  and  $B_1$  discussed in the previous section several trends are for the exchange parameters are clearly visible in Tab. 6.10. One is certainly the change of the sign as function of the band filling represented here by the different elements of the  $3d$  transition metal series. It can be seen that  $J_1$  is negative for V, Cr and Mn, and changes sign between Mn and Fe. A closer look reveals that the magnitude of  $J_1$  first increases from V to Cr and then decreases again from Cr to Mn, and as said changes sign and becomes positive between Mn and Fe showing again a large magnitude for Fe. It nicely resembles an oscillatory function on a coarse grid.  $J_2$  changes sign between Cr and Mn. In contrast to  $J_1$  it is positive for V and Cr and negative for Mn and Fe.  $J_3$  and  $K_1$  show basically the same behavior as  $J_2$ , but the magnitude of  $J_3$  for Fe/Ag is already quite small.

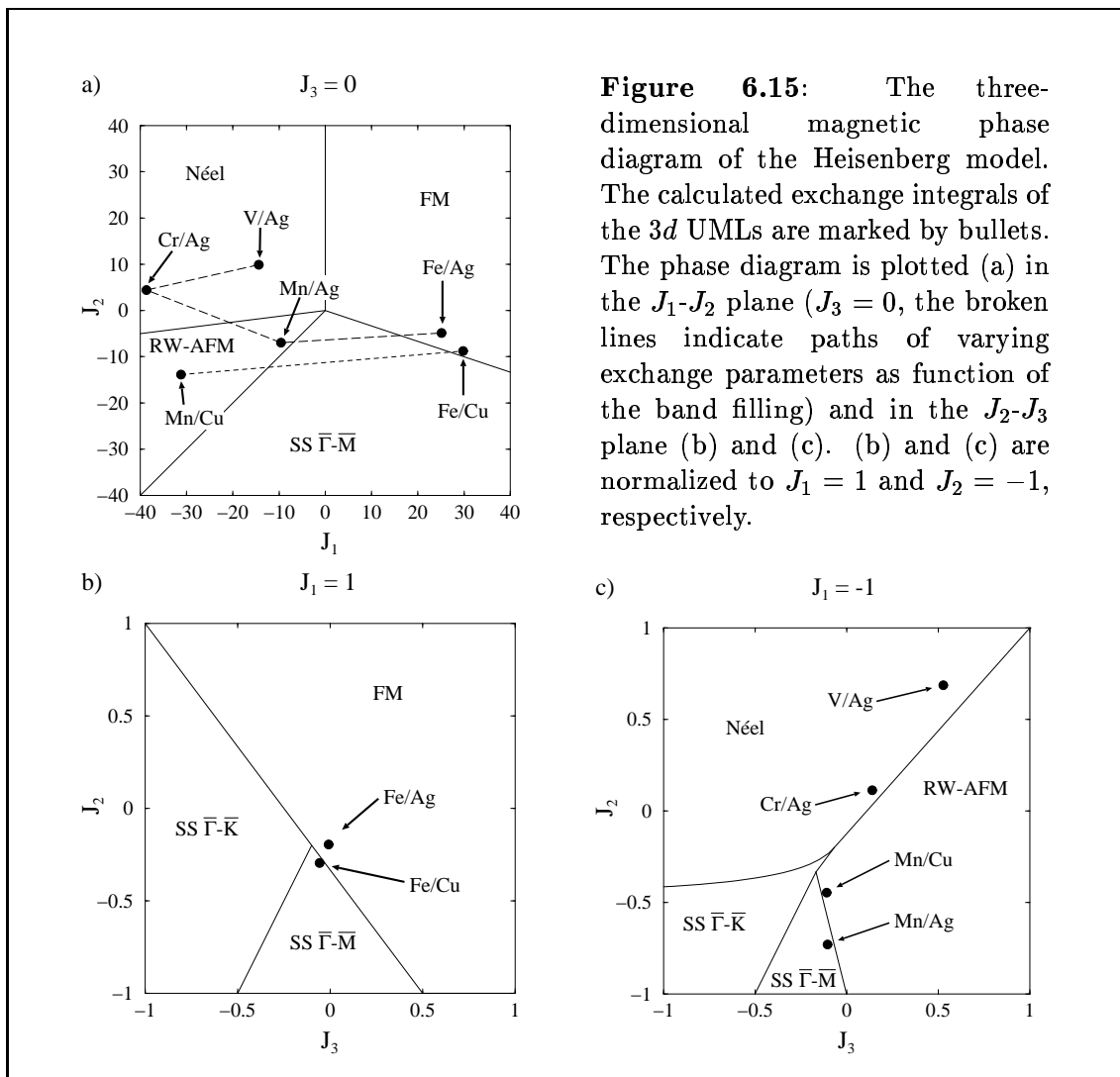


An additional change of sign for  $J_3$  is expected for a band filling slightly larger than Fe.  $B_1$  changes sign for every element.  $B_1$  is positive for V and Mn and negative for Cr and Fe. So far, the discussion on the signs holds for the UMLs on the Cu(111) as well as the Ag(111) lattice constant and we speculate that it is intrinsic to the electronic structure of the UMLs. In a second step we compare the magnitude of the different exchange parameters. It can be seen that in general the exchange integrals decrease from  $J_1$  to  $J_3$ .  $K_1$  and  $B_1$  are typically one order of magnitude smaller than  $J_1$ , but comparable in magnitude to  $J_3$ , and thus cannot be neglected. Comparing the exchange parameters of Mn and Fe on the Cu(111) lattice with those of the Ag(111) lattice several observations can be made: in general the magnitudes of  $J_2$ ,  $J_3$  and  $K_1$ , and to some extent also  $J_1$ , are significantly larger at the Cu lattice constant than at the Ag lattice constant, irrespective of the size of the magnetic moments, which are larger on the Ag lattice constant. We attribute this trend to the larger overlap of the 3d wave functions of neighboring atoms due to the smaller lattice constant of Cu. The exchange parameter for the biquadratic exchange  $B_1$  does not follow the trend of  $J_1 - J_3$  and  $K_1$ . Instead  $B_1$  is in general larger for the unsupported transition metal monolayers on the Ag lattice constant than on the Cu lattice constant. It might be that the biquadratic exchange is more strongly dependent of the size of the local moment or the intra-atomic exchange, i.e. the local Coulomb interaction, respectively. We have not investigated this point, but we see that the ratio of  $K_1/B_1$  changes significantly between the monolayers on Cu and Ag lattice constant. This change has an important effect on the magnetic ground state. For Mn/Cu(111) and Mn/Ag(111) the RW-AFM state has the lowest energy among all spin-spiral states, but the ground state of the Mn/Cu(111) is the 3Q state since  $2K_1 > B_1$ , while the ground state of Mn/Ag(111) is the RW-AFM state since  $2K_1 < B_1$  (actually  $2K_1 \approx B_1$  within the accuracy of the calculation). We suspect that the ratio  $K_1/B_1$  depends sensitively on the hybridization with the substrate. Finally, we would like to mention a further apparent trend, the decrease of  $J_2$  and in particular  $J_3$  from V to Fe. This trend could reflect that with increasing nuclear number the localization of the 3d wave function increases, which leads then to a smaller overlap of the 3d wave function with the second and third nearest neighbor atoms. On the other hand the values given in Tab. 6.10 may exaggerate this effect, since the maxima of  $J_2$  and  $J_3$  as function of the band filling might be at fractional values of the nuclear number, which we have not calculated.

As a next step it is very interesting to discuss the calculated exchange integrals in terms of the phase diagram of the Heisenberg model that was derived in Sec. 6.2.3. Let us begin with the two-dimensional phase diagram ( $J_3 = 0$ , Fig. 6.15 a). V and Cr have a negative  $J_1$  and a positive  $J_2$ . Thus, they are found in the upper left quadrant of the phase diagram as indicated in Fig. 6.15 a, which corresponds to the Néel state. Mn has a negative  $J_2$  and the magnitude of  $J_2$  is between  $1/8J_1$  and  $J_1$  on both lattice constants. Thus, Mn lies in the region of the RW-AFM ground state. Fe has a positive  $J_1$  and a negative  $J_2$ , which is larger than  $-1/3J_1$ . Hence, it lies in the region of the FM ground state. However, for the UML Fe/Cu(111) the magnitude of

$J_2$  is almost 1/3 of the magnitude of  $J_1$ , i.e. Fe/Cu(111) is very close to the border between the FM and the spin-spiral ground state. If we assume continuously varying exchange coupling constants as function of the band filling the lines connecting the points in Fig. 6.15 a are interpreted as paths of the band filling in the phase diagram. It is interesting to notice that the path from Mn to Fe crosses the region of the spin-spiral state on the high symmetry line  $\bar{\Gamma}-\bar{M}$ . Including  $J_3$  modifies the phase boundaries and an additional phase, the spin-spiral state on the symmetry line  $\bar{\Gamma}-\bar{K}$ , is crossed. Thus, slight changes of the band filling, and hence the electronic structure and the exchange parameters, may lead to a drastic change of the magnetic ground state. Therefore, without accurate ab-initio total energy calculations including spin-spirals, predictions of the magnetic ground state of films made of MnFe alloys will be impossible. We will return to this point below.

As said before, when  $J_3$  is included in the discussion the problems get slightly more involved. Fig. 6.15 b and c show magnified details of Fig. 6.9 b and c. The



exchange integrals have been normalized to  $J_1 = 1$  and  $J_1 = -1$  respectively. V and Cr are found in the Néel region, though Cr is very close to the border of the RW-AFM state. Mn/Cu and Mn/Ag are both extremely close to the border between the RW-AFM and the spin-spiral state on the symmetry line  $\bar{\Gamma}-\bar{M}$ . In fact, the UML Mn/Ag is just in the region of the spin-spiral ground state in disagreement with our ab-initio results (Tab. 6.7 and Fig. 6.12). A similar problem is found for Fe. Fe/Ag lies in the FM region, but Fe/Cu lies in the region of the spin-spiral, again very close to the border of that region. The tendency towards a spin-spiral ground state can be seen for both these systems, Fe/Cu and Mn/Ag, in Fig. 6.11 and 6.12. In the case of Fe/Cu  $E_{SS}(\mathbf{q})$  has an extremely flat shape around the  $\bar{\Gamma}$ -point. In particular, the first 2–3 points on the line  $\bar{\Gamma}-\bar{M}$  have almost the same energy as the  $\bar{\Gamma}$ -point. A slightly more negative value of  $J_2$  would create a minimum in that region and the corresponding spin-spiral state would become the ground state of the system. A similar feature is found close to the  $\bar{M}$ -point of Mn/Ag. Here, the first three points on the line  $\bar{M}-\bar{\Gamma}$  are practically on one level and again a stronger contribution of  $J_2$  would lead to a new ground state.

As we have discussed previously, the exchange integrals are oscillating functions of the band filling. We found that  $J_1$  changes sign between Mn and Fe, but  $J_2$  is negative for both elements. Therefore, we expect  $J_1$  to become small compared to  $J_2$  for a band filling in between Mn and Fe. Such systems can be realized by an alloy of the two metals. In the theoretical calculation we can also model this kind of alloy by using fractional nuclear numbers. In order to investigate the properties of a possible Mn/Fe alloy we have performed a spin-spiral calculation of an UML with a nuclear number of  $Z = 25.5$  (cf.  $Z_{\text{Mn}} = 25$ ,  $Z_{\text{Fe}} = 26$ ). The result of this calculation is presented in Fig. 6.16. The energy is a global minimum for a spin-spiral with a  $q$ -vector of about  $0.6 \bar{M}$ . Hence, the ground state is in fact a spin-spiral on this symmetry line. On the other hand, this  $q$ -vector is six-fold degenerate in the Brillouin zone of the two-dimensional hexagonal lattice. Thus, due to higher order spin interactions a particular high symmetry superposition of several spin-spiral states might be the magnetic ground state. Another pronounced minimum is found at about  $1/3 \bar{K}$  on the line  $\bar{\Gamma}-\bar{K}$ . The energy of the second minimum is only about 12 meV ( $\approx 150$  K) higher than the ground state. For temperatures below 150 K we expect that only spin-waves with spin-wave modes around the local minimum between  $\bar{\Gamma}$  and  $\bar{M}$  will also be excited. For higher temperatures around 150 K and higher, spin-wave around the second minimum will be excited. In this case the dynamical and thermodynamic properties of the magnetic film become more complex which requires a treatment by a mode-mode-coupling theory. This is beyond the scope of this work. As a side remark, I would like to remind the reader that for ultrathin films the critical temperature of the magnetization is determined by the inter-atomic exchange interaction and the magnetic anisotropy. The latter is not considered here and the critical temperature cannot be determined. However, in case the critical temperature comes in the order of 150 K or higher, the second minimum must be taken in consideration to reliably predict the Néel temperature. If such an

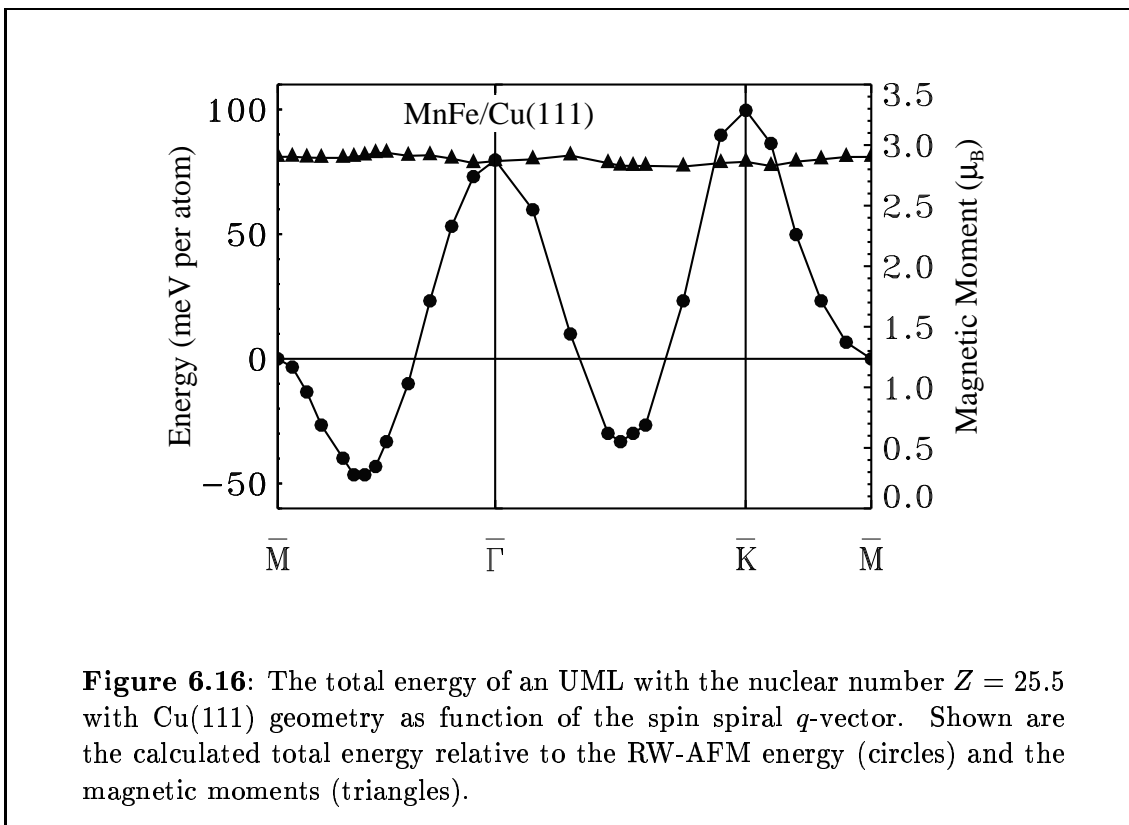


**Figure 6.16:** The total energy of an UML with the nuclear number  $Z = 25.5$  with Cu(111) geometry as function of the spin spiral  $q$ -vector. Shown are the calculated total energy relative to the RW-AFM energy (circles) and the magnetic moments (triangles).

alloy can be grown in an actual experiment, it might even be possible to influence the ground state and the  $q$ -vector of the ground state by changing the composition. A thorough investigation of the exchange constants as function of the nuclear number  $J_i(Z)$  represents a very interesting project for the future. Not only as a model for possible alloys, but also to compare with the theoretical predictions of Terakura et al.[THOA82]

## 6.5 Results for monolayers on substrate

So far we have considered unsupported monolayers as model system for monolayers (ML) on an actual noble metal substrate. In order to confirm the results from the UMLs and to obtain reliable predictions for the more realistic systems, the monolayer on the substrate, we repeated the calculations including the substrate. However, due to the enormous computational expenditure of such calculations, we concentrated on the most important magnetic states. We performed this investigation in two steps. First we established the geometry of systems by atomic force calculations. We relaxed all atoms in a symmetric film with 7 layers of substrate and  $3d$ -metal monolayers on top of both film surfaces. The relaxations were carried out for the ferromagnetic MLs, except for the case of Cr on Cu, where the antiferromagnetic ML was used, because a ferromagnetic solution does not exist. These calculations were carried out in the

generalized gradient approximation (GGA). The GGA is known to greatly improve the lattice constants of 3d-metals, when the exchange and correlation potentials are treated beyond the atomic sphere approximation [ASH<sup>+</sup>99]. Therefore, we applied the GGA during the force calculations. In the second step we calculated the magnetic energies for the different configurations using the local density approximation (LDA). Due to the large computational effort of these non-collinear calculations we used asymmetric films with 4 layers of substrate and 1ML of the 3d metal on only one side of the film. The atomic positions obtained from the structural optimization in the first step were used for all magnetic configurations.

### 6.5.1 Structural optimization of 3d-monolayers on Cu(111) and Ag(111)

During the structural optimization we used a symmetric 9-layer film. The structural optimization was performed for the ferromagnetic configuration. Thus, the surface unit cell contained only one atom. Only for the Cr/Cu(111) system we relaxed the atoms in the antiferromagnetic configuration, since no stable ferromagnetic solution could be found. For the lateral lattice constants we used the values obtained from bulk calculations of the respective substrates. We determined a lattice constant of  $a_{\text{Cu}} = 6.83$  a.u. for Cu, which is in very good agreement (+0.2%) with the experimental value ( $a_{\text{Cu,exp}} = 6.81$  a.u.), while the value we obtained for Ag,  $a_{\text{Ag}} = 7.84$  a.u. is slightly too large (+1.4%), compared to the experimental value  $a_{\text{Cu,exp}} = 7.73$  a.u.). Starting from the atomic positions of a truncated fcc Cu or Ag crystal, respectively, all atoms in the film were relaxed using the atomic forces. These forces were calculated according to Yu et al. [YSK91].

Our calculations are based on the density functional theory in the generalized gradient approximation (GGA) as formulated by Perdew et al. [PW92]. Using a scalar-relativistic Hamiltonian, we employed a planewave cutoff of  $k_{\text{max}} = 4.0$  a.u.<sup>-1</sup> for the MLs on Cu(111) and  $k_{\text{max}} = 3.5$  a.u.<sup>-1</sup> for the MLs on Ag(111), respectively. Both cutoffs correspond to about 95 basis functions per atom. For the expansion of the charge density we used a planewave cutoff of  $G_{\text{max}} = 12.0$  a.u.<sup>-1</sup> for the MLs on Cu(111) and  $G_{\text{max}} = 10.5$  a.u.<sup>-1</sup> for the MLs on Ag(111), respectively. The muffin-tin radii were chosen 2.15 a.u. for both Cu substrate atoms and the 3d-metals of the MLs and in the case of the MLs on Ag 2.60 a.u. for the Ag substrate atoms and 2.40 a.u. for the 3d-metals. The angular momentum expansion of the charge density inside the muffin-tin spheres was truncated at  $l_{\text{max}} = 8$ . For the  $k$ -space integration 40 special  $k$ -points were used in the irreducible wedge of the two-dimensional Brillouin zones of the unit cells containing one surface atom, which corresponds to 361  $k$ -points in the full Brillouin zone. For the calculation with two atoms in the surface unit cell, i.e. for Cr/Cu(111), 45  $k$ -points in the irreducible wedge, corresponding to 180  $k$ -points in the full Brillouin zone, were used. A structure was considered relaxed, when all the forces on the atoms were smaller than 1 mRyd/a.u.

The relaxed atom positions are presented in table 6.11. All relaxations are given

ML	$\Delta d_{12}$ (%)	$\Delta d_{23}$ (%)	$\Delta d_{34}$ (%)	$\Delta d_{45}$ (%)
Cr/Cu <sup>a</sup>	+7.3	+3.1	+2.5	+2.4
Mn/Cu	+4.4	+1.6	+1.7	+1.1
Fe/Cu	+2.0	+1.0	+1.6	+1.0
V/Ag	-2.9	+2.8	+2.1	+2.1
Cr/Ag	-3.0	+1.0	+0.1	-0.3
Mn/Ag	-5.0	+0.9	-0.1	-0.1
Fe/Ag	-8.8	+0.4	+0.1	+0.2

**Table 6.11:** Calculated relaxations of  $3d$ -monolayer on Cu(111) and Ag(111). The  $\Delta d_{ij}$  are the relative change of the interlayer distance with respect to the theoretical GGA values of fcc Cu and Ag.

<sup>a</sup>The relaxation of the ML Cr/Cu(111) was calculated in the RW-AFM configuration, since no stable ferromagnetic solution was found for this system.

in terms of the relative change of the interlayer distance compared to a truncated fcc Cu and Ag crystal, respectively. The layers are numbered 1 (surface) to 5 (center of the film). Thus, for example the relative change of the interlayer distance for the MLs on Cu(111) between the surface and the subsurface layer is defined as  $\Delta d_{12} = (d_{12} - d_{\text{Cu}})/d_{\text{Cu}}$ , where  $d_{12}$  is the relaxed interlayer distance and  $d_{\text{Cu}}$  is the interlayer distance of the Cu ideal bulk crystal. Comparing the results with the Cu(111) and the Ag(111) substrate shows a clear difference. While on Cu all  $3d$ -monolayers relax outwards compared to the bulk interlayer distance ( $\Delta d_{12} > 0$ ), the opposite is true for the ML on Ag. This is a consequence of the larger lattice constant of Ag. There is an obvious trend for the different  $3d$ -metals on the same substrate. The distance between the ML and the first substrate layer decreases monotonously from V (Cr) to Fe. The reduction of the interlayer distance with increasing nuclear number of the ML is also visible below the surface. In particular for the distance between the first two substrate layers ( $\Delta d_{32}$ ) this tendency becomes very obvious. Generally, the size of the relaxations decreases from the surface to the bulk, though there are some oscillations, e.g. in the Fe/Cu system. In the Ag substrate this decline is much faster than in Cu, probably due to the larger lattice constant of Ag. Only in the case of Cr/Cu and V/Ag the relaxations reach far into the substrate. At the first glance the monotonic decrease of the interlayer distance between the monolayer and the substrate when we move across the period from V to Fe is a surprise. It is well known that the lattice constant of the bulk  $3d$  metal is smallest at the center of the transition metal series, i.e. around Cr and Mn, as most of the bonding states are filled and most of the anti-bonding states are empty. But magnetism has a very strong influence on the relaxations of these monolayers and changes the picture. From the comparison to a calculation of a non-magnetic Mn ML on Cu(111) [BKB00], which hardly relaxes compared to the atomic position of the truncated Cu crystal, we know that the outwards relaxation of Mn is driven by magnetism. Calculations for Mn/Cu(100)

show the same effect, but much more strongly, since the number of nearest neighbors is smaller [Blü96]. The influence of magnetism can also directly be perceived from our calculated relaxations on Ag(111). While the interlayer distance between the ML and the substrate reduces by 2% from Cr to Mn and by 3.8% from Mn to Fe, V and Cr have almost the same distance between the first and the second layer. This is a consequence of the fact, that the V atoms have much smaller magnetic moment than in particular Cr and Mn.

Tab. 6.12 contains the magnetic moments of the monolayer atoms in the relaxed positions. The largest magnetic moments are found for Mn as expected from Hund's

ML	V	Cr	Mn	Fe
Cu(111)	–	2.58 <sup>a</sup>	3.05	2.69
Ag(111)	1.98	3.75	3.94	3.09

**Table 6.12:** Local magnetic moments of the ferromagnetic monolayers on Cu(111) and Ag(111).

<sup>a</sup>Moment of the RW-AFM configuration

rule. The moments calculated including the substrate show the same trend and are in fairly good agreement with those of the unsupported monolayers (cf. Tab. 6.2 and 6.4). V and Cr react more strongly to the substrate than Mn and Fe (cf. the discussion in Sec. 6.1.2). However, comparing the results of the UMLs with those of the MLs on the substrate it has to be taken into account that the calculations on the substrate were performed applying the GGA, which is known to increase the magnetic moments compared to the LDA. In addition we used the slightly larger GGA lattice constant for the substrate, which also causes a larger magnetic moment. Thus, if the calculations with and without the substrate were performed using the same exchange correlation potential and the same substrate lattice constants, the difference between the magnetic moments would be somewhat larger.

### 6.5.2 Results for the monolayers on the Cu(111) and Ag(111) substrate

With the structural parameters determined in the previous section we repeated the investigation of the different collinear and non-collinear magnetic states including the substrate. Because of the enormous computational expenditure of the non-collinear calculations we used asymmetric five-layer films with four layers of substrate and one monolayer of the 3d-metal. In addition, we repeated the calculations only for the relevant magnetic states, i.e. FM, Néel, RW-AFM, 3Q, the spin-spiral state in the case of Mn and the FI (ferrimagnetic) state in the case of V. Most of these magnetic configurations, FM, Néel, RW-AFM and the spin-spirals, are described by a single  $q$ -vector. Therefore, these states can be explored by a spin-spiral calculation. This method has the advantage that only one atom in the surface unit cell is needed,

which reduced the computational effort. Only the 3Q state and the FI state have to be calculated in real space using surface unit cells containing four and three atoms, respectively. Due to the complexity of the magnetic states no symmetry operations could be applied to reduce the size of the irreducible wedge of the two-dimensional Brillouin zone. In fact, some of the states, e.g. the Néel state, do have a larger symmetry according to the spin space group (SSG) (cf. Chap. 4 Eqn. (4.5)). However, the current version of our FLAPW program can only deal with space group operations of the type  $\{\mathbf{I}|\alpha_R|\mathbf{t}\}$ , i.e. operations that leave the spin invariant. For the spin-spiral calculations we used the same  $k$ -point sets as for the UML calculations (cf. 6.3.1), which ranged between 256 and 1024  $k$ -points depending on the system. For the calculations of the 3Q and the FI state we used 256 in the full Brillouin zone. The calculations are based on the local density approximation (LDA) applying the parameterization according to Moruzzi, Janak and Williams [MJW78]. The planewave cutoff for the wave functions was set to  $k_{\max} = 3.7$  a.u. $^{-1}$  for the MLs on Cu(111) and  $k_{\max} = 3.3$  a.u. $^{-1}$  for the MLs on Ag(111). For the expansion of the charge density we chose a cutoff of  $G_{\max} = 13.2$  a.u. $^{-1}$  for the MLs on Cu(111) and  $G_{\max} = 11.1$  a.u. $^{-1}$  for the MLs on Ag(111). The muffin-tin radii were 2.18 a.u. for both, the Cu substrate atoms and the 3d-metals of the ML, and in the case of the MLs on Ag, the muffin-tin radii for the Ag substrate atoms were 2.60 a.u. and 2.40 a.u. for the 3d-metals. The angular momentum expansion of the charge density inside the muffin-tins spheres was truncated at  $l_{\max} = 8$ .

Tab. 6.13 lists the energies of all relevant magnetic states of the 3d-monolayers. For all MLs we found the same ground state as for the corresponding UMLs (cf. Tab.

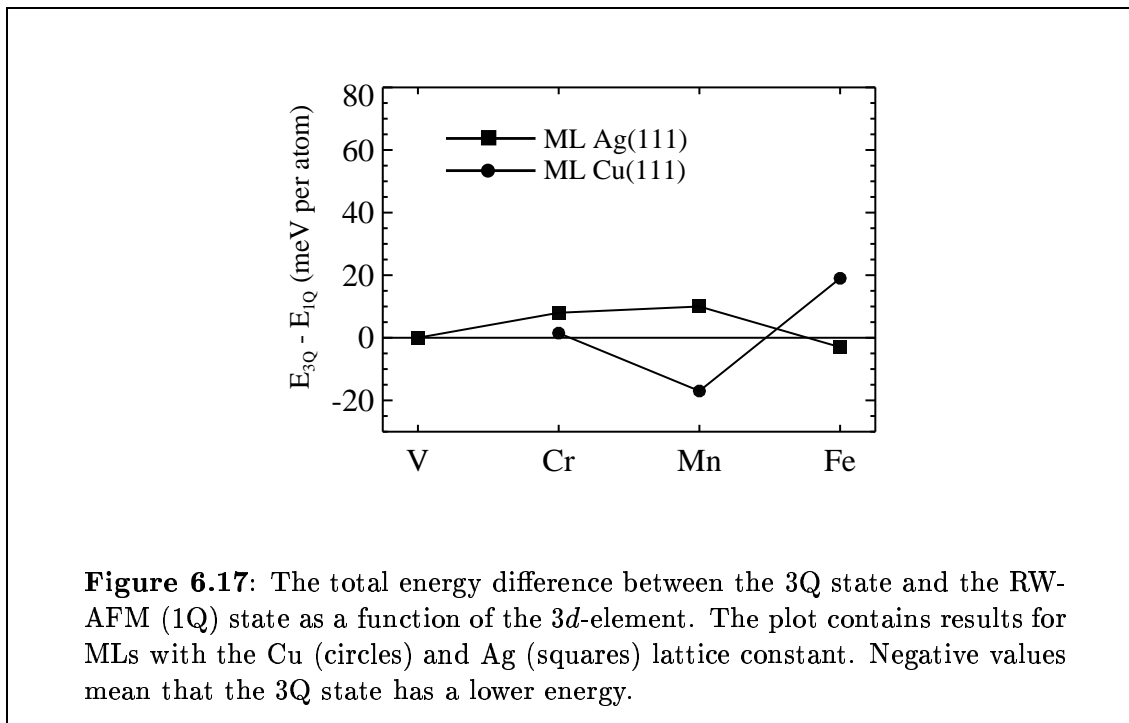
ML	FM	FI	SS	Néel	3Q	ground state
Cr/Cu	–	–	–	–53	$\approx 1.5$	Néel
Mn/Cu	261	–	21	77	–17	3Q
Fe/Cu	–105	–	–	35	19	FM
V/Ag	98	–26	–	–44	16	Néel
Cr/Ag	311	–	–	–22	8	Néel
Mn/Ag	94	–	15	20	10	RW–AFM
Fe/Ag	–127	–	–	10	–3	FM

**Table 6.13:** Energies of the different magnetic configurations relative to the energy of row-wise antiferromagnetic (1Q) configuration in meV/atom. The Cr/Cu system does not have a stable ferromagnetic solution.

6.7), except for the ML of V on Ag, where the Néel becomes clearly lower than the FI state when the substrate is included. Furthermore, the energetic ordering of the magnetic states of the MLs is the same as that of the UMLs with only two exceptions: the energy difference between the 3Q state and the RW-AFM state of Cr/Cu and Fe/Ag changes sign, when the substrate is taken into account. It should be noted that these two systems showed the smallest energy difference between 3Q and RW-



AFM of all UMLs and this difference becomes even smaller for the MLs.  $E_{3Q} - E_{1Q}$  is plotted as a function of the 3d-element in Fig. 6.17. Comparing this plot to the



result of the UMLs Fig. 6.13 shows, that, apart from Cr/Cu and Fe/Ag, the most prominent change is found for V/Ag. The rather large value of  $E_{3Q} - E_{1Q}$  is reduced significantly due to the inclusion of the substrate. The largest change compared to the UML results (cf. Tab. 6.7) is found for V/Ag. This result is not surprising, because this system also shows the most drastic change of the magnetic moment when the substrate is included. In the case of the UML the FM state and the 3Q state have practically the same energy, while the energy of the ferromagnetic ML is clearly the largest of all magnetic states. In most other cases the substrate does not only reduce the magnetic moment, but also reduces the energy differences between the magnetic configurations. However, the qualitative result remains unchanged. The magnetic moment of all system in the different magnetic configurations are listed in Tab. 6.14.

The UMLs of Mn show a local minimum in the total energy for spin-spirals with  $q$ -vectors on the symmetry line  $\bar{\Gamma}-\bar{K}$  for both substrates. Since, the energy of these minima are close to the energy of the RW-AFM state, we have performed calculations with  $q$ -vectors close to the minima including the substrate. The results are presented in Fig. 6.18. The ML results are marked by solid symbols and include the high symmetry points in addition to the  $q$ -vectors around the minima. The comparison with the results of the UMLs shows again how the substrate reduces the magnetic moments and also the energy difference between the FM state and the RW-AFM state. In both cases the energy of the minima remains above the energy of that at

ML	FM	RW-AFM	Néel	3Q
Cr/Cu	–	2.09 $\mu_B$	2.35 $\mu_B$	2.20 $\mu_B$
Mn/Cu	2.78 $\mu_B$	3.00 $\mu_B$	3.00 $\mu_B$	2.74 $\mu_B$
Fe/Cu	2.63 $\mu_B$	2.43 $\mu_B$	2.43 $\mu_B$	2.43 $\mu_B$
V/Ag	1.74 $\mu_B$	2.21 $\mu_B$	2.19 $\mu_B$	2.10 $\mu_B$
Cr/Ag	3.73 $\mu_B$	3.69 $\mu_B$	3.65 $\mu_B$	3.64 $\mu_B$
Mn/Ag	3.88 $\mu_B$	3.91 $\mu_B$	3.99 $\mu_B$	3.88 $\mu_B$
Fe/Ag	3.02 $\mu_B$	3.03 $\mu_B$	3.05 $\mu_B$	3.02 $\mu_B$

**Table 6.14:** Magnetic moment of different magnetic states inside the muffin-tin spheres for the MLs on Cu and Ag(111).

the  $\bar{M}$ -point. The position of the minima is slightly different for the MLs. In the case of Mn/Cu with substrate the spin-spiral minimum shifts towards the  $\bar{\Gamma}$ -point, from  $\mathbf{q} \approx 0.7\bar{K}$  to  $\mathbf{q} \approx 0.6\bar{K}$ , while it shifts in the opposite direction, from  $\mathbf{q} \approx 0.6\bar{K}$  to  $\mathbf{q} \approx 0.7\bar{K}$ , for Mn/Ag.

Although, we found no qualitative difference between the results of the UMLs and the MLs on an actual substrate, we performed test calculations with seven layer films, to make sure that the results are not affected by the film thickness. To save computer time we used  $k$ -point sets with 256  $k$ -points instead of 529  $k$ -points in the full Brillouin zone. This  $k$ -point set is not large enough to calculate highly accurate energies, but it suffices to investigate the effect of the film thickness. The interlayer distance of the two additional substrate layer has been set to the value of the corresponding bulk metals. We restricted the calculation to three magnetic states, the FM, the Néel and the RW-AFM state. We chose two systems, Mn/Cu and Mn/Ag, for this test. Tab. 6.15 contains the calculated energies and magnetic moments of the different configurations. The results of the seven layer calculations confirms those obtained

ML	$E_{\text{FM}}$	$E_{\text{Néel}}$	$\mu_{\text{FM}}$	$\mu_{\text{Néel}}$	$\mu_{\text{RW-AFM}}$
Mn/Cu 5l	259	69	2.78	2.98	2.98
Mn/Cu 7l	246	72	2.85	2.98	2.97
Mn/Ag 5l	103	22	3.89	3.98	3.91
Mn/Ag 7l	95	21	3.92	3.98	3.91

**Table 6.15:** Comparison between results obtained with five and with seven layer thick films. Shown are the energy differences with respect to the RW-AFM state in meV/atom and the local magnetic moments in  $\mu_B$ .

with five layers. The energy differences change quantitatively, but the changes are small. The changes of the magnetic moments are negligible. From this result we would not expect any qualitative change if thicker films were used.

We also carried out tests to investigate whether the choice of the exchange correlation potential has an effect on our results. Spišák and Hafner [SH00] performed cal-

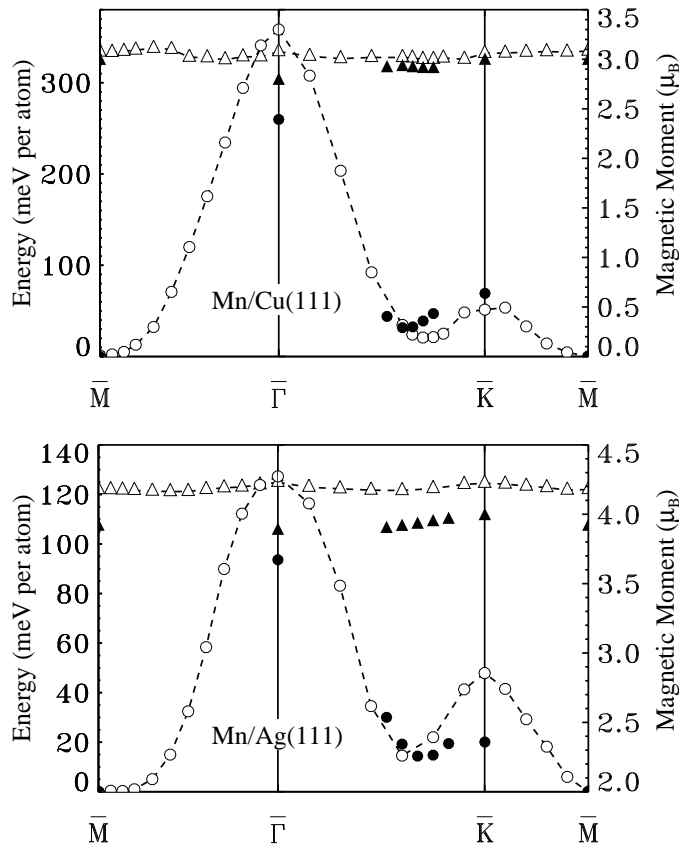


**Figure 6.18:** The total energy (solid circles) and the magnetic moments (solid triangles) of the relevant spin-spiral states of Mn MLs on Cu(111) (top panel) and Ag(111) (bottom panel). The results for the UMLs are included for comparison (open symbols).

culations on the Mn/Cu(111) system using a real-space tight-binding LMTO method and came to a different conclusion than we do. They found that the Néel state has a lower energy than the RW-AFM state. The 3Q state was not included in their study. They claimed that the difference between their results and our results is due to the choice of the local density approximation (LDA) in our investigation, rather than in the generalized gradient approximation (GGA) in their study. However, the results of our GGA calculation (Tab. 6.16) clearly shows that this is not the case. All parameters were chosen exactly as during the LDA calculation of the five layer Mn/Cu film. The only difference is the application of the GGA exchange correlation potential according to Perdew et al. [PW92]. It can be seen that the use of the GGA does not change the energetic order of the three magnetic configurations considered. In fact, the energy difference between the RW-AFM and the Néel state becomes even larger when the GGA is applied. The GGA increases both, the magnetic moments

ML	$E_{\text{FM}}$	$E_{\text{Néel}}$	$\mu_{\text{FM}}$	$\mu_{\text{Néel}}$	$\mu_{\text{RW-AFM}}$
Mn/Cu LDA	261	77	2.78	3.00	3.00
Mn/Cu GGA	296	89	2.88	3.10	3.10

**Table 6.16:** Comparison between results obtained with the local density approximation (LDA) and the generalized gradient approximation (GGA). Shown are the energy differences with respect to the RW-AFM state in meV/atom and the local magnetic moments in  $\mu_B$ .

and the energy differences, though the changes are not drastic. The conclusion, that the Néel state is not the ground state of the Mn/Cu system remains valid. Very recently Hobbs and Hafner submitted results that confirm our findings [HH00]. These results were obtained with a projector augmented planewave method different from the method of Spišák and Hafner [SH00].

In summary we can say that the calculations of the MLs on an actual substrate confirm the results obtained for the unsupported monolayers. The energy difference between the magnetic configurations do change quantitatively, but the physical picture developed during the investigation of the UMLs remains unaltered.

### 6.5.3 Tests of the convergence with respect to numerical cut-offs

In addition to the test calculations described in the previous section we tested the convergence with respect to the numerical cutoffs, i.e. the k-point sampling and the planewave cutoff for the basis functions.

During the force calculation the aim was to determine the positions of the atoms of the relaxed surface. Therefore, we applied the following test: At the end of the calculation of the relaxations, when all forces were smaller than 1 mRyd/a.u., we performed self-consistent calculations with larger cutoffs verifying the forces once more. We increased the planewave cutoff  $k_{\text{max}}$  from 4.0 a.u.<sup>-1</sup> to 4.4 a.u.<sup>-1</sup>, i.e. from 85 to 115 basis functions per atom, for the MLs on Cu(111) and from 3.5 a.u.<sup>-1</sup> to 3.9 a.u.<sup>-1</sup>, i.e. from 85 to 120 basis functions per atom, for the MLs on Ag(111). In separate calculations we increased the number of  $k$ -points from 40 to 70 for both substrates. We found that in all cases the forces stayed smaller than 1 mRyd/a.u.

Another parameter that can be critical is the choice of the vacuum boundary. If the vacuum boundary is too close to the outmost atom the total energy becomes inaccurate. This problem typically occurs when the distance between the vacuum boundary and the outmost muffin-tin sphere becomes smaller than 0.5 a.u. A characteristic symptom of this problem is that the atomic configuration that corresponds to the minimum of the total energy and the configuration for which the forces vanish do not coincide. During our force calculations this happened twice, for Cr/Cu and V/Ag. In both case increasing the distance between the outmost muffin-tin sphere

and the vacuum boundary removed the problem.

With our non-collinear calculations we investigated the energetics of various magnetic configuration. Therefore, we tested the convergence of selected energy differences between magnetic states with respect to the number of  $k$ -points and the planewave cutoff. The tests were carried out in the same way as described in Sec. 6.3.3 for the unsupported monolayers. We chose the energy difference  $E_{\text{FM}} - E_{\text{RW-AFM}}$  and in some cases  $E_{\text{Néel}} - E_{\text{RW-AFM}}$  for the test calculations. As in Sec. 6.3.3 we tested with spin-spiral calculations, since they have the smallest unit cell. During the tests we began with a small  $k$ -point set and then increased the number of  $k$ -points. Since we found no significant change of the convergence behavior of the MLs on the substrate compared to the UMLs we did not go beyond the maximum  $k$ -point set used for the UMLs. In order to test the planewave cutoff convergence we increased  $k_{\text{max}}$  from 3.7 to 4.1 a.u.<sup>-1</sup> (80 to 110 basis functions per atom) for Mn/Cu(111) and from 3.3 to 3.7 a.u.<sup>-1</sup> (85 to 120 basis functions per atom) for Mn/Ag(111). Due to the large cost of the non-collinear calculation we performed the planewave cutoff test only for the Mn monolayers. The change of the energy difference was 0.4 meV for Mn/Cu and 0.8 meV for Mn/Ag.

## 6.6 Calculated STM images of non-collinear magnetic states

All of the ground state spin-structures that have been presented in the last sections are spin-structures on the atomic-scale. This is a length scale below the resolution of current experimental techniques for the investigation of surface magnetism. However, the real-space observation with high spatial resolution is of great importance to determine the magnetic structure of complex magnetic systems and to verify our theoretical predictions. In general a method that combines magnetic sensitivity and atomic resolution would provide an experimental tool to gain an understanding of the magnetic interaction in these nano-magnets. Unfortunately, such a technique combining surface sensitivity and magnetic resolution on the atomic scale is at present unavailable. In this section we propose the spin-polarized scanning tunneling microscope used in the imaging mode to be the experimental tool of choice.

The scanning tunneling microscope (STM) is one of the key tools in the nano-sciences and in nano-technology. It has revolutionized our approach to surface science, as atomic resolution of semiconductor and metal surfaces is now routinely available. Recently, the use of a spin-polarized STM (SP-STM), which is realized for example using magnetic coated tips, has opened the field of nano-magnetism. The topological antiferromagnetism of Cr(001) [WGG<sup>+</sup>90, KBRW00], ferromagnetic domains of thin films [BGW98] domains at the surfaces of ferromagnetic materials [WK99], and dipolar antiferromagnetism of Fe nano-wires on W(110) [PKBW00] have been investigated with SP-STM. On the atomic scale these magnetic structures are ferromagnetic and may couple antiferromagnetically on a mesoscopic or microscopic scale of 10 nm to

1000 nm. The magnetic order, i.e. the domains, in these structures has been visualized with the SP-STM using the spectroscopy mode in most cases, i.e. measuring the spin-dependent differential conductivity. By comparing a map of the differential conductivity with the simultaneously measured topography of the sample domain boundaries and other features can be correlated to the morphology. The magnetic resolution of this method has been reported down to 1 nm. Only one of the SP-STM studies mentioned above [WGG<sup>+</sup>90] applied the STM in the topography mode.

In the following we introduce an approach to image complicated magnetic structures of surfaces directly on the atomic scale by SP-STM [HKW<sup>+</sup>00]. By generalizing the Tersoff-Hamann model to the case of SP-STM and applying the expansion of the STM image into two-dimensional planewaves [HBP<sup>+</sup>98] we show that in general the SP-STM image of any magnetic superstructure within an arrangement of chemically equivalent atoms leads to an SP-STM image displaying a pattern corresponding to the magnetic configuration. This is in contradiction to the intuitive expectation that spin-polarization is a small effect, and consequently the non-spin-polarized STM image reflecting the chemical structure is only slightly modulated in the SP-STM experiment. This approach extends the use of STM from the exploration of the topological, chemical and ferromagnetic structure of surfaces to the inherently much more difficult investigation of antiferromagnetic surfaces and surfaces with non-collinear spin structures with ultimate, atomic resolution.

The approach has been already verified experimentally. Very recently the SP-STM has been used successfully to prove the existence of collinear two-dimensional antiferromagnetism in monolayer Mn films on W(110) [HBK<sup>+</sup>00]. Here, we explain how the SP-STM can be applied to resolve arbitrary laterally periodic spin-structures, e.g. complex non-collinear spin structures. Taking the Néel state of Cr/Ag(111) and the 3Q state of Mn/Cu as an example, we discuss the expectations for the STM picture and thus show how the magnetic ground state of a magnetic surface can be verified experimentally.

### 6.6.1 Principle of the SP-STM on the atomic scale

In the derivation of the tunneling current by Tersoff and Hamann [TH83] the spin of the electron has been taken into account only by the double occupation of single-particle states. However, in order to describe the tunneling in the set-up of the spin-polarized STM (SP-STM) we need to take the spin-polarized electronic structure of both tip and sample explicitly into consideration. The SP-STM can be realized by coating a common STM tip with a magnetic material, for example Fe or Gd have been successfully used [PKBW00, BGW99], and using this spin-sensitive probe to scan the surface of the magnetic sample. In the following we assume the coated tip to be ferromagnetic with a spin-polarized band structure of spin-up ( $\uparrow$ ) and spin-down ( $\downarrow$ ) states with respect to a quantization axis given by the magnetization axis  $\mathbf{M}_T$  of the tip. This means that we assume a collinear tip magnetization, which is certainly an excellent approximation for tips with ferromagnetic coating. The orientation of the

magnetization axis  $\mathbf{M}_T$  of the tip with respect to the geometric axis of the tip depends on the tip material and the actual geometric structure of the tip [PKBW00, BGW99].

To understand the working principle of the SP-STM we go one step back to the Transfer Hamiltonian Method of Bardeen [Bar61], which is the basis of the Tersoff-Hamann model. The Transfer Hamiltonian Method is based on several assumptions. First of all, the electron tunneling is treated as a one-particle process, i.e. it is neglected that electrons can interact while tunneling. In particular loss of spin information by scattering processes connected with a spin-flip in the tunneling barrier is not considered. For the vacuum tunneling of STM this can be excluded to a high degree since the only scattering processes are given by many-particle processes which seem to play a minor role in most cases. Further, we assume elastic tunneling, i.e. no energy loss of the electrons by interaction with quasi-particles of the electrodes, e.g. plasmons or phonons, is considered. And finally, a direct interaction of tip and sample resulting in the formation of coupled electronic states is not taken into account. In this approximation the tunneling current between a magnetic tip at position  $\mathbf{R}_T$  and a magnetic sample can be calculated using Fermi's Golden Rule:

$$I(\mathbf{R}_T, V) = \frac{2\pi e}{\hbar} \sum_{\mu, \nu\sigma} \left[ f(E_\mu^S - E_F^S) - f(E_{\nu\sigma}^T - E_F^T) \right] \times \delta(E_{\nu\sigma}^T - E_\mu^S - eV) |M_{\nu\sigma, \mu}(\mathbf{R}_T)|^2, \quad (6.43)$$

where  $V$  is the applied bias voltage,  $f$  is the Fermi distribution function,  $E_F^S$  and  $E_F^T$  are the Fermi energies of the sample (S) and the tip (T), and  $E_\mu^S$  and  $E_{\nu\sigma}^T$  are the energies of a sample state  $\mu$  and tip state  $\nu$  with spin  $\sigma$ , respectively. The  $\delta$ -function guarantees the energy conservation. Eqn. (6.43) contains only one spin summation over the spins of the tip. As a consequence of the assumption of a collinear tip magnetization the tip states can be written as pure spin-up and pure spin-down state. However, we do not make this assumption for the sample states, to allow the treatment of samples with a non-collinear magnetic state. Thus, the sample states are written as general Pauli-spinors that can contain contributions in both spin components:

$$\boldsymbol{\psi}_\mu^S(\mathbf{r}) = \begin{pmatrix} \psi_{\mu\uparrow}^S(\mathbf{r}) \\ \psi_{\mu\downarrow}^S(\mathbf{r}) \end{pmatrix}. \quad (6.44)$$

In the following we drop the  $\mathbf{r}$  dependence of the wave functions. The key problem is to calculate the matrix elements given by:

$$M_{\nu\sigma, \mu}(\mathbf{R}_T) = \langle \boldsymbol{\psi}_{\nu\sigma}^T | U_T | \boldsymbol{\psi}_\mu^S \rangle, \quad (6.45)$$

where  $U_T$  is the tip potential. The integration is over the volume of the tip, which is separated by an hypothetical boundary surface from the volume of the sample. Eqn. (6.43) contains only one spin summation over the spins of the tip. As a consequence of the assumption of a collinear tip magnetization the tip states can be written as pure spin-up and pure spin-down state. However, we do not make this assumption for the sample states, to allow the treatment of samples with a non-collinear magnetic

state. Thus, the sample states are written as general Pauli-spinors that can contain contributions in both spin components.

In order to simplify the calculation of the tunneling current further we apply the Tersoff-Hamann model. Tersoff and Hamann introduced several approximations to allow the calculation of the matrix elements  $M_{\nu\sigma,\mu}(\mathbf{R}_T)$ . All of the approximations concern the electronic structure of the tip. First, they assume that the tip can be replaced by a single atom with spherical wave functions. Since both, the sample and the tip wave functions, decay exponentially into the vacuum, the main contributions to the matrix element come from a region between sample and tip where both wave functions still have finite values<sup>1</sup>. Therefore, the wave function of the tip can be replaced by the solution of the vacuum Schrödinger equation, which is given by the Bessel function  $k_0$ :

$$\psi_{\nu\sigma}^T(\mathbf{r}) = C_\sigma k_0(\kappa_\sigma \rho) \chi_\sigma = C_\sigma \frac{\exp(-\kappa_\sigma \rho)}{\kappa_\sigma \rho} \chi_\sigma, \quad (6.46)$$

where  $\rho = |\mathbf{r} - \mathbf{R}_T|$  and  $\kappa_\sigma$  is the decay constant of the tip states that depends on the energy of the tip state and the tip potential. Now the matrix elements can be calculated:

$$M_{\nu\sigma,\mu}(\mathbf{R}_T) = \langle \psi_{\nu\sigma}^T | U_T | \psi_\mu^S \rangle = -\frac{2\pi C_\sigma \hbar^2}{\kappa_\sigma m} (\chi_\sigma)^* \psi_\mu^S(\mathbf{R}_T). \quad (6.47)$$

We assume that the spin-up and spin-down  $s$ -wave states can be characterized by the same decay constant  $\kappa = \kappa_\uparrow = \kappa_\downarrow$  and the same coefficient  $C = C_\uparrow = C_\downarrow$ . At this point, we can already see that the projection of the spin-polarized sample wave function onto the magnetization direction of the tip,  $(\chi_\sigma)^* \psi_\mu^S$ , enters into the equation. In the next step we assume that the density of states (DOS) of the spin-up  $n_\uparrow^T(\epsilon)$  and spin-down  $n_\downarrow^T(\epsilon)$  tip states is constant in energy. However, For a magnetic tip the DOS of spin-up and spin-down states are non-equal. Inserting the matrix elements into the equation for the tunneling current, Eqn. (6.43), leads to:

$$I(\mathbf{R}_T, V) = \frac{2\pi e}{\hbar} \int d\epsilon g_{V,T}(\epsilon) \sum_\mu \delta(\epsilon_\mu - \epsilon) \times [n_\uparrow^T |M_{\mu,\nu\uparrow}(\mathbf{R}_T)|^2 + n_\downarrow^T |M_{\mu,\nu\downarrow}(\mathbf{R}_T)|^2], \quad (6.48)$$

where the summation over the tip and sample states has been replaced by an energy integration, and  $g_{V,T}(\epsilon) = f(\epsilon - E_F^S) - f(\epsilon + eV - E_F^T)$ . Inserting the matrix elements in the Tersoff-Hamann approximation into Eqn. (6.48) and after some algebra we arrive at the final result of the current in the case of SP-STM:

$$I(\mathbf{R}_T, V) = \frac{4\pi^3 C^2 \hbar^3 e}{\kappa^2 m^2} \times [n_T N_S(\mathbf{R}_T, V) + \mathbf{m}_T \mathbf{M}_S(\mathbf{R}_T, V)], \quad (6.49)$$

---

<sup>1</sup>The integration over the volume of the tip can be replaced by an integration over the boundary surface between the sample and the tip using Green's theorem. This shows that only the value of the tip wave function on the boundary surfaces is important for the matrix element. A detailed discussion of the derivation can be found in the original paper or e.g. in [Hei00]



where  $n_T$  is the density of states (DOS) of the tip, given by the sum of  $n_{\uparrow}^T$  and  $n_{\downarrow}^T$ ,  $n_T = n_{\uparrow}^T + n_{\downarrow}^T$ .  $\mathbf{m}_T$  is the spin-polarized density of states (SDOS), which is given by the difference of  $n_{\uparrow}^T$  and  $n_{\downarrow}^T$ ,  $|\mathbf{m}_T| = n_{\uparrow}^T - n_{\downarrow}^T$ , and has the direction of the magnetization of the tip. In addition, we have introduced the integrated local density of states (ILDOS) of the sample  $N_S(\mathbf{R}_T, V)$  and the integrated local spin density of states (ISLDOS) of the sample  $\mathbf{M}_S(\mathbf{R}_T, V)$  given by an energy integral of the SLDOS,  $\mathbf{m}_S(\mathbf{R}_T, \epsilon)$ :

$$\begin{aligned} \mathbf{M}_S(\mathbf{R}_T, V) &= \int d\epsilon g_{V,T}(\epsilon) \sum_{\mu} \delta(\epsilon_{\mu} - \epsilon) \boldsymbol{\psi}_{\mu}^{S\dagger}(\mathbf{R}_T) \boldsymbol{\sigma} \boldsymbol{\psi}_{\mu}^S(\mathbf{R}_T) \\ &= \int d\epsilon g_{V,T}(\epsilon) \mathbf{m}_S(\mathbf{R}_T, \epsilon). \end{aligned} \quad (6.50)$$

The ILDOS of the sample  $N_S(\mathbf{R}_T, V)$  is also defined by Eqn. (6.50) if we replace  $\boldsymbol{\sigma}$  by the unity matrix.

Eqn. (6.49) states that the tunneling current can be separated into a non-spin-polarized part depending on the local density of states of the sample at the position of the tip and a contribution due to the spin-polarization of tip and sample given by the projection of the vector of the local spin-density of states to the magnetization direction of the tip. In the case of a non-spin-polarized STM experiment, i.e. using a non-magnetic tip, the second part vanishes and the current reduces to the result of the Tersoff-Hamann model. The important question to be answered now is, whether or in which cases the spin-polarized contribution can become dominant which is desired in order to observe large magnetic contrasts in the measurements.

The ILDOS of a periodic surface can be written in terms of a two-dimensional Fourier expansion:

$$N_S(\mathbf{r}_{\parallel}, z, V) = \sum_{\mathbf{G}_{\parallel}} N_{\mathbf{G}_{\parallel}}(z, V) \exp(i\mathbf{G}_{\parallel}\mathbf{r}_{\parallel}). \quad (6.51)$$

$\mathbf{G}_{\parallel}$  denotes the reciprocal lattice vectors in two dimensions, and  $N_{\mathbf{G}_{\parallel}}(z, V)$  are the tip-sample distance ( $z$ ) and bias-voltage ( $V$ ) dependent expansion coefficients. A similar expansion is possible for the three components of the SLDOS. As we have described in Sec. 3.5 the plane waves of symmetry related reciprocal lattice vectors  $\mathbf{G}_{\parallel}^n$  can be summarized to a two-dimensional star function  $\phi_s^{2D}(\mathbf{r}_{\parallel})$ . Inserting into the tunneling current, Eqn. (6.49), we obtain:

$$I(\mathbf{r}_{\parallel}, z, V) \propto n_T \sum_s N(z, V) \phi_s^{2D}(\mathbf{r}_{\parallel}) + \mathbf{m}_T \sum_s \mathbf{M}_S(z, V) \phi_s^{2D}(\mathbf{r}_{\parallel}), \quad (6.52)$$

with a representative vector  $\mathbf{G}_{\parallel}^s$  for each star function  $\phi_s^{2D}$ . Due to the tunneling of electrons through the vacuum barrier these coefficients decrease exponentially with increasing length  $G_{\parallel}^s$  [HBP<sup>+</sup>98], and to a good approximation the topographic STM image or, to be more precise, the constant current STM image, is determined by the lowest star function  $\phi_1^{2D}$ , which is laterally non-constant, corresponding to the

smallest non-vanishing  $\mathbf{G}_{\parallel}^s$ -vector:

$$\Delta I(\mathbf{r}_{\parallel}, z, V) \approx I_1(V) \phi_1^{2D}(\mathbf{r}_{\parallel}) \times \exp \left[ -2z \sqrt{2m/\hbar^2 |E_F + eV| + (G_{\parallel}^{(1)}/2)^2} \right]. \quad (6.53)$$

Since in this context we are only interested in the dependence of the exponential decrease on the representative reciprocal lattice vector  $G_{\parallel}^s$  the  $k_{\parallel}$ -point dependent exponential term has been replaced by the dominating high symmetry point of the two-dimensional Brillouin zone, i.e.  $\mathbf{k}_{\parallel} = -\mathbf{G}_{\parallel}^{(1)}/2$ .

Any magnetic superstructure lowers the translational symmetry, and the additional tunneling current,  $\Delta I \propto \mathbf{m}_T \cdot \mathbf{m}_S$ , due to spin-polarized electrons, is sensitive to the unit cell of the superstructure. Therefore, star coefficients of stars formed by smaller reciprocal lattice vectors become relevant for the STM image. Since these new star functions possess exponentially larger coefficients they dominate the STM-image, even in the case of small effective spin-polarization  $\mathbf{m}_T \mathbf{M}_S$ , for example if the angle between the sample magnetization and the tip magnetization is close to  $90^\circ$ . Thus the corrugation amplitude  $\Delta z$  (the maximum difference in tip height while it scans the surface) is directly proportional to the effective spin-polarization.

These arguments are quite general and in principle applicable to any magnetic superstructure. The electronic structure, contained in  $I_{s>1}(V)$  of Eqn. (6.53), of a specific surface can still compete with this effect, and first-principles calculations need to be performed in order to interpret the experiments unambiguously.

## 6.6.2 Calculated SP-STM images of Cr/Ag(111) and Mn/Cu(111)

To demonstrate the potential of the SP-STM to unravel the non-collinear magnetic structures predicted in the preceding sections we apply our theory to two monolayers with two different non-collinear magnetic ground states: the planar Néel state and the three-dimensional 3Q-state. The Néel state is predicted as the ground state of a Cr monolayer on the Ag(111) surface and for the Mn/Cu(111) system we found the lowest energy for the 3Q state (cf. Tab. 6.13 Sec. 6.5.2). For these two systems we have calculated the SP-STM image for the magnetic ground state and the most important competing magnetic state. Comparing the result of an actual experiment with the theoretical STM images will allow to determine the magnetic state of such systems experimentally. For the STM calculations we used monolayers on an actual substrate as in Sec. 6.5, after all atom positions have been relaxed. All computational parameters have been chosen as discussed in Sec. 6.5.

We begin with the STM images of the RW-AFM state and the Néel state of Cr/Ag(111). Fig. 6.19 shows the calculated STM images for the RW-AFM structure. The left panel shows an image as it would be produced by conventional STM without magnetic contrast. The light areas correspond to a large (I)LDOS, i.e. protrusions of the topographic map obtained from an experiment in the constant current mode. All atoms are imaged equivalently as protrusions. The superimposed schematics of the

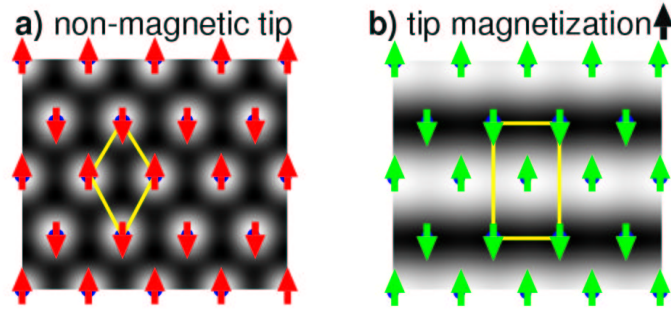
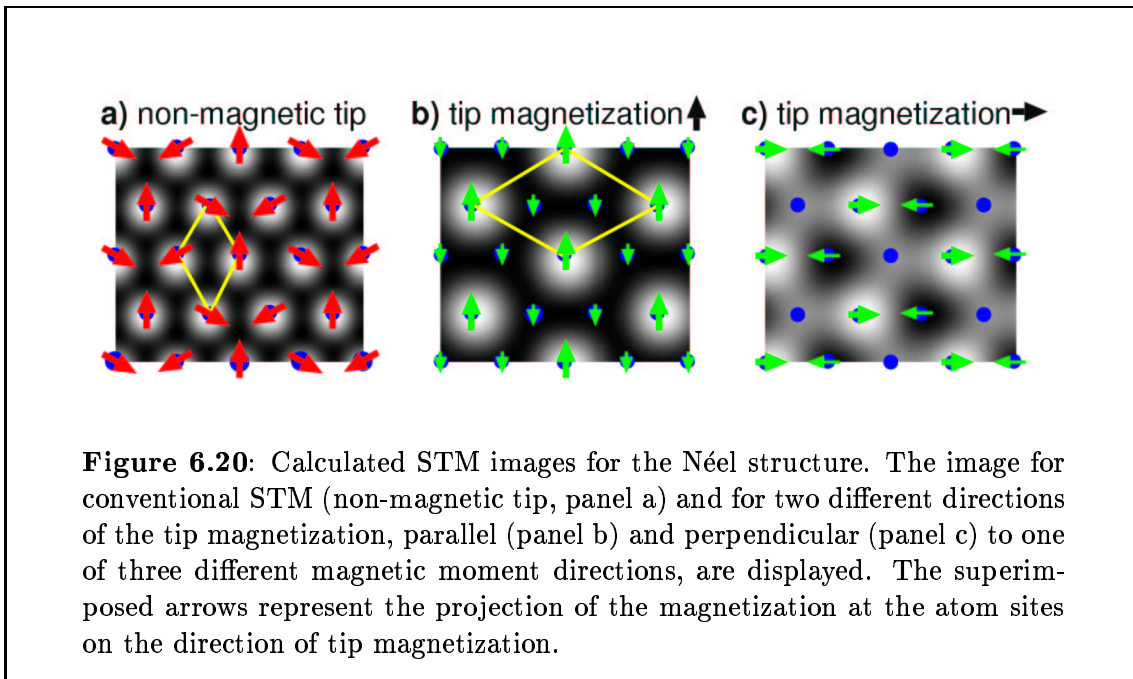


**Figure 6.19:** Calculated STM images for the RW-AFM structure. Both the image for conventional STM (non-magnetic tip, panel a) and for SP-STM (magnetic tip, panel b) are shown. The atomic positions and the magnetic moments are superimposed on the STM image.

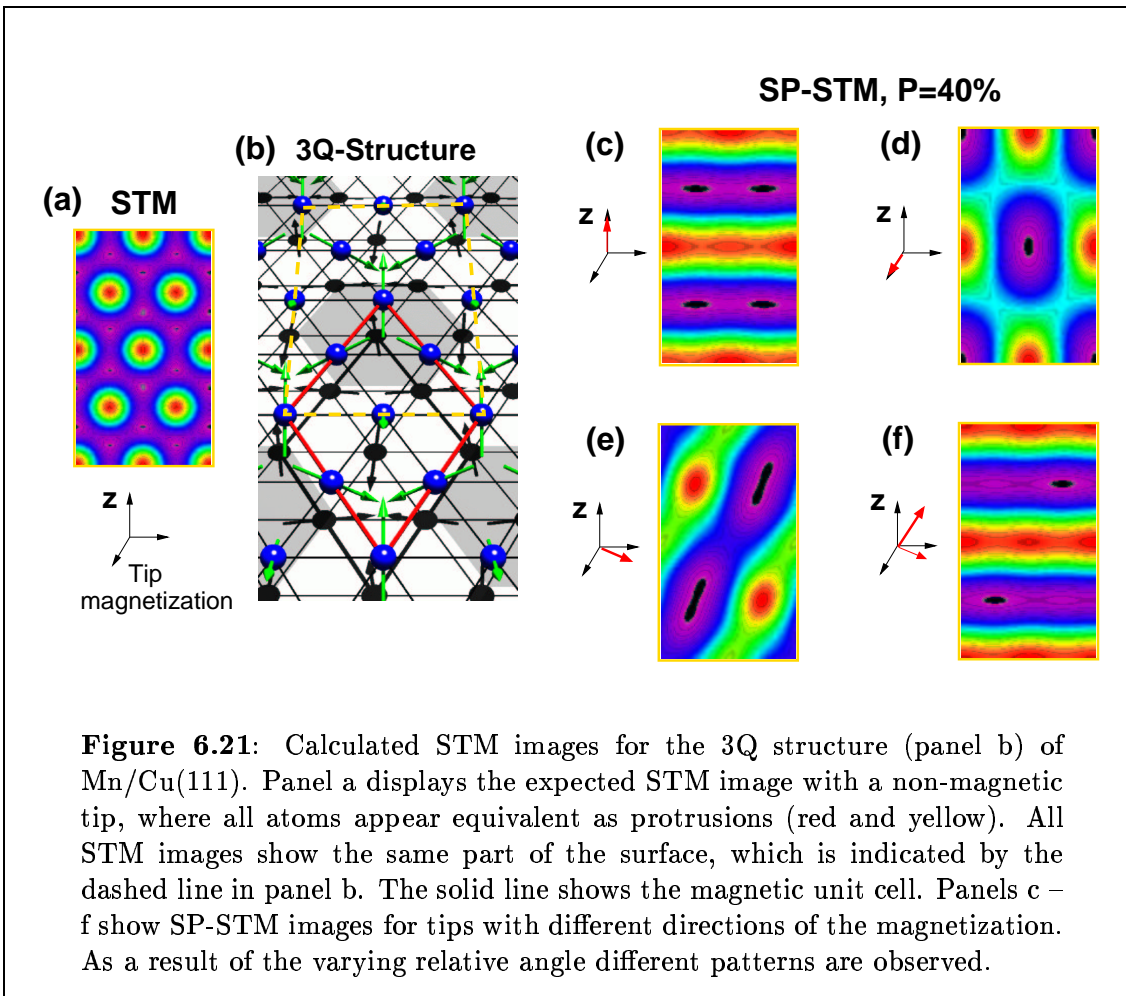
unit-cell shows the positions of the atoms as well as the orientation of the magnetic moments at each atom site. The right panel of fig. 6.19 displays the STM image calculated for an magnetic tip with a magnetization direction parallel to the magnetization direction of the sample. The equivalence of the atoms with opposite spin direction is lifted and the two different types of atoms can clearly be distinguished. The atoms that have a magnetic moment parallel to the moment of the tip are imaged as protrusions while the atoms with opposite magnetic moment are shown as depressions. This setup obviously provides maximal magnetic contrast as the angle between the direction of the magnetization of the tip and the magnetization of the sample is zero. A different angle would simply lead to a reduction of the magnetic contrast without changing the stripe pattern. If the magnetization of the tip was exactly perpendicular to the magnetization of the monolayer, the magnetic contrast would disappear, and the magnetic tunneling current would be determined only by the non-spin-polarized contribution. Thus, one would obtain the same STM image as with a non-magnetic tip (fig. 6.19 left panel). However, a small parallel component of the tip magnetization is enough to find the stripe pattern, as we have discussed in the previous section.

The second magnetic state we consider is the Néel state, which is a non-collinear configuration. The magnetic moments of all atoms lie within one plane. Hence, a tip with a magnetic moment in this plane would result in the strongest magnetic contrast and the magnetic contrast vanishes when the tip magnetization is perpendicular to the plane. Different orientations of the tip magnetization in the plane of the magnetic moments of the monolayer result in qualitatively different images, all of which show a magnetic contrast. Therefore, we have calculated the STM image using two different in-plane tip magnetizations. Analogously to Fig. 6.19 panel a of Fig. 6.20 shows the STM image as expected for a non-spin-polarized tip showing all atoms equivalently as



protrusions. Panels b and c of Fig. 6.20 correspond to STM images with magnetic tips for two different in-plane angles of magnetization. The arrows in the superimposed structure represent the projection of the magnetization at the atom sites on the direction of the magnetization of the tip. Panel b shows the image that is obtained if the tip magnetization is parallel to the magnetic moment of one of the three atoms in the magnetic unit cell. Consequently, this atom appears as the highest protrusions (large bright spots) in the SP-STM image. The projection of the magnetic moment of the other two atoms onto the direction of the tip magnetization is equal, i.e.  $\mathbf{m}_T \mathbf{M}_S(\mathbf{R}_T, V)$  (cf. Eqn. (6.49)) has the same value for both atoms. Hence, they appear with the same “height” in the STM image. The bright spots of the atoms with the parallel magnetic moment mark the corner points of the  $(\sqrt{3} \times \sqrt{3})$  superstructure, which can therefore be clearly identified from the STM image. This  $(\sqrt{3} \times \sqrt{3})$  superstructure can also be found in the right STM image displayed in Fig. 6.19. However, in this geometry the projection of the magnetic moments of the atoms on the direction of the magnetization of the tip reveals three different types of atoms and hence the STM image differs from the one discussed above.

As a final example we present SP-STM images of the 3Q state of a Mn monolayer on Cu(111). Fig. 6.21 a shows the STM image for a non-magnetic tip, where all atoms appear equivalently as protrusions (red and yellow). The 3Q state is a three-dimensional spin structure. Therefore, a magnetic contrast is obtained independent of the direction of the tip magnetization. The 3Q state is shown in Fig. 6.21 b. Since, we performed the calculation in the scalar-relativistic approximation, i.e. spin-orbit coupling has been neglected, the relationship between the lattice and the magnetic moments is undetermined. However, this is not crucial, because only the relative angle



between the magnetic moments and the direction of the tip magnetization, which is also unknown, is important for the STM image. In fact, the magnetic configuration shown here is rotated with respect to that presented in Fig. 6.7 on page 112. Here two of the four moments in the magnetic unit cell are in the  $x$ - $z$ -plane and the other two moments are in the  $y$ - $z$ -plane. All moments span the same angle with the  $x$ - $y$ -plane, but the projection of the moments in the  $x$ - $z$ -plane onto the  $z$ -axis has the opposite sign ( $-$ ) than that of the moments in the  $y$ - $z$ -plane. Consequently, an STM tip with a magnetization in  $z$ -direction (Fig. 6.21 c) would image the atoms with the moments in the  $x$ - $z$ -plane as protrusions (red and yellow) and the atoms with the moments in the  $y$ - $z$ -plane as depressions (violet and blue), resulting in a stripe pattern. When the tip magnetization is in  $y$ -direction (Fig. 6.21 d) the two atoms with moments in the  $x$ - $z$ -plane appear with the same “height” in the STM image. One of the atoms in the  $y$ - $z$ -plane has positive projection on the  $y$ -axis and is therefore imaged as protrusions, appearing as bright red spots in the image, that mark the corner points of the magnetic unit cell. The other atom in the  $y$ - $z$ -plane comes out as a depression. With a more general direction of the tip magnetization (Fig. 6.21 e and f) all atoms

in the unit cell appear at a different “height” in the SP-STM image, resulting in further different patterns. For the RW-AFM state and the Néel state of Mn/Cu(111) we expect a qualitatively equivalent result as for Cr/Ag(111) (Fig. 6.19 and 6.20). Comparing these SP-STM images shows that it is generally possible to distinguish between the different magnetic state. This is, however, not true for all directions of the tip magnetization. For example the STM images of Fig. 6.21 c and f can easily be mistaken with the image of the RW-AFM state in Fig. 6.19 b.

In conclusion, we can say that the SP-STM is a powerful tool for the investigation of magnetic surfaces. Depending on the direction of the tip magnetization we expect SP-STM images with different patterns that reflect the magnetic super-structure. In general, the magnetic unit cell can be identified from these patterns, which will allow to distinguish between the different magnetic states. Hence, with the SP-STM it becomes possible to determine the ground state of surfaces with complex magnetic structures on the atomic scale, which allows to verify the predictions of our total energy calculations experimentally.



# Chapter 7

## Magnetism and electronic structure of hcp Gd and the Gd(0001) surface

The rare earth metals are of great practical interest because of their role in hard magnetic intermetallics [FHLB93] and high density storage media [Whi85]. They are distinguished by their unique magnetic, electric and optical properties. The open shell of highly localized  $4f$  electrons is responsible for their large magnetic moments. However, the overlap of the  $4f$  shells on neighboring lattice sites is negligible. Therefore, the  $6s$ ,  $6p$  and  $5d$  states play an essential role in the magnetism, because they mediate the magnetic interaction by a Ruderman-Kittel-Kasuya-Yosida (RKKY)-type exchange, although their contribution to the magnetic moment is small. This complicated coupling mechanism leads to exotic magnetically ordered structures like helical spin structures [JM91, NM00]. The rare earth metals are strongly correlated materials. Due to their localized  $f$  electrons that lie in the same energy range as the itinerant  $s$ ,  $p$  and  $d$  electrons they represent a challenge for first-principle theory.

In particular Gd, one of the four ferromagnetic elementary metals (Fe, Co, Ni and Gd) known to occur in nature, has been studied intensively by experiment and theory. It has become a model system for the application of new relativistic theoretical methods [KH77, SK85, KS89], because of the unique combination of ferromagnetism and relativistic effects. Experimentally many of the magnetic properties of Gd metal are well understood. The half filled  $4f$  shell ( $S = 7/2$ ,  $L = 0$ ) leads to the formation of a well-localized spin-only magnetic moment. These moments couple via a RKKY-type exchange to form a ferromagnetic Heisenberg system with a bulk Curie temperature of  $T_C^B = 293$  K. The  $f$  electron moment polarizes the valence electrons resulting in a magnetic moment of  $7.63 \mu_B$ . However, the appropriate treatment of the localized  $4f$  electrons in first-principle calculations is still a matter of debate. Several approaches have been suggested in addition to the treatment of the  $4f$  bands as valence state, including the treatment as core states, the application of Hartree Fock exchange [BK94c, BK94b, BK94a] and the LDA+U method [SLP99, SPF00].



The  $4f$ -core model has already been introduced by a very early study [DF64]. Within the  $4f$ -core model the  $4f$  electrons are treated as core states, i.e. hybridization of the  $4f$  states with other (valence) states and also with any states from other lattice sites is neglected. Much later Sticht and Kübler [SK85] performed self-consistent calculations in the local density approximation (LDA) comparing the  $4f$ -core model and the  $4f$ -band model, where the  $4f$  electrons are treated as valence states. They obtained an much larger value for the magnetic moment ( $8.43 \mu_B$ ) from their  $4f$ -core model calculation and concluded that this model was not an acceptable approximation. However, the large magnetic moment has not been reproduced by latter  $4f$ -core model calculations, e.g. [AWJE93]. From their  $4f$ -band model calculation Sticht and Kübler found a magnetic moment of  $7.52 \mu_B$  in better agreement with experiment. By a comparison of the density of states (DOS) at the Fermi energy to specific heat experiments they found that the calculated DOS was too large. They noted that the subtraction of the  $4f$  contribution to the DOS results in a much better agreement. They also remarked that the binding energy of the majority  $4f$  states was too small ( $4.5$  eV) compared to photoemission data. Singh [Sin91] carried out a detailed study using the  $4f$ -band model, also finding that the DOS at the Fermi energy was too large. In accord with Sticht and Kübler he assigns a significant part of the DOS to minority  $4f$  states. However, he concludes that the band model is more appropriate for Gd, because he found Fermi surface sections in agreement with de Haas van Alphen experiments [SSHK76, MY77] that depend on the hybridization of the  $4f$  bands with other valence bands. This conclusion was contradicted by Ahuja et al. [AAJB94], who stated that they believe that one does not need to explicitly include the  $f$ - $d$  hybridization in the calculation in order to describe the small orbits (of the Fermi surface).

The first total-energy FLAPW calculation of the magnetic ordering at the Gd(0001) surface [WLFF91] using the  $4f$ -core model reported an antiferromagnetic coupling of the surface layer with respect to the bulk, in agreement with an early interpretation of experimental data [WAG<sup>+</sup>85]. This result stimulated a number of theoretical studies by several authors, investigating the magnetic coupling of Gd, both at the (0001) surface and in the bulk. Subsequently Bylander and Kleinman published a series of studies [BK94c, BK94b, BK94a], concentrating on the adequacy of LDA for the Gd  $4f$  states. By comparing Hartree-Fock with LDA atomic calculations [BK94c] they concluded that the minority  $4f$  resonance in the metal right above  $E_F$ , which is responsible for the enhanced  $N(E_F)$ , is an artifact of the LDA. In a second paper the authors suggested a new approach, treating the majority  $4f$  states as localized and fully occupied and the minority states in the band Hamiltonian. The effective potential in the latter calculations was constructed from Hartree-Fock theory for the core density and from LDA for the valence charge density. A single parameter was used to fit the calculated bulk magnetic moment to the experimental value. This constraint on the calculation has the effect of pushing the minority  $4f$  states to higher energies. In fact, the authors found the minority  $4f$  states at a much higher energy ( $8.4$  eV above  $E_F$ ) than an inverse photoemission (IPE) experiment [LBC77] ( $4.3$  eV).

With this method they found a much smaller value of  $N(E_F)$  and also an equilibrium lattice constant in good agreement with experiment. Motivated by a paper of Heine-  
mann and Temmerman [HT94], who found ferromagnetic coupling for hcp Gd with  
LDA and antiferromagnetic coupling with the generalized gradient approximation  
(GGA), using the linear muffin-tin orbital (LMTO) method in the atomic sphere ap-  
proximation (ASA), Bylander and Kleinman also performed total energy calculations  
for the AFM bulk phase. However, they found the correct FM ground state. They  
extended their study to the Gd(0001) surface [BK94a], using the same method as in  
the previous publication. In contrast to a former study [WLFF91], which predicted  
an outward relaxation by 6.3% for the ferromagnetic surface, they found a contrac-  
tion by 3.4% in agreement with a low-energy electron-diffraction (LEED) experiment  
[QLJF92]. Comparing FM and AFM coupling of the first layer to the bulk they  
discovered a lower total energy for the FM configuration, which also contradicted the  
results of [WLFF91]. Eriksson et al. [EAO<sup>+</sup>95] investigated the magnetic coupling for  
hcp bulk Gd and the Gd(0001) surface. They applied the full-potential linear muffin-  
tin orbital (FP-LMTO) method. Applying the 4*f*-band model they found an AFM  
ground state for bulk Gd irrespective of whether they used LDA or GGA. However,  
the application of the 4*f*-core model led to the prediction of the correct FM ground  
state. Thus, Eriksson et al. adopted this approach for their surface calculation, also  
finding FM coupling of the first layer and an inwards relaxation of 4.4% in reasonable  
agreement with the results of Bylander et al. Another approach has been used by  
Shick et al. [SLP99, SPF00]. They apply the so-called LDA+U energy functional  
[AAL96] for the description of the localized 4*f* electrons. Within this method the  
strong intra-atomic interactions of the localized states is introduced and treated in a  
Hartree-Fock-like manner. One effect of this method is that the occupied and unoc-  
cupied 4*f* state split apart. The minority 4*f* states are shifted away from the Fermi  
energy to higher energies, removing the artifact from the LDA. At the same time the  
majority 4*f* states are shifted to lower energies. In contrast to the 4*f*-core model,  
using the LDA+U description the majority 4*f* states still hybridize slightly with the  
states of the neighboring atoms. They found the correct FM ground state for hcp  
Gd and also FM coupling of the first layer of Gd(0001). In addition they reported  
that surface relaxation led to a 90% enhancement of the FM surface to bulk effec-  
tive exchange coupling, resulting in a 30% increase of the surface Curie temperature,  
in agreement with several photoemission and photoelectron diffraction experiments  
[TWW<sup>+</sup>93, VCR93, WSLM<sup>+</sup>96, TPY<sup>+</sup>98].

A very interesting contribution has been made by Sandratskii and Kübler  
[SK93, SK98]. There has been an ongoing discussion about which of the two physical  
pictures, the Stoner mean-field picture or the picture of local magnetic fluctuations  
(often referred to as spin-mixing), is more appropriate for the description of the mag-  
netism of the valence electrons (*s*, *p*, *d*) of Gd at finite temperature. Within the Stoner  
picture the size of the local moments decreases with temperature and with it the ex-  
change splitting of the electronic states with up and down-spin character, while all mo-  
ments stay parallel. The spin-mixing picture allows for both, fluctuations of the size

and the direction of the local moments. In this description it is not a priori clear what happens to the spin-splitting at finite temperature. Still, the question which picture is more suitable is commonly discussed in terms of the experimentally observed spin-splitting. Recent photoemission experiments [LPB<sup>+</sup>95, WSLM<sup>+</sup>96, DGP96] found that the spin-splitting of certain valence bands vanish when the temperature approaches the bulk Curie temperature. These results are interpreted as support for the Stoner picture. On the other hand, optical experiments [KT75, BEG84, KS91] observe a spin-splitting that stays constant with changing temperature. Thus, the topic is controversial. Sandratskii and Kübler argued that the different experiments are governed by different parts of the electronic states, i.e. they probe the bandstructure of the sample in different regions of the Brillouin zone. They modeled the effect of temperature by performing calculations in various non-collinear magnetic configurations, including spin-spirals as a model for magnons but also “random” magnetic states that resemble the paramagnetic state of Gd metal above the Curie temperature. They used calculations with different relative angles between neighboring atoms to model different temperatures. The results showed that, as expected, the large  $4f$  local magnetic moment is very stable in size and does not change significantly with the magnetic configuration. They also found that the valence local moment stays finite for all magnetic states. It reduces by no more than about a factor of 2 even for the largest relative angles between the atoms. The magnetic configuration has a strong influence of the electronic structure, i.e. the bandstructure and the density of states (DOS), of Gd. In the FM state all atoms have a definite spin projection onto the global spin quantization axis and both, the bandstructure and the DOS, show an exchange splitting of 0.8 – 0.9 eV. When the angles between the local moments increase states of different spin character hybridize, and thus cannot be assigned to one spin character anymore. The spin-splitting of the DOS decreases. At large angles between neighboring atoms a spin-splitting of the DOS cannot be observed. In fact, the DOS becomes very similar to that of (hypothetical) non-magnetic Gd. By a detailed analysis of the bandstructure Sandratskii and Kübler can account for both, the results of the photoemission experiments as well as the optical experiments.

The experimental results at the Gd(0001) surface are even more controversial than in the bulk. An early study [WAG<sup>+</sup>85] suggested a possible AFM coupling of the surface layer to the underlying bulk. This finding was subsequently supported by the calculations of Wu et al. [WLFF91]. However, more recent photoemission experiments [MGE92, TWW<sup>+</sup>93, LPB<sup>+</sup>95] did not confirm AFM coupling. Instead, the in-plane component of the surface magnetization was observed to be parallel to the bulk, although one study [TWW<sup>+</sup>93] found an additional perpendicular component of the surface magnetization. Another controversial topic is the possibility that the Curie temperature of the surface  $T_C^S$  is larger than the bulk Curie temperature. Such an enhancement has only been observed for three ferromagnets, including Tb and FeNi<sub>3</sub>, and leads to unusual critical behavior. In general the Curie temperature is lower at the surface due to the reduced coordination. At the Gd(0001) surface the enhancement of the Curie temperature was first found by Rau et al. [Rau83].

This effect has been studied by several authors using different techniques, including photoemission [TWW<sup>+</sup>93, VCR93, LPB<sup>+</sup>95, WSLM<sup>+</sup>96, TPY<sup>+</sup>98], inverse photoemission [DGP96] and magneto-optic Kerr effect measurements [WAG<sup>+</sup>85]. Most of the studies, but not all [DGP96], found an enhanced surface Curie temperature. However, the values of the enhancement vary between 10 – 85 K.

Similarly to the bulk, the temperature dependence of the spin-splitting of  $d_{z^2}$  surface states of Gd is very controversial. This surface state has been observed by various techniques, including photoemission (PE) [MGE92, LPB<sup>+</sup>95, WSLM<sup>+</sup>96], inverse photoemission (IPE) [WSLM<sup>+</sup>96, DGP96] and also scanning tunneling spectroscopy (STS) [BGH<sup>+</sup>98, GBH<sup>+</sup>98, GBHW99]. All experiments agree in that the surface state is spin-split. At low temperatures the majority part of the surface state is occupied and is located about 200 – 250 meV below the Fermi energy ( $E_F$ ). The unoccupied minority part of the surface state is found at about 400 – 500 meV above  $E_F$ . Some of these experiments have been performed at temperatures as low as 29 K. While the position of the majority state is in reasonable agreement with the calculation of Wu et al. [WLFF91], the theoretically predicted position of the minority state is much higher (1 eV) than found experimentally. The experimental results agree not only upon the position of the surface state at low temperature, but also in the fact that both parts of the surface state approach  $E_F$  and the spin-splitting decreases. It should be noted here that the PE and IPE experiments can only observe the occupied (majority) and unoccupied (minority) part of the surface state, respectively. Therefore, two experiments, often carried out with different samples of even by different groups, are necessary to determine the spin-splitting. The question that remains controversial is whether a finite splitting of the surface state remains at large temperatures. While, for example, Weschke et al. [WSLM<sup>+</sup>96] found a collapse of the spin-splitting at about 350 K by a combined PE and IPE study, the STS experiments [BGH<sup>+</sup>98, GBH<sup>+</sup>98, GBHW99] still observed two distinct peaks, which were split by 400 meV, at the same temperature.

In the following section we present a study similar to that of Sandratskii and Kübler, however for the Gd(0001) surface. We simulate the effect of temperature on the electronic structure and in particular the  $d_{z^2}$  surface state by non-collinear calculations. But before we turn to the surface we investigate hcp bulk Gd.

## 7.1 hcp bulk Gd

As we have discussed in the previous section, the treatment of the  $4f$  states in first principles calculations has been a matter of extensive debates in the literature. Therefore, before we started to investigate the Gd(0001) surface we performed bulk calculations in order to find out which method was most appropriate for our study. We investigate the effect of the application of the different methods on the ground state properties such as the lattice constant, the magnetic moment and in particular the ground state magnetic configuration. We also studied how the different ways of treating the  $4f$  states affected the  $s$ ,  $p$  and  $d$  valence states. The study includes the

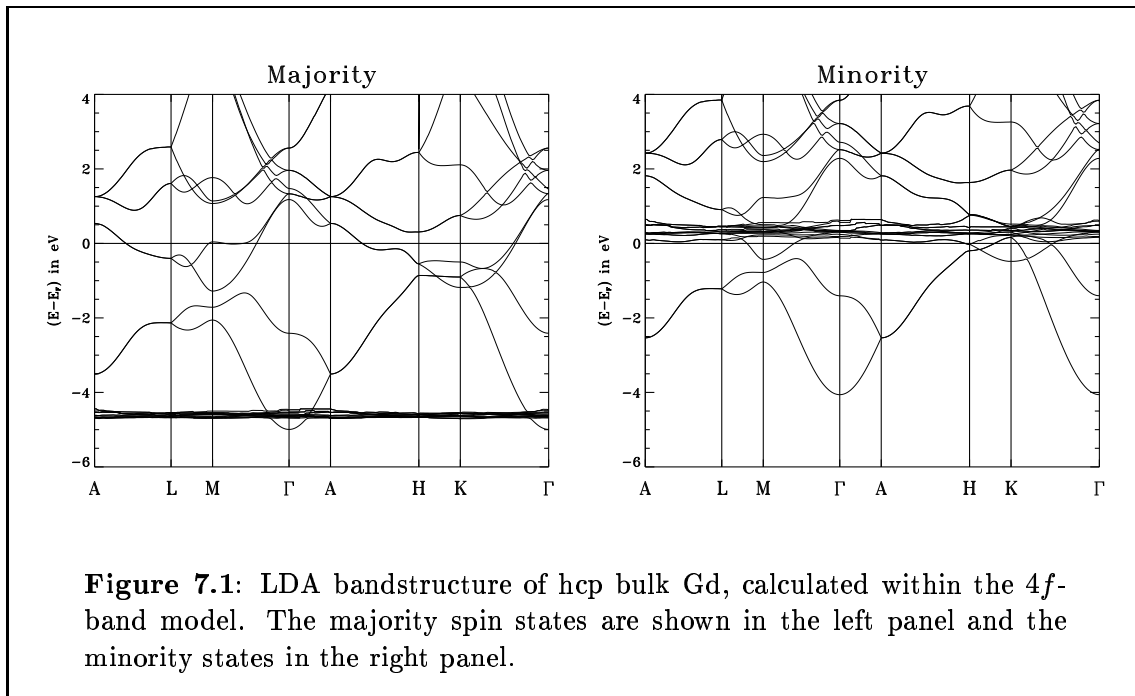
application of LDA as well as GGA potentials and a comparison between the 4*f*-band and the 4*f*-core method

### 7.1.1 Computational details

We performed self-consistent calculations in the local density approximation (LDA) applying the parameterization according to Moruzzi, Janak and Williams [MJW78] and also in the generalized gradient approximation (GGA) of Perdew and Wang [PW91]. We chose the experimental Gd lattice constant,  $a_{Gd} = 6.858$  a.u. and the experimental  $c/a$  ratio of 1.597 [BLS54]. During the calculation of the lattice constant the  $c/a$  ratio was kept at the experimental value. The planewave cutoff for the basis functions was set to  $K_{max} = 3.0$  a.u.<sup>-1</sup>. This corresponds to about 100 basis functions per atom. The charge density and the potential were expanded up to a cutoff  $G_{max} = 9.0$  a.u.<sup>-1</sup>. We set the muffin-tin radii to  $R_{MT} = 2.80$  a.u. The wave functions as well as the density and the potential were expanded up to  $l_{max} = 8$  inside the muffin-tin spheres. The 5*s* and 5*p* semi-core states were treated in a separate energy window. We have used  $k$ -point sets that correspond to 320 and 1152  $k$ -points in the full Brillouin zone in the semi-core and the valence window, respectively.

### 7.1.2 Results

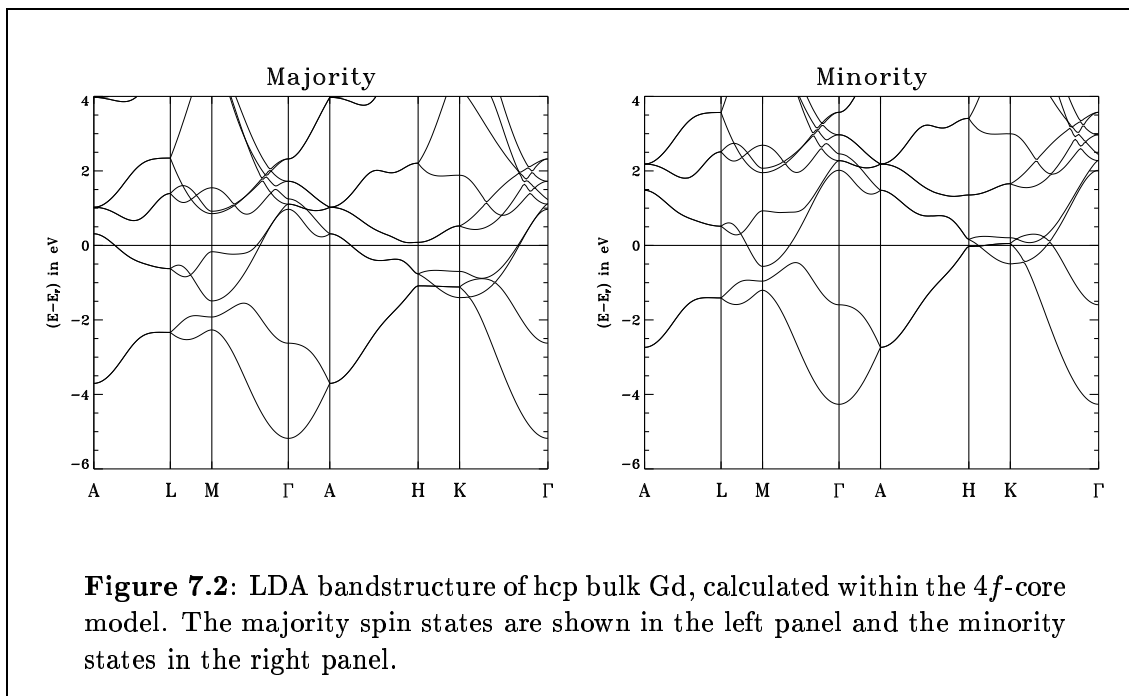
First we present results of a LDA calculation in the 4*f*-band model, where the 4*f* electrons are treated as valence electrons on the same footing as the 6*s* and 5*d* states. The bandstructure calculated at the experimental lattice constant is shown in Fig. 7.1. The most prominent feature are the majority 4*f* bands about 4.5 eV below the Fermi energy (left panel) and the minority 4*f* bands directly above the Fermi energy (right panel). The result is in good agreement with previous first principle calculations that used the 4*f*-band model, e.g. [KS89, Sin91]. However, these studies used fully relativistic methods, while we applied the scalar relativistic approximation, which neglects the spin-orbit coupling. The spin-orbit coupling leads to a splitting of the 4*f* bands. Therefore, the bandwidth of the 4*f* band, in particular the majority part, we found is smaller than in previous studies. Experimentally the majority and minority 4*f* bands are found at about 8 eV below and 4.5 eV above the Fermi energy, respectively. Thus, the wrong energetic positions of the 4*f* bands are an artifact of the local density approximation. The LDA overestimates the itinerancy of the 4*f* electrons. The minority 4*f* state, located just above  $E_F$ , leads to an additional density of states at  $E_F$ . Close to the Fermi energy the 4*f* states hybridize with the *d* states in that energy region. In fact, we found about 0.12 electrons with *f* character inside the muffin-tin spheres (cf. Tab. 7.1). Hence, parts of the minority 4*f*, or the *f*-*d* hybridized, bands are occupied, which is unphysical, and has direct consequences on the magnetic order, as we will discuss below. Another band that has been observed by photoemission is the spin-split  $\Delta_2$  band, which is the second lowest minority band at the  $\Gamma$ -point and its majority counterpart. The calculation shows that it has mainly



$d$ , but also considerable  $s$  character. At the  $\Gamma$ -point we found the majority state  $\Delta_{2\uparrow}$  at the at 2.4 eV and the minority state  $\Delta_{2\downarrow}$  at 1.4 eV below the Fermi energy, in agreement with earlier calculations [KS89, Sin91]. Experimentally the  $\Delta_{2\uparrow}$  and  $\Delta_{2\downarrow}$  bands are found 2.4 eV and 1.7 eV below  $E_F$ , respectively [MGE92].

The difference between the results obtained in LDA and GGA are marginal, when the calculations are performed at the experimental lattice constant. The majority  $4f$  bands are found about 0.2 eV lower than in the LDA calculation. The changes of the other bands are much smaller than this. Therefore, we will not present the GGA bandstructure.

Next we present the result of an LDA calculation with the  $4f$ -core method. Within this method, the majority  $4f$  electrons are treated as core electrons, i.e. they are not allowed to hybridize with any other states on neighboring atoms. Thus, the bonding of the  $4f$  electrons is neglected. At the same time we have to prevent the majority and minority  $4f$  bands from appearing in the valence window. This is done by moving the all  $4f$  energy parameter to a value far above the Fermi energy. In all  $4f$ -core calculations presented here the valence  $f$  energy parameter has been set to about 9.5 eV above  $E_F$ . Thus, we have practically removed the  $f$  functions from the basis set. The calculated bandstructure is shown in Fig. 7.2. The  $4f$  states are not in the valence bandstructure any more. If the core electrons were included into the bandstructure plot, the majority  $4f$  electrons would appear at almost the same energy as in Fig. 7.1 as a dispersion less straight line. Another difference to the result of the  $4f$ -band calculation is that the Fermi energy is shifted upwards by about 0.2 eV. In the  $4f$ -band method  $E_F$  was pushed down by the large density of states of the minority  $4f$  states. Due to the change of  $E_F$  the  $\Delta_{2\uparrow}$  band is now found



at 2.6 eV below  $E_F$  at the  $\Gamma$ -point and the  $\Delta_{2\downarrow}$  is found at 1.6 eV below  $E_F$ . Apart from this shift the bandstructure of the valence bands is largely unchanged. Only the minority  $d$  bands that are in the region of the 4*f* states right above the Fermi energy in the 4*f*-band calculation differ from those of the 4*f*-core calculation by typically less than 0.2 eV. This is probably a consequence of the unphysical hybridization with the 4*f* states. As in the 4*f*-band calculation the GGA results are very similar to the LDA results and therefore the GGA bandstructure is not shown here.

Tab. 7.1 gives an overview over the calculated magnetic moments and the 4*f* charge obtained with the different methods. The total magnetic moment per atom

method		$M$ ( $\mu_B$ )	val. ( $\mu_B$ )	$d$ ( $\mu_B$ )	tot. ( $\mu_B$ )	$f \uparrow$ ( $e^-$ )	$f \downarrow$ ( $e^-$ )
LDA	4 <i>f</i> -band	7.21	7.21	0.34	7.63	6.94	0.127
	4 <i>f</i> -core	7.41	0.41	0.36	7.80	–	–
GGA	4 <i>f</i> -band	7.22	7.22	0.34	7.65	6.65	0.116
	4 <i>f</i> -core	7.41	0.41	0.35	7.81	–	–

**Table 7.1:** Magnetic moment and 4*f* charge calculated at the experimental lattice constant with different methods. The first three columns contain the magnetic moment in the muffin-tin sphere and the valence and  $d$  electron contribution to it. The fourth column contains the total magnetic moment per atom, including the interstitial contribution. All moments are in units of  $\mu_B$ . The last two columns contain the majority and minority 4*f* charge in units of electrons.

is given in the fourth column. All other quantities are integrated only over the muffin-tin region. In the FLAPW method the muffin-tins do not cover the whole volume of the unit cell, i.e. the contribution from the interstitial region adds to these quantities. The size of this difference can be appreciated from a comparison of the first column, which contains the magnetic moment in the muffin-tin spheres, and column four, which contains the total moment per atom. The total moment per atom is in excellent agreement with other recent LDA  $4f$ -band model results, e.g. [SLP99, JTA<sup>+</sup>00], and also the experimental value of  $7.63 \mu_B$ . However, the  $4f$ -core method yields a slightly larger value, which has already been observed by other authors, e.g. [EAO<sup>+</sup>95]. The moment of the  $4f$ -core calculation is in nearly perfect agreement with the LDA+U calculation of Shick et al. [SLP99]. Irrespective of the method used, the  $d$  moment in the muffin-tins is always  $\approx 0.35 \mu_B$ . The total moment in the sphere using the  $4f$ -band model is  $7.21 \mu_B$ . This is smaller than one would expect from the  $7 \mu_B$  of the  $4f$  electrons and the polarization of the  $s$  and  $p$  electrons. In the  $4f$ -core model the valence moment in the sphere amounts to  $0.41 \mu_B$  (here the  $4f$ -electrons are excluded from the valence), i.e. the total valence moment is larger than the  $d$  moment due to the contribution of the  $s$  and  $p$  electrons. The difference between the  $4f$ -band and the  $4f$ -core results is mainly due to the minority  $4f$  occupation in the  $4f$ -band model, which reduces the total  $4f$  moment. The majority  $4f$  states are always fully occupied. However, the majority  $4f$  charge in the muffin-tins (fifth column of Tab. 7.1) is slightly smaller than  $7 e^-$ , because the majority  $4f$  states are not completely localized inside the muffin-tin sphere in both, LDA and GGA. In general it can be said that the differences between LDA and GGA are marginal irrespective of whether the  $4f$ -band or the  $4f$ -core model is used. The only difference that might be important is that the unphysical minority  $4f$  occupation in the  $4f$ -band model is slightly reduced, when the GGA is applied.

In the next step we investigated the magnetic ground state of hcp Gd. We performed total energy calculations to determine the equilibrium lattice constant in the ferromagnetic and antiferromagnetic configurations. The antiferromagnetic configuration consists of antiferromagnetic layers in the (0001) direction, i.e. the magnetic moments of the two atoms of the hcp unit cell are aligned anti-parallel. The total energy as a function of the lattice constant obtained using the LDA  $4f$ -band method, the GGA  $4f$ -band method and the LDA  $4f$ -core method are presented in Fig. 7.3. The  $4f$ -band method calculations predict an AFM ground state irrespective of whether the LDA or the GGA is applied. This result is in agreement with previous full-potential calculations [EAO<sup>+</sup>95, SLP99]. However, it was reported [HT94, JTA<sup>+</sup>00] that using the GGA  $4f$ -band model in combination with the LMTO method in the atomic sphere approximation (ASA) yields the correct ferromagnetic ground state. The picture changes when the  $4f$ -core model is used (right panel). The LDA  $4f$ -core method predicts the FM ground state. This is also true for the GGA  $4f$ -core method, which is not shown in Fig. 7.3.

All calculations that use the  $4f$ -band model agree in that they found the minority  $4f$  states very close to the Fermi energy. This leads to density of states at the Fermi



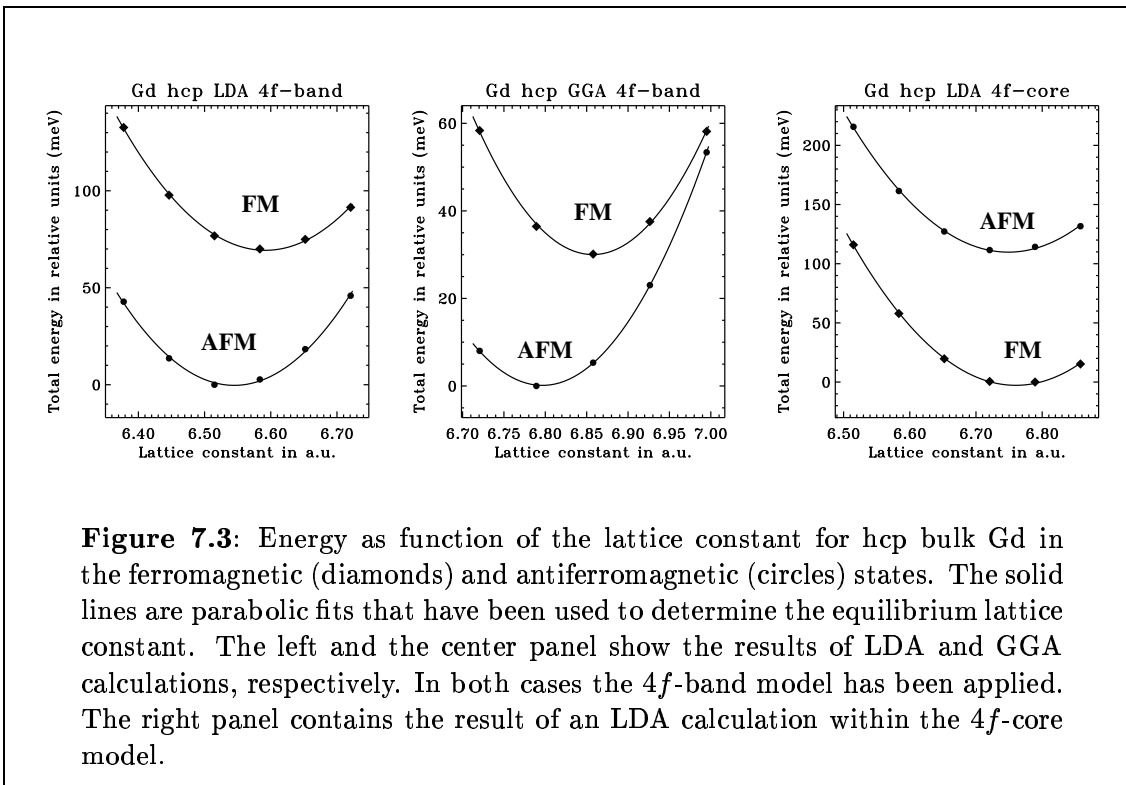


**Figure 7.3:** Energy as function of the lattice constant for hcp bulk Gd in the ferromagnetic (diamonds) and antiferromagnetic (circles) states. The solid lines are parabolic fits that have been used to determine the equilibrium lattice constant. The left and the center panel show the results of LDA and GGA calculations, respectively. In both cases the  $4f$ -band model has been applied. The right panel contains the result of an LDA calculation within the  $4f$ -core model.

energy, which is too large compared to experiment and to an unphysical partial occupation of the  $4f$  states. From the discussion of the  $3d$  metals [THOA82] we know that the  $d$ - $d$  hybridization at half band filling causes a strong antiferromagnetic susceptibility. These arguments are quite general and can also be applied to the  $4f$  states. Due to the  $4f$ -minority states close to the Fermi energy we expect a direct  $4f$ - $4f$  hybridization with a strong antiferromagnetic susceptibility. This suggests that the incorrect description of these states in the LDA (GGA) is the reason for the prediction of the wrong magnetic ground state. In fact, methods that have the effect of pushing the  $4f$  states away from the Fermi energy, like the Hartree-Fock treatment of the exchange between the core and the valence electrons [BK94b] of the LDA+U method [SLP99], or methods that do not allow for  $4f$  electron in the valence region like the  $4f$ -core model [EAO<sup>+</sup>95] found the correct ground state. To substantiate the argument on the role of the minority  $4f$  states presented above states we performed a further calculation using a “hybrid” approach, where we treat the majority  $4f$  electrons as valence electrons, but remove the minority  $4f$  electrons from the valence region by shifting the minority  $f$  energy parameter far above the Fermi energy as in the  $4f$ -core calculation. In fact, this calculation predicts the FM ground state. The total energy difference between the FM and AFM state is very close to that calculated with the  $4f$ -core model (cf. Tab. 7.2)

Tab. 7.2 summarizes the calculated lattice constants, the magnetic moments at the equilibrium lattice constant and the energy difference between the ferromagnetic and the antiferromagnetic configuration. As we have already pointed out, the  $4f$ -

method		$a_{0,\text{FM}}$	$M_{\text{FM}}$	$a_{0,\text{AFM}}$	$M_{\text{AFM}}$	$E_{\text{FM}} - E_{\text{AFM}}$
LDA	4 <i>f</i> -band	-3.9%	7.15 $\mu_B$	-4.6%	7.10 $\mu_B$	+0.07 eV
	4 <i>f</i> -core	-1.4%	7.41 $\mu_B$	-1.7%	7.32 $\mu_B$	-0.11 eV
	hybrid	-2.7%	7.38 $\mu_B$	-2.8%	7.29 $\mu_B$	-0.12 eV
GGA	4 <i>f</i> -band	-0.0%	7.22 $\mu_B$	-0.9%	7.13 $\mu_B$	+0.03 eV
	4 <i>f</i> -core	+1.6%	7.41 $\mu_B$	+1.5%	7.34 $\mu_B$	-0.11 eV
$a_{0,\text{exp}} = 3.629 \text{ \AA}$ [BLS54]						

**Table 7.2:** Equilibrium lattice constants (relative to the experimental value), magnetic moments and the energy difference between the ferromagnetic and the antiferromagnetic state for hcp bulk Gd, calculated using different methods to treat the 4*f* states.

band model predicts the incorrect magnetic ground state. In contrast, the 4*f*-core model and also the hybrid approach, which treats the majority 4*f* electrons as band electrons but removes the minority 4*f* electrons from the vicinity of the Fermi energy, yield the FM ground state. Apparently, the half occupied 4*f* band that crosses the Fermi energy is the reason for the antiferromagnetic coupling, in analogy with half occupied 3*d* bands that have a strongly antiferromagnetic susceptibility. Thus, it is the unphysical partial occupation of the minority 4*f* bands that causes the incorrect description of the magnetic ground state of Gd in the LDA/GGA 4*f*-band model. The LDA/GGA 4*f*-core model and the hybrid approach predict almost the same energy difference between the FM and AFM state. These energy differences are also in reasonable agreement with other methods that remove the minority 4*f* states from the region close to the Fermi energy (Hartree Fock valence-core exchange: -0.12 eV [BK94b]; LDA 4*f*-core: -0.08 eV; GGA 4*f*-core: -0.10 eV [EAO<sup>+</sup>95]; LDA+U: -0.06 eV [SLP99]). In addition to the incorrect description of the magnetic coupling, the LDA 4*f*-band method yields a lattice constant that is 3.9% too small, which is more than the usual LDA error. This is a result of the fact that LDA overestimates the itinerancy of the 4*f* states and thus the 4*f* bonding. With the hybrid approach this error becomes smaller. The 4*f*-core model yields a value with is only 1.4% smaller than experiment. However, in the latter method all 4*f* bonding is neglected. The lattice constant calculated using the GGA 4*f*-core method is 1.5% too large. A similar deficiency of the GGA was found for the 4*d* and 5*d* transition metals [ASH<sup>+</sup>99].

## 7.2 Results for the Gd(0001) surface

We began our study of the Gd(0001) with the determination of the atomic structure. We focus first exclusively on ferromagnetic Gd(0001). Using self-consistent total energy calculations we determined the relaxation of the surface layer, applying three different methods, the LDA/GGA 4*f*-band method and the LDA 4*f*-core method. The surface calculations were performed using a symmetric 10 layer Gd film. All

cutoff parameters were chosen as during the bulk calculations. The integrations over the two-dimensional Brillouin zone were carried out using  $k$ -point sets that correspond to 81 and 361  $k$ -points in the full two-dimensional Brillouin zone for the semi-core and the valence window, respectively. We started from the ideal bulk atomic positions of the respective bulk calculation, i.e. the LDA/GGA 4*f*-band result and the LDA 4*f*-core result. We then varied the interlayer spacing between the surface and the subsurface layer to find the equilibrium position of the surface layer. Fig. 7.4 shows the total energy per surface atom as function of the interlayer distance. With the

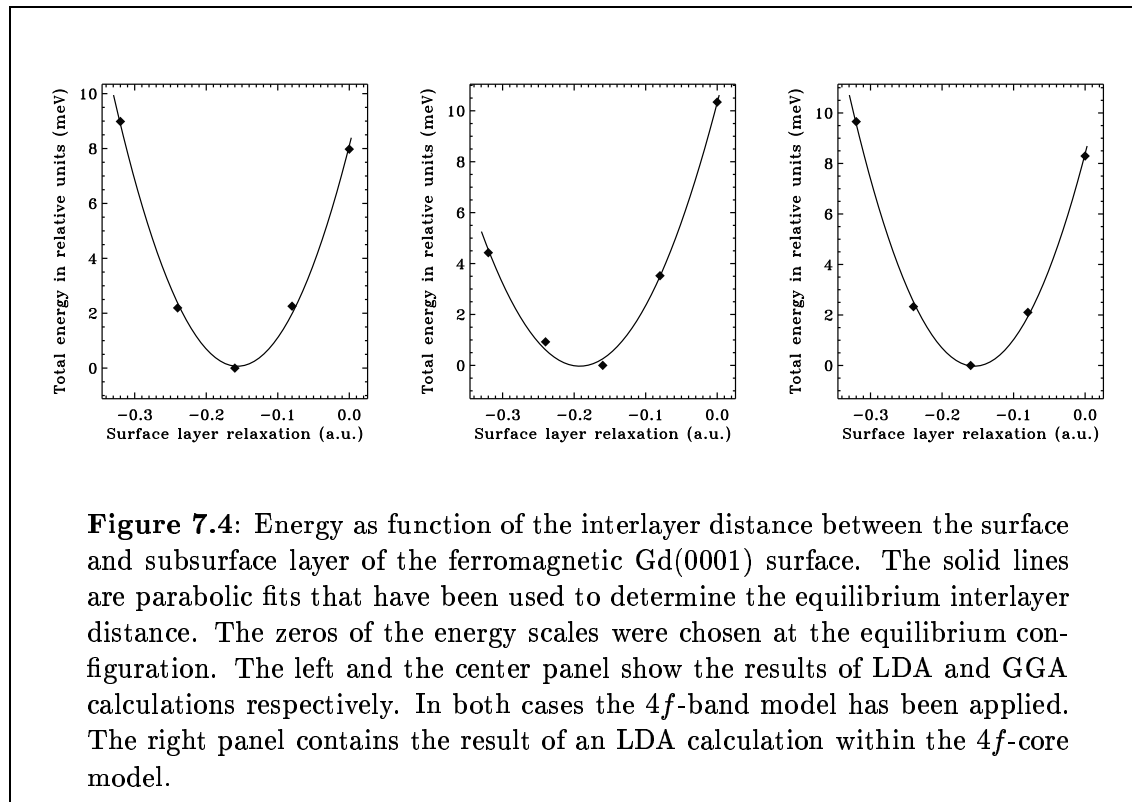


**Figure 7.4:** Energy as function of the interlayer distance between the surface and subsurface layer of the ferromagnetic Gd(0001) surface. The solid lines are parabolic fits that have been used to determine the equilibrium interlayer distance. The zeros of the energy scales were chosen at the equilibrium configuration. The left and the center panel show the results of LDA and GGA calculations respectively. In both cases the 4*f*-band model has been applied. The right panel contains the result of an LDA calculation within the 4*f*-core model.

GGA 4*f*-band method we obtain an inwards relaxation of 3.5% of the bulk interlayer distance and with the LDA 4*f*-band/4*f*-core method we obtain a 3.0% and 2.9% relaxation, respectively. These results are in good agreement with the experimental LEED result of  $3.5 \pm 1.0\%$  [QLJF92]. Recent first principle calculation found a relaxation of 4.4% [EAO<sup>+</sup>95] and 3.4% [BK94a].

Tab. 7.3 summarizes the relaxation and also contains the magnetic moments of all atoms in the 10 layer film. The magnetic moments have been calculated with the surface atom in the relaxed position. However, the moment do not depend critically on the relaxation. In fact, we found exactly the same moment of the surface atom with the ideal bulk truncated position, e.g. for the LDA 4*f*-core calculation. A major difference between the 4*f*-band calculations and the 4*f*-core calculation is found for the magnetic moment of the surface atom. While the 4*f*-band model does not show an indication of an enhanced surface moment, the 4*f*-core model predicts a surface

method		$\Delta d_{12}$	$M_S$	$M_{S-1}$	$M_{S-2}$	$M_{S-3}$	$M_{S-4}$
LDA	4 <i>f</i> -band	-3.0%	7.21 $\mu_B$	7.19 $\mu_B$	7.20 $\mu_B$	7.18 $\mu_B$	7.20 $\mu_B$
	4 <i>f</i> -core	-2.9%	7.55 $\mu_B$	7.41 $\mu_B$	7.40 $\mu_B$	7.42 $\mu_B$	7.41 $\mu_B$
GGA	4 <i>f</i> -band	-3.5%	7.20 $\mu_B$	7.21 $\mu_B$	7.22 $\mu_B$	7.22 $\mu_B$	7.24 $\mu_B$

**Table 7.3:** Relaxation of the surface layer of the Gd(0001) surface and the magnetic moments of the different layers ( $S$  = surface,  $S - 1$  = subsurface, ...).  $\Delta d_{12}$  is the relative change of the distance between the surface and the subsurface layer with respect to the respective bulk value.

moment enhancement of about 0.15  $\mu_B$ , in good agreement with previous calculations [EAO<sup>+</sup>95, SPF00]. We attribute this enhancement of the surface moment to the increase of the  $d$  moment due to the  $d$  band narrowing as result of the reduced number of nearest neighbors at the surface. The enhancement of the  $d$  moment is canceled by an increased occupation of the minority 4*f* bands in the 4*f*-band calculation.

In addition to the ferromagnetic surface we also performed calculations for the surface layer coupling antiferromagnetic to the underlying bulk using the LDA 4*f*-core model. These calculations were carried out with the surface atom in the ideal bulk position as well as in the equilibrium positions of the ferromagnetic surfaces. In

method		$E_{\text{AFM}} - E_{\text{FM}}$ unrelaxed	$E_{\text{AFM}} - E_{\text{FM}}$ relaxed
LDA	4 <i>f</i> -band	25	20
	4 <i>f</i> -core	100	108
	hybrid	99	106

**Table 7.4:** Energy difference (in meV per surface atom) between ferromagnetic (FM) and antiferromagnetic (AFM) coupling of the surface layer of the Gd(0001) surface. The energies were calculated with the surface atom in the ideal truncated bulk position (unrelaxed) and in the relaxed position using the 4*f*-band, the 4*f*-core and the hybrid method, respectively.

both cases we found that the ferromagnetic surface has a clearly lower energy. In the relaxed position we obtained an energy difference of 108 meV per surface atom (cf. Tab. 7.4) in good agreement with the result of Eriksson et al. (95 meV). However, Shick et al. found a larger energy difference in the relaxed position (135 eV). In the ideal bulk position Shick et al. found a much smaller value of 72 meV. Upon this large energy increase between ferromagnetic and antiferromagnetic coupling in the relaxed position of the surface layer they argued that the increased magnetic coupling strength between the surface and the subsurface layer is the origin of the enhanced surface Curie temperature that has been observed by many experiments. This result of an enhancement of the ferromagnetic coupling for the relaxed surface is also supported

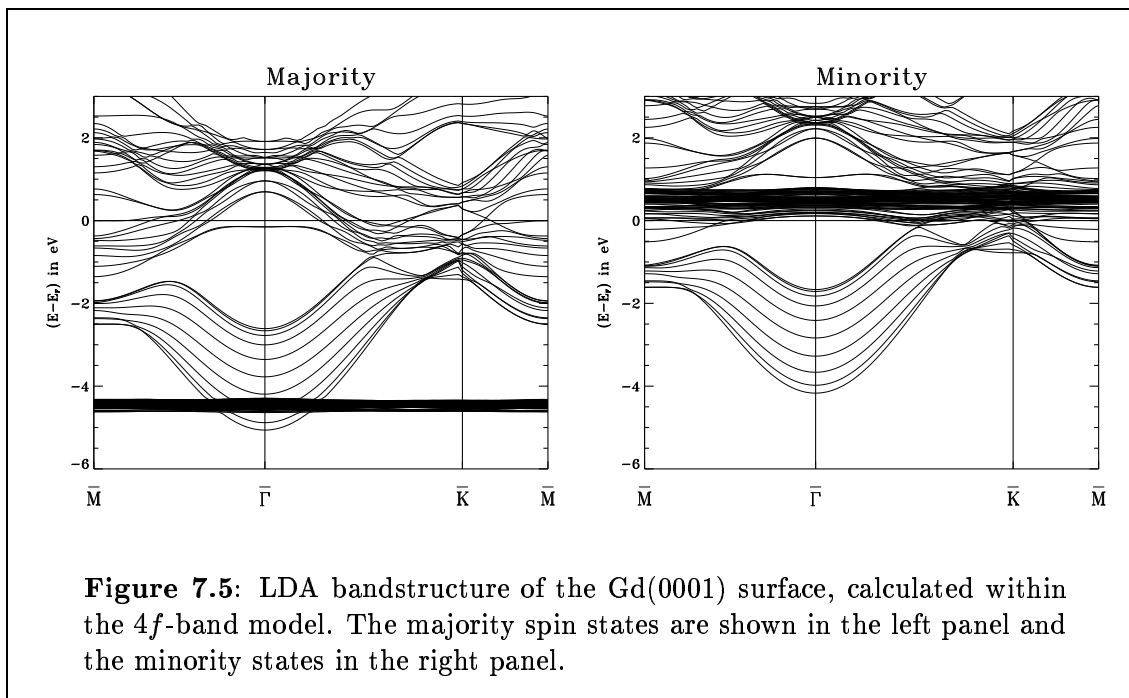


**Figure 7.5:** LDA bandstructure of the Gd(0001) surface, calculated within the  $4f$ -band model. The majority spin states are shown in the left panel and the minority states in the right panel.

by the work of Jenkins et al. [JTA<sup>+</sup>00], who found a clear dependence of the magnetic coupling on the  $c/a$  ratio for hcp bulk Gd using the  $4f$ -band model. According to their results a smaller interlayer distance favors a ferromagnetic coupling. We found only a small reduction of the energy difference at the ideal bulk position (100 meV). Likewise the results of Eriksson et al., who applied the  $4f$ -core model, do not show a reduction of the energy difference between the FM and AFM surface. This could be an indication that the hybridization of the majority  $4f$  states, which is neglected in the  $4f$ -core model, is the origin of the dependence of the magnetic coupling strength on the interlayer distance. However, subsequent calculations within the  $4f$ -band model and the hybrid approach (cf. Tab. 7.4) do not support this hypothesis. In both cases we did not find an enhanced ferromagnetic coupling, though both methods treat the majority  $4f$  electrons as valence states and thus allow for hybridization of these states. Even within the LDA  $4f$ -band method we obtained a lower energy for the ferromagnetic surface. However, the energy difference between the ferromagnetic and the antiferromagnetic configuration is much smaller than calculated with the  $4f$ -core or the hybrid method. Thus, the surface results confirm the result of the bulk calculations, i.e. that the minority  $4f$ -states right above the Fermi energy act in favor of antiferromagnetic coupling.

After the determination of the ground state structure we investigated the electronic structure of the Gd(0001) surface. As in the case of hcp bulk Gd we present the bandstructure determined within the LDA  $4f$ -band method (Fig. 7.5) and the LDA  $4f$ -core method (Fig. 7.6) both calculated in the respective equilibrium structure. The most important feature of the bandstructure is the surface state that is found in a gap of the projected bulk bandstructure around the  $\bar{\Gamma}$ -point. The occupied majority

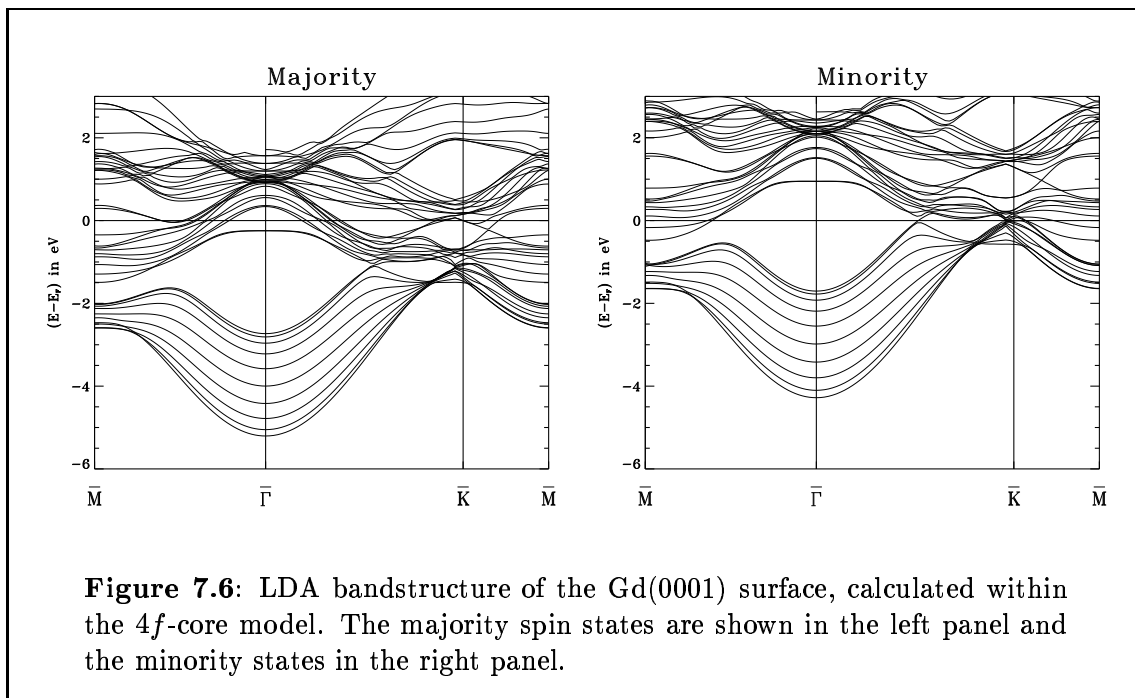


**Figure 7.6:** LDA bandstructure of the Gd(0001) surface, calculated within the  $4f$ -core model. The majority spin states are shown in the left panel and the minority states in the right panel.

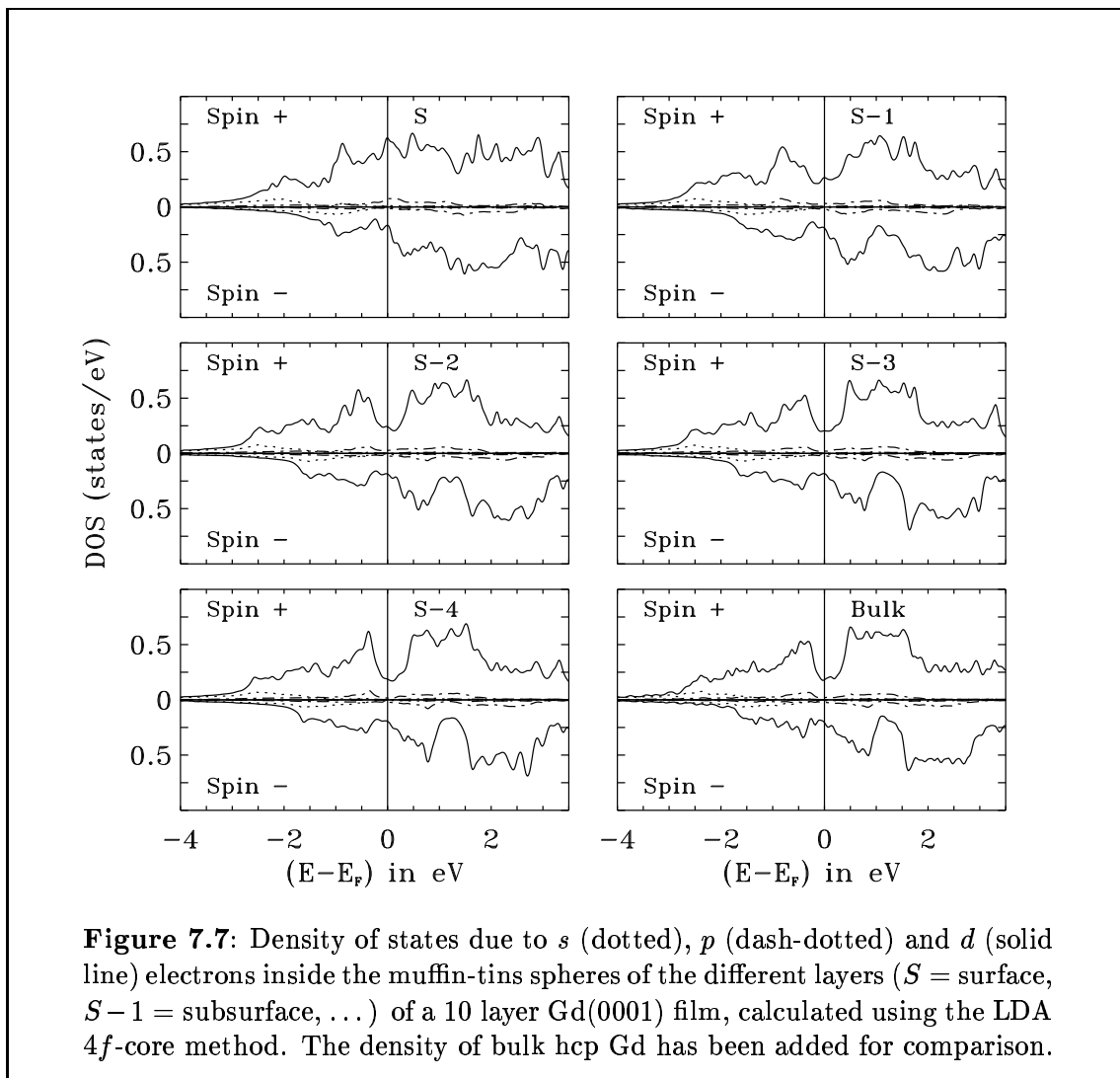
part of the surface state (left panel of Fig. 7.5) is found 0.15 eV below the Fermi energy. This surface state has been investigated experimentally by various techniques, including photoemission and scanning tunneling spectroscopy, and is found a 0.20 – 0.25 eV below the Fermi energy. The unoccupied minority part of the surface state can be seen in the right panel of Fig. 7.5. It lies directly above the minority  $4f$  bands. At the  $\bar{\Gamma}$ -point we found it at 1.04 eV above the Fermi energy. Experimentally it is found at 0.40 – 0.50 eV above the Fermi energy. Both, the minority and the majority part of the surface state, are strongly localized at the surface. Our calculations show that over 70% of their charge density is found in the surface layer and the vacuum region. An analysis of the surface state in the muffin-tins shows that it has mainly  $d$ -character. Our bandstructure is in excellent agreement with the results of Wu et al. [WLFF91], who also found the minority part of the surface state more than 1 eV above the Fermi energy. However, they used a six layer Gd film. As a consequence, a splitting of the surface state due to the finite size of the film is clearly visible in their calculation. With a ten layer film such a splitting is not visible around the  $\bar{\Gamma}$ -point.

Fig. 7.6 shows the bandstructure obtained within the  $4f$ -core model. The  $4f$  states that are clearly visible in Fig. 7.5 have been removed from the valence band region. Similar to the bulk case the main difference between the two methods to treat the  $4f$  electrons is a shift of the Fermi energy. At the surface this shift amounts to about 0.1 eV. Thus, at the  $\bar{\Gamma}$ -point the majority and minority part of the surface state are now found at 0.24 eV below and 0.95 eV above the Fermi energy, respectively. The spin-splitting of the surface state remains unchanged. Hence, the binding energy of majority part of the surface state is in even better agreement with experiment. However, the minority part is still found about 0.40 eV higher than observed

experimentally. As said above the surface state is mostly localized in the surface and vacuum region, which causes the interaction with the Gd substrate to be small. This argument is further substantiated by the very small dependence of the binding energy of the minority and majority part of the surface state upon the interlayer relaxation. In the ideal bulk truncated structure the two parts of the surface state are at 0.22 eV below and 0.98 eV above the Fermi energy, respectively. However, the dependence on the in-plane lattice constant could be different. Therefore, we have repeated the LDA 4*f*-core model calculation on the experimental lattice constant using the calculated relaxation (2.9%) of the surface layer. The experimental in-plane lattice constant is 1.4% larger than in the LDA 4*f*-core calculation. Using the experimental lattice constant the majority and minority part of the surface state at the  $\bar{\Gamma}$ -point are found at 0.21 eV below and 0.98 eV above the Fermi energy, respectively. Hence, also the variation of the binding energy with changing in-plane lattice constant is also small. Still, all results that follow in this chapter have been obtained using the experimental lattice constant.

The density of states (DOS) obtained from the LDA 4*f*-core calculation is presented in Fig. 7.7 for all atoms in the film. It can clearly be seen that the main contribution to the DOS comes from *d* electrons. The DOS of the *s* and *p* electrons is very small. Moving from the surface (S) to the subsurface layer (S-1) the DOS changes rapidly becoming more and more bulk-like. The DOS of the inner six (S-2, S-3, S-4) layers of the film are very similar to the bulk density of states. The majority part bulk DOS shows a pronounced depression (pseudo bandgap) at the Fermi energy. Due to the spin-splitting the minority counterpart of this gap is found about 1.2 eV above the Fermi energy. The two spin components of the surface state fall exactly into this energy region (cf. Fig. 7.6). The density of states due to the surface state fills these gaps. Consequently, these gaps are not visible in the DOS of the surface layer. However, already in the subsurface layer the gaps are clearly visible, which shows again the strong surface localization of the surface state.

Within the Tersoff-Hamann model the tunneling current of a scanning tunneling microscope (STM) is proportional to the local density of states at the position of the tip (cf. Sec. 6.6.1). Thus, to allow a comparison with scanning tunneling spectroscopy (STS) experiments, we investigate the local density of states (LDOS) in the vacuum region of the Gd(0001) film. This quantity is shown in Fig. 7.8 for several distances from the surface layer. The two spin components of the surface state are clearly visible as two pronounced peaks in the majority and minority LDOS respectively. These peaks are directly observed in a STS experiment, e.g. [GBH<sup>+</sup>98], which probes the total LDOS. However, as we have pointed out before, the minority peak is found much closer to the Fermi energy experimentally than in our calculation. Fig. 7.8 also contains density plots of both, the occupied majority surface state and its unoccupied minority counterpart. From this plot the surface state can be identified as a  $d_{z^2}$  state. Also the strong surface localization is clearly visible. A large fraction of the charge density of the surface state is found above the surface layer.



### 7.2.1 Spin-spirals at the Gd(0001) surface

The temperature dependence of the electronic structure of the Gd(0001) surface has been a matter of extensive debate, as we have pointed out in the introduction of this chapter. In particular, the change of the binding energy of both, the majority and minority part of the  $d_{z^2}$  surface state, with temperature has been discussed controversially in the literature. While some experimental studies, e.g. [WSLM<sup>+</sup>96], found a collapse of the spin-splitting of the surface state at a temperature of 350 K, which is taken as support for the applicability of the Stoner picture for the Gd surface, other authors [BGH<sup>+</sup>98, GBH<sup>+</sup>98, GBHW99] observed a finite splitting of 400 meV at the same temperature.

To reveal trends in the temperature variation of the conduction-electron states of the Gd(0001) surface we studied non-collinear magnetic configurations. We performed spin-spiral calculations with  $q$ -vectors parallel to the surface along the high



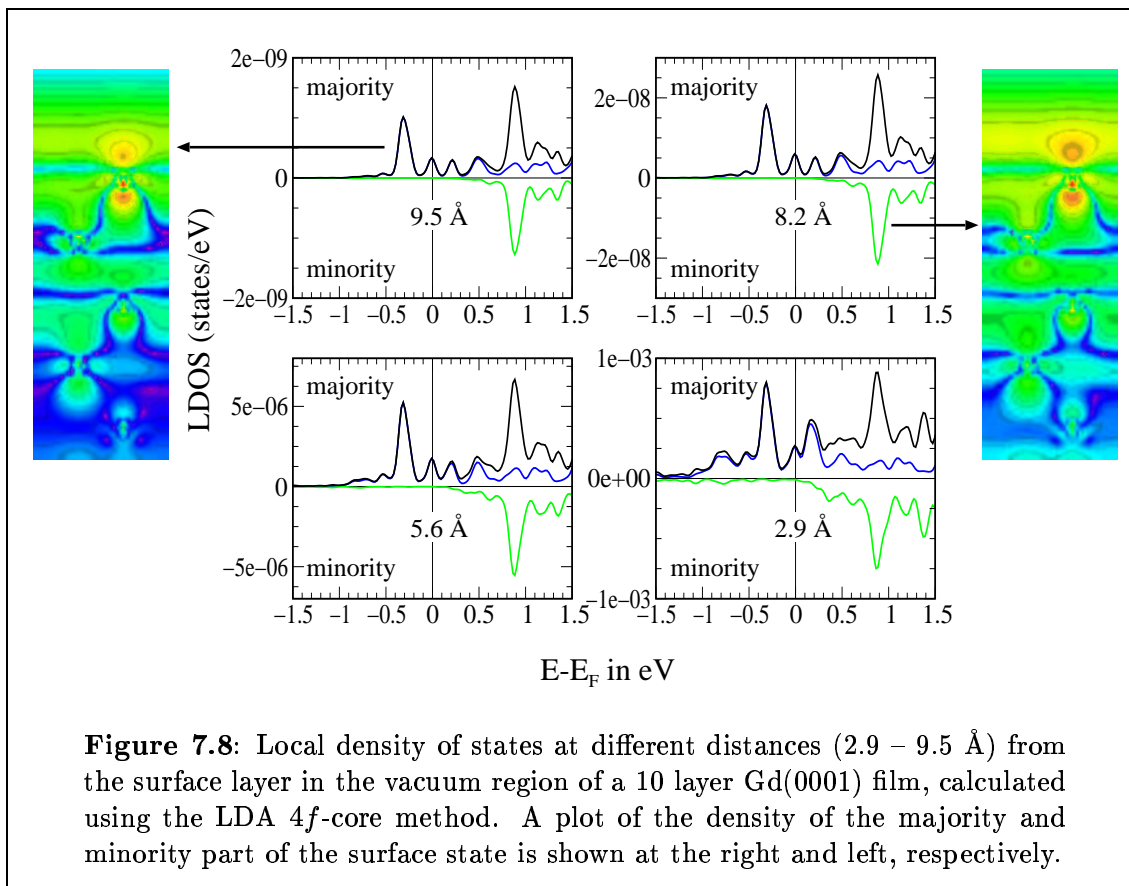
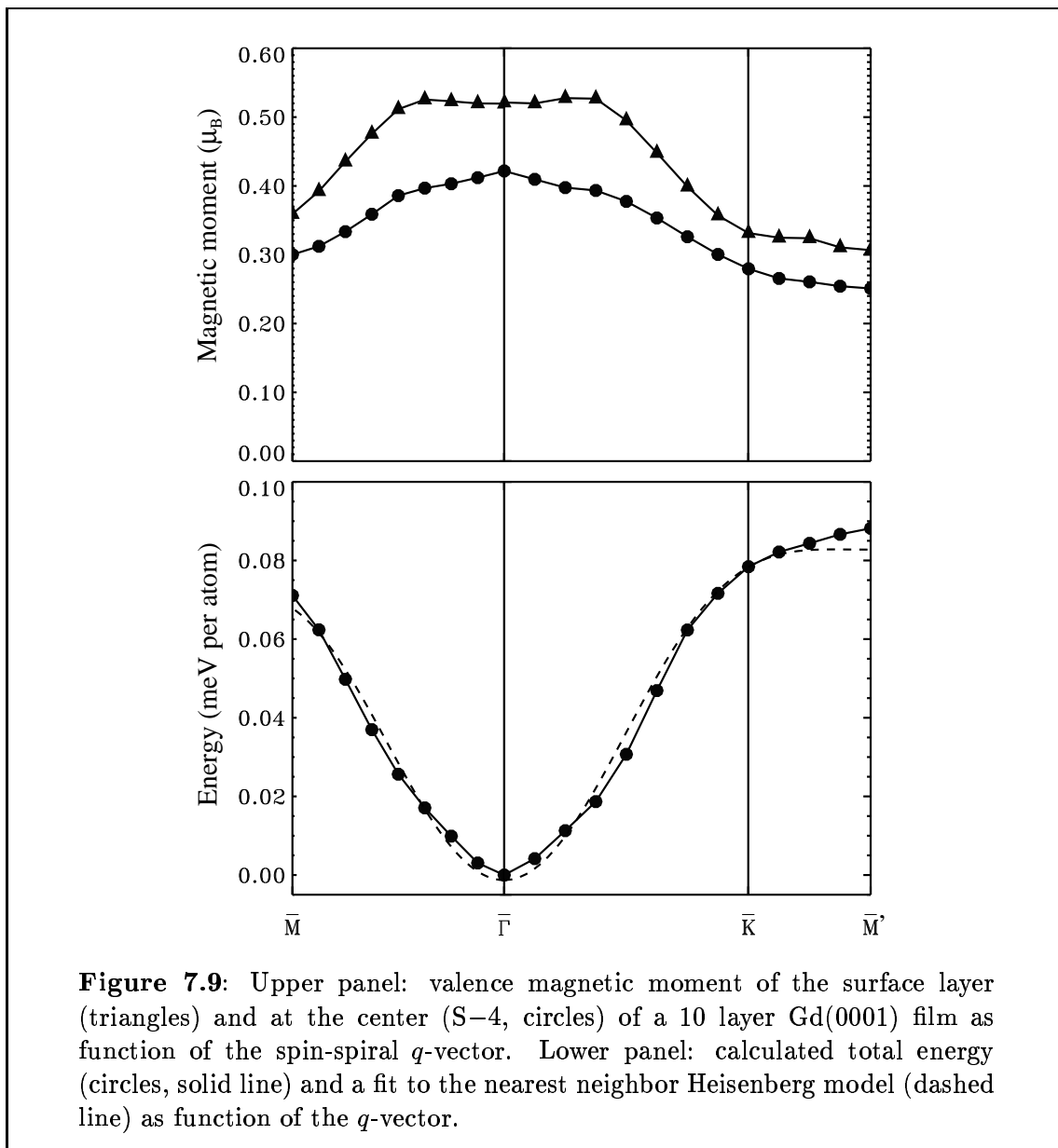


**Figure 7.8:** Local density of states at different distances (2.9 – 9.5 Å) from the surface layer in the vacuum region of a 10 layer Gd(0001) film, calculated using the LDA 4*f*-core method. A plot of the density of the majority and minority part of the surface state is shown at the right and left, respectively.

symmetry lines of the two-dimensional Brillouin zone. Such spin-spiral configurations can be interpreted as a model for magnetic excitations, thus they are frequently referred to as “frozen magnons”.  $q$ -vectors with different magnitude correspond to different angles between the magnetic moments of neighboring atoms. At the ferromagnetic Gd surface, spin-spirals with large  $q$ -vectors have larger total energies, as we will show below. Hence, they correspond to higher temperatures. Due to the strong surface localization of the Gd surface state, we expect spin-spirals with  $q$ -vectors parallel to the surface to have a much greater effect on the surface state than spin-spirals with  $q$ -vectors perpendicular to the surface. Therefore, we used only surface-parallel  $q$ -vectors throughout our study.

We performed the spin-spiral calculations within the 4*f*-core model. Using a 10 layer Gd(0001) film with the experimental in-plane lattice constant and the calculated inwards relaxation of the surface layer of 2.9% as determined in the previous section, all parameters have been chosen as discussed there. Only the  $k$ -point set was changed: due to the reduced symmetry of the spin-spiral configuration we had to distribute the  $k$ -points in the full two-dimensional Brillouin zone. The  $k$ -point sets contained 16  $k$ -points in the semi-core window and 64  $k$ -points in the valence window. Tests with a  $k$ -point set with 64 and 256  $k$ -points in the semi-core and valence window, respectively, showed that the convergence of the total energy difference between the



two magnetic states with the largest energy difference ( $\mathbf{q} = 0$  and  $\mathbf{q} = \bar{M}$ , cf. Fig. 7.9) was better than 2 meV per atom. A test with  $k_{\max} = 3.3 \text{ a.u.}^{-1}$  showed that the convergence of the energy difference between the same states with respect to the planewave cutoff was better than 4 meV per atom.

The results of the self-consistent spin-spiral calculations are presented in Fig. 7.9. The upper panel of Fig. 7.9 shows the valence magnetic moment of the  $s$ ,  $p$  and  $d$  electrons within the muffin-tin sphere as function of the spin-spiral  $q$ -vector. The valence moment of the surface atoms is marked by triangles. The valence moment of the atoms at the center of the 10 layer film, 4 layers below the surface, is marked by circles. The surface enhancement of the magnetic moment is clearly visible for

all values of  $\mathbf{q}$ . For all magnetic configurations we found a finite valence magnetic moment, being always larger than  $0.30 \mu_B$  at the surface and  $0.25 \mu_B$  at the center of the film, even for the largest values of  $\mathbf{q}$ . In their study of non-collinear states in hcp bulk Gd, Sandratskii and Kübler [SK98] also found that a finite value of the valence moment remains for large spin-spiral  $q$ -vectors. However, the absolute value of the magnetic moment cannot be compared to our results, since they use space filling spheres around the atoms. To verify that the stability of the induced moment is not a consequence of the high symmetry of the spin-spiral configuration they carried out calculations for disordered magnetic configurations, which confirmed the stability of the valence moments. Therefore, we expect the magnetic moments of disordered configurations at the surface to be of similar size as found for the spin-spiral calculations.

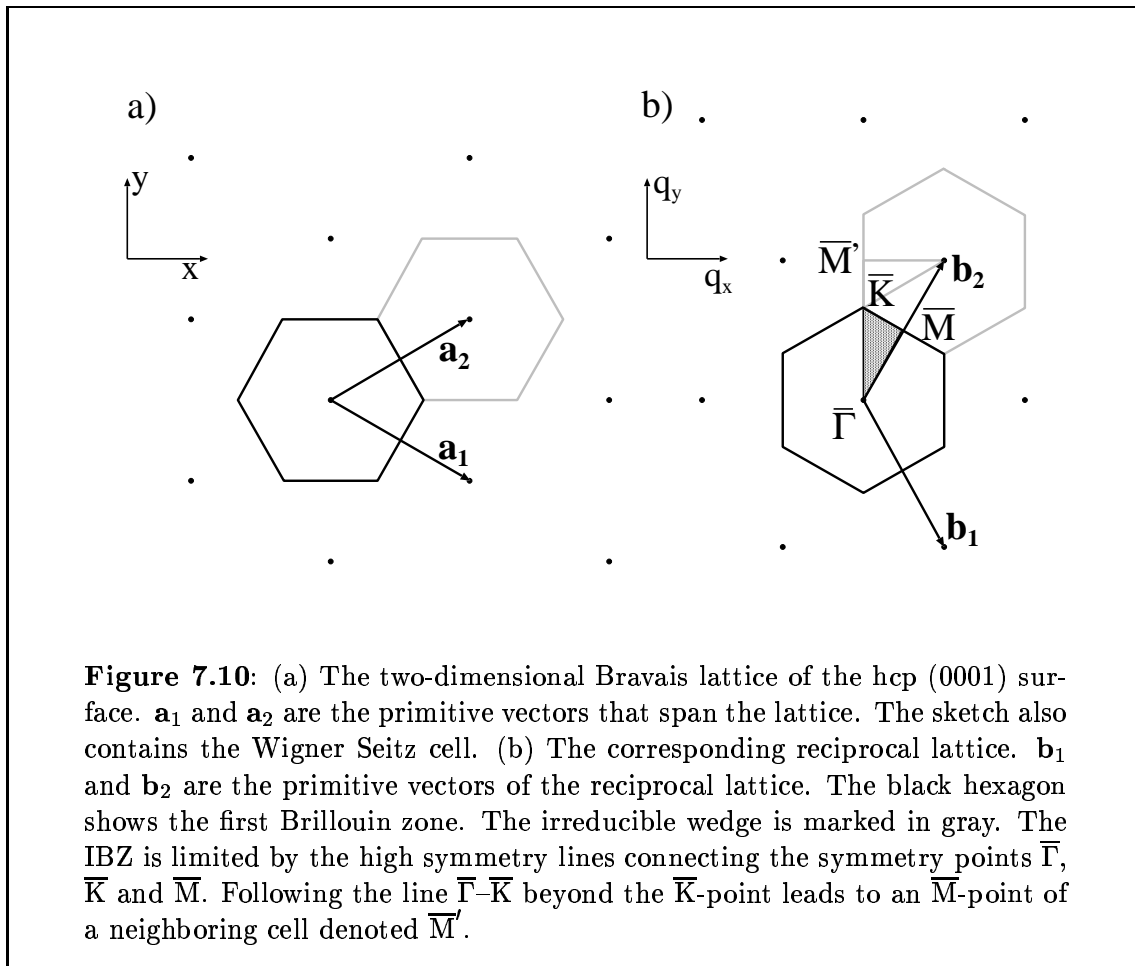
The total energy as function of the spin-spiral  $q$ -vector  $E(\mathbf{q})$  is plotted in the lower panel of Fig. 7.9.  $E(\mathbf{q})$  possesses a pronounced minimum at the  $\bar{\Gamma}$ -point, corresponding to a ferromagnetic ground state. With growing  $\mathbf{q}$ , i.e. increasing angle between the magnetic moment of neighboring atoms, the energy increases quickly. In contrast to the results of the  $3d$  monolayers on the Cu and Ag(111) surface (cf. Chap. 6), which have the same two-dimensional Brillouin zone, the energies at the two  $\bar{M}$ -points at the right-hand side and the left-hand side of the plot are not equal. The actual  $q$ -vectors of these two points that have been used for the calculations are different. For the calculation of  $E(\mathbf{q})$  along  $\bar{\Gamma}$ - $\bar{K}$ - $\bar{M}'$  we used  $q$ -vectors on a straight line in reciprocal space. The point  $\bar{M}'$  at the end on this line is not on the border of the first Brillouin zone but on the border of a neighboring cell in reciprocal space (cf. Fig. 7.10). The magnetic atoms of a monolayer on a (111) oriented fcc surface form a two-dimensional triangular lattice (Bravais lattice) without a basis. In this case the energy of  $E(\mathbf{q})$  at the two  $\bar{M}$ -points is always the same. However, in the case of the (0001) surface of Gd there are two magnetic atoms in the unit cell, i.e. it is a lattice with a basis. To clarify the consequences we discuss the classical nearest neighbor Heisenberg model for the hcp (0001) surface in the following section.

### 7.2.2 The nearest neighbor Heisenberg model for hcp bulk and the hcp (0001) surface

In this section we present a brief discussion of the classical nearest neighbor (n.n.) Heisenberg model (cf. Sec. 6.2) for the hcp lattice and the hcp (0001) surface. We begin with bulk hcp. First we define the primitive vectors of the hcp Bravais lattice and the reciprocal lattice:

$$\begin{aligned} \mathbf{a}_1 &= a(\sqrt{3}/2, -1/2, 0), & \mathbf{a}_2 &= a(\sqrt{3}/2, 1/2, 0), & \mathbf{a}_3 &= c(0, 0, 1) \\ \mathbf{b}_1 &= \frac{2\pi}{a}(1/\sqrt{3}, -1, 0), & \mathbf{b}_2 &= \frac{2\pi}{a}(1/\sqrt{3}, 1, 0), & \mathbf{b}_3 &= \frac{2\pi}{c}(0, 0, 1). \end{aligned} \quad (7.1)$$

Naturally, we will later use  $\mathbf{a}_1$  and  $\mathbf{a}_2$  as the primitive vectors of the two-dimensional Bravais lattice of the Gd(0001) surface. The two-dimensional lattice and reciprocal lattice including the primitive vectors are shown in Fig. 7.10.



In order to calculate the Fourier transform of the exchange constants according to Eqn. 6.7, we need to sum over all nearest neighbors of the magnetic atoms and, since we study a lattice with a basis, over the atoms in the unit cell. For the actual ab-initio calculations we chose the atom positions ( $\mathbf{p}$ ) such that we obtain an inversion center at the origin. Here, we make the same choice again:

$$\mathbf{p} = \pm(1/3\mathbf{a}_1 + 1/3\mathbf{a}_2 + 1/4\mathbf{a}_3). \quad (7.2)$$

Eqn. 6.7 contains the distance vectors ( $\mathbf{R}_\delta$ ) from each of the two atoms in the unit cell to its 12 nearest neighbors. Each atom has 6 neighbors in the  $\mathbf{a}_1$ - $\mathbf{a}_2$ -plane, as well as 3 neighbors above and 3 neighbors below this plane. In the following we list all vectors  $\mathbf{R}_\delta$  for the two atoms in the hcp bulk unit cell.

Atom1:  $\mathbf{R}_\delta$  to the 6 neighbors in the  $\mathbf{a}_1$ - $\mathbf{a}_2$ -plane:

$$\mathbf{a}_1, \mathbf{a}_2, -\mathbf{a}_1, -\mathbf{a}_2, \mathbf{a}_1 - \mathbf{a}_2, \mathbf{a}_2 - \mathbf{a}_1 \quad (7.3)$$

Atom1:  $\mathbf{R}_\delta$  to the 6 neighbors above and below the  $\mathbf{a}_1$ - $\mathbf{a}_2$ -plane:

$$-\frac{1}{3}\mathbf{a}_1 - \frac{1}{3}\mathbf{a}_2 \pm \frac{1}{2}\mathbf{a}_3, \quad \frac{2}{3}\mathbf{a}_1 - \frac{1}{3}\mathbf{a}_2 \pm \frac{1}{2}\mathbf{a}_3, \quad -\frac{1}{3}\mathbf{a}_1 + \frac{2}{3}\mathbf{a}_2 \pm \frac{1}{2}\mathbf{a}_3, \quad (7.4)$$

Atom2:  $\mathbf{R}_\delta$  to the 6 neighbors in plane the  $\mathbf{a}_1$ - $\mathbf{a}_2$ -plane:

$$\mathbf{a}_1, \mathbf{a}_2, -\mathbf{a}_1, -\mathbf{a}_2, \mathbf{a}_1 - \mathbf{a}_2, \mathbf{a}_2 - \mathbf{a}_1 \quad (7.5)$$

Atom2:  $\mathbf{R}_\delta$  to the 6 neighbors above and below the  $\mathbf{a}_1$ - $\mathbf{a}_2$ -plane:

$$\frac{1}{3}\mathbf{a}_1 + \frac{1}{3}\mathbf{a}_2 \pm \frac{1}{2}\mathbf{a}_3, \quad -\frac{2}{3}\mathbf{a}_1 + \frac{1}{3}\mathbf{a}_2 \pm \frac{1}{2}\mathbf{a}_3, \quad \frac{1}{3}\mathbf{a}_1 - \frac{2}{3}\mathbf{a}_2 \pm \frac{1}{2}\mathbf{a}_3, \quad (7.6)$$

Writing the  $q$ -vector as

$$\mathbf{q} = q_1\mathbf{b}_1 + q_2\mathbf{b}_2 + q_3\mathbf{b}_3, \quad (7.7)$$

we obtain for the Fourier transform of the exchange integrals  $J_{\text{hcp}}(\mathbf{q})$ :

$$\begin{aligned} J_{\text{hcp}}(\mathbf{q}) = & J_1 [4 \cos(2\pi q_1) + 4 \cos(2\pi q_2) + 4 \cos(2\pi(q_1 - q_2)) \\ & + 2 \cos(2\pi(\frac{1}{3}q_1 + \frac{1}{3}q_2 - \frac{1}{2}q_3)) + 2 \cos(2\pi(\frac{1}{3}q_1 + \frac{1}{3}q_2 + \frac{1}{2}q_3)) \\ & + 2 \cos(2\pi(\frac{2}{3}q_1 - \frac{1}{3}q_2 + \frac{1}{2}q_3)) + 2 \cos(2\pi(\frac{2}{3}q_1 - \frac{1}{3}q_2 - \frac{1}{2}q_3)) \\ & + 2 \cos(2\pi(\frac{1}{3}q_1 - \frac{2}{3}q_2 - \frac{1}{2}q_3)) + 2 \cos(2\pi(\frac{1}{3}q_1 - \frac{2}{3}q_2 + \frac{1}{2}q_3))] . \end{aligned} \quad (7.8)$$

After  $J_{\text{hcp}}(\mathbf{q})$  has been determined the energy of spin-spiral states can be calculated as function of the  $q$ -vector using Eqn. 6.11. We consider first the symmetry line  $\Gamma$ - $\text{K}$ - $\text{M}'$  of the three-dimensional Brillouin zone. As mentioned above the  $\text{M}'$ -point is not on the border of the first Brillouin zone, but on the border of a neighboring cell in reciprocal space. All three symmetry points are in the  $\mathbf{b}_1$ - $\mathbf{b}_2$ -plane ( $q_3 = 0$ ). Hence, this symmetry line corresponds exactly to the line  $\bar{\Gamma}$ - $\bar{\text{K}}$ - $\bar{\text{M}}'$  shown in Fig. 7.10. The line  $\Gamma$ - $\text{K}$ - $\text{M}'$  can be parameterized by, e.g. (cf. Fig. 7.10)

$$\mathbf{q} = -x\mathbf{b}_1 + x\mathbf{b}_2, \quad 0 \leq x \leq 0.5, \quad (7.9)$$

i.e.  $q_1 = -x$  and  $q_2 = x$ . Substituting into Eqn. 7.8 and using Eqn. 6.11, we obtain the energy as function of the  $q$ -vector:

$$E_{\text{hcp}}(\mathbf{q}) = S^2 J_1 [4 \cos(4\pi x) + 16 \cos(2\pi x) + 4], \quad (7.10)$$

which is  $2\pi$ -periodic. Thus,  $E_{\text{hcp}}(\mathbf{q})$  has the periodicity of the reciprocal lattice. The symmetry line  $\Gamma$ - $\text{M}$  can be parameterized by, e.g.

$$\mathbf{q} = x\mathbf{b}_2, \quad 0 \leq x \leq 0.5. \quad (7.11)$$

On this symmetry line we obtain

$$E_{\text{hcp}}(\mathbf{q}) = S^2 J_1 \left[ 8 \cos(2\pi x) + 4 \cos\left(\frac{4\pi}{3}x\right) + 8 \cos\left(\frac{2\pi}{3}x\right) + 4 \right] \quad (7.12)$$

for  $E_{\text{hcp}}(\mathbf{q})$ . This function is  $6\pi$ -periodic, i.e.  $E_{\text{hcp}}(\mathbf{q})$  has a larger periodicity than the reciprocal lattice for  $q$ -vectors along the direction  $\Gamma$ - $\text{M}$ . However, since we investigate

the temperature dependence of the electronic structure of Gd we are mainly interested in small  $q$ -vectors. Therefore, we will not discuss  $E_{\text{hcp}}(\mathbf{q})$  beyond the M-point. At this point, we can already see that the energy at M and M' are in fact different within the n.n. Heisenberg model.

To calculate  $E_{\text{film}}(\mathbf{q})$  for the Gd(0001) surface we make the simplifying assumption that the n.n. exchange constant  $J_1$  is the same for all pairs of atoms, even at the surface. Using this assumption,  $E_{\text{film}}(\mathbf{q})$  for the 10 layer film used in our ab-initio calculation is simply given by five times  $E_{\text{hcp}}$  minus the terms that are missing because of the reduced coordination of the surface atoms. Thus, we obtain

$$\begin{aligned} J_{\text{film}}(\mathbf{q}) = 5J_{\text{hcp}}(\mathbf{q}) & - 2J_1 \cos(2\pi(\frac{1}{3}q_1 + \frac{1}{3}q_2 - \frac{1}{2}q_3)) \\ & - 2J_1 \cos(2\pi(\frac{2}{3}q_1 - \frac{1}{3}q_2 + \frac{1}{2}q_3)) \\ & - 2J_1 \cos(2\pi(\frac{1}{3}q_1 - \frac{2}{3}q_2 - \frac{1}{2}q_3)) \end{aligned} \quad (7.13)$$

for the Fourier transform of the exchange integrals, and hence,

$$E_{\text{film}}(\mathbf{q}) = S^2 J_1 [20 \cos(4\pi x) + 76 \cos(2\pi x) + 18] \quad (7.14)$$

and

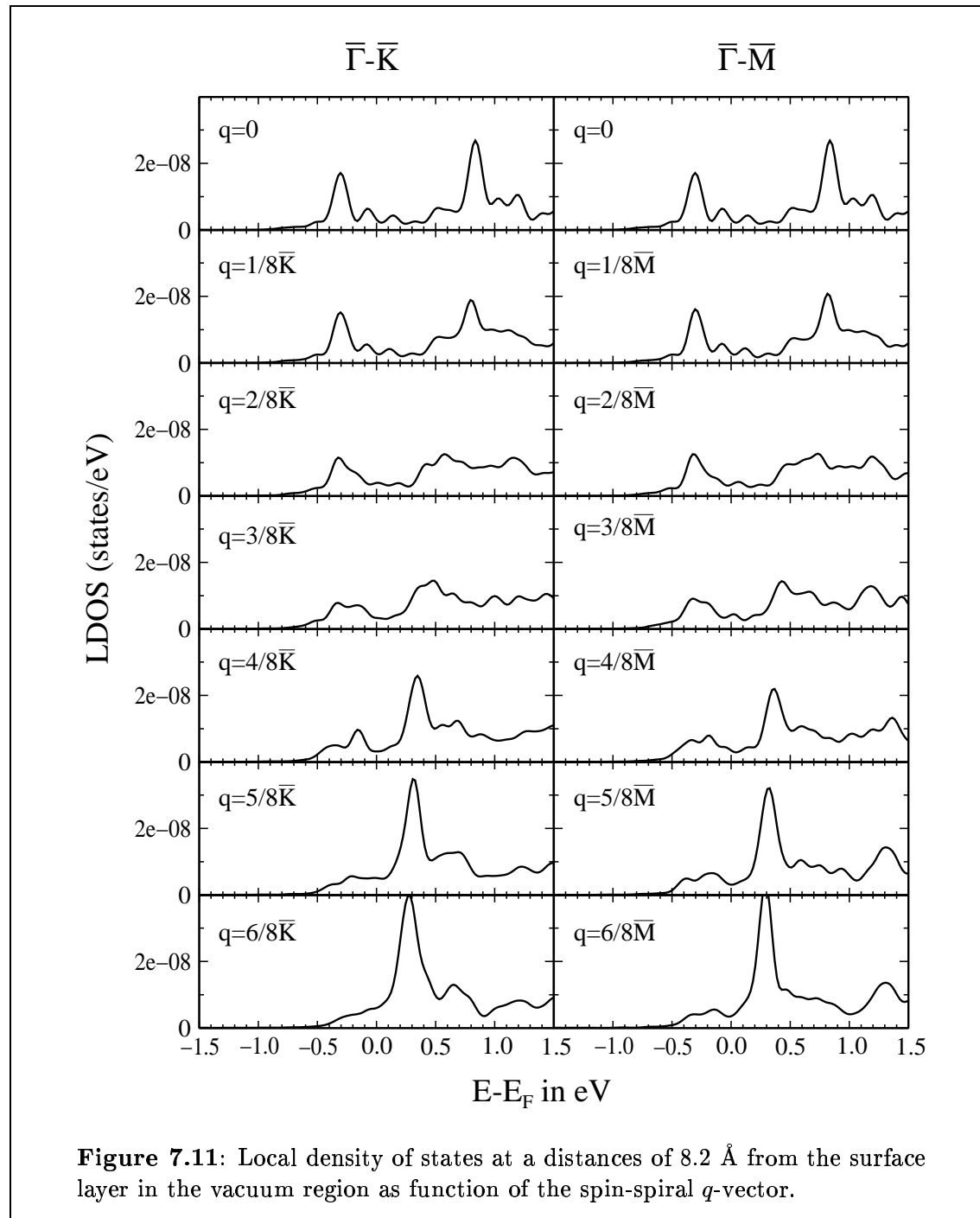
$$E_{\text{film}}(\mathbf{q}) = S^2 J_1 \left[ 40 \cos(2\pi x) + 18 \cos(\frac{4\pi}{3}x) + 36 \cos(\frac{2\pi}{3}x) + 20 \right] \quad (7.15)$$

for the energy of the 10 layer Gd(0001) film as function of the spin-spiral  $q$ -vector along the lines  $\bar{\Gamma}$ - $\bar{K}$ - $\bar{M}'$  and  $\bar{\Gamma}$ - $\bar{M}$ , respectively. We performed a fit of these functions to our ab-initio results. The fitted function is shown as dashed line in Fig. 7.9. From this fit we obtained a value of  $S^2 J_1 = 5.5$  meV for the n.n. exchange integral.

### 7.2.3 The electronic structure of the Gd(0001) surface as function of the spin-spiral $q$ -vector

In this section we investigate the electronic structure of the Gd(0001) surface as function of the spin-spiral  $q$ -vector: to model the temperature dependence of the electronic states. In particular, we are interested in the change of the binding energy of the surface state. Therefore, and to be able to compare the results with the scanning tunneling spectroscopy (STS) experiments, we calculated the local density of state in the vacuum region. Within the Tersoff-Hamann model this is exactly the quantity measured by a (non-spin-polarized) STS experiment (cf. Sec. 6.6.1).

In Fig. 7.11 we present the calculated local density of state (LDOS) in the vacuum region for different spin-spiral  $q$ -vectors on the high symmetry lines  $\bar{\Gamma}$ - $\bar{K}$  and  $\bar{\Gamma}$ - $\bar{M}$ . Since the electronic states are generally spin-hybridized in non-collinear magnetic configurations and are therefore not of pure spin-up or down character any more, we present only the total LDOS. The LDOS for  $\mathbf{q} = 0$  is identical to the result of the



collinear ferromagnetic calculation (cf. Fig. 7.8). First of all it can be seen that the behavior of the LDOS is very similar for  $q$ -vectors on both symmetry lines,  $\bar{\Gamma}-\bar{K}$  and  $\bar{\Gamma}-\bar{M}$ . Though, it should be noted that the “step size” of the  $q$ -vector grid is slightly different on the two lines, since the distance from  $\bar{\Gamma}$  to  $\bar{K}$  in reciprocal space is by a factor of  $2/\sqrt{3}$  ( $\approx 15\%$ ) larger than the distance from  $\bar{\Gamma}$  to  $\bar{M}$ .

At  $\mathbf{q} = 0$ , the two peaks of the LDOS due to the spin-split surface state are clearly visible. With increasing  $\mathbf{q}$  the spin-splitting decreases. In particular the unoccupied minority surface state moves towards the Fermi energy. For larger values of  $\mathbf{q}$  ( $\mathbf{q} = 2/8\bar{K}$  to  $4/8\bar{K}$  and  $\mathbf{q} = 2/8\bar{M}$  to  $5/8\bar{M}$ ) the intensity of the peaks decreases and two double peak structures can be observed. For even larger  $\mathbf{q}$ 's again two pronounced peaks emerge. However, the occupied peak below the Fermi energy is now much smaller than for small  $q$ -vectors and finally disappears for  $\mathbf{q} = 6/8\bar{K}$  and  $\mathbf{q} = 6/8\bar{M}$ , respectively. At the same time the intensity of the peak in the unoccupied region, which is now only about 300 meV above the Fermi energy, increases. These trends are in good agreement with temperature dependent STS experiments [BGH<sup>+</sup>98, GBH<sup>+</sup>98, GBHW99], which also found a decrease of the splitting of the two peaks with temperature and a decreasing intensity of the peak below the Fermi energy for high temperature. However, the initial splitting at 20 K is found to be 700 meV, which is much smaller than our result of 1.1 eV for the ferromagnetic configuration.

In Fig. 7.12 the positions of the two peaks in the occupied and unoccupied region of the vacuum LDOS (circles) are plotted versus the energy of the corresponding spin-spiral per atom. The bulk Curie temperature of Gd of  $T_C^B = 293$  K corresponds an energy of about  $k_B T_C^B \approx 25$  meV. However, a direct comparison between our calculations and an experiment at a certain temperature is difficult for two reasons: First, in a real experiment at a finite temperature many magnons with excitation energies up to a certain value will be present simultaneously. Thus, there will always be a superposition of magnons with  $q$ -vectors of different directions and different lengths, while our calculations were carried out for a single  $q$ -vector each. And secondly, we know from the bulk calculations (cf. Sec. 7.1) that the calculated magnetic energies depend significantly on the treatment of the  $4f$  states. Comparing the total energy difference between ferromagnetic and antiferromagnetic hcp Gd calculated within the  $4f$ -core model and the LDA+U method, we could conclude that the  $4f$ -core model might overestimate the magnetic energies by up to 50%. This would of course correspond to a substantial change of the temperature scale. On the other hand our results show the effect of non-collinear magnetic order present in a real material at finite temperature on the electronic structure. And they allow to understand the general trends in the temperature variation of the electronic valence states.

Coming back to Fig. 7.12, it can be seen that the two peaks in the occupied and the unoccupied region of the vacuum LDOS approach the Fermi energy, and also that the results for  $q$ -vectors on the two different symmetry lines are similar. In this figure we marked two values for the occupied peak in the region of  $\mathbf{q}$  where the double peak structure is visible in Fig. 7.11. By a detailed analysis of the electronic states we traced the majority and minority part of the surface state at the  $\bar{\Gamma}$ -point. The corresponding binding energies are included as triangles in Fig. 7.12. The energies of the surface states at the  $\bar{\Gamma}$ -point are in good agreement with the peak positions of the vacuum LDOS. The analysis of the states shows that in the ferromagnetic configuration both, the majority and in particular the minority surface state, have



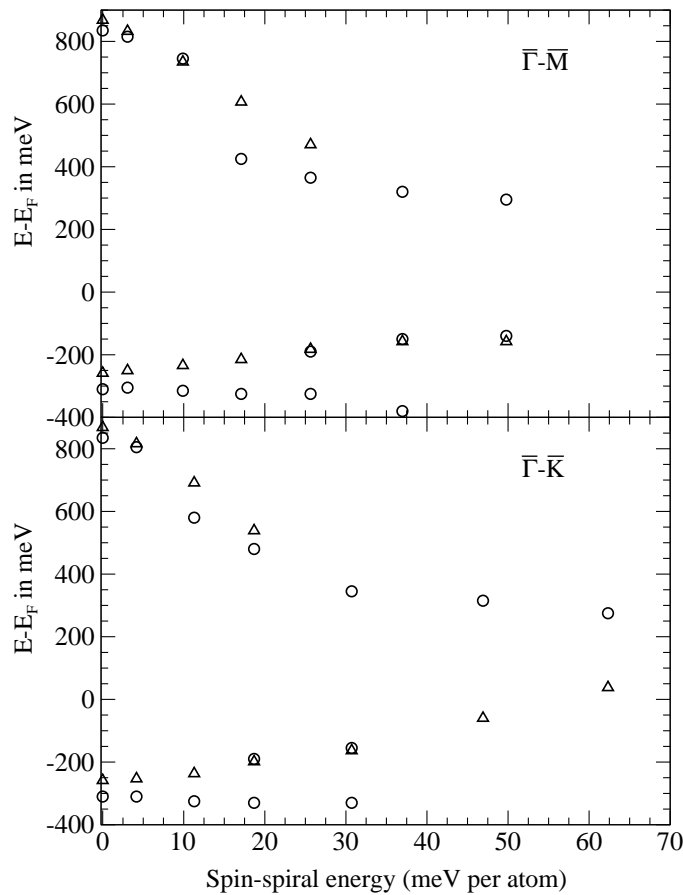


**Figure 7.12:** Position of the occupied and unoccupied peak in the vacuum local density of states (circles) and of the spin-split surface state at the  $\bar{\Gamma}$ -point (triangles) as function of the spin-spiral energy for  $q$ -vectors on the line  $\bar{\Gamma}$ - $\bar{M}$  (upper panel) and  $\bar{\Gamma}$ - $\bar{K}$  (lower panel).

an enormous amount of charge in the vacuum region. More than 20% of the charge of these states is found in the vacuum region of the FLAPW method, which starts above the muffin-tin spheres of the surface atoms. However, the minority part of the surface state quickly loses its surface localization with increasing  $\mathbf{q}$ . Presumably, this is due to the increasing possibility to hybridize with bulk majority states in the same energy region. An analysis of the charge distribution of the states at the  $\bar{\Gamma}$ -point shows that, while the minority surface state loses surface localization and more of its charge is found in muffin-tins far from the surface, the vacuum charge of other (majority) states of the same energy, that have little surface localization in the ferromagnetic state, grows. Due to the hybridization with other states it is difficult to trace the minority part of the surface state beyond the first 4  $q$ -vectors of our calculation. The majority part of the surface state also loses surface localization with increasing  $\mathbf{q}$ , but more slowly than the minority part. Since it falls into a gap of both,

majority and minority state, in the ferromagnetic configuration, there are no states with similar energy available for hybridization (for small values of  $\mathbf{q}$ ).

In conclusion, we can say that the change of the electronic structure, in particular the vacuum local density of states, of spin-spiral calculations with  $q$ -vectors of different size nicely resembles the trends found in temperature dependent scanning tunneling spectroscopy experiments. However, a direct comparison of the theoretical results to an experiment at a certain temperature is difficult. With increasing  $q$ -vector the character of the surface states changes drastically due to hybridization with other states, also with states that originally have a different spin-character in the ferromagnetic configuration. For very large values of  $\mathbf{q}$  we found only a single peak in the vacuum local density of states. In that configuration the valence magnetic moment is still as large as  $0.4 \mu_B$  at the surface. Hence, the decreasing and finally vanishing splitting of the peak of the density of states due to the surface state cannot be taken as support for the applicability of the Stoner model in the sense of a vanishing valence magnetic moment.



# Chapter 8

## Conclusions and Outlook

In the present work we developed and applied a self-consistent full-potential non-collinear vector spin-density ab-initio program for bulk, surfaces and thin films on the basis of the FLAPW method. In order to be able to deal with arbitrary magnetic configurations, which are not necessarily the magnetic ground state or a stationary state of the system under consideration, we implemented the constrained local moment method. On the basis of a generalization of the Bloch theorem for spiral magnetic states we have extended the vector spin-density FLAPW method to also allow commensurate and incommensurate spin-spiral calculations using only the chemical unit cell of the crystal, without the need for large super-cells. Thus, we are able to cover a comprehensive set of magnetic configurations, which is only limited by the available computer time. With the combination of the predictive power of the density functional theory and the accuracy of the FLAPW method, which is ideally suited for open structures, we have obtained a unique and powerful tool to study the non-collinear magnetism of surfaces, thin films and systems with reduced symmetry in general.

We have applied this method to perhaps the classical problem of geometric frustration: the two-dimensional antiferromagnet on a triangular lattice. We have performed self-consistent calculations for the  $3d$  transition metal monolayers V, Cr, Mn and Fe on the (111) oriented surfaces of Cu and Ag. We investigated the magnetism, the interlayer relaxation, and the energetics of a nearly complete set of magnetic states and found an amazing variety of different magnetic ground states: ferromagnetic for Fe/Cu(111) and Fe/Ag(111); row-wise antiferromagnetic for Mn/Ag(111); the  $120^\circ$  Néel state, a two-dimensional non-collinear state in which the direction of the magnetic moment changes by  $\pm 120^\circ$  with respect to the neighboring atoms, for V/Ag(111), Cr/Cu(111) and Cr/Ag(111); and the so-called 3Q state, a complex three-dimensional non-collinear state, which is a superposition of three spin-waves (a picture is shown at the beginning of this thesis), for Mn/Cu(111). In addition, a calculation, that uses a fractional nuclear charge as a model for alloys, suggests the possibility of a spiral magnetic ground state for a monolayer alloy of Fe and Mn.

In order to shed more light on the physical nature of the magnetism of these systems we presented a detailed discussion of the classical Heisenberg model on the

two-dimensional triangular lattice. We developed a  $T = 0$  phase diagram in the parameter space of the exchange integrals. The structure of this phase diagram becomes very rich and complex, when exchange integrals beyond the nearest neighbors are taken into account. Depending on the exchange integrals  $J_1$ ,  $J_2$  and  $J_3$  the magnetic ground state can be collinear, ferromagnetic or row-wise antiferromagnetic, or non-collinear, i.e. the Néel state or spin-spirals that propagate in different high symmetry directions. We tested the validity of the Heisenberg model by calculating the functional dependence of the energy and the magnetic moments with respect to the angle describing the relative orientation of the local moments. Comparing our self-consistent calculations to the Heisenberg model, we found significant deviations. The results of our self-consistent ab-initio calculations show that terms that go beyond the Heisenberg model, like the biquadratic of the 4-spin interaction, play an important role for the itinerant  $3d$  metals. In the case of the Mn monolayer on Cu(111) the higher order terms lead to the stabilization of the 3Q structure. The size of the higher order terms can be appraised directly from the energy difference between the 3Q and the row-wise antiferromagnetic state, because the two states are degenerate within the Heisenberg model irrespective of how many nearest neighbors are taken into account. The physical picture of the magnetism of the two-dimensional antiferromagnets on a triangular lattice has been developed for unsupported monolayers. But all essential results have been confirmed by calculations that included the actual Cu or Ag(111) substrate. The results do not change qualitatively, which means that  $3d$  transition metals on noble metal substrates are a good physical realization of two-dimensional magnets.

We summarize this part of the investigation by concluding that any realistic description of two-dimensional itinerant antiferromagnets on a triangular lattice requires exchange interactions not only beyond the nearest neighbors but also exchange interactions beyond the Heisenberg model. This is an important discovery for the development of models dealing with the quantum fluctuations in these systems.

In the row-wise antiferromagnetic state, the  $120^\circ$  Néel state and in the 3Q state the atoms are chemically indistinguishable and the total magnetic moment integrated over the unit cell is zero. We show that an experimental verification of our predictions will be possible with the spin-polarized scanning tunneling microscope (SP-STM). Depending on the direction of the magnetization of a spin-polarized tip relative to the magnetization of the sample, the SP-STM image will in general display patterns that reflect the magnetic super-structure. By an investigation of the electronic structure of the magnetic monolayers in the vacuum region we verify that it is possible to distinguish between the different magnetic states on the atomic scale using the SP-STM with atomic resolution.

The localized  $4f$  states of Gd represent a challenge for first-principle theory. Our calculations support the findings of previous authors that within the LDA the itinerancy of the  $4f$  states is overestimated. In particular, the large density of states at the Fermi energy due to the minority  $4f$  electrons is unphysical, and our results show that this is the origin of the incorrect prediction of the antiferromagnetic ground state

for hcp Gd by many LDA and GGA calculations. We show that different methods of removing these states from the region close to the Fermi energy, e.g. the treatment of the  $4f$  electrons as localized core electrons, lead to the prediction of the correct ferromagnetic ground state. With these methods ground state properties like the magnetic moment and the equilibrium lattice constant can be determined in good agreement with experiment.

To model the temperature dependence of the electronic structure of the Gd(0001) surface, which has been a matter of extensive debate, we performed non-collinear spin-spiral calculations. We calculated the local density of states, which is probed by scanning tunneling spectroscopy (STS) experiments, as function of the spin-spiral  $q$ -vector. In the ferromagnetic configuration, which would correspond to a zero temperature experiment, we found two pronounced peaks in the local density of states in the vacuum, which originate from the spin-split  $d_{z^2}$  surface state of Gd. These peaks were also observed in actual STS experiments. However, the experimentally observed splitting at low temperatures is smaller (700 meV) than the splitting obtained from the calculation (1.1 eV). With increasing  $q$ -vector, i.e. increasing angle between neighboring atoms, the two peaks in the local density of state approach the Fermi energy from below and above and the splitting decreases. Finally, only a single peak is visible. In all magnetic configuration we found a finite valence magnetic moment. Hence, the decreasing and finally vanishing splitting of the peak of the local density of states due to the surface state cannot be taken as support for the applicability of the Stoner model in the sense of a vanishing valence magnetic moment.

Non-collinear ab-initio calculations on the basis of the FLAPW method have proven to be a powerful tool to investigate non-collinear magnetic states, in particular at surface and in systems with reduced symmetry. The constrained local moment method allows calculations of arbitrary magnetic configurations. Thus, in particular, the total energy of a magnetic system can be calculated as a function of the angle of the local moment. Analogous calculations can be performed as a function of the spin-spiral  $q$ -vector. The results can be fitted to model Hamiltonians, e.g. the Heisenberg model. The parameters that are obtained from such fits can then be used in the framework of the corresponding model to investigate, for example, the finite temperature behavior. Spin-spiral calculations could be used to determine the energies that are associated with the formation of domain walls in ferromagnetic materials, both in the bulk, but also in magnetic films. In combination with calculations of the magneto-crystalline anisotropy, valuable information about the stability and size of domain walls in magnetic films could be obtained. Magnetic frustration will play a growing role in the world of nano-magnetism. The frustration at step edges of interfaces between ferromagnetic and antiferromagnetic materials is one example, which is technologically consequential for the exchange bias effect. Other examples are magnetic molecules, magnetic clusters in the gas phase or deposited on surfaces. A first-principle quantum mechanical description of such systems will become more important, also to understand and optimize technologically relevant effects. Non-collinear calculations are also an important input to determine dynamical properties

such as spin-waves.

In summary, we have developed a powerful tool — a massively parallelized ab-initio full-potential vector spin-density FLAPW program — to deal with constrained and unconstrained, commensurate and incommensurate non-collinear magnetism in the bulk, at surfaces, in thin films, in low-dimensional and open structures and systems with low symmetry in general. In combination with the capability to calculate the total energy and to optimize the structure this tool opens new vistas in the investigation of the magnetic ground state properties, the dynamical properties and the temperature properties in the field of nano-magnetism.

# Appendix A

## Spin Rotations and Coordinate Transformations

The implementation of non-collinear magnetism presented in chapter 5 uses different spin coordinate frames. A global frame  $S^g$ , defining the global spin z-axis and also the x- and y-axis, is used for the interstitial and vacuum region. At each atom we define a local frame  $S^\alpha$  with the local z-axis parallel to the direction of the local magnetic moment. As a consequence, we have to deal with coordinate transformations of three-dimensional real vectors ( $\mathbf{m}$ ,  $\mathbf{B}$ ), two-dimensional complex Pauli spinors ( $\chi$ ) and complex  $2 \times 2$  matrices ( $\boldsymbol{\rho}$ ,  $\mathbf{V}$ ). The aim of this section is to clarify the convention and notation used and to state the formulae that are used in the actual implementation.

### A.1 Euler Angles

A common way to specify a general three-dimensional rotation is the use of the Euler Angles. Here the rotation is separated into three rotations about the axes of a coordinate frame. These rotations are represented by  $3 \times 3$  matrices, e.g. a rotation around the x-axis by an angle  $\varphi$  is performed by applying the matrix

$$\mathbf{R}_x(\varphi) = \begin{pmatrix} 1 & 0 & 0 \\ 0 & \cos \varphi & -\sin \varphi \\ 0 & \sin \varphi & \cos \varphi \end{pmatrix}. \quad (\text{A.1})$$

There are different ways to choose the axes of the three rotations. We use the convention of rotations around the z- and y-axis, where the axes of the coordinate system we rotate around are kept fixed during the whole rotation. The three rotations are as follows. First, we rotate around the z-axis by an angle  $\gamma$ . Second, we rotate around the y-axis by an angle  $\beta$  and the last rotation is again around the z-axis by an angle  $\alpha$ . Thus, a general rotation matrix takes the form

$$\mathbf{R}(\alpha, \beta, \gamma) = \mathbf{R}_z(\alpha) \cdot \mathbf{R}_y(\beta) \cdot \mathbf{R}_z(\gamma) = \quad (\text{A.2})$$



$$\begin{pmatrix} \cos \alpha \cos \beta \cos \gamma - \sin \alpha \sin \gamma & -\cos \alpha \cos \beta \sin \gamma - \sin \alpha \cos \gamma & \cos \alpha \sin \beta \\ \sin \alpha \cos \beta \cos \gamma + \cos \alpha \sin \gamma & -\sin \alpha \cos \beta \sin \gamma + \cos \alpha \cos \gamma & \sin \alpha \sin \beta \\ -\sin \beta \cos \gamma & \sin \beta \sin \gamma & \cos \beta \end{pmatrix}.$$

Here we use the active interpretations of rotations, i.e. the three-dimensional vectors are rotated, not the coordinate system.

## A.2 Coordinate frame transformations

Due to the usage of different spin coordinate frames it is necessary to transform quantities, like for example the integrated local moment inside the muffin-tin sphere  $\alpha$ ,  $\mathbf{M}^\alpha$ , from one spin frame to another. An additional index is added to distinguish between the representations in the different spin frames. When a quantity is represented within the global frame it is notified by an index  $g$ , e.g.  $\mathbf{M}^{\alpha g}$ . The same quantity represented in the local frame or the frame of the effective  $B$ -field is denoted  $\mathbf{M}^{\alpha l}$  or  $\mathbf{M}^{\alpha B}$ , respectively. Before we start to work with the coordinate transformations, we have to define the local spin frames. The reason to introduce a local frame is to work in a frame, that has its  $z$ -axis parallel to the direction of the local magnetization  $\hat{\mathbf{e}}^\alpha$ . Thus, we still have the freedom to rotate the local frame around its  $z$ -axis. We make a choice by setting the Euler angle  $\gamma = 0$  for the rotation that rotates the global frame  $S^g$  into the local frame  $S^\alpha$ . The corresponding rotation matrix is

$$\mathbf{R}^{\alpha g l} = \mathbf{R}(\alpha, \beta, 0) = \begin{pmatrix} \cos \alpha \cos \beta & -\sin \alpha & \cos \alpha \sin \beta \\ \sin \alpha \cos \beta & \cos \alpha & \sin \alpha \sin \beta \\ -\sin \beta & 0 & \cos \beta \end{pmatrix}. \quad (\text{A.3})$$

With this choice, the Euler angles  $\alpha$  and  $\beta$  are equal to the standard polar angles of the local  $z$ -axis in the global frame,  $\alpha = \varphi$  and  $\beta = \vartheta$ . Hence, the basis vectors of the global frame  $\hat{\mathbf{e}}_i^g$  are related to the basis vectors of the local frame  $\hat{\mathbf{e}}_i^\alpha$  by  $\mathbf{R}(\alpha, \beta, 0) \hat{\mathbf{e}}_i^g = \hat{\mathbf{e}}_i^\alpha$ . Defining  $\mathbf{R}^{\alpha l g} = (\mathbf{R}^{\alpha g l})^{-1} (= (\mathbf{R}^{\alpha g l})^{tr})$ , the relation between the representations of a vector quantity, e.g.  $\mathbf{M}^\alpha$ , is given by

$$\mathbf{M}^{\alpha l} = \mathbf{R}^{\alpha l g} \cdot \mathbf{M}^{\alpha g} \quad (\text{A.4})$$

The coordinate frame transformation matrices have the same representation in both, the local and the global frame. This becomes immediately obvious, when a transformation is applied to  $\mathbf{R}^{\alpha l g}$ . For example, to obtain  $\mathbf{R}^{\alpha l g}$  in the local frame it has to be multiplied by  $\mathbf{R}^{\alpha l g}$  and  $\mathbf{R}^{\alpha g l}$  from the left and right, respectively, yielding  $\mathbf{R}^{\alpha l g} \mathbf{R}^{\alpha l g} \mathbf{R}^{\alpha g l} = \mathbf{R}^{\alpha l g} \mathbf{R}^{\alpha l g} (\mathbf{R}^{\alpha l g})^{-1} = \mathbf{R}^{\alpha l g}$ .

### A.3 Spin Rotation Matrices

The corresponding matrix of the rotation matrix in the two-dimensional space of Pauli spinors is the spin 1/2 rotation matrix  $\mathbf{U}$ .

$$\mathbf{U}(\alpha, \beta, \gamma) = \begin{pmatrix} e^{-\frac{i(\alpha+\gamma)}{2}} \cos(\frac{\beta}{2}) & -e^{-\frac{i(\alpha-\gamma)}{2}} \sin(\frac{\beta}{2}) \\ e^{\frac{i(\alpha-\gamma)}{2}} \sin(\frac{\beta}{2}) & e^{\frac{i(\alpha+\gamma)}{2}} \cos(\frac{\beta}{2}) \end{pmatrix} \quad (\text{A.5})$$

The unitary matrix  $\mathbf{U}$  is derived in most standard textbooks, e.g. [OH93]. Again, we use the active interpretation of the rotation, i.e. the wave function (spinor) is rotated. In other words, the expectation value of the rotated spinor with the operator  $\sigma$ , which has the meaning of a magnetic moment, is rotated by the corresponding three-dimensional rotation.

$$\langle \mathbf{U}(\alpha, \beta, \gamma) \chi | \sigma | \mathbf{U}(\alpha, \beta, \gamma) \chi \rangle = \mathbf{R}(\alpha, \beta, \gamma) \langle \chi | \sigma | \chi \rangle \quad (\text{A.6})$$

The proof of this equation is straightforward, but cumbersome. The coordinate system transformation rules are equivalent to (A.4).

$$\chi^{\alpha l} = \mathbf{U}^{\alpha l g} \chi^{\alpha g} \quad (\text{A.7})$$

Where  $\mathbf{U}^{\alpha l g}$  is given by  $\mathbf{U}^{\alpha l g} = (\mathbf{U}(\alpha, \beta, 0))^{-1}$  and the unitary  $U$ -matrices fulfill the condition  $\mathbf{U}^{\alpha l g} = (\mathbf{U}^{\alpha g l})^{-1} = (\mathbf{U}^{\alpha g l})^\dagger$ . The  $2 \times 2$  matrix quantities  $\boldsymbol{\rho}$  and  $\mathbf{V}$  transform like operators, e.g.

$$\boldsymbol{\rho}^{\alpha l} = \mathbf{U}^{\alpha l g} \boldsymbol{\rho}^{\alpha g} \mathbf{U}^{\alpha g l} = (\mathbf{U}^{\alpha g l})^\dagger \boldsymbol{\rho}^{\alpha g} \mathbf{U}^{\alpha g l}. \quad (\text{A.8})$$



# Bibliography

- [AAJB94] R. Ahuja, S. Auluck, B. Johansson, and M.S.S. Brooks. Electronic structure, magnetism, and Fermi surfaces of Gd and Tb. *Phys. Rev. B*, 50:5147, 1994.
- [AAL96] V.I. Anisimov, F. Aryasetiawan, and A.I. Lichtenstein. First-principles calculations of the electronic structure and spectra of strongly correlated systems: the LDA+U method. *J. Phys.: Condens. Matter*, 9:767, 1996.
- [AB98] R. Abt and S. Blügel. First-principles investigation of the formation of Mn/Ag(100) surface alloy. *Phil. Mag. B*, 78:659, 1998.
- [AFM<sup>+</sup>96] S. Andrieu, H.M. Fischer, M.Piecuch, A. Traverse, and J. Mimault. Structure of Mn films grown on (111) and (001) fcc Ir determined by EXAFS and the multiple-scattering approach. *Phys. Rev. B*, 54:2822, 1996.
- [AHP<sup>+</sup>87] A.S. Arrott, B. Heinrich, S.T. Purcell, J.F. Cochran, and L.B. Urquhart. Engineering magnetic materials on the atomic scale. *J. Appl. Phys.*, 61:3721, 1987.
- [AKH<sup>+</sup>96] V.P. Antropov, M.I. Katsnelson, B.N. Harmon, M. van Schilfgaarde, and D. Kusnezov. Spin dynamics in magnets: Equation of motion and finite temperature effects. *Phys. Rev. B*, 54:1019, 1996.
- [AKvSH95] V.P. Antropov, M.I. Katsnelson, M. van Schilfgaarde, and B.N. Harmon. Ab initio spin dynamics in magnets. *Phys. Rev. Lett.*, 75:729, 1995.
- [AM76] N.W. Ashcroft and N.D. Mermin. *Solid State Physics*. Saunders College, Philadelphia, 1976.
- [And75] O.K. Andersen. *Phys. Rev. B*, 12:3060, 1975.
- [APW<sup>+</sup>98] M. Albrecht, J. Pohl, H. Wider, E.U. Malang, J. Kohler, K. Friemelt, and E. Bucher. V and Cr on Ru surfaces. *Surf. Sci.*, 397:354, 1998.
- [ASH<sup>+</sup>99] M. Asato, A. Settels, T. Hoshino, T. Asada, S. Blügel, R. Zeller, and P.H. Dederichs. Full-potential KKR calculations for metals and semiconductors. *Phys. Rev. B*, 60:5202, 1999.

- [AWJE93] R. Ahuja, J.M. Wills, B. Johansson, and O. Eriksson. Crystal structures of Ti, Zr, and Hf under compression: Theory. *Phys. Rev. B*, 22:16269, 1993.
- [Bar61] J. Bardeen. *Phys. Rev. Lett.*, 6:57, 1961.
- [BD89] S. Blügel and P.H. Dederichs. Ferromagnetism and antiferromagnetism of 3d-metal overlayers on noble metal substrates. *Europhys. Lett.*, 9:597, 1989.
- [BDZD89] S. Blügel, D. Drittler, R. Zeller, and P.H. Dederichs. Magnetic properties of 3d-monolayers on metal substrates. *Appl. Phys. A*, 49:547, 1989.
- [BE66] W. Brinkman and R. Elliot. *Proc. R. Soc. A*, 294:343, 1966.
- [BEG84] A.B. Beznosov, V.V. Eremenko, and V.P. Gnezdilov. d-f exchange resonance in gadolinium: theory and experiment. *J. Magn. Magn. Mater.*, 43:243, 1984.
- [BF97] A. Berger and E.E. Fullerton. Phase diagram of imperfect ferromagnetic/antiferromagnetic bilayers. *J. Magn. Magn. Mater.*, 165:471, 1997.
- [BGH<sup>+</sup>98] M. Bode, M. Getzlaff, S. Heinze, R. Pascal, and R. Wiesendanger. Magnetic exchange splitting of the Gd(0001) surface state studied by variable-temperature scanning tunneling spectroscopy. *Appl. Phys. A*, 66:121, 1998.
- [BGW98] M. Bode, M. Getzlaff, and R. Wiesendanger. Spin-polarized vacuum tunneling into the exchange split surface state of Gd(0001). *Phys. Rev. Lett.*, 81:4256, 1998.
- [BGW99] M. Bode, M. Getzlaff, and R. Wiesendanger. *J. Vac. Sci. Technol. A*, 17:2228, 1999.
- [BHB<sup>+</sup>98] P. Bödeker, A. Hucht, J. Borchers, F. Güthoff, A. Schreyer, and H. Zabel. Reorientation of spin density waves in Cr(001) films induced by Fe(001) cap layers. *Phys. Rev. Lett.*, 81:914, 1998.
- [BJA94] P.E. Blöchl, O. Jepsen, and O.K. Andersen. Improved tetrahedron method for Brillouin-zone integrations. *Phys. Rev. B*, 49:16223, 1994.
- [BK94a] D.M. Bylander and L. Kleinman. Ab initio calculation of the properties of the Gd(0001) surface. *Phys. Rev. B*, 50:4996, 1994.
- [BK94b] D.M. Bylander and L. Kleinman. Elimination of local-spin-density approximation errors from electronic-structure calculations of Gd. *Phys. Rev. B*, 50:1363, 1994.

- [BK94c] D.M. Bylander and L. Kleinman. Why the local-spin-density approximation fails to predict the energy bands of Gd correctly. *Phys. Rev. B*, 49:1608, 1994.
- [BK98] D.M. Bylander and L. Kleinman. Full potential ab initio calculations of spiral spin density waves in fcc Fe. *Phys. Rev. B*, 58:9207, 1998.
- [BKB00] G. Bihlmayer, Ph. Kurz, and S. Blügel. Overlayers, interlayers, and surface alloys on the Cu(111) surface. *Phys. Rev. B*, 62:4726, 2000.
- [BLS54] J.R. Banister, S. Legvold, and F.H. Spedding. Structure of Gd, Dy and Er at low temperature. *Phys. Rev.*, 94:1140, 1954.
- [Blü88] S. Blügel. First principles calculations of the electronic structures of magnetic overlayers on transition metal surfaces. Jül. Report 2197, Forschungszentrum Jülich, 1988.
- [Blü95] S. Blügel. Groundstate properties of ultrathin magnetic films, Habilitation. RWTH Aachen, 1995.
- [Blü96] S. Blügel. Magnetically stabilized surface alloys. *Appl. Phys. A*, 63:595, 1996.
- [BR82] G. Binnig and H. Rohrer. Scanning tunnelling microscopy. *Helv. Phys. Acta*, 55:726, 1982.
- [BWD88] S. Blügel, M. Weinert, and P.H. Dederichs. Ferromagnetism and antiferromagnetism of 3d-metal overlayers on metals. *Phys. Rev. Lett.*, 60:1077, 1988.
- [CA80] D.M. Ceperley and B.J. Alder. Ground state of the electron gas by a stochastic method. *Phys. Rev. Lett.*, 45:566, 1980.
- [CBL91] D.J. Crockford, D.M. Bird, and M.W. Long. Band structures of non-collinear magnets in  $\gamma$ -Mn and  $\gamma$ -Fe. *J. Phys.: Condens. Matter*, 3:8665, 1991.
- [CC73] D.J. Chadi and Marvin L. Cohen. Special points in the brillouin zone. *Phys. Rev. B*, 8:5747, 1973.
- [CCT<sup>+</sup>99] L. Capriotti, A. Cuccoli, V. Tognetti, P. Verrucchi, and R. Vaia. Thermodynamics of the quantum easy-plane antiferromagnet on the triangular lattice. *Phys. Rev. B*, 60:7299, 1999.
- [CP97] M.F. Collins and O.A. Petrenko. Triangular antiferromagnets. *Can. J. Phys.*, 75:605, 1997.

- [CTS99] L. Capriotti, A.E. Trumper, and S. Sorella. Long-range Néel order in the triangular Heisenberg model. *Phys. Rev. Lett.*, 82:3899, 1999.
- [Cun74] S.L. Cunningham. Special k-points in 2 dimensions. *Phys. Rev. B*, 10:4988, 1974.
- [DBZA84] P.H. Dederichs, S. Blügel, R. Zeller, and H. Akai. Ground states of constrained systems: Application to cerium impurities. *Phys. Rev. Lett.*, 53:2512, 1984.
- [DF64] J.O. Dimmock and A.J. Freeman. Band structure and magnetism of gadolinium metal. *Phys. Rev. Lett.*, 13:750, 1964.
- [DG90] R.M. Dreizler and E.K.U. Gross. *Density Functional Theory: An Approach to the Quantum Many-Body Problem*. Springer-Verlag, Berlin, 1990.
- [DGP96] M. Donath, B. Gubanka, and F. Passek. Temperature-dependent spin polarization of magnetic surface state at Gd(0001). *Phys. Rev. Lett.*, 77:5138, 1996.
- [EAO<sup>+</sup>95] O. Eriksson, R. Ahuja, A. Ormeci, J. Trygg, O. Hjortstam, P. Söderlind, B. Johansson, and J.M. Wills. Bulk and surface magnetism and interplanar spacings in Gd from first-principles calculations. *Phys. Rev. B*, 52:4420, 1995.
- [EI71] Y. Endoh and Y. Ishikawa. Antiferromagnetism of  $\gamma$ -iron manganese alloys. *J. Phys. Soc. Japan*, 30:1614, 1971.
- [FFOW85] A.J. Freeman, C.L. Fu, S. Ohnishi, and M. Weinert. page 3. World Scientific, Singapore, 1985.
- [FHLB93] M. Fähnle, K. Hummler, M. Liebs, and T. Beuerle. Ab initio electron theory for hard-magnetic rare-earth-transition-metal intermetallics. *Appl. Phys. A*, 57:67, 1993.
- [FHW92] T. Flores, M. Hansen, and M. Wuttig. Structure and growth of Mn on Cu(100). *Surf. Sci.*, 279:251, 1992.
- [FPB<sup>+</sup>90] L.M. Falicov, D.T. Pierce, S.D. Bader, R. Gronsky, K.B. Hathaway, H.J. Hopster, D.N. Lambeth, S.S.P. Parkin, G. Prinz, M. Salamon, I.K. Schuller, and R.H. Victora. Surface, interface, and thin-film magnetism. *J. Mater. Res.*, 5:1299, 1990.
- [FW91] A.J. Freeman and R. Wu. Electronic structure theory of surface, interface and thin-film magnetism. *J. Magn. Magn. Mater.*, 100:497, 1991.

- [GBH<sup>+</sup>98] M. Getzlaff, M. Bode, S. Heinze, R. Pascal, and R. Wiesendanger. Temperature-dependent exchange splitting of the magnetic Gd(0001) surface state. *J. Magn. Magn. Mater.*, 184:155, 1998.
- [GBHW99] M. Getzlaff, M. Bode, S. Heinze, and R. Wiesendanger. New insight into the surface magnetic properties of Gd(0001). *Appl. Surf. Sci.*, 142:558, 1999.
- [GF98] O. Grotheer and M. Fähnle. Ab initio calculations of the torques acting on localized magnetic moments including incomplete-basis-set corrections. *Phys. Rev. B*, 59:13965, 1998.
- [GSFW99] I.L. Grigorov, I-Liang Siu, M.R. Fitzsimmons, and J.C. Walker. Observation and analysis of multidomain epitaxy of  $\alpha$ -Mn on MgO(111). *Phys. Rev. Lett.*, 82:5309, 1999.
- [GSP<sup>+</sup>86] P. Grünberg, R. Schreiber, Y. Pang, M.B. Brodsky, and H. Sowers. Layered magnetic structures: evidence for antiferromagnetic coupling of Fe layers across Cr interlayers. *Phys. Rev. Lett.*, 57:2442, 1986.
- [GW97] I.L. Grigorov and J.C. Walker. Structural and magnetic properties of Mn epitaxially grown on Cu(111). *J. Appl. Phys.*, 81:3907, 1997.
- [GWH<sup>+</sup>98] I.L. Grigorov, J.C. Walker, M.E. Hawley, G.W. Brown and M. Lütt, and M.R. Fitzsimmons. Structural and magnetic properties of “expanded” Mn. *J. Appl. Phys.*, 83:7010, 1998.
- [Ham79] D.R. Hamann. Semiconductor charge densities with hard-core and soft-core pseudopotentials. *Phys. Rev. Lett.*, 212:662, 1979.
- [HBK<sup>+</sup>00] S. Heinze, M. Bode, A. Kubetzka, O. Pietzsch, X. Nie, S. Blügel, and R. Wiesendanger. Real-space imaging of two-dimensional antiferromagnetism on the atomix scale. *Science*, 288:1805, 2000.
- [HBP<sup>+</sup>98] S. Heinze, S. Blügel, R. Pascal, M. Bode, and R. Wiesendanger. Prediction of bias-voltage-dependent corrugation reversal for STM images of bcc (110) surfaces: W(110), Ta(110), and Fe(110). *Phys. Rev. B*, 58:16432, 1998.
- [Hei00] S. Heinze. *First-Principles Theory of Scanning Tunneling Microscopy Applied to Transition-Metal Surfaces*. PhD thesis, Universität Hamburg, 2000.
- [Her66] C. Herring. Academic, New York, 1966.
- [HH00] D. Hobbs and J. Hafner. Fully unconstrained noncollinear magnetism in triangular Cr and Mn monolayers and over-layers on Cu(111) substrates. submitted to *J. Phys.: Condens. Matter*, 2000.



- [HK64] P. Hohenberg and W. Kohn. Inhomogeneous electron gas. *Phys. Rev.*, 136:B864, 1964.
- [HKH00] D. Hobbs, G. Kresse, and J. Hafner. Fully unconstrained noncollinear magnetism within the projector augmented wave method. submitted to *Phys. Rev. B*, 2000.
- [HKW<sup>+</sup>00] S. Heinze, Ph. Kurz, D. Wortmann, G. Bihlmayer, and S. Blügel. Resolving complex atomic-scale spin-structures by SP-STM. submitted to *Phys. Rev. Lett.*, 2000.
- [HPW95] A.B. Hayden, P. Pervan, and D.P. Woodruff. Inverse photoemission of the Cu(001)–Mn phase. *J. Phys.: Condens. Matter*, 7:1139, 1995.
- [HT94] M. Heinemann and W.T. Temmerman. Magnetic structures of hcp bulk gadolinium. *Phys. Rev. B*, 49:4348, 1994.
- [IA99] O. Ivanov and V.P. Antropov. Molecular magnetism: Noncollinear ordering and spin dynamics. *J. Appl. Phys.*, 85:4821, 1999.
- [JA71] O. Jepsen and O.K. Andersen. *Solid State Commun.*, 9:1763, 1971.
- [Jac83] J.D. Jackson. *Klassische Elektrodynamik*. Walter de Gruyter, Berlin, New York, 1983.
- [JG89] R.O. Jones and O. Gunnarsson. The density functional formalism, its applications and prospects. *Rev. Mod. Phys.*, 61:689, 1989.
- [JM91] J. Jensen and A.K. Mackintosh. *Rare Earth Magnetism*. Oxford University Press, Oxford, 1991.
- [JTA<sup>+</sup>00] A.C. Jenkins, W.M. Temmerman, R. Ahuja, O. Eriksson, B. Johansson, and J. Wills. The relationship between interlayer spacing and magnetic ordering in gadolinium. submitted to *Phys. Rev. B*, 2000.
- [Kaw98] H. Kawamura. Universality of phase transitions of frustrated antiferromagnets. *J. Phys.: Condens. Matter*, 10:4707, 1998.
- [KBB00] Ph. Kurz, G. Bihlmayer, and S. Blügel. Noncollinear magnetism of Cr and Mn monolayers on Cu(111). *J. Appl. Phys.*, 87:6101, 2000.
- [KBRW00] M. Kleiber, M. Bode, R. Ravlic, and R. Wiesendanger. submitted to *Phys. Rev. Lett.*, 2000.
- [KE96] M. Körling and J. Ergon. Gradient-corrected *ab initio* calculations of spin-spiral states in fcc-Fe and the effects of the atomic-spheres approximation. *Phys. Rev. B*, 54:8293, 1996.

- [KH77] D.D. Koelling and B.N. Harmon. A technique for relativistic spin-polarized calculations. *J. Phys. C.*, 10:3107, 1977.
- [KHSW88a] J. Kübler, K.H. Höck, J. Sticht, and A.R. Williams. Density functional theory of non-collinear magnetism. *J. Phys. F: Met. Phys.*, 18:469, 1988.
- [KHSW88b] J. Kübler, K.H. Höck, J. Sticht, and A.R. Williams. Local spin-density functional theory of noncollinear magnetism. *J. Appl. Phys.*, 63:3482, 1988.
- [KK63] J.S. Kouvel and J.S. Kasper. *J. Phys. Chem. Sol.*, 24:529, 1963.
- [KK65] J.S. Kouvel and J.S. Kasper. In *Proc. Int. Conf. on Magnetism, Nottingham 1964*, page 169, London, 1965. Institute of Physics and Physical Chemistry.
- [KKO<sup>+</sup>98] W. Kim, W. Kim, S.-J. Oh, J. Seo, J.-S. Kim, H.-G. Min, and S.-C. Hong. Formation of a bilayer ordered surface alloy Mn/Ag(001). *Phys. Rev. B*, 57:8823, 1998.
- [KKP<sup>+</sup>68] E. Krén, G. Kádár, G. Pál, L. Sólyom, P. Szabó, and T. Tarnoczi. *Phys. Rev.*, 140:574, 1968.
- [KKPS67] E. Krén, G. Kádár, G. Pál, and P. Szabó. *J. Appl. Phys.*, 38:1265, 1967.
- [Koe72] D.D. Koelling. *Phys. Rev. B*, 2:290, 1972.
- [Koh85] W. Kohn. *Highlights of Condensed Matter Theorie*. North Holland, Amsterdam, 1985.
- [KPF79] H. Krakauer, M. Posternak, and A.J. Freeman. Linearized augmented plane-wave method for the electronic band structure of thin films. *Phys. Rev. B*, 19:1706, 1979.
- [KS65] W. Kohn and L.J. Sham. Self-consistent equations including exchange and correlation effects. *Phys. Rev.*, 140:A1133, 1965.
- [KS89] B.C.H. Krutzen and F. Springelkamp. Spin-polarized relativistic electronic structure calculations. *J. Phys.: Condens. Matter*, 1:8369, 1989.
- [KS91] Y.V. Knyazev and L.M. Sandratskii. Effect of exchange splitting on the low-energy optical absorption in heavy rare-earth metals. *J. Phys.: Condens. Matter*, 3:9667, 1991.
- [KT75] J. Krizek and K.N.R. Taylor. Optical properties of rare earth films in paramagnetic and magnetically ordered phase. *J. Phys. F: Met. Phys.*, 5:774, 1975.

- [KTMA00] P. Krüger, M. Taguchi, and S. Meza-Aguilar. Magnetism of 3d transition-metal monolayers on Cu(111) and Ag(111). *Phys. Rev. B*, 61:15277, 2000.
- [Küb81] J. Kübler. Magnetic moments of ferromagnetic and antiferromagnetic bcc and fcc iron. *Phys. Lett.*, 81A:81, 1981.
- [Küb95] J. Kübler. Derivation of the single-particle schrödinger equation: Density and spin-density functional theory and the magnetic susceptibility, noncollinear ground states, towards the curie temperature. 1995. Lecture Notes from: Workshop on Condensed Matter Physics.
- [LBC77] J.K. Labg, Y. Baer, and P.A. Cox. Study of the 4f and valence band density of states in rare-earth metals: II. experiment and results. *J. Phys. F: Met. Phys.*, 7:1219, 1977.
- [Lev79] M. Levy. Universal variational functionals of electron densities, first-order density matrices, and natural spin-orbits and solutions of the v-representability problem. In *Proc. Natl. Acad. Sci. USA*, volume 76, page 6062, 1979.
- [LF85] J. Tersoff L.M. Falicov, R.H. Victora. In *The Structure of Surfaces*, volume 2 of *Springer Ser. Surf. Sci.*, page 453, Berlin and Heidelberg, 1985. Springer.
- [LJNL86] D.H. Lee, J.D. Joannopoulos, J.W. Negele, and D.P. Landau. Symmetry analysis and Monte Carlo study of a frustrated antiferromagnetic planar (XY) model in two dimensions. *Phys. Rev. B*, 33:450, 1986.
- [Lou67] T. Loucks. *Augmented Plane Wave Method*. Benjamin, New York, 1967.
- [LPB<sup>+</sup>95] D. Li, J. Pearson, S.D. Bader, D.N. McIlroy, C. Waldfried, and P.A. Dowben. Spin-polarized photoemission studies of the exchange splitting of the Gd 5d electrons near the Curie temperature. *Phys. Rev. B*, 51:13895, 1995.
- [LT72] G. Lehmann and M. Taut. On the numerical calculation of the density of states and related properties. *Status Solidi B*, 54:469, 1972.
- [MFL96] O.N. Mryasov, A.J. Freeman, and A.I. Lichtenstein. Theory of non-Heisenberg exchange: Results for localized and itinerant magnets. *J. Appl. Phys.*, 79:4805, 1996.
- [MGE92] G.A. Mulhollan, K. Garrison, and J.L. Erskine. Surface magnetism of Gd(0001): Evidence of ferromagnetic coupling to bulk. *Phys. Rev. Lett.*, 69:3240, 1992.

- [MJW78] V.L. Moruzzi, J.F. Janak, and A.R. Williams. Pergamon, New York, 1978.
- [MLSG91] O.N. Mryasov, A.N. Lichtenstein, L.M. Sandratskii, and V.A. Gubanov. Magnetic structure of fcc iron. *J. Phys. C.*, 3:7683, 1991.
- [MLSG92] O.N. Mryasov, A.I. Lichtenstein, L.M. Sandratskii, and V.A. Gubanov. Spiral-spin-density-wave states in fcc iron: Linear-muffin-tin-orbital band-structure approach. *Phys. Rev. B*, 45:12330, 1992.
- [MM90] V.L. Moruzzi and P.M. Marcus. Antiferromagnetism in 3d transition metals. *Phys. Rev. B*, 42:8361, 1990.
- [MY77] P.G. Mattocks and R.C. Young. The de Haas-van Alphen effect and Fermi surface of gadolinium. *J. Phys. F: Met. Phys.*, 7:1219, 1977.
- [NKD86] W. Ning, C. Kailai, and W. Dingsheng. Work function of transition-metal surface with submonolayer alkali-metal coverage. *Phys. Rev. Lett.*, 56:2759, 1986.
- [NM00] L. Nordström and A. Mavromaras. Magnetic ordering of the heavy rare earths. *Europhys. Lett.*, 49:775, 2000.
- [NS96] L. Nordström and D.J. Singh. Noncollinear intra-atomic magnetism. *Phys. Rev. Lett.*, 76:4420, 1996.
- [NS99] J. Nogues and I.K. Schuller. Exchange bias. *J. Magn. Magn. Mater.*, 192:203, 1999.
- [OH93] G. Otter and R. Honecker. *Atome Moleküle Kerne, Band I Atomphysik*. B.G. Teubner, Stuttgart, 1993.
- [OPC98] T. Oda, A. Pasquarello, and R. Car. Fully unconstrained approach to noncollinear magnetism: Application to small Fe clusters. *Phys. Rev. Lett.*, 80:3622, 1998.
- [OT94] W.L. O'Brien and B.P. Tonner. Enhanced magnetic moment and magnetic ordering in MnNi and MnCu surface alloys. *J. Appl. Phys.*, 76:6468, 1994.
- [OVH<sup>+</sup>94] K. Ounadjela, P. Venegues, Y. Henry, A. Michel, V. Pierron-Bohnes, and J. Arabski. Structural changes in metastable epitaxial Co/Mn superlattices. *Phys. Rev. B*, 49:8561, 1994.
- [OZD85] A. Oswald, R. Zeller, and P.H. Dederichs. Magnetische 3d-Fremdatome und ihre Wechselwirkung in Kupfer, Silber und Palladium. Berichte der Kernforschungsanlage Jülich – Nr. 2015, ISSN 0366-0885, Forschungszentrum Jülich, 1985.

- [OZT93] W.L. O'Brien, J. Zhang, and B.P. Tonner. Local magnetic properties and magnetic ordering of the two-dimensional surface alloy  $c(2\times 2)$  Mn/Cu(001). *J. Phys.: Condens. Matter*, 5:L515, 1993.
- [Pen96] R. Pentcheva. Ab-initio Rechnungen zum Zusammenhang zwischen Magnetismus und Struktur ultradünner Filme. Diplomarbeit, Universität Köln, 1996.
- [PKBW00] O. Pietzsch, A. Kubetzka, M. Bode, and R. Wiesendanger. Real-space observation of dipolar antiferromagnetism in magnetic nanowires by spin-polarized scanning tunneling spectroscopy. *Phys. Rev. Lett.*, 84:5212, 2000.
- [PW91] P. Perdew and Y. Wang. In *Electronic Structure of Solids*, volume 11, Berlin, 1991. Akademie Verlag.
- [PW92] P. Perdew and Y. Wang. *Phys. Rev. B*, 45:13244, 1992.
- [PZ81] J.P. Perdew and A. Zunger. Self-interaction correction to density-functional approximations for many-electron systems. *Phys. Rev. B*, 23:5048, 1981.
- [QLJF92] J. Quinn, Y.S. Li, F. Jona, and D. Fort. Atomic structure of a Gd(0001) surface. *Phys. Rev. B*, 46:9694, 1992.
- [Rau83] C. Rau. Magnetic order at surfaces and electron capture spectroscopy (ECS). *J. Magn. Magn. Mater.*, 31-34:874, 1983.
- [RGC+97] O. Rader, W. Gudat, C. Carbone, E. Vescovo, S. Blügel, R. Kläsges, W. Eberhardt, M. Wuttig, J. Redinger, and F.J. Himpsel. Electronic structure of two-dimensional magnetic alloys:  $c(2\times 2)$  Mn on Cu(100) and Ni(100). *Phys. Rev. B*, 55:5404, 1997.
- [Ros61] E.M. Rose. *Relativistic Electron Theory*. Wiley, New York, 1961.
- [San86] L.M. Sandratskii. Energy band structure calculations for crystals with spiral magnetic structure. *Status Solidi B*, 136:167, 1986.
- [San91] L.M. Sandratskii. Symmetry analysis of electronic states for crystals with spiral magnetic order. I. general properties. *JPCM*, 3:8565, 1991.
- [San98] L.M. Sandratskii. Noncollinear magnetism in itinerant-electron systems: theory and application. *Advances in Physics*, 47:91, 1998.
- [SDKW96] A.B. Shick, V. Drchal, J. Kudrnovsky, and P. Weinberger. Electronic structure and magnetic properties of random alloys: fully relativistic spin-polarized linear muffin-tin-orbital method. *Phys. Rev. B*, 54:1610, 1996.

- [SG86] L.M. Sandratskii and P.G. Guletskii. Symmetrised method for the calculation of the band structure of noncollinear magnets. *J. Phys. F: Met. Phys.*, 16:L43, 1986.
- [SG89] L.M. Sandratskii and P.G. Guletskii. Energy band structure of bcc iron at finite temperatures. *J. Magn. Magn. Mater.*, 79:306, 1989.
- [SG93] D. Stoeffler and F. Gautier. Magnetic couplings in Fe/Mn and Fe/Cr superlattices. *J. Magn. Magn. Mater.*, 121:259, 1993.
- [SG95] D. Stoeffler and F. Gautier. Theoretical investigations of the magnetic behaviour of Cr monolayers deposited on a Fe(001) substrate: role of a mono-atomic step. *J. Magn. Magn. Mater.*, 147:260, 1995.
- [SG99] M. Sambì and G. Granozzi. Ultrathin V films on Pt(111): a structural study by means of X-ray photoelectron spectroscopy and diffraction. *Surf. Sci.*, 426:235, 1999.
- [SH00] D. Spišák and J. Hafner. Ultrathin Mn films on Cu(111): Frustrated antiferromagnetic order. *Phys. Rev. B*, 61:12728, 2000.
- [SHK89] J. Sticht, K.H. Höck, and J. Kübler. Non-collinear itinerant magnetism: the case of  $\text{Mn}_3\text{Sn}$ . *J. Phys.: Condens. Matter*, 1:8155, 1989.
- [Sie92] H.C. Siegmann. Surface and 2D magnetism. *J. Phys.: Condens. Matter*, 4:8395, 1992.
- [Sin91] D.J. Singh. Adequacy of the local-spin-density approximation for Gd. *Phys. Rev. B*, 44:7451, 1991.
- [Sin94] D. Singh. *Planewaves, Pseudopotentials and the LAPW Method*. Kluwer Academic Publishers, Boston/Dordrecht/London, 1994.
- [SK85] J. Sticht and J. Kübler. Electronic structure of ferromagnetic Gd. *Solid State Commun.*, 53:529, 1985.
- [SK93] L.M. Sandratskii and J. Kübler. Local magnetic moments of conduction electrons in gadolinium. *Europhys. Lett.*, 23(9):661, 1993.
- [SK98] L.M. Sandratskii and J. Kübler. Conduction electron states in gadolinium at finite temperatures. *Proceedings of Magnetism and Electronic Correlations in Local-Moment Systems: Rare-Earth Elements and Compounds*, page 271, 1998.
- [SKHG97] P. Schieffer, C. Krembel, M.C. Hanf, and G. Gewinner. Room-temperature instability of the Mn/Ag(100) interface in the monolayer range. *Phys. Rev. B*, 55:13884, 1997.

- [SKHG98] P. Schieffer, C. Krembel, M.C. Hanf, and G. Gewinner. Formation of a two-dimensional Ag(001) monolayer on epitaxially stabilized Mn(001). *Surf. Sci.*, 398:332, 1998.
- [Sla37] J.C. Slater. *Phys. Rev.*, 51:846, 1937.
- [SLP99] A.B. Shick, A.I. Liechtenstein, and W.E. Pickett. Implementation of the LDA+U method using the full-potential linearized augmented plane-wave basis. *Phys. Rev. B*, 60:10763, 1999.
- [SPF00] A.B. Shick, W.E. Pickett, and C.S. Fadley. Electron correlation effects and magnetic ordering at the Gd(0001) surface. *Phys. Rev. B*, 61:9213, 2000.
- [SRCE96] D. Schmitz, O. Rader, C. Carbone, and W. Eberhardt. Temperature dependence of the magnetic circular dichroism of the c(2\*2) Mn/Ni (100) surface alloy. *Phys. Rev. B*, 54:15352, 1996.
- [SSHK76] E. Schirber, F.A. Schmidt, B.N. Harmon, and D.D. Koelling. Comment on de Haas-van Alphen measurements on gadolinium. *Phys. Rev. Lett.*, 36:448, 1976.
- [SSL<sup>+</sup>00] A. Scholl, J. Stöhr, J. Lüning, J.W. Seo, J. Fompeyrine, H. Siegwart, J.-P. Locquet, F. Nolting, S. Anders, E.E. Fullerton, M.R. Scheinfein, and H.A. Padmore. Observation of antiferromagnetic domains in epitaxial thin films. *Science*, 287:1014, 2000.
- [Sto94] J. Stoer. *Numerische Mathematik 1*. Springer-Verlag, Berlin, 1994.
- [SUW<sup>+</sup>98] G.M. Stocks, B. Ujfalussy, Xin-Dong Wang, D.M.C. Nicholson, W.A. Shelton, Yang Wang, A. Canning, and B.L. Györffy. Towards a constrained local moment model for first principles spin dynamics. *Phil. Mag. B*, 78:665, 1998.
- [TBJ92] D. Tian, A.M. Begley, and F. Jona. New metastable phase of Mn by epitaxy on Cu(111). *Surf. Sci. Lett.*, 273:393, 1992.
- [Ter87] K. Terakura. volume 49 of *Studies in Physical and Theoretical Chemistry*. Elsevier, Amsterdam, 1987.
- [TH83] J. Tersoff and D.R. Hamann. Theory and application for the scanning tunneling microscope. *Phys. Rev. Lett.*, 50:1998, 1983.
- [THOA82] K. Terakura, N. Hamada, T. Oguchi, and T. Asada. Local and non-local spin susceptibilities of transition metals. *J. Phys. F: Met. Phys.*, 12:1661, 1982.

- [TLJ90] D. Tian, R.F. Lin, and F. Jona. A low-energy electron diffraction study of the Pd(001) Mn adsorbed system. *Solid State Commun.*, 74:1017, 1990.
- [TLW<sup>+</sup>92] D. Tian, H. Li, S.C. Wu, F. Jona, and P.M. Marcus. Atomic and electronic structure of thin films of Mn on Pd(111). *Phys. Rev. B*, 45:3749, 1992.
- [TNJ<sup>+</sup>00] A. Taga, L. Nordström, P. James, B. Johansson, and O. Eriksson. Non-collinear states in magnetic sensors. *Nature*, 406:280, 2000.
- [TPY<sup>+</sup>98] E.D. Tober, F.J. Palomares, R.X. Ynzunza, R. Denecke, J. Morais, Z. Wang, G. Bino, J. Liesegang, Z. Hussain, and C.S. Fadley. Observation of a ferromagnetic-to-paramagnetic phase transition on a ferromagnetic surface using spin-polarized photoelectron diffraction: Gd(0001). *Phys. Rev. Lett.*, 81:2360, 1998.
- [Tsu89] Y. Tsunoda. Spin-density wave in cubic  $\gamma$ -Fe and  $\gamma$ -Fe<sub>100-x</sub>Co<sub>x</sub> precipitates in Cu. *J. Phys.: Condens. Matter*, 1:10427, 1989.
- [TWW<sup>+</sup>93] H. Tang, D. Weller, T.G. Walker, J.C. Scott, C. Chappert, H. Hopster, A.W. Pang, D.S. Dessau, and D.P. Pappas. Magnetic reconstruction of the Gd(0001) surface. *Phys. Rev. Lett.*, 71:444, 1993.
- [USK92] M. Uhl, L.M. Sandratskii, and J. Kübler. Electronic and magnetic states of  $\gamma$ -Fe. *J. Magn. Magn. Mater.*, 103:314, 1992.
- [USK94] M. Uhl, L.M. Sandratskii, and J. Kübler. Spin fluctuations in  $\gamma$ -Fe and in Fe<sub>3</sub>Pt Invar from local-density-functional calculations. *Phys. Rev. B*, 50:291, 1994.
- [UUD99] S. Uzdin, V. Uzdin, and C. Demangeat. Magnetic trimer on non-magnetic substrate: From frustration towards non-collinearity. *Europhys. Lett.*, 47:556, 1999.
- [UWN<sup>+</sup>99] B. Ujfalussy, Xin-Dong Wang, D.M.C. Nicholson, W.A. Shelton, G.M. Stocks, Yang Wang, and B.L. Györffy. Constrained density functional theory for first principles spin dynamics. *J. Appl. Phys.*, 85:4824, 1999.
- [vBH72] U. von Barth and L. Hedin. A local exchange-correlation potential for the spin polarized case: I. *J. Phys. C.*, 5:1629, 1972.
- [VCR93] E. Vescovo, C. Carbone, and O. Rader. Surface magnetism of Gd(0001) films: Evidence for an unexpected phase transition. *Phys. Rev. B*, 48:7731, 1993.



- [VSDD95] A. Vega, D. Stoeffler, D. Dreyssé, and C. Demangeat. Magnetic-order transition in thin Fe overlayers on Cr: role of the interfacial roughness. *Europhys. Lett.*, 31:561, 1995.
- [VWN80] S.H. Vosko, L. Wilk, and N. Nusair. Accurate spin-dependent electron liquid correlation energies for local spin density calculations: a critical analysis. *Can. J. Phys.*, 58:1200, 1980.
- [WAG<sup>+</sup>85] D. Weller, S.F. Alvarado, W. Gudat, K. Schröder, and M. Campagna. Observation of surface-enhanced magnetic order and magnetic surface reconstruction on Gd(0001). *Phys. Rev. Lett.*, 54:1555, 1985.
- [Wan50] G.H. Wannier. *Phys. Rev.*, 79:357, 1950.
- [WB93] M. Weinert and S. Blügel. First-principles calculations of magnetic interfaces and multilayers. In L.H. Bennett and R.E. Watson, editors, *Magnetic Multilayers*, Singapore, 1993. World Scientific.
- [Wei81] M. Weinert. Solution of Poisson's equation: beyond Ewald-type methods. *J. Math. Phys.*, 22:2433, 1981.
- [WFF95] M. Wuttig, B. Feldmann, and T. Flores. The correlation between structure and magnetism for ultrathin metal films and surface alloys. *Surf. Sci.*, 331–333:659, 1995.
- [WGG<sup>+</sup>90] R. Wiesendanger, H.-J. Güntherodt, G. Güntherodt, R.J. Gambino, and R. Ruf. Observation of vacuum tunneling of spin-polarized electrons with the scanning tunneling microscope. *Phys. Rev. Lett.*, 65:247, 1990.
- [Whi85] R.M. White. Opportunities in magnetic materials. *Science*, 229:11, 1985.
- [WK99] W. Wulfhekel and J. Kirschner. Spin-polarized tunneling microscopy on ferromagnets. *Appl. Phys. Lett.*, 75:1944, 1999.
- [WKWF81] E. Wimmer, H. Krakauer, M. Weinert, and A.J. Freeman. Full-potential self-consistent linearized-augmented-plane-wave method for calculating the electronic structure of molecules and surfaces: O<sub>2</sub> molecule. *Phys. Rev. B*, 24:864, 1981.
- [WLFF91] R. Wu, C. Li, A.J. Freeman, and C.L. Fu. Structural, electronic, and magnetic properties of rare-earth metal surfaces: hcp Gd(0001). *Phys. Rev. B*, 44:9400, 1991.
- [WSLM<sup>+</sup>96] E. Weschke, C. Schlüssler-Langeheine, R. Meier, A.V. Fedorov, K. Starke, F. Hübinger, and G. Kaindl. Temperature dependence of the exchange splitting of the surface state on Gd(0001): Evidence against spin-mixing behavior. *Phys. Rev. Lett.*, 77:3415, 1996.

- [WT93] M. Wuttig and J. Thomassen. Structure determination for Fe films on Cu(100). *Surf. Sci.*, 282:237, 1993.
- [WWF82] M. Weinert, E. Wimmer, and A.J. Freeman. Total-energy all-electron density functional method for bulk solids and surfaces. *Phys. Rev. B*, 26:4571, 1982.
- [Yos96] K. Yosida. *Theory of Magnetism*. Springer-Verlag, Berlin, 1996.
- [YSK91] R. Yu, D. Singh, and H. Krakauer. All-electron and pseudopotential force calculations using the linearized-augmented-plane-wave method. *Phys. Rev. B*, 43:6411, 1991.
- [ZKD97] Lanping Zhang, M. Kuhn, and U. Diebold. Growth and structure of ultrathin Cr films on Pt(111). *Surf. Sci.*, 371:223, 1997.



# Veröffentlichungen

Teile der vorliegenden Arbeit wurden an folgenden Stellen veröffentlicht:

- D. Wortmann, S. Heinze, Ph. Kurz, G. Bihlmayer, and S. Blügel  
“*Resolving Complex Atomic-Scale Spin-Structures by SP-STM*”,  
submitted to Phys. Rev. Lett.
- Ph. Kurz, G. Bihlmayer, K. Hirai, S. Blügel, and T. Asada,  
Comment on “*Ultrathin Mn films on Cu(111) substrates: Frustrated antiferromagnetic order*”,  
submitted to Phys. Rev. B.
- Ph. Kurz, G. Bihlmayer, K. Hirai, and S. Blügel,  
“*Three-dimensional spin-structure on a two-dimensional lattice: Mn/Cu(111)*”,  
submitted to Phys. Rev. Lett.
- G. Bihlmayer, Ph. Kurz, and S. Blügel,  
“*Overlayers, interlayers, and surface alloys of Mn on a Cu(111) surface*”,  
Phys. Rev. B **62**, 4726 (2000)
- Ph. Kurz, G. Bihlmayer, F. Föster, S. Blügel and L. Nordström  
“*FLAPW goes Non-collinear*”  
<http://psi-k.dl.ac.uk/psi-k/highlights.html>, Newsletter 35 (2000)
- P. Kurz, G. Bihlmayer, and S. Blügel,  
“*Non-Collinear Magnetism of Cr und Mn Monolayers on Cu(111)*”,  
J. Appl. Phys. **9**, 6101 (2000)
- T. Asada, G. Bihlmayer, S. Handschuh, S. Heinze, Ph. Kurz, and S. Blügel,  
“*First-principles theory of ultra-thin magnetic films*”,  
J. Phys.: Condens. Matter **11**, 9347 (1999).



# Danksagung

An erster Stelle möchte ich meinem Betreuer Dr. Stefan Blügel für die intensive Unterstützung dieser Arbeit danken. Von den unzähligen Diskussionen, zu denen Stefan jederzeit bereit war und für die er sich immer viel Zeit genommen hat, habe ich sehr viel gelernt und sehr profitiert. Durch seine freundschaftliche Art und durch seine unerschöpfliche Begeisterung hat er eine Atmosphäre geschaffen die meine Kreativität förderte und mir immer wieder neue Motivation gab.

Herrn Prof. Dr. P.H. Dederichs danke ich für die freundliche Übernahme des Korreferats, sowie für sehr hilfreiche Gespräche über die Methode des “constraints”.

Herrn Prof. Dr. W. Eberhardt danke ich für die Möglichkeit, an seinem Institut promovieren zu können.

Besonders genossen habe ich die Zeit in der ich das Büro zunächst mit Stefan Heinze und dann mit Gustav Bihlmayer geteilt habe. Beide haben auf ihre Art für eine lustige Büroatmosphäre gesorgt und so besonders dazu beigetragen, daß die Arbeit viel Spaß bereitet hat. Nach Stefans Rückkehr nach Hamburg haben Dunja und ich uns immer auf seine Besuche in Aachen/Jülich gefreut. Gustavs Rat beim Umgang mit dem FLEUR (FLAPW) Programm ist unersetzlich. Er hat mir mehr als einmal wertvolle Unterstützung beim Aufspüren und der Lösung technischer Probleme geleistet, und ohne seine Hilfe wäre das “unerklärliche ghost-band Problem” des nichtkollinearen Programms wahrscheinlich heute noch nicht gelöst. Auch seine geduldigen Bemühungen mir die österreichische Lebensart und den Dialekt nahe zu bringen weiß ich sehr zu schätzen.

Ein großer Dank gilt Sean Clarke, Daniel Wortmann, Friedrich Förster, Xiliang Nie und Robert Abt für die gute Zusammenarbeit in unserer Gruppe. Zu der ausgezeichneten und freundschaftlichen Arbeitsatmosphäre haben sie alle auf ihre Weise beigetragen. Besonders möchte ich mich bei Sean für seine große Geduld bei der Beantwortung meiner Fragen bezüglich der englische Sprache und beim Korrekturlesen und bei Daniel für die STM Auswertung der nichtkollinearen Rechnungen bedanken.

Allen Mitarbeitern der Institute IEE und Theorie III danke ich für die Hilfsbereitschaft, für die angenehme Arbeitsatmosphäre, für viele interessante Diskussionen und auch für viele unterhaltsame Gespräche, die nichts mit der Physik zu tun hatten.

I am very thankful to Prof. Dr. Börje Johansson and Dr. Lars Nordström for their invitation to the University of Uppsala, Sweden. In many stimulating discussions with Lars I learned a lot about non-collinear magnetism, in particular spin-spirals, and the FLAPW method.

It is my great pleasure to thank Prof. Dr. Kunitomo Hirai, who introduced me to the Heisenberg model and the world beyond the Heisenberg as well, for our very fruitful collaboration.

Ein besonders großer Dank gilt meiner Freundin Dunja, für ihre liebevolle Unterstützung und ihr Verständnis, mit dem sie mich während der gesamten Arbeit begleitete.

Nicht zuletzt danke ich meinen Eltern, die mich über die Jahre hinweg immer unterstützt haben und mir Rückhalt gaben, nicht nur während der Promotion, sondern während meiner gesamten Ausbildung. Dadurch kommt ihnen ein besonderer Anteil an der Entstehung dieser Arbeit zu.

# Lebenslauf

- persönliche Daten
  - Name: Philipp Kurz
  - geboren am: 08. Juni 1971 in Haan
  - Familienstand: ledig, keine Kinder
  - Adresse: Franzstr. 103  
D-52064 Aachen  
Tel.: (0241) 405802
  - Email: p.kurz@fz-juelich.de
- Schulbildung
  - 08/77 – 06/81 Gemeinschaftsschulen Nützenberger Straße, Wuppertal
  - 08/81 – 06/90 Städtisches Gymnasium an der Bayreuther Straße, Wuppertal  
Abschluß: Abitur
- Wehrdienst
  - 07/90 – 06/91 Generaloberst Hoepner-Kaserne, Wuppertal
- Studium
  - 10/91 – 03/97 Physik-Studium an der RWTH Aachen
  - 10/93 – 07/94 Physik-Studium am Imperial College, London  
Abschluß: Imperial College International Diploma (ICIP)
  - 09/97 – 01/97 Diplomarbeit im Forschungszentrum Jülich, Institut für Festkörperforschung  
Thema: "Non-Collinear Magnetism of Ultrathin Magnetic Films"
  - 03/97 Abschluß: Dipl.-Phys.
- Promotion
  - seit 04/97 Promotion am Forschungszentrum Jülich  
Thema: "Non-Collinear Magnetism at Surfaces and in Ultrathin Films"
  - 08/98 – 10/98 Arbeit als wissenschaftlicher Assistent am Institut für Physik, Uppsala Universität, Schweden
- praktische Tätigkeiten
  - SS 94/95 Studentische Hilfskraft am Lehrstuhl für Theoretische Physik C der RWTH Aachen  
Leitung von Übungsgruppen
  - seit 04/97 Wissenschaftlicher Mitarbeiter im Forschungszentrum Jülich